

# Corrosion of Structural Materials for Advanced Supercritical Carbon- Dioxide Brayton Cycle

---

**Reactor Concepts  
Research Development and Demonstration**

**Kumar Sridharan**  
University of Wisconsin, Madison

Brian Robinson, Federal POC  
Matt Walker, Technical POC



Final Report for Project:

# Corrosion of Structural Materials for Advanced Supercritical Carbon- Dioxide Brayton Cycle

**U.S. DoE-NERI Grant No.:** DE-NE0000677

**Grant Period:** December 5<sup>th</sup> 2013 to December 5<sup>th</sup> 2016

**Principal Investigator/Project Director:** Dr. Kumar Sridharan

**Co-Principal Investigator:** Dr. Mark Anderson

University of Wisconsin, Madison

**Project Contact:** Kumar Sridharan (kumar@engr.wisc.edu)

Date: May 13<sup>th</sup>, 2017

**This page intentionally left blank**

## TABLE OF CONTENTS

EXECUTIVE SUMMARY	4
CHAPTER 1: SC-CO <sub>2</sub> BRAYTON CYCLE FOR POWER CONVERSION	6
CHAPTER 2: SC-CO <sub>2</sub> AUTOCLAVE CORROSION TEST FACILITY, MATERIALS, AND CHARACTERIZATION	11
CHAPTER 3: EVALUATION OF CORROSION OF STRUCTURAL MATERIALS IN SC-CO <sub>2</sub> ENVIRONMENT (450°C – 750°C)	18
CHAPTER 4: CORROSION OF 316 AND 310 STAINLESS STEELS AND ALLOY 709 IN HIGH TEMPERATURE SC-CO <sub>2</sub>	51
CHAPTER 5: EFFECT OF SC-CO <sub>2</sub> CORROSION ON SOLID STATE DIFFUSION BONDING FOR HEAT EXCHANGER APPLICATIONS	60
CHAPTER 6: WEAR AND SPALLATION OF OXIDE LAYERS ON STRUCTURAL ALLOYS FORMED IN HIGH TEMPERATURE SC-CO <sub>2</sub> ENVIRONMENT	77
CHAPTER 7: STRESS CORROSION CRACKING IN HIGH TEMPERATURE SC-CO <sub>2</sub> ENVIRONMENT – A BRIEF SURVEY	91
CHAPTER 8: EXPERIMENTS-SUPPORTED MODELING OF CORROSION OF FERRITIC STEELS IN HIGH TEMPERATURE SC-CO <sub>2</sub> ENVIRONMENT	97



## Executive Summary

The supercritical carbon-dioxide (referred to as SC-CO<sub>2</sub> hereon) Brayton cycle is being considered for power conversion systems for a number of nuclear reactor concepts, including the sodium fast reactor (SFR), fluoride salt-cooled high temperature reactor (FHR), and high temperature gas reactor (HTGR), and several types of small modular reactors (SMR). The SC-CO<sub>2</sub> direct cycle gas fast reactor has also been recently proposed. The SC-CO<sub>2</sub> Brayton cycle (discussed in Chapter 1) provides higher efficiencies compared to the Rankine steam cycle due to less compression work stemming from higher SC-CO<sub>2</sub> densities, and allows for smaller components size, fewer components, and simpler cycle layout. For example, in the case of a SFR using a SC-CO<sub>2</sub> Brayton cycle instead of a steam cycle would also eliminate the possibility of sodium-water interactions. The SC-CO<sub>2</sub> cycle has a higher efficiency than the helium Brayton cycle, with the additional advantage of being able to operate at lower temperatures and higher pressures. In general, the SC-CO<sub>2</sub> Brayton cycle is well-suited for any type of nuclear reactor (including SMR) with core outlet temperature above ~ 500°C in either direct or indirect versions.

In all the above applications, materials corrosion in high temperature SC-CO<sub>2</sub> is an important consideration, given their expected lifetimes of 20 years or longer. Our discussions with National Laboratories and private industry early on in this project indicated materials corrosion to be one of the significant gaps in the implementation of SC-CO<sub>2</sub> Brayton cycle. Corrosion can lead to a loss of effective load-bearing wall thickness of a component and can potentially lead to the generation of oxide particulate debris which can lead to three-body wear in turbomachinery components. Another environmental degradation effect that is rather unique to CO<sub>2</sub> environment is the possibility for simultaneous occurrence of carburization during oxidation of the material. Carburization can potentially lead to embrittlement of structural alloys in SC-CO<sub>2</sub> Brayton cycle. An important consideration in regards to corrosion is that the temperatures can vary widely across the various sections of the SC-CO<sub>2</sub> Brayton cycle, from room temperature to 750°C, with even higher temperatures being desirable for higher efficiencies. Thus the extent of corrosion and corrosion mechanisms in various components and SC-CO<sub>2</sub> Brayton cycle will be different, requiring a judicious selection of materials for different sections of the cycle.

The goal of this project was to address materials corrosion-related challenges, identify appropriate materials, and advance the body of scientific knowledge in the area of high temperature SC-CO<sub>2</sub> corrosion. The focus was on corrosion of materials in SC-CO<sub>2</sub> environment in the temperature range of 450°C to 750°C at a pressure of 2900 psi for exposure duration for up to 1000 hours. The Table below lists the materials tested in the project. The materials were selected based on their high temperature strength, their code certification status, commercial availabilities, and their prior or current usage in the nuclear reactor industry. Additionally, pure Fe, Fe-12%Cr, and Ni-22%Cr were investigated as simple model materials to more clearly understand corrosion mechanisms. This first phase of the project involved testing in research grade SC-CO<sub>2</sub> (99.999% purity). Specially designed autoclaves with high fidelity temperature, pressure, and flow control capabilities were built or modified for this project.

Test Alloys		Tests Completed				
		200 hours	400 hours	600 hours	800 hours	1000 hours
Ferritic up to 450°C	T22 (450°C)					
	T92 (450°C)					
	T122 (450°C)					
Austenitic 550-650°C	310 SS (550°C)					
	347 SS (650°C)					
	Alloy 709 (650°C)					
	Alloy 709 (750°C)					
Ni-based Austenitic >650°C	Haynes 230 (650°C)					
	IN617 (650°C)					
	IN740 (750°C)					
	Haynes 282 (750°C)					
Ceramics >700°C	SiC - Hexoloy™ (750°C)					
Reference Test Alloys	Fe	450°C	450°C	450°C	450°C	450°C
	Fe-12Cr	450°C	450°C	450°C	450°C	450°C
	Ni-22Cr	750°C	750°C	750°C	750°C	750°C

For the ferritic steels tested, an outer magnetite Fe-oxide and a protective inner spinel (Fe, Cr)-oxide layer developed on the steel surface and the corrosion resistance increased with increasing Cr content (Chapters 3 & 8). These steels also developed a deep carburized layer which could have an embrittling effect in the bulk of the

material (Chapter 8). The depth of the carburized region varied inversely as the Cr content of the steel. There was conclusive evidence that oxidation and carburization phenomena were mechanistically interlinked. An exhaustive modeling effort (perhaps the most detailed to-date) was undertaken to model the growth of oxide layer (using the 'available space model') and the carburized layer in these ferritic steels, with excellent agreement with experimental data (Chapter 8). The theoretical foundations set forth by this modeling effort could be extended to other alloys and form the basis for long-term prediction for corrosion in SC-CO<sub>2</sub> environments. From an oxidation standpoint, the results indicate that these ferritic steels would not be suitable for temperatures higher than 450°C, and embrittlement effects of carburization may potentially preclude the use of these steels even at this temperature.

The corrosion of austenitic stainless steels 316 and 310 in SC-CO<sub>2</sub> environments was compared with that of alloy 709, an alloy with higher creep rupture strength (Chapter 4). The corrosion performance of alloy 709 was significantly superior to 316, and also higher than 310 in tests performed at 650°C. The higher Cr content of alloy 709 promoted the formation of an outer Cr-rich oxide layer rather than a less protective magnetite layer that formed on 316 stainless steel. Thus while 300-grade austenitic stainless steels can be used up to 550°C, alloy 709 would be preferred at this temperature and up to 650°C. The Ni-based superalloys exhibited very good performance at 650°C and 750°C with protective self-limiting oxide layer growth (Chapter 3). Of the alloys tested in this category, Haynes 230 and 617 exhibited superior corrosion performance. The nature of the oxide layer formed on these alloys has been evaluated in detail, and mechanisms of corrosion have been explained in detail using the well-known Boudouard reaction ( $2\text{CO} = \text{CO}_2 + \text{C}$ ) as well as chemical equilibrium conditions. Experiments involving exposure of pure graphite to SC-CO<sub>2</sub> environments at 650°C and 750°C showed that the kinetics of the Boudouard reaction occur on time scales relevant to the testing conducted. CO is a 'self-generated impurity' in corrosion in SC-CO<sub>2</sub> environments and its effects must be considered in carbonization and carbide formation. Silicon-carbide exhibited a small initial weight loss, followed by a very low corrosion weight gain due to oxidation. Although differences in corrosion were observed when tested in research grade and industrial grade (99.5% purity) CO<sub>2</sub>, overall corrosion performance in the two environments were not statistically significantly. Experiments with intentional additions of oxygen impurity (10 and 100ppm) showed a dramatic increase in corrosion, suggesting the need to control oxygen impurity at ppm levels. Carburization was not a significant concern in austenitic stainless steel and Ni-based alloys although formation of corrosion-induced carbide phase was observed beneath the oxide layer in some cases.

Solid state diffusion bonding is being considered for fabricating compact heat exchangers for the SC-CO<sub>2</sub> Brayton cycle. The effectiveness of diffusion bonds of 316/316, 310/310, Haynes 230/Haynes 230 against SC-CO<sub>2</sub> corrosion at 650°C was investigated (Chapter 5). The diffusion bonds were fabricated by a private company specializing in this area. The diffusion bonds performed very well for 310/310 and Haynes 230/Haynes 230 couples, but for 316/316 couple, intergranular carbides close to the edge of the sample exposed to SC-CO<sub>2</sub>, were observed indicating that the diffusion bond interface may facilitate material degradation. Regardless, the high temperatures required for fabrication of diffusion bonds (>1000°C) did lead to microstructural changes in all three alloys and must be considered in the future. Wear testing of the oxide layers generated by SC-CO<sub>2</sub> corrosion was performed to evaluate their mechanical fragility (Chapter 6). The tests were intended to determine the wear resistance of oxide layers and also their propensity for delamination or mechanical disintegration under SC-CO<sub>2</sub> flow conditions. Advanced digital image analysis methods were implemented to evaluate and establish metrics for oxide wear and spallation. Finally, preliminary tests were conducted to evaluate the propensity for stress corrosion cracking (SCC) in SC-CO<sub>2</sub> environments using U-bend tests of 316 stainless steel and Haynes 230 alloy (Chapter 7). A comparison was made between SCC samples tested in air (as a non-carbon bearing environment) and in SC-CO<sub>2</sub> environments. No detectable cracking was observed in the samples exposed to SC-CO<sub>2</sub> environment. However, the testing procedure had many limitations and pointed to the need for performing thin sample tensile tests after SC-CO<sub>2</sub> corrosion testing or still better, *in situ* tensile testing in SC-CO<sub>2</sub> environment.

During its three-year term, the project played an important role in initiating other national research programs and collaborations in the area of materials corrosion for SC-CO<sub>2</sub> Brayton cycle application. Collaborations with Oak Ridge National Laboratory (on the materials aspects) and Sandia National Laboratories (on the SC-CO<sub>2</sub> Brayton cycle aspects) organically evolved during this project. The project also involved limited but productive collaboration with CEA, France (French Atomic Energy Commission) where considerable prior work has been performed in this area on ferritic steels. The project has provided a rich scientific environment for training and educating students. Two Masters degree students and a Doctoral degree student (all majors in nuclear engineering) performed research in this project. Additionally, three undergraduate students and two post-doctoral researchers were actively involved in this project.

We thank the U.S. Department of Energy – NEUP program for providing the funding for this project.

# CHAPTER 1: SC-CO<sub>2</sub> BRAYTON CYCLE FOR POWER CONVERSION

## 1.1. Introduction and Motivation

The US Energy Information Agency (EIA) predicts that worldwide electricity demand will increase by 69% over the timeframe 2012-2040, particularly in developing, non-OECD countries. Figure 1.1 depicts the predicted world net electricity generation by energy source as a function of time. In light of the competing interests between increasing electricity demand and emergent concerns about climate change, innovative technologies are required to ensure that increasing electricity demand can be satisfied while minimizing the environmental impact of electricity production. The proposed supercritical carbon dioxide (SC-CO<sub>2</sub>) Brayton cycle is a versatile power conversion cycle that shows promise for marked improvement in heat transfer efficiency and can be connected to many different heat sources including, nuclear, coal, natural gas, and concentrated solar power. As depicted in Figure 1.2, the potential efficiencies of the SC-CO<sub>2</sub> Brayton cycle approach 50% and exceed those of helium-cooled or traditional steam Rankine cycles at elevated temperatures. The SC-CO<sub>2</sub> Brayton cycle is well-suited for advanced reactor technologies such as HTGR, SFR, and FHR which will operate in the high temperatures regimes where such a cycle is ideally suited for providing high efficiencies and improved economics.

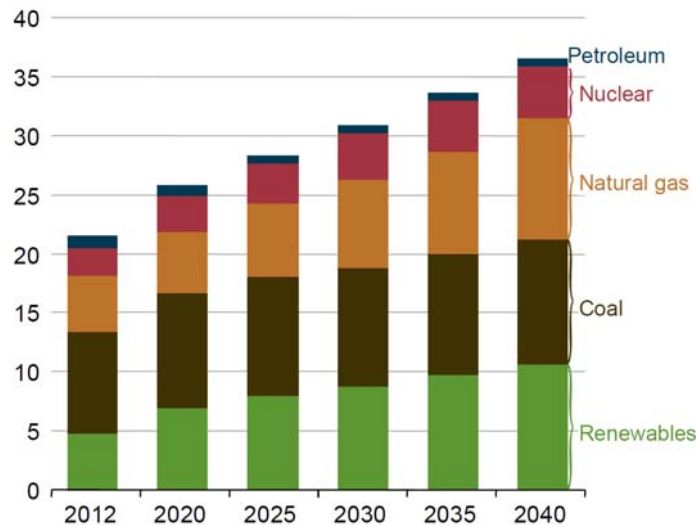


Figure 1.1: World net electricity generation by energy source, 2012-2040 [trillion kWh].

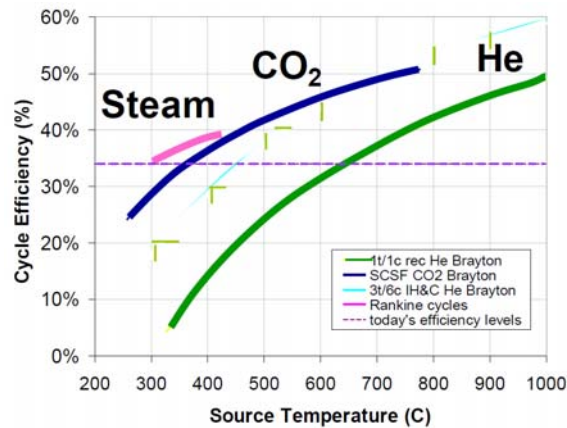


Figure 1.2: Comparison of theoretical efficiencies between different power conversion cycle fluids.

## 1.2. Supercritical CO<sub>2</sub> Brayton Cycle

The basis of the SC-CO<sub>2</sub> Brayton cycle is the implementation of supercritical CO<sub>2</sub> as the working fluid. The use of supercritical fluids in power conversion cycles seeks to take advantage of the fact that these fluids exhibit properties of both the liquid and gaseous states. Figure 1.3 shows the phase regimes specific to CO<sub>2</sub>. The critical point of CO<sub>2</sub> is 30.98°C and 7.38 MPa. The first main advantage of SC-CO<sub>2</sub> is the compressibility of the fluid. Figure 1.4 depicts the compressibility factor of CO<sub>2</sub> plotted for multiple pressures from 7.3-7.5 MPa where the compressibility is defined as the molecular volumetric ratio of a fluid compared with an ideal gas. Alternatively, it describes how much the fluid behaves like an ideal gas. When the compressibility is near unity, it behaves like an ideal gas; when the compressibility is zero it is considered to be an incompressible fluid. Near the critical point for SC-CO<sub>2</sub>, the compressibility of the fluid is on the order of 0.2-0.5, suggesting that the compression work can be substantially decreased within a very small temperature range near the critical point. This behavior is one of the primary reasons the SC-CO<sub>2</sub> Brayton cycle has the potential for increases power cycle efficiency.

As a byproduct of the first advantage described, the second advantage of SC-CO<sub>2</sub> is the drastically reduced size of the turbomachinery. Figure 1.5 shows the relative sizes of turbines that are used in a typical Rankine, a proposed helium-cooled cycle, and the SC-CO<sub>2</sub> Brayton cycle. The reason that the turbomachinery can be reduced so drastically is similar to the compressibility of the fluid; the minimum pressure required for the SC-CO<sub>2</sub> Brayton cycle is much higher ( 7400 kPa) than the steam Rankine cycle (a few kPa), or gas Brayton cycle ( 100 kPa) [4]. The fluid is denser due to the higher pressure, and thus reduces the volumetric flow rate substantially. The third advantage of SC-CO<sub>2</sub> is the higher outlet temperature of the fluid out of the turbine, which increases the thermal efficiency of the power conversion system however this advantage comes with a drawback that the SC-CO<sub>2</sub> Brayton cycle has a much lower cycle pressure ratio. As a result of the high outlet temperature and the low pressure ratio, a large amount of heat is required to be recuperated in order for efficiencies to be realized. Figure 1.6 depicts a typical cycle configuration overlaid atop of a Temperature-Entropy diagram for a proposed SC-CO<sub>2</sub> closed Brayton cycle that relies on intercoolers to obtain high efficiencies. Idealized temperatures and pressures for different iterations of the SC-CO<sub>2</sub> Brayton cycle are shown in Figure 1.7.

Theoretically, the SC-CO<sub>2</sub> Brayton cycle possesses many distinct, positive qualities that show promise for the development of versatile next generation power conversion system, however, long-term corrosion of candidate structural materials in SC-CO<sub>2</sub> continues to be technical gap that must be addressed. This is the focus of the present project.

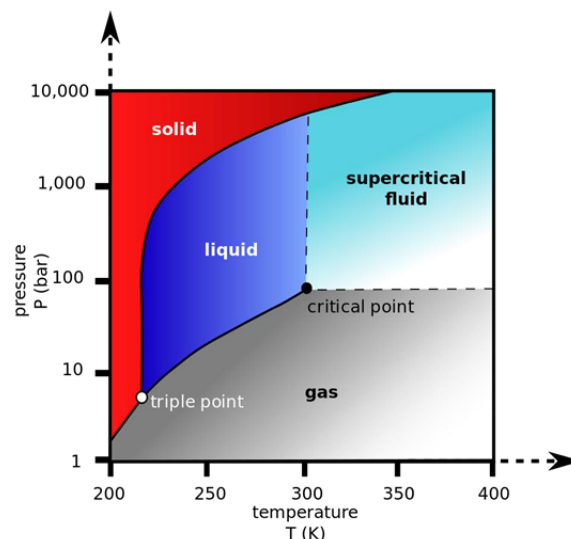


Figure 1.3: Pressure-Temperature Diagram of CO<sub>2</sub> depicting phases including supercritical regime.

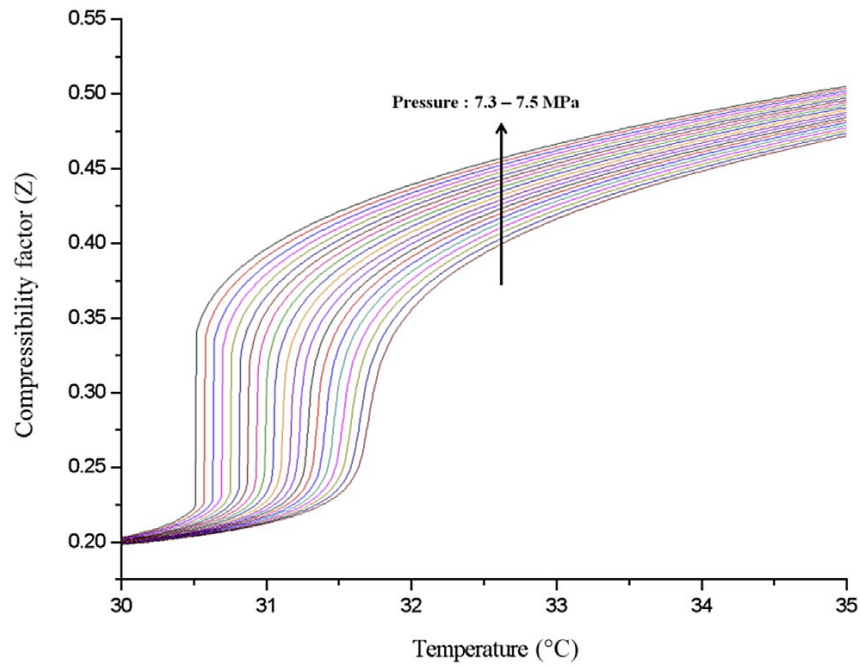


Figure 1.4:  $\text{CO}_2$  compressibility factor near the critical point ( $30.98^\circ\text{C}$ , 7.38 MPa).

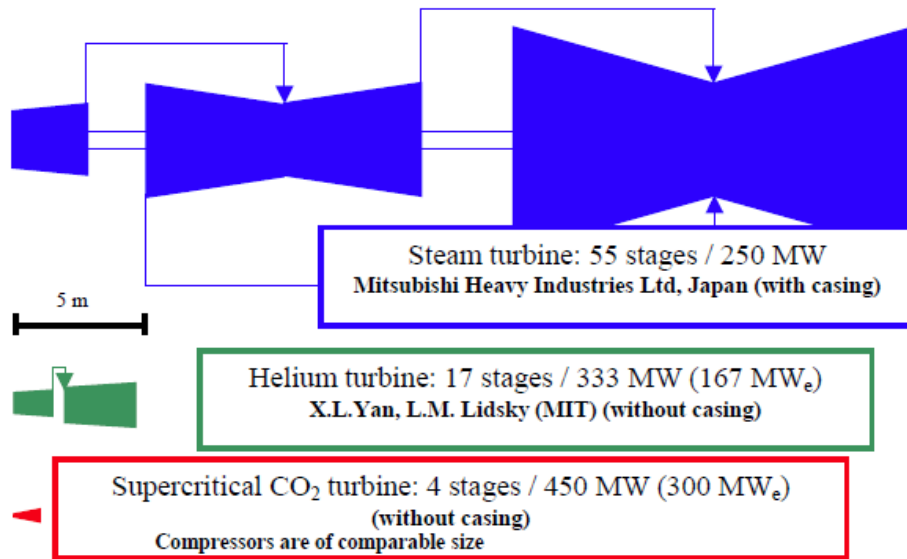


Figure 1.5: Comparison of turbomachinery size between different power conversion cycles.

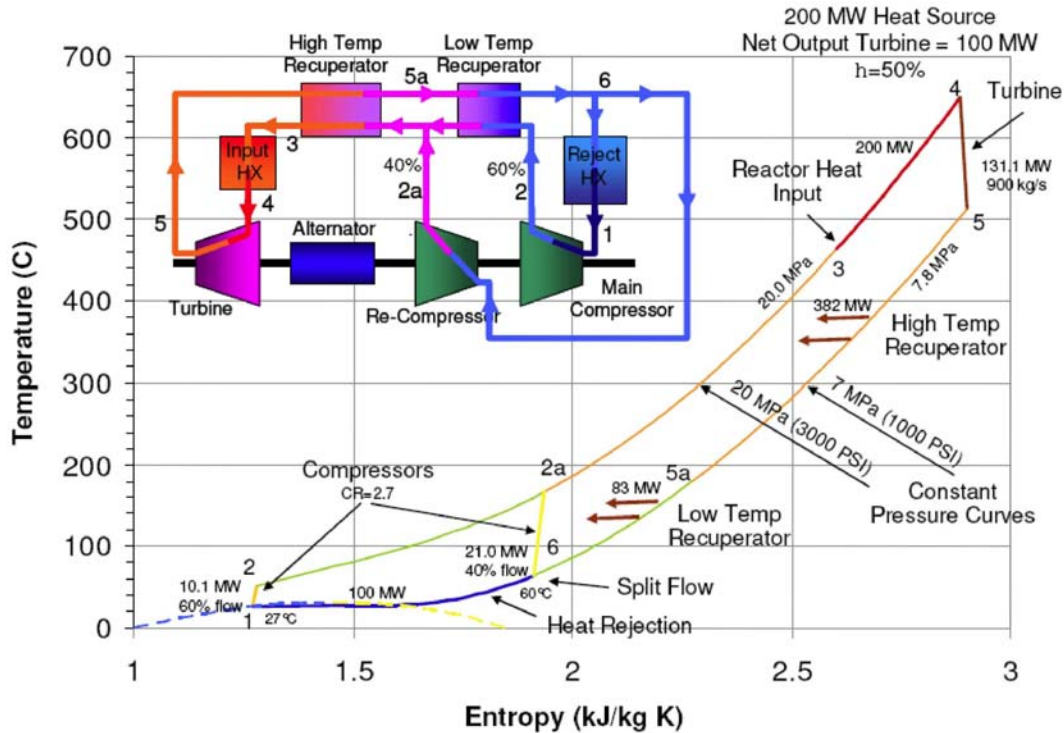


Figure 1.6: Depiction of T-S diagram and cycle layout for Sandia National Laboratories' SC-CO<sub>2</sub> closed Brayton cycle facility.

Application	Organization	Motivation	Size [MWe]	Temperature [C]	Pressure [MPa]
Nuclear	DOE-NE	Efficiency, Size, Water Reduction	10 – 300	350 – 700	20 – 35
Fossil Fuel (Indirect heating)	DOE-FE, DOE-NETL	Efficiency, Water Reduction	300 – 600	550 – 900	15 – 35
Fossil Fuel (Direct heating)	DOE-FE, DOE-NETL	Efficiency, Water Reduction, Facilitates CO <sub>2</sub> Capture	300 – 600	1100 – 1500	35
Concentrating Solar Power	DOE-EE, DOE-NREL	Efficiency, Size, Water Reduction	10 – 100	500 – 1000	35
Shipboard Propulsion	DOE-NNSA	Efficiency, Size	10 – 100	500 – 1000	35
Shipboard House Power	ONR	Efficiency, Size	< 1 – 10	230 – 650	15 – 35
Waste Heat Recovery	DOE-EERE, ONR	Efficiency, Size, Simple Cycles	1 – 10	< 230 – 650	15 – 35
Geothermal	DOE-EERE	Efficiency	1 – 50	100 – 300	15

Figure 1.7: Idealized operating parameters for proposed SC-CO<sub>2</sub> Brayton cycle applications in various energy sectors.

## Bibliography Consulted



Vaclav Dostal, Michael J Driscoll, and Pavel Hejzlar. A supercritical carbon dioxide cycle for next generation nuclear reactors. *Massachusetts Institute of Technology. Dept. of Nuclear Engineering, Cambridge, MA, Paper No. MIT-ANP-TR-100*, 2004.

U.S. Energy Information Administration. International energy outlook 2016 doe/eia- 0484. Technical report, May 2016.

Robert Moore and Thomas Conboy. Metal corrosion in a supercritical carbon dioxide- liquid sodium power cycle. *SAND2012-0184, Sandia National Laboratories, Albuquerque, NM*, 2012.

Yoonhan Ahn, Seong Jun Bae, Minseok Kim, Seong Kuk Cho, Seungjoon Baik, Jeong Ik Lee, and Jae Eun Cha. Review of supercritical  $\{CO_2\}$  power cycle technology and current status of research and development. *Nuclear Engineering and Technology*, 47 (6):647 – 661, 2015. ISSN 1738-5733. doi: <http://dx.doi.org/10.1016/j.net.2015.06.009>.

UR <http://www.sciencedirect.com/science/article/pii/S1738573315001606>.

Steven A Wright, Ross F Radcliff, Milton E Vernon, Gary E Rochau, and Paul S Pickard. Operation and analysis of a supercritical  $CO_2$  brayton cycle. *Sandia Report, No. SAND2010-0171*, 2010.

Jim Pasch. Closed brayton cycle research progress and plans at sandia national labs. Technical report, Sandia National Laboratories (SNL-NM), Albuquerque, NM (United States), 2012.

## CHAPTER 2: SC-CO<sub>2</sub> AUTOCLAVE CORROSION TEST FACILITY, MATERIALS, AND CHARACTERIZATION

### 2.1.1. Facility Overview

Three SC-CO<sub>2</sub> corrosion testing facilities comprising five autoclaves were used in this project. This section provides a detailed description of these facilities. Although many of these facilities existed prior to the commencement of the project, a significant expansion of capabilities was undertaken to further enhance ensure quality assurance and to accommodate the large number of material samples that were evaluated in this project. A schematic illustration and a photograph of the high temperature SC-CO<sub>2</sub> corrosion testing autoclave facility used in this project is shown in Figure 2.1. The autoclave is capable of withstanding tests at temperatures and pressures of 750°C and 3000 psi, respectively. The facility is equipped with temperature, pressure, and flow rate control to ensure consistency between various tests. The dimensions of the autoclave are 127cm x 213cm and 281 cm tall. The system draws approximately 125 amps/240 volts AC power for heaters, 10 amps/120 volts AC power for computing/actuators, and 10 amps/10 volts DC power for heating inlet/outlet lines.

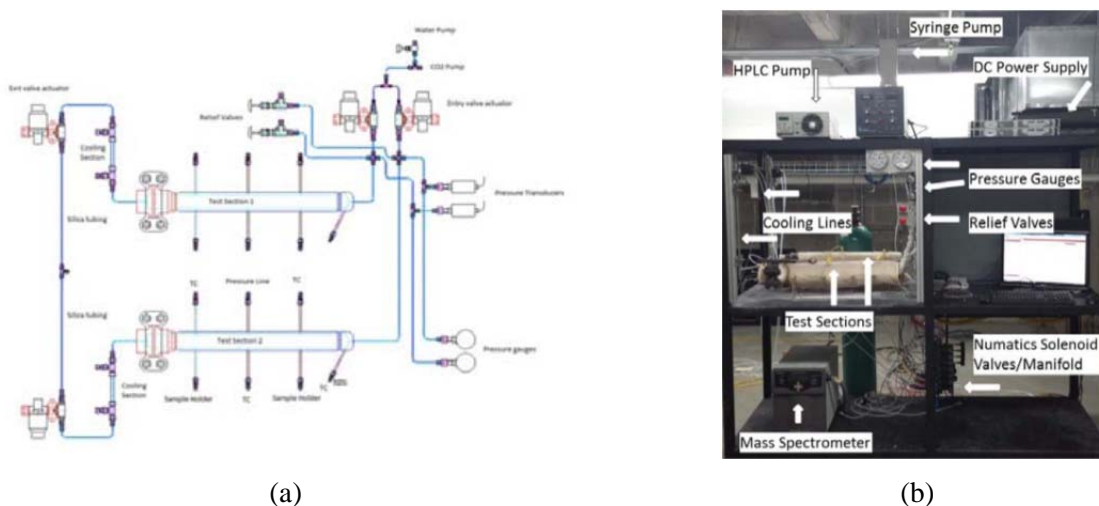


Figure 2.1. (a) Schematic illustration of the SC-CO<sub>2</sub> corrosion autoclave test facility used in this project and (b) photograph of the facility.

### 2.1.2. Gas Supply System

The gas supply system of the corrosion autoclave supplies the test sections CO<sub>2</sub> (research or industrial grade) while also providing the ability to mix impurity species gases such as CO, H<sub>2</sub>O, or O<sub>2</sub>. The system delivers low but constant flow rate enough to refresh the autoclave about every two hours. Based on this refresh rate the flow rate from the pumps was calculated to be about 1.7 ml/min of CO<sub>2</sub> gas.

### 2.1.3. Pumping System

The CO<sub>2</sub> gas is pumped through the system using a Chrom Tech HPLC Supercritical 24 dual piston pump. This pump has a pressure threshold of 10,000 psi with an accuracy limit of 60 psi. The pump has a maximum flow rate of 24 ml/min, and an accuracy of +/- 89 microliters/min. This pump is capable of pressures of up to 10,000 psi with an accuracy limit of 60 psi. Figure 2.2 shows the two pumps used in the project (photographs autoclave and ports for diagnostics, and sample holder are also shown in this figure). These pumps operate at 3,000 psi, and well under the maximum flow rate mentioned earlier. For introduction of impurities, separate liquids can be mixed in a Swagelok tee, and then supplied to the test sections.



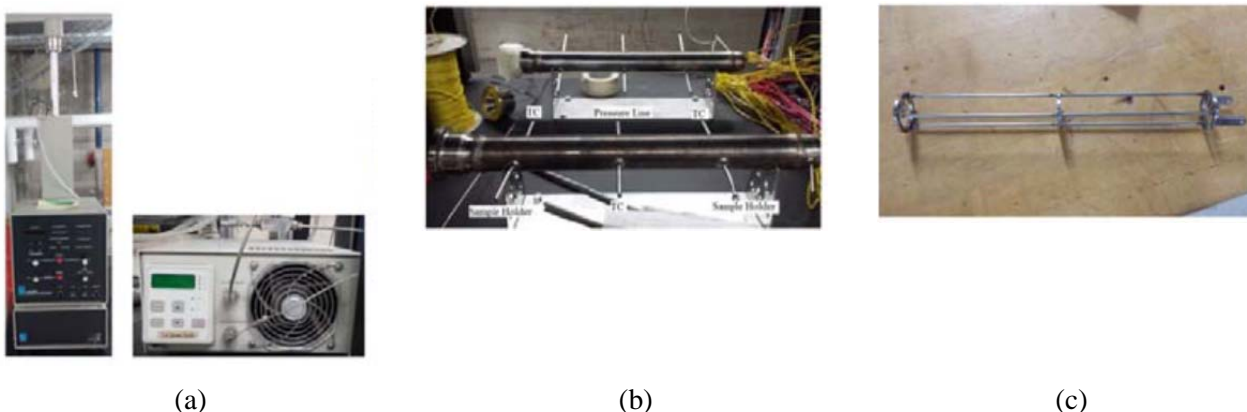


*Figure 2.2. Photographs of the components of the SC-CO<sub>2</sub> corrosion test system: (a) syringe pump (left) and HPLC pump (right), (b) the autoclave and labelled ports, and (c) Inconel 625 sample holder used for holding test material samples.*

#### **2.1.4. Corrosion Test Autoclaves**

Each autoclave is 25 inches long, and made with 2 inch schedule Inconel 625 tubing. The autoclaves have been tested for durability by testing at high pressures of up to 10,000psi at room temperature. Each autoclave has six separate ports, three on each side. The ports allow thermocouples for monitoring the internal temperature of the system, and for measurements of pressure. The autoclave and labeled ports are shown in Figure 2.2b. Each autoclave has been designed to fit a Greyloc fitting and Greyloc caps are attached or removed to insert or remove samples from the test chamber.

In order to suspend the samples evenly throughout the autoclave, a custom sample holder is used (Figure 2.2c). The sample holder is made with Inconel 625, and the samples are suspended along a alumina rod that fits down the slot in the center of the holder. Each sample is separated from the adjacent samples using 1/16 inch alumina spacers to avoid contact between samples. Each sample holder can hold up to 60 samples, allowing for a total of 120 samples to be tested simultaneously in this system.

#### **2.1.5. Heating**

Each test section has separate heating elements to allow for different temperature test in each autoclave. Nichrome wire is taped to the tubing and heated by DC current. The entry lines are wrapped in alumina wool insulation. This entry section supplies heat to maintain constant temperatures in the test section which can reach 750°C. Each autoclave has three sections of attached heating tape which are powered by AC current. The test sections are wrapped in alumina wool and pyrogel insulations. Figure 2.3a shows the heating system and insulation. Nichrome wire is wrapped around the Greyloc fittings to supply heat at the ends of the test section, and to maintain thermal consistency throughout the test section. Once the mixture leaves the test sections, it is cooled from its testing temperature down to 100°C by a water-cooled exterior line. The water cooling section is shown in Figure 2.3b and the gas mixture is maintained at 100°C until vented.



Figure 2.3. Photographs of heating and cooling systems for SC-CO<sub>2</sub> corrosion facility: (a) heating and insulation systems and (b) cooling section with water inlet and exit lines.

### 2.1.6. Temperature Control

Temperature data is collected continuously during the tests. There are several thermocouples that control heating zones across both test sections. These thermocouples (labeled TCX) and heating zones (SCRX/ZX) are labeled in Figure 2.4. In order to get an accurate temperature of the CO<sub>2</sub> in the system, three thermocouples are inserted inside the test sections at the front, middle, and rear of the autoclave. These thermocouples are labeled in Figure 4 as TC1, TC2, and TC3 for test section one, and TC11, TC12, and TC13 for test section 2. Test temperature variations are typically less than  $\pm 1^{\circ}\text{C}$  as shown in sampling of values in Table 2.1.

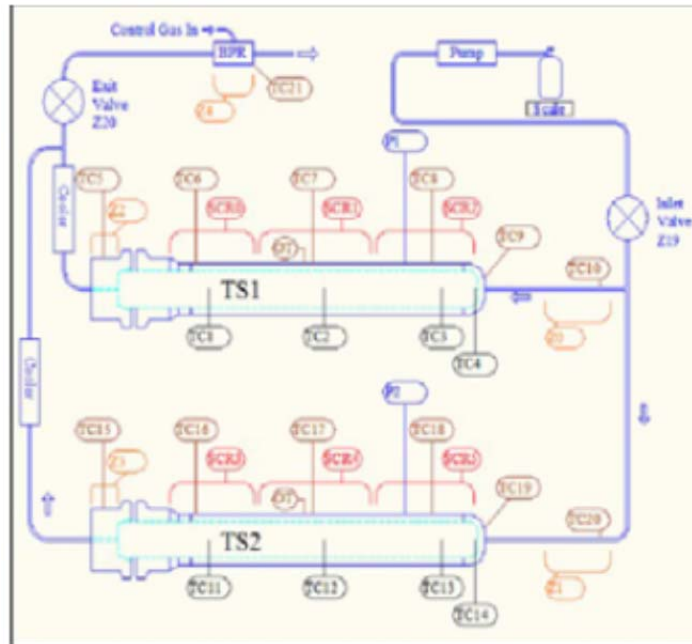


Figure 2.4. Schematic of test facility showing thermocouple and heating zones.

Table 2.1: Sample temperature control data for test sections 1 and 2.

	Test Section 1			Test Section 2		
	TC1 (°C)	TC2 (°C)	TC3 (°C)	TC11(°C)	TC12(°C)	TC13(°C)
Average	550.16	550.08	549.84	450.31	450.06	450.08
St Dev	0.78	0.54	0.79	0.83	0.6	0.63
Max	551.72	551.07	551.5	451.82	451.02	451.3
Min	548.36	549.21	548.55	448.84	449.15	448.88

### 2.1.7. Pressurization

After being cooled to 100°C, the mixture flows to a capillary tube and drops in pressure. The capillary tube used is 30 micrometer ID silica tubing which is inserted into 1/8 inch stainless tubing that is wrapped in Nichrome wire to maintain a constant temperature throughout the capillary tubing. It was calculated that approximately 1.5 meters of the capillary tubing would be required to reach the desired pressure of 3000 psi at the calculated flow rate. Figure 2.5 shows the stainless steel coils that the capillary tube runs through. Once the gas leaves the capillary tubing, it is vented to air at close to atmospheric pressure and at less than 100°C.



Figure 2.5. 1/8" stainless steel tubing wrapped in Nichrome wire with 30m ID capillary tubing.

### 2.1.8. Pressure Control

A crucial aspect of the SC-CO<sub>2</sub> corrosion testing is the ability to maintain a specific pressure for the duration of the test interval. Pressure readings are recorded every ten seconds by Omega brand pressure transducers. Table 3 shows the pressure values from the same 100 hour increment as the temperature readings shown in Table 2.2.

Table 2.2. Characteristics of pressure control statistics of the test facility.

	Pressure (PSI)
Average	2900.2
St Dev	1.1
Max	2913.3
Min	2886.6

### 2.1.9. Flow Rate Control

A system refresh rate for CO<sub>2</sub> was every two hours. The refresh rate is directly related to the flow rate of CO<sub>2</sub> through the system, which is a function of temperature. Calculations for a two hour refresh rate showed that flow rates of 0.12 and 0.18 kg/hr for temperatures of 750°C and 450°C, respectively are needed. Mass change of the CO<sub>2</sub> bottles is recorded, and based on this data that the average mass flow rate was determined to be 0.11 kg/hr.

### 2.1.10 Computer Control

The entire system operation is controlled by Labview. Once the desired pump settings and initial settings are entered into Labview, the system becomes completely automated. The previous system has shown that the PID controls can hold the temperature constant within a 1°C variation for an entire 200 hour run. Temperature and pressure measurements are recorded every 5 seconds, and saved for analysis at the end of each test.

## 2.2. Experimental Parameters

### 2.2.1. Materials for SC-CO<sub>2</sub> Corrosion Testing

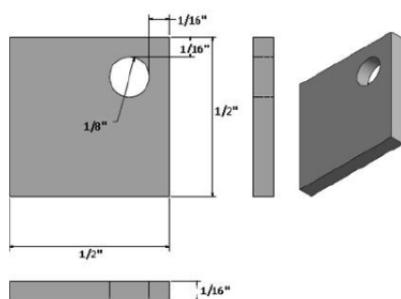
Table 2.3 shows the nominal compositions of materials used in this project. The materials and test temperature ranges of materials were strategically selected so as to span a wide range of components in the S-CO<sub>2</sub> Brayton cycle operating at different temperatures. The materials test matrix focuses more on higher temperature ranges where primary materials challenges in S-CO<sub>2</sub> Brayton cycle are expected. Simpler model alloys were tested in many of these experiments to aid in achieving more fundamental understanding corrosion mechanisms. Additionally, a commercial silicon-carbide, Hexoloy was also investigated. This novel form of silicon carbide is produced by pressure-less sintering of  $\alpha$ -silicon carbide and procured commercially.

*Table 2.3: Nominal composition of alloys (materials) investigated in this study.*

Test Alloys		Reference	Composition (wt.%)										
		Material	C	Al	Si	Ti	V	Cr	Fe	Co	Ni	Mo	W
Ferritic up to 450°C	T22 (450°C)	Fe	0.1	-	0.5	-	-	2.25	Bal.	-	-	1	-
	T92 (450°C)	-	0.12	0.02	0.1	-	0.2	8.94	Bal.	-	0.21	0.5	1.91
	T122 (450°C)	Fe-12Cr	0.11	0.01	0.27	-	0.2	10.7	Bal.	-	0.41	0.35	1.90
Austenitic 550-650°C	310 SS (550°C)	-	0.25	-	1.5	-	-	25	Bal.	-	20.5	-	-
	347 SS (650°C)	-	0.08	-	1	-	-	18	Bal.	-	11	-	-
	Alloy 709 (650°C)	-	0.15	-	0.5	0.1	-	20	Bal.	-	25	1.5	-
Ni-based Austenitic >650°C	Haynes 230 (650°C)	Ni-22Cr	0.1	0.3	-	-	-	22.5	1.8	0.3	Bal.	1.2	14.1
	IN617 (650°C)		0.08	1.5	-	0.4	-	22.1	1.09	12.4	Bal.	9.6	-
	IN740 (750°C)		0.03	0.9	-	-	1.8	25	0.7	20	Bal.	0.5	-
	Haynes 282 (750°C)		0.06	1.5	-	2.1	-	20	1.5	10	-	8.5	-
Ceramics >700°C	SiC- Hexoloy™ (750°C)	CVD-SiC											

### 2.2.2. Sample Preparation and Evaluation Procedures

Test samples of the above materials were sectioned by electrical discharge machining (EDM) to dimensions of 0.5" x 0.5" x 0.0625" and a hole 0.125" in diameter was drilled at one of the corners for suspending the samples in the autoclave from an alumina rod holder as depicted in Figure 2.6a. The samples were ground with 800 grit silicon-carbide paper on both sides prior to the tests and cleaned in an acetone bath. An image of a typical, polished, untested sample is shown in Figure 2.6b. The dimensions of the samples were measured with a micrometer which had an accuracy limit of 0.002mm. Three length and width measurements are taken along the edges, and five thickness measurements were made across different locations on the surface to accurately calculate the entire surface area of the samples. Prior to testing, the samples were weighed ten times in a balance with an accuracy limit of 2 micrograms. Between each individual sample measurement, a mass standard was weighed to ensure balance calibration.



(a)



(b)

Figure 2.6. Depictions of samples for SC-CO<sub>2</sub> corrosion testing: (a) sample dimensions and (b) photograph of the actual sample testing.

Testing was conducted in 200 hour increments up to 1000 hours. Six samples of a specific alloy were loaded into the autoclave at the beginning of tests, with one sample being removed at each 200 hour interval, leaving two samples exposed for 1000 hours. After each 200 hour increment samples were removed for weight change measurements and analysis. Weight change measurements (per unit area of sample, as an initial metric of corrosion) was performed using Sartorius CPA26P high accuracy weighing balance with an accuracy of  $\pm 1\mu\text{g}$ . Scanning Electron Microscopy (SEM) coupled with Energy Dispersive Spectroscopy (EDS) (LEO 1530 and JEOL 6100) were used for high magnification imaging of corrosion layers both in both plan view and cross-sectional imaging. EDS was used for compositional analysis in the microstructure (both point analysis and line-scan analysis were used). Bruker D8 Advance X-ray diffractometer was used to determine the phases constituting the corrosion product layers. Pin-on-disk wear testing was used to measure the wear resistance of the oxide layers formed on various alloys and a Zygo white-light interferometer was used to evaluate the dimensions of the wear track produced from wear experiments. Vickers microhardness measurements were used to evaluate carburization effects, if any that might occur within the alloys.

### 2.2.3. Gas Purity

Testing was conducted in research and industrial grade CO<sub>2</sub> (purity limits shown in Table 2.4) in 200 hour increments. All testing was performed at a pressure of 2900psi.

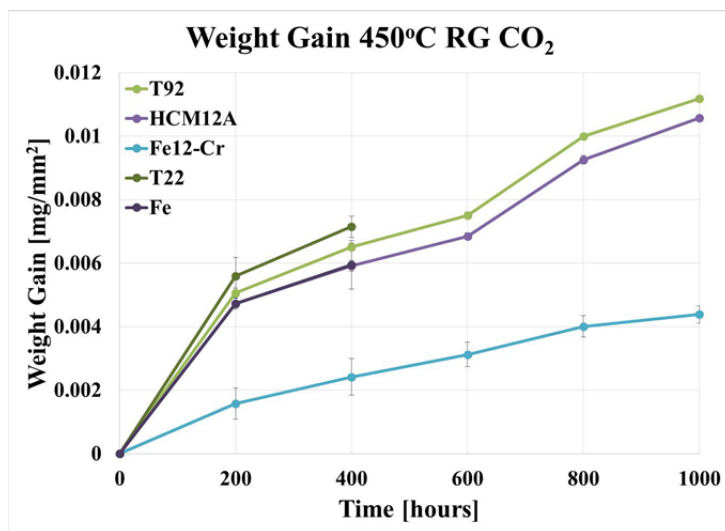
*Table 2.1: Gas composition specifications received from Airgas Company for research and industrial grades CO<sub>2</sub> used in this project.*

<b>Research Grade CO<sub>2</sub></b>			<b>Industrial Grade CO<sub>2</sub></b>	
Component	Purity Limits		Component	Purity Limits
CO <sub>2</sub>	99.999%		CO <sub>2</sub>	99.5%
Ar+O <sub>2</sub> +CO	<1 ppm		Oxygen	<50 ppm
Total Hydrocarbons	<1 ppm		Total Hydrocarbons	<50 ppm
Moisture	<3 ppm		Moisture	<32 ppm
Nitrogen	<5 ppm		Non-Volatile Residue	<10 ppm

## CHAPTER 3: EVALUATION OF CORROSION OF STRUCTURAL MATERIALS IN SC-CO<sub>2</sub> ENVIRONMENT (450°C – 750°C)

### 3.A Evaluation Corrosion in RG SC-CO<sub>2</sub> at 450°C, 650°C, and 750°C

The weight gain data for after corrosion testing at 450°C is shown in Figure 3.1. At this temperature we investigated only ferritic steels, given that it would not be cost-effective to used austenitic alloys, including stainless steels and Ni-based alloys at these relatively low temperatures. As expected, alloys containing higher Cr exhibit lower oxidation as evidenced by the lower weight gain. All alloys exhibit a generally parabolic oxide growth trend. Of the commercial alloys, T122 (~12%Cr, HCM12A) exhibited the lowest weight gain whereas T22 (~2%Cr) experiences the highest weight gain. The weight gain for T92 steel (~9%Cr) was only slightly higher than T122 steel. Interestingly, the reference test alloy Fe exhibits weight gains that are very similar to T122 for the first 400 hours of exposure whereas the Fe-12Cr alloy exhibits the lowest weight gain of all alloys tested at 450C; however, with a larger deviation in recorded. This could be due to the nodular growth expected with binary alloys.



(a)

Figure 3.1. Weight gain for ferritic steels after testing in RG SC-CO<sub>2</sub> at 450°C.

SEM and EDS analyses were conducted on alloy T92 after exposure to 450°C SC-CO<sub>2</sub> for 1000 hours. Figure 3.2 shows cross-sectional SEM micrograph of the oxide layer and the corresponding EDS elemental line-scan analysis. A duplex oxide layer was observed to form on the T92 ferric steel exposed to 450 °C SCO<sub>2</sub> for 1000 hours, the top layer primarily comprised of a magnetite iron-oxide and the layer underneath was comprised of (Fe-Cr)-oxide spinel oxide layer.



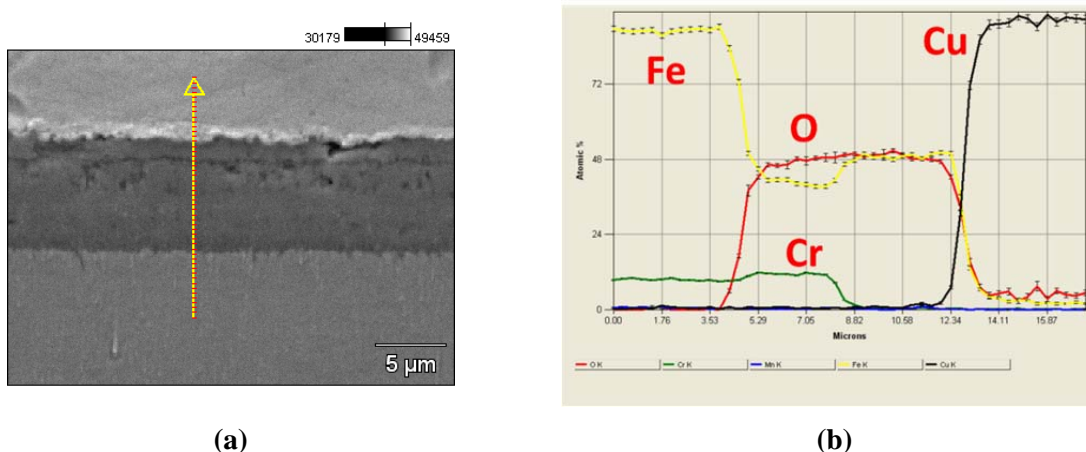


Figure 3.2: (a) SEM cross section micrograph and (b) corresponding EDS line-scan of alloy T92 after exposure to 450°C RG SC-CO<sub>2</sub> for 1000 hours.

The weight gain data for after corrosion testing in RG SC-CO<sub>2</sub> at 650°C is shown in Figure 3.3. Ferritic steels were not tested at this temperature due to the anticipated high corrosion rate and spallation. 347 stainless steel exhibited oxide layer spallation as evidenced by weight loss, while 316 stainless steel exhibited para-linear oxide growth behavior and unacceptable levels of weight gain. Ni-based alloys 617 and Haynes 230 exhibited very low weight gains, while alloy 709 and 310 steels also performed significantly better than 316 and 347 stainless steels.

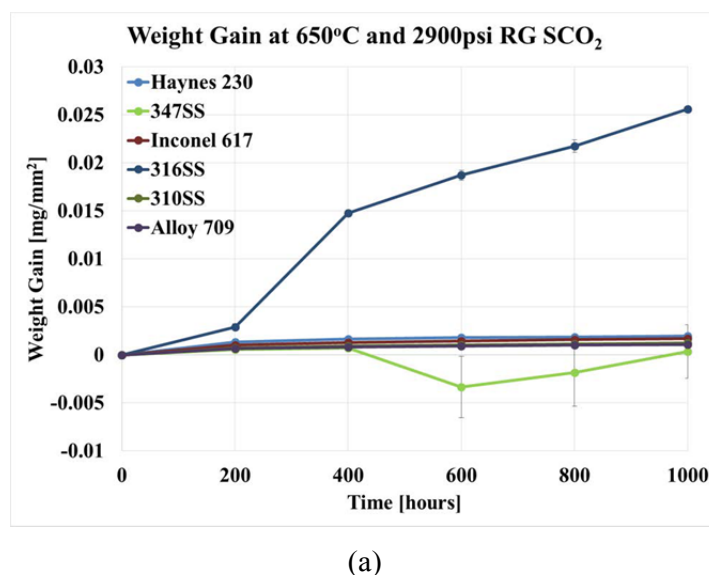
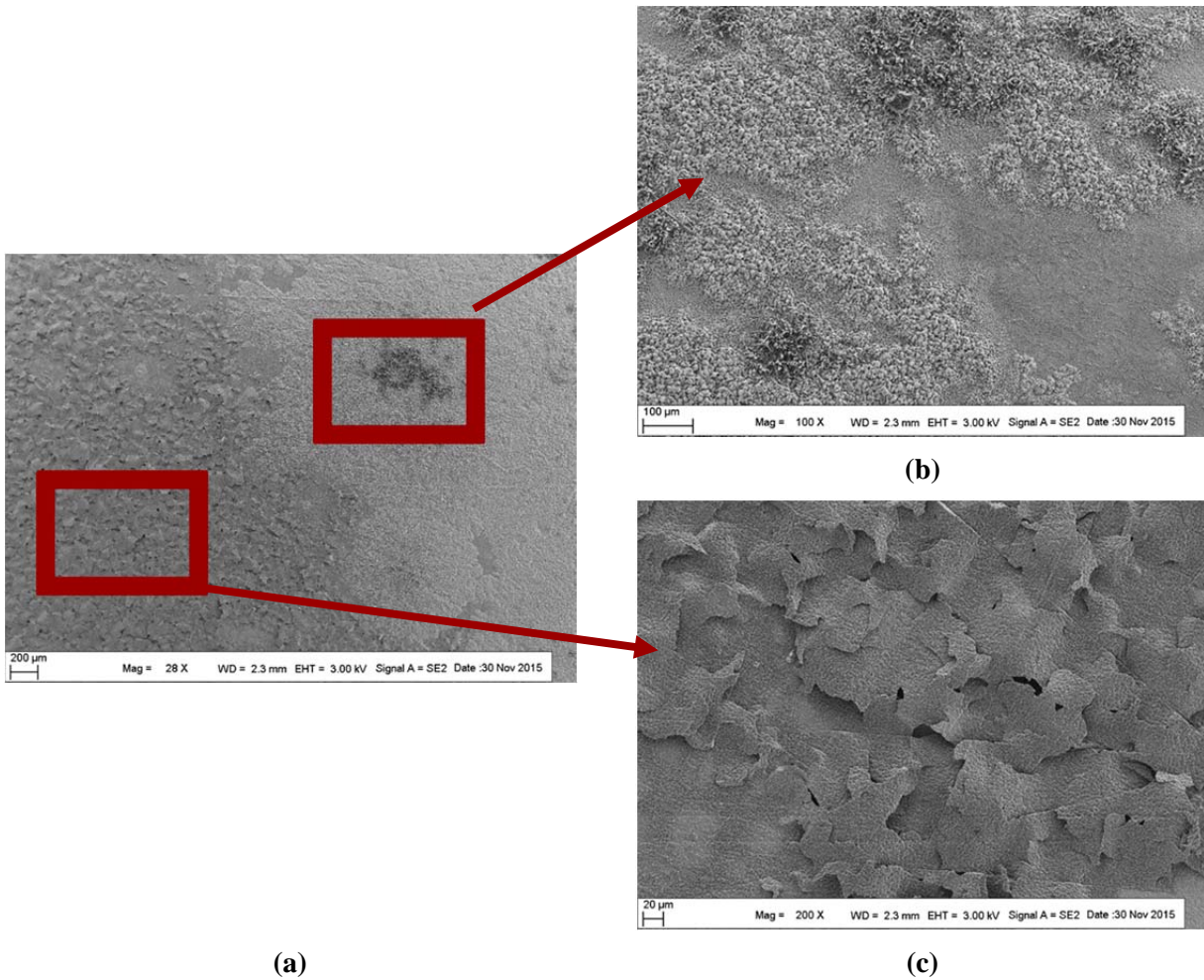


Figure 3.3. Weight gain for austenitic alloys after testing in RG SC-CO<sub>2</sub> at 650°C.

Of particular interest is rather poor performance of the widely used, code certified 316 stainless steel. Figures 3.4 and 3.5 show the cross-sectional SEM micrographs presented earlier where both oxide layers were present and not present. Figure 3.4 depicts a plan view SEM micrographs shows the development of an oxide layer as well as oxide cracking. Figure 3.5 shows an accompanying EDS elemental mapping for the SEM micrograph depicted in Figure 3.4. Areas of crystalline oxide development appear to be a duplex oxide magnetite/spinel with a non-negligible contribution from carbon, whereas areas of oxide cracking appear to be chromium rich with signal from Ni, Mo and Mn.





*Figure 3.4: (a) SEM plan view micrograph of 316 stainless steel after 200 hours exposure to 650°C in research grade CO<sub>2</sub> depicting (b) oxide layer formation and (c) cracking of the oxide layer.*

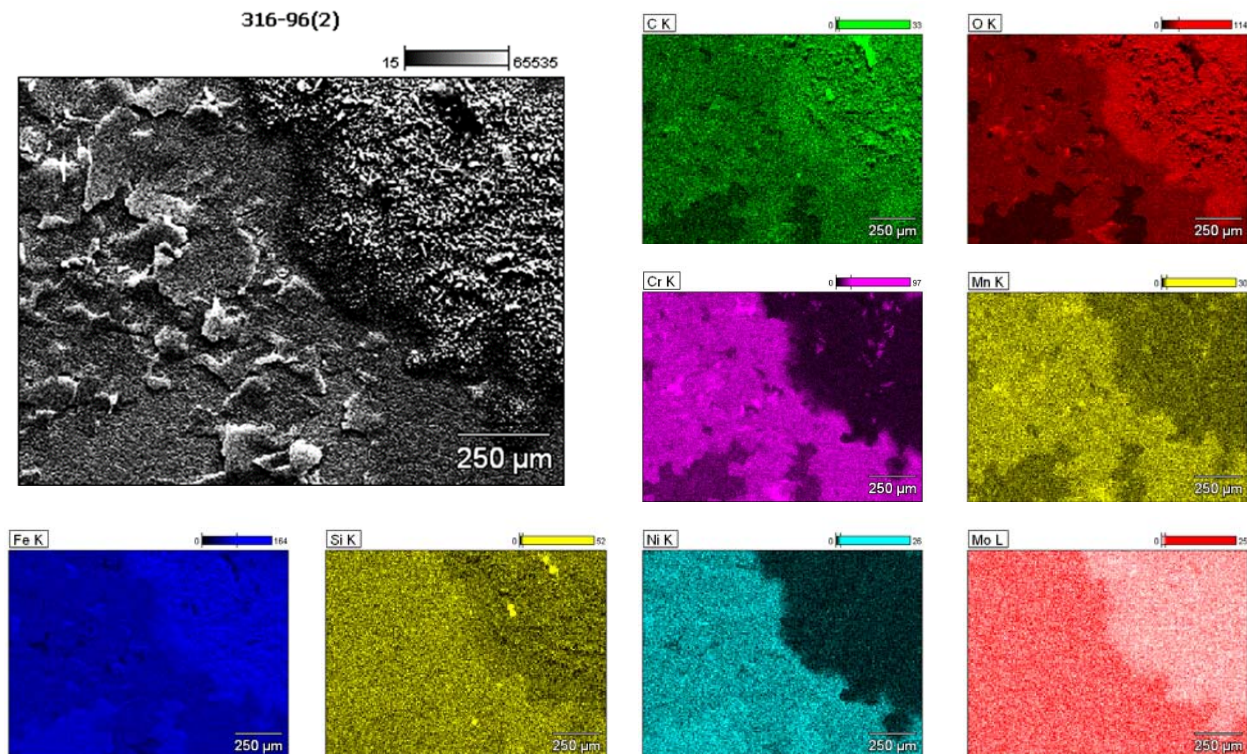


*Figure 3.5: SEM plan view micrograph of 316SS after 200 hours exposure to 650°C in research grade CO<sub>2</sub> and accompanying EDS elemental mapping depicting the formation of two different oxide layer phases and spallation.*

Testing at 750°C was performed for Ni-based alloys Haynes 230, Haynes 282, and Inconel 740, model binary alloy Ni-22%Cr and SiC ceramic (Figure 3.6). All Ni-base alloys and model alloy Ni-22%Cr exhibited diffusion-limited protective oxide layer growth - Haynes 230 exhibited the smallest weight gain and Haynes 282 exhibited the highest weight gain - however, the magnitude of the weight gain was small enough such that the alloys should not be necessarily ranked from this data in terms of corrosion resistance. SiC exhibited an initial weight loss followed by weight gains, and effect that could be attributed to the initial removal of carbon from SiC through the Boudouard reaction followed by the creation of a protective SiO<sub>2</sub> oxide layer.

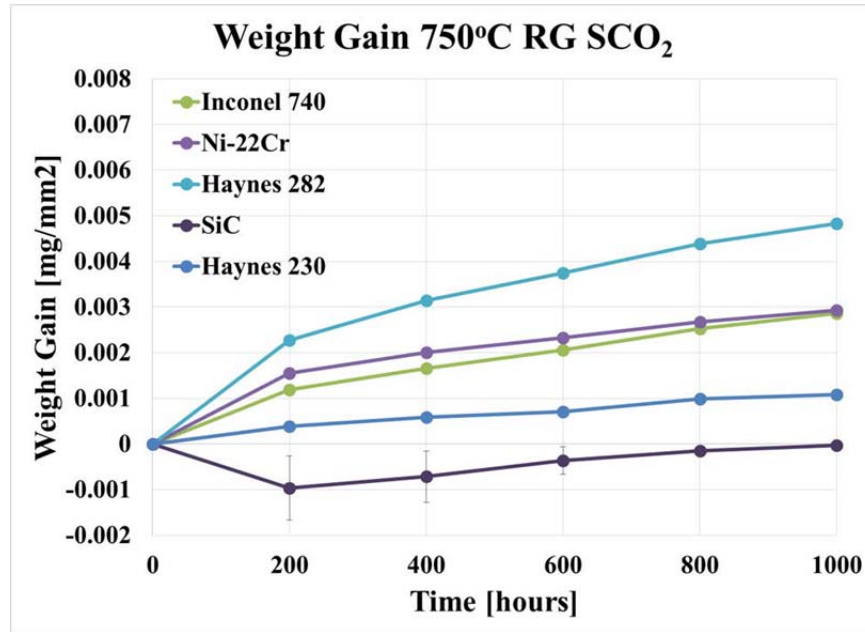


Figure 3.6. Weight gain for austenitic alloys after testing in RG SC-CO<sub>2</sub> at 750°C.

### Section 3.B: Corrosion in SC-CO<sub>2</sub> with impurities

Thus far we have reported results using research grade CO<sub>2</sub>, however we are also investigating corrosion industrial grade CO<sub>2</sub> as well. The available compositions of the two grades of CO<sub>2</sub> provided by the commercial vendor are shown in Table 3.1. Preliminary data indicates that corrosion rates are lower in industrial grade CO<sub>2</sub> for nickel-based alloys. It is hypothesized that an impurity present in the industrial grade CO<sub>2</sub> that is not present in the research grade CO<sub>2</sub> may be responsible for this unexpected behavior.

Table 3.1: Gas composition specifications received from Airgas Company for research and industrial grades CO<sub>2</sub>.

Research Grade CO <sub>2</sub>			Industrial Grade CO <sub>2</sub>	
Component	Purity Limits		Component	Purity Limits
CO <sub>2</sub>	99.999%		CO <sub>2</sub>	99.5%
Ar+O <sub>2</sub> +CO	<1 ppm		Oxygen	<50 ppm
Total Hydrocarbons	<1 ppm		Total Hydrocarbons	<50 ppm
Moisture	<3 ppm		Moisture	<32 ppm
Nitrogen	<5 ppm		Non-Volatile Residue	<10 ppm

Figure 3.7 shows SEM plan view images of Haynes 230 after exposure in 650°C SC-CO<sub>2</sub> for 400 hours. The most notable difference between corrosion of this alloy in the two grades of CO<sub>2</sub> was the presence of carbon clusters on the surface of the samples tested in research grade CO<sub>2</sub>. Elemental x-ray mapping showed these clusters to be composed of carbon due to decomposition of CO<sub>2</sub>. These carbon clusters did not form on the surface of the sample tested in industrial grade CO<sub>2</sub>.



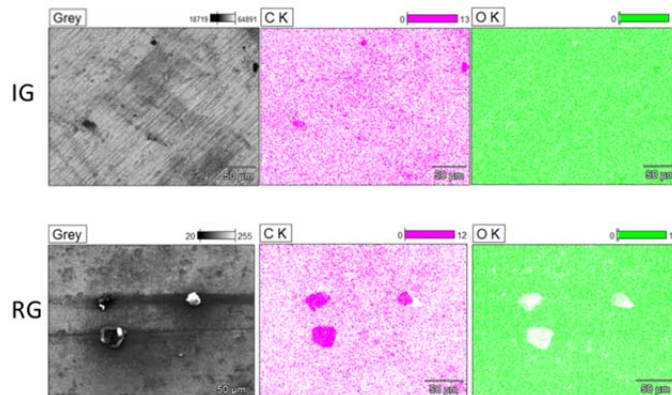


Figure 3.7. SEM surface images and elemental x-ray maps of Haynes 230 after corrosion testing in SC-CO<sub>2</sub> at 650°C for 600 hours: industrial grade (top row) and research grade (bottom row).

Table 3.1 details the difference between research and industrial grade CO<sub>2</sub>. The purity limits do not define the composition of the gas, but rather they merely set as a minimum standard for which the gas can be classified as industrial or research grade. In order to understand how impurities may be contributing to the reduced corrosion rate of samples in the industrial grade CO<sub>2</sub>, a sample of the industrial grade CO<sub>2</sub> was sent to an external testing facility (Airborne Labs) for analysis to determine the composition of the gas more accurately. Airborne Labs tested the concentration of approximately 50 different impurities in this sample and the results of their analysis are shown in Table 3.2.

The total hydrocarbon concentration was less than 0.1 ppm. Since no hydrocarbons were detected, the detectable impurities, nitrogen and oxygen, were investigated using HSC Chemistry software to develop a rationale on what effect they could have on corrosion rates.

Table 3.2: Results of composition analysis of industrial grade CO<sub>2</sub> from Airborne Laboratories.

Test Description	Result	LOQ (ppm)
CO <sub>2</sub> Purity	99.99+	5
Water vapor	"--"	1
Oxygen (O <sub>2</sub> +Ar)	5.4	10
Nitrogen	27	10
Total Hydrocarbon	nd	0.1
Sulfur	0.011	0.01
Carbonyl Sulfide (COS)	0.011	0.01

The first step in determining the effect of both of these impurities was to check the free energy of formation for any reaction that that could occur given a base metal (nickel and chromium), CO<sub>2</sub>, and varying amounts of the impurity. HSC chemistry software was used to determine equilibrium concentrations for as a function of impurity concentration. The system was set to 650°C, 20 MPa, and the impurity concentration was increased from 0 to 40% gas concentration. The results of the HSC analysis are shown in Figure 3.8.

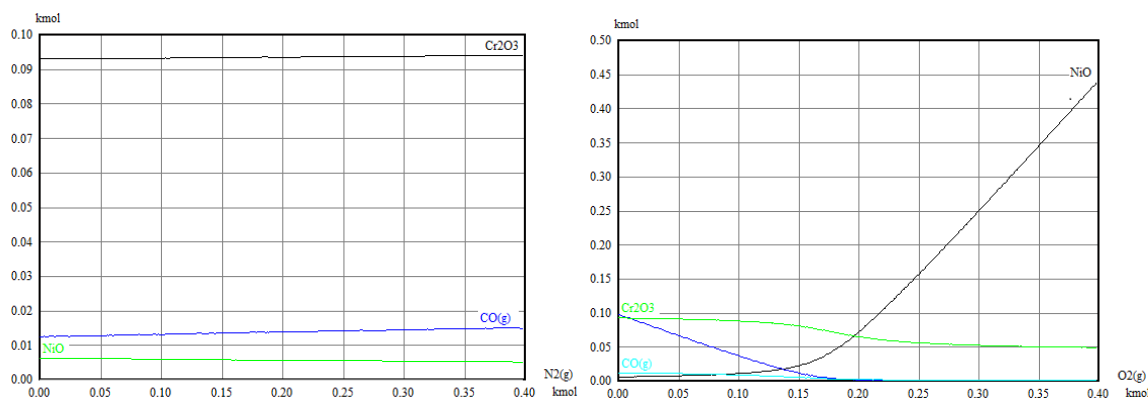


Figure 3.8. HSC Equilibrium calculator for base metal 75%Ni-25%Cr) with 1 kmol of CO<sub>2</sub>, and 0-0.4 kmol N<sub>2</sub> (left) O<sub>2</sub> (right). Note the different scales for each plot.

The left graph in Figure 3.8 shows the effect of increasing the nitrogen concentration for the equilibrium of all possible oxides and carbides that can form. There is almost no change for the two oxides that appear under these conditions. The right graph shows the effect of increasing the oxygen concentration. This plot shows that there are some changes in the oxide formation, and that the oxygen concentration has an effect on the equilibrium concentrations.

Based on the HSC results, the effect of oxygen as the impurity was analyzed in greater detail. Free energy diagrams for the oxidation of carbon and CO are shown in Figure 3.9. These reactions are very favorable based on the large negative  $\Delta G_f$  values. Free energy values can only be used to determine final equilibrium concentrations, but it is important to point out that the shift in the favorability of these reactions as temperature increases. As temperature increases, the oxidation of carbon to CO becomes more favorable, the oxidation of carbon to CO<sub>2</sub> remains constant, and the oxidation of CO to CO<sub>2</sub> becomes less favorable. This effect is due to the entropy changes from the change in the number of moles of gas produced in each reaction. These reactions give some insight on why carbon is observed in the research grade (no O<sub>2</sub>), and no carbon is observed on the surface in industrial grade CO<sub>2</sub> (5.4 ppm O<sub>2</sub>). The increased oxygen concentration will react with the free carbon left over from the oxidation of the base metal to form CO/CO<sub>2</sub> that is flushed out of the system. It is our hypothesis presently that the additional oxygen may be stabilizing the protective oxide layer. This hypothesis will be tested by intentionally adding up to 100ppm of oxygen to research grade CO<sub>2</sub> and evaluate corrosion performance of materials.

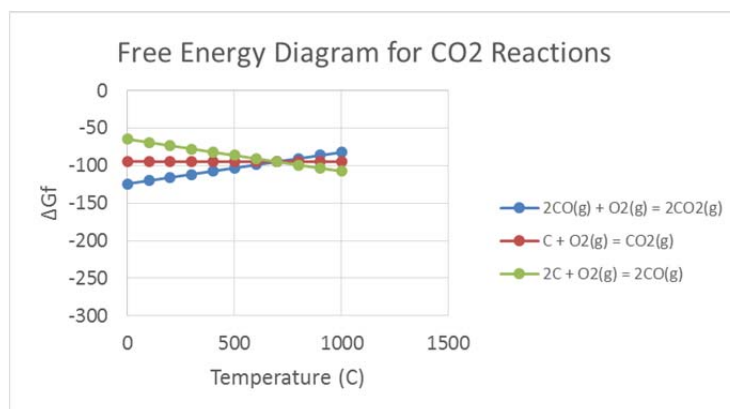


Figure 3.9. Free energy diagram of various surface reactions with increasing temperature.

Testing of superalloys Haynes 230 (H230) and Haynes 625 (H625) was completed at temperatures of 550, 650, and 750°C in CO<sub>2</sub> purities of industrial grade, research grade, 7ppm oxygen-doped research grade,

and 100ppm oxygen-doped research grade CO<sub>2</sub>. Testing of the two alloys at 550°C showed very little weight gain, as was expected for chromia forming superalloys. SEM imaging confirmed that very there was little oxide growth on samples exposed to 550°C (in Figure 3.30). More significant oxidation was observed as temperatures increased to 650 and 750°C. These samples started to show more uniform and complete oxides on the surface of the materials (Figure 3.30). The weight change data has been converted to oxide thickness values by an averaged oxide density. This data is plotted in Figure 3.10 for the two alloys at both 650 and 750°C in all purities of CO<sub>2</sub>. The average density was calculated to be  $1.79 \pm .25$  g/cm<sup>3</sup>.

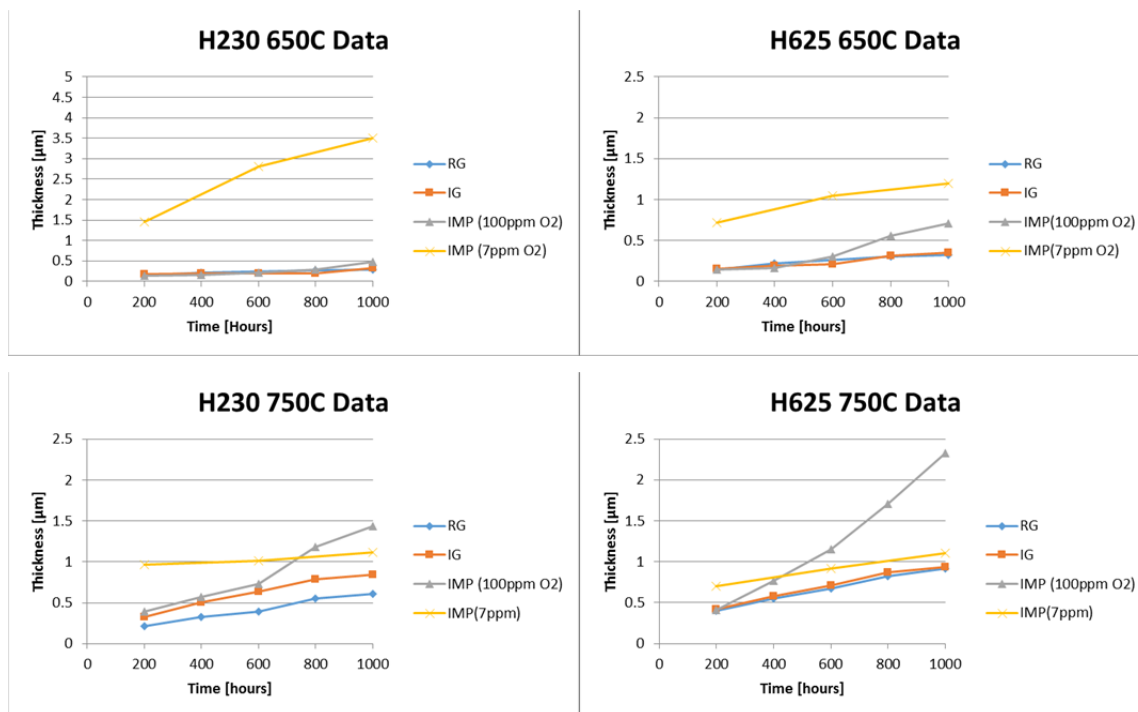


Figure 3.10. Weight change data for H230 and H625 at different temperatures and CO<sub>2</sub> purity.

Statistical evaluation of data in Figure 3.10 for samples removed at the 1000 hour time interval was compiled. The following data sets are not statistically different according to a 95% confidence interval: H230 650°C IG vs RG, H230 750°C 7ppm O<sub>2</sub> vs 100ppm O<sub>2</sub>, H230 750°C IG vs 7ppm O<sub>2</sub>, H625 750°C RG vs IG. Using the calculated thickness measurements in Figure 3.10, yearly estimates of the oxide thickness were calculated using a power law. These results are plotted in Figure 3.11.

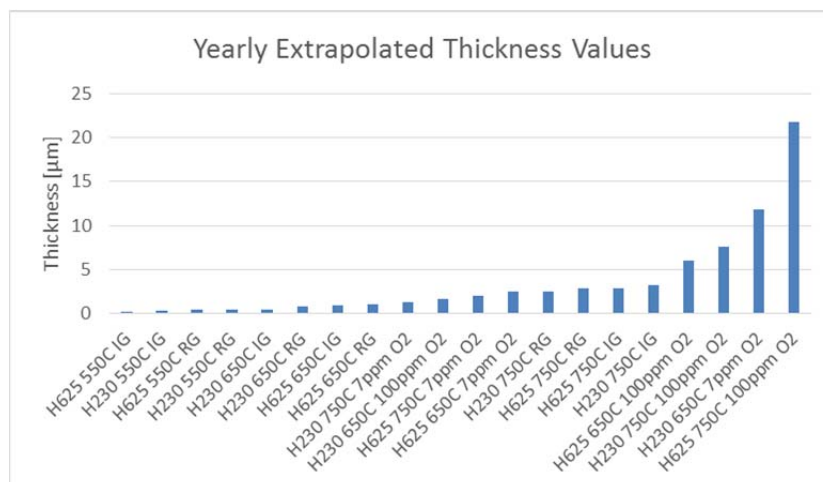


Figure 3.11. Extrapolated thickness values for all conditions using power law fit.

All of the extrapolated data in Figure 3.11 shows less than 30 microns per year of oxide growth. Cross-sectional SEM images for the samples after 1000 hours of testing in each condition are shown in Figure 3.30. A list of null hypotheses were constructed to evaluate the differences in corrosion between RG and IG CO<sub>2</sub>.

- **Null Hypothesis 1:** The corrosion rate for Haynes 625 samples exposed to Research Grade CO<sub>2</sub> is not greater than the corrosion rate for Haynes 625 samples exposed to Industrial Grade CO<sub>2</sub>, all other conditions being held equal.
- **Alternate Hypothesis 1:** The corrosion rate for Haynes 625 samples exposed to Research Grade CO<sub>2</sub> is greater than Haynes 625 samples exposed to Industrial Grade CO<sub>2</sub>, all other conditions being held equal.
  - For 550/650, not 750
- **Null Hypothesis 2:** The corrosion rate for Haynes 230 samples exposed to Research Grade CO<sub>2</sub> is not greater than the corrosion rate for Haynes 230 samples exposed to Industrial Grade CO<sub>2</sub>, all other conditions being held equal.
- **Alternate Hypothesis 2:** The corrosion rate for Haynes 230 samples exposed to Research Grade CO<sub>2</sub> is greater than Haynes 230 samples exposed to Industrial Grade CO<sub>2</sub>, all other conditions being held equal.
  - For 550,650,750 (Very close, statistically significant, but not physically relevant compared to oxygen doped testing)

Since IG CO<sub>2</sub> has a wide range for impurities and concentration limits, it was necessary to select a given impurity to mix with RG CO<sub>2</sub> in order to eliminate any other factors. The main goal of mixing impurities into CO<sub>2</sub> was to characterize the effects that changing the partial pressure of oxygen (pO<sub>2</sub>) and activity of carbon (a<sub>C</sub>) have on the system. Since pure CO<sub>2</sub> has a significantly lower pO<sub>2</sub> than air, the oxidation reactions for several metals were studied to determine if some reactions were not possible in CO<sub>2</sub>. The pO<sub>2</sub> needed to oxidize a given metal has been plotted as a function of temperature in figure 3.12. The pO<sub>2</sub> produced from pure CO<sub>2</sub> dissociation as well as 50 ppm and a 1% carbon monoxide mixture is plotted as well to determine which oxides were thermodynamically allowed in each condition.

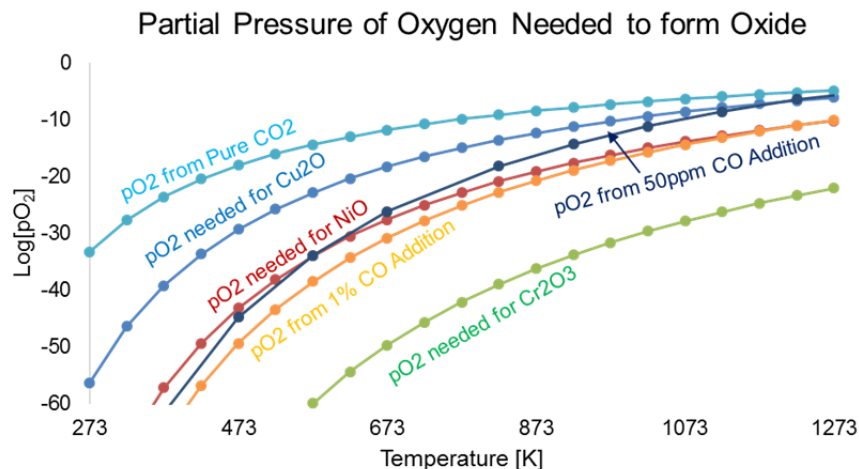


Figure 3.12. Partial pressure of oxygen needed to form oxides of Nickel, copper, and chromium in  $s\text{CO}_2$  environments.

The thermodynamics presented in figure 3.12 show that oxides of chromium, nickel, and copper can all form from the partial pressure of oxygen produced from the dissociation of pure  $\text{CO}_2$ . Once 50ppm of carbon monoxide is added, copper and nickel oxides become unfavorable at some temperatures. When 1% carbon monoxide is added, the formation of copper and nickel oxide only form at very high temperatures. It is important to point out that these calculations are only valid for 100% pure  $\text{CO}_2$  and a pure metal atoms with no restrictions, and an infinite amount of time. In order to understand kinetics, actual testing had to be conducted.

The development of a procedure for mixing minute impurities into the  $\text{CO}_2$  gas was implemented previously in order to quantify the effect of small impurities in  $\text{CO}_2$  has upon corrosion rates. Initial studies have focused on additions of small amounts of oxygen to research grade  $\text{CO}_2$ . As described in the previous yearly reports, an Alpha-Omega Series 3000 Trace Oxygen Analyzer is used for determining the oxygen impurity levels in  $\text{CO}_2$  gas during impurities testing in the inlet and outlet sections of the autoclave. In order to establish a baseline for the behavior of the corrosion testing system with respect to the addition of the oxygen impurity, a dry test run was first performed without the presence of any samples in the dual autoclave. Figure 3.13 depicts the oxygen concentration measured at the three points described and the oxygen consumed in each autoclave (calculated by subtracting the outlet concentration from the inlet concentration for each autoclave) as a function of time for this baseline test. The purpose of the test was to investigate the potentiality of a measurable oxygen reaction rate. Three features of the plot are elaborated upon:

- 1) Apparent in both Figure 3.13 and Figure 3.14, the decreasing oxygen concentration as a function of time is the result of the mixing procedure. The oxygen injected is calculated assuming a homogeneous mixing and solubility of oxygen in the entire  $\text{CO}_2$  mass within the bottle. However, the  $\text{CO}_2$  in the bottles used is a two phase mixture with the liquid phase at the bottom of the bottle and the gas phase at the top of the bottle. The bottles contain a dip tube and draw  $\text{CO}_2$  from the liquid phase of the gas. Oxygen is injected into the  $\text{CO}_2$  bottle through the dip tube however, oxygen is more soluble in the gas phase of the  $\text{CO}_2$  compared to the liquid phase. As more liquid  $\text{CO}_2$  is drawn through the dip tube in time, the volume of the  $\text{CO}_2$  gas phase increases and oxygen preferentially migrates from the liquid phase to the gas phase due to the greater solubility; thus, the oxygen concentration in the  $\text{CO}_2$  available to the autoclaves decreases as a function of time.



- 2) Outlet oxygen concentrations from approximately 0 minutes to 600 minutes appear to decrease significantly and then increase slightly, and then decrease again. This behavior is believed to be attributable to that the system not being flushed of all atmosphere. The increase is believed to be the result of a steady state reaction being established by the system.
- 3) A temperature modification was made around 2200 minutes (designated by “Temp Change (-50C) on both Figure 3.13(a) and (b)) and was done so to investigate if changing the temperature would have an effect on the reaction rate. The outlet oxygen concentration changes significantly in both autoclaves and is believed to be the result of the establishment of a new steady state reaction rate for oxygen within the autoclave.

The data obtained from the test indicates that there exists a steady state reaction rate for the oxygen within the autoclave. Figure 3.13(b) demonstrates that between approximately 1500 minutes and 2200 minutes and between 2800 minutes and 3500 minutes a steady state oxygen reaction rate is established for both autoclaves. The figures also demonstrate that the oxygen reaction rate is greater at higher temperatures (i.e. the reaction rate is greater at 750°C than at 650°C).

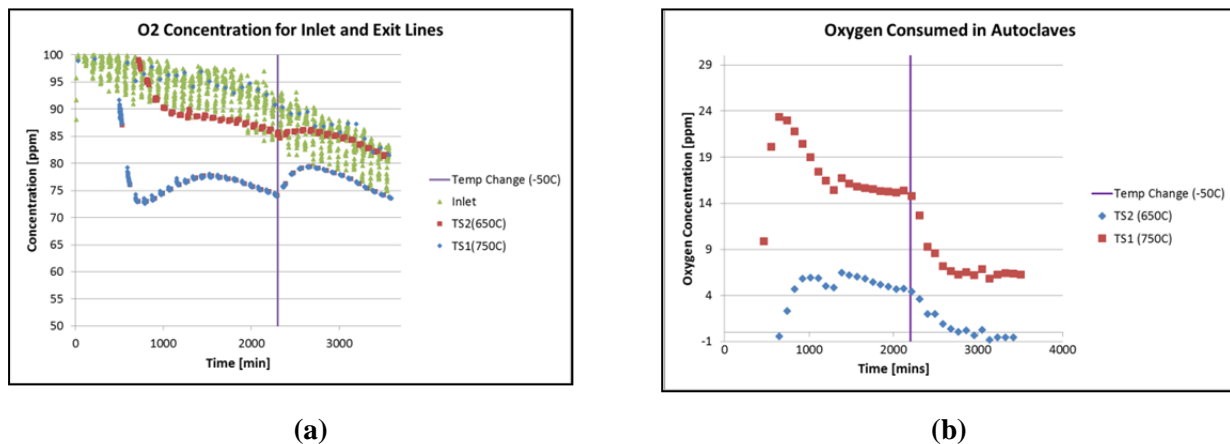


Figure 3.13. (a) oxygen concentration and (b) oxygen consumed in autoclaves measured as a function of time for the baseline impurity test which contained no samples.

A 200 hour oxygen impurities test that contained samples was conducted. Figure 3.14 depicts a similar plot to that depicted in Figure 3.13: (a) oxygen concentration measured at the inlet and outlets and (b) the oxygen consumed in each autoclave as a function of time. Similar reaction rate behavior was exhibited in this test. At approximately 2700 minutes and 4200 minutes bottles were changed out and the oxygen concentration dramatically changes. Figure 3.14(b) demonstrates that the reaction rate re-establishes equilibrium oxygen reaction rate values after the bottle is swapped. Figure 3.14 also demonstrates that the oxygen reaction rate is greater at 750C than at 650°C.

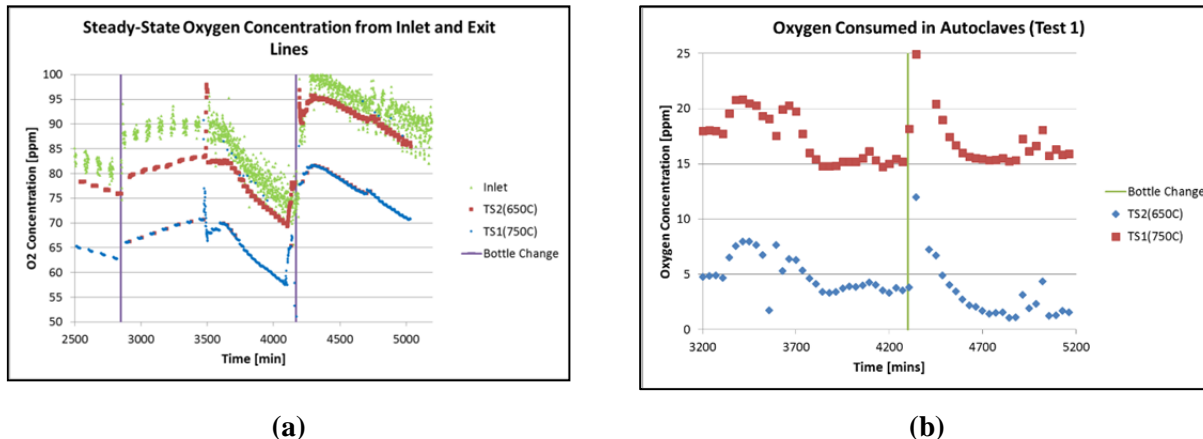


Figure 3.14. (a) Oxygen concentration and (b) oxygen consumed in autoclaves measured as a function of time for a portion of the first oxygen impurity test containing samples.

Figure 3.15 depicts the oxygen concentration as a function of time for the test containing samples. It appears as if in the first 1600 minutes a reaction between the bare samples occurs because the measured oxygen concentration at the outlet is much lower than the steady state concentration depicted in Figure 3.13 (i.e. the oxygen reaction rate is much greater in the first 1600 minutes than at steady state).

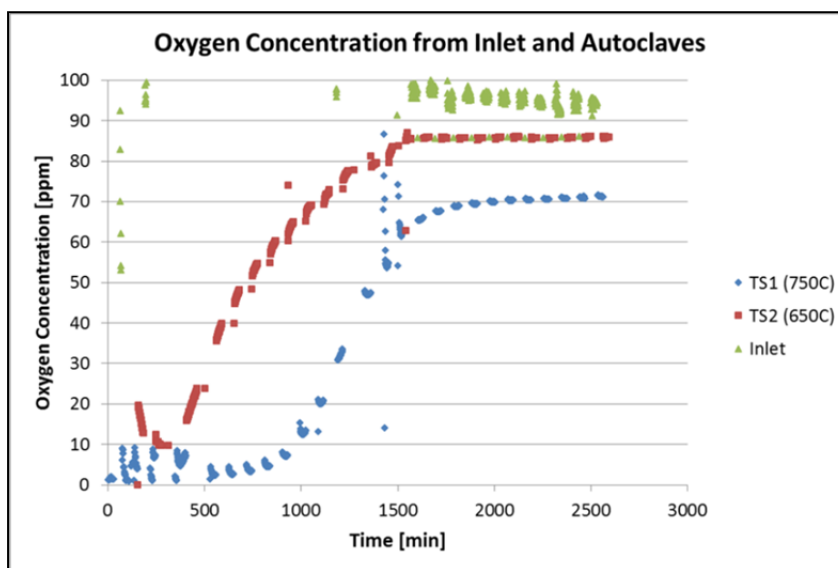


Figure 3.15. Oxygen concentration measured as a function of time for a portion of the first oxygen impurity test containing samples.

As depicted in previous yearly reports, amorphous carbon deposits were found on the surface of samples exposed to RG SC-CO<sub>2</sub> but not found on IG SC-CO<sub>2</sub>. It was believed these deposits were not present on samples exposed to IG SC-CO<sub>2</sub> due to a higher O<sub>2</sub> concentration in the IG gas compared to the RG gas. It is believed the chemical reaction responsible for this behavior is given in Equation 1, also known as the Boudouard reaction.



The software program HSC chemistry was used to calculate the thermodynamic favorability of this reaction at 650°C and 2900psi, along with a reaction describing the reaction of O<sub>2</sub> with free carbon to create CO given in Equation 2, as a function of temperature and is depicted in Figure 3.16.

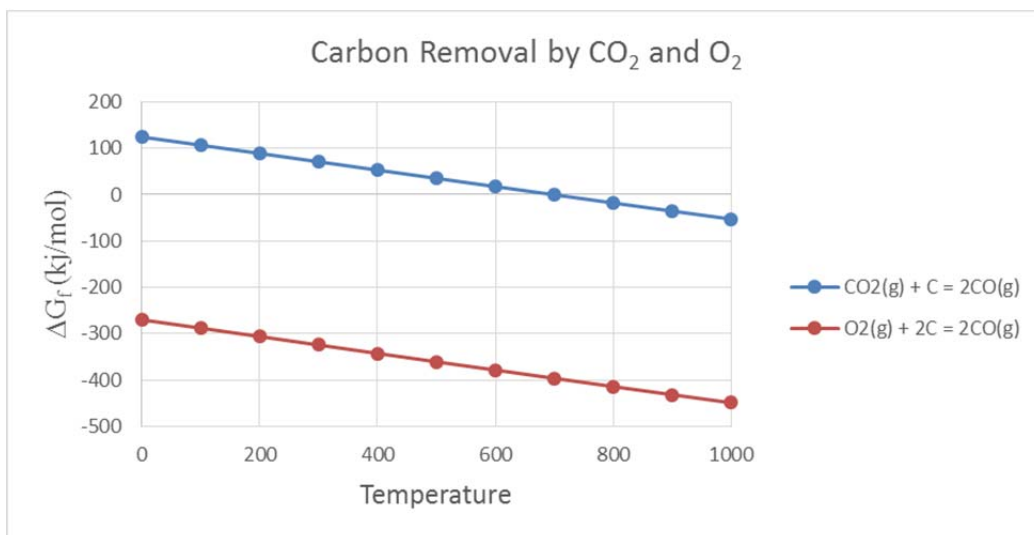


Figure 3.16. Gibbs free energy diagrams for carbon removal in  $\text{CO}_2$  and  $\text{O}_2$

The results obtained from HSC Chemistry align with weight gain trends observed in that the Boudouard reaction becomes favorable around  $700^\circ\text{C}$ , suggesting that free carbon will be removed when the reaction becomes favorable.

In order to prove that  $\text{CO}_2$  reacts with carbon in the system, two independent tests were set up. The first test was designed to determine how reactive  $\text{CO}_2$  is to carbon. Reactor grade graphite (NBG-18) was exposed to RG SC- $\text{CO}_2$  at  $650^\circ\text{C}$  and  $750^\circ\text{C}$  for 400 hours. After 400 hours of testing at  $750^\circ\text{C}$ , significant weight loss was observed, along with severe attack of the surface of the samples.  $750^\circ\text{C}$  testing was concluded after 400 hours due to extreme spallation from the surface leading to larger inaccuracies of weight change measurements. 200 hours of testing at  $650^\circ\text{C}$  indicates that weight loss is much less dramatic than at  $750^\circ\text{C}$ . The data for graphite weight loss is depicted in Figure 3.17 below.

Further testing of research grade  $\text{CO}_2$  with 100ppm  $\text{O}_2$  has been conducted in order to quantify the effect of small impurities in  $\text{CO}_2$  has on corrosion rates. The weight loss of samples exposed to  $650^\circ\text{C}$  RG containing 100 ppm of  $\text{O}_2$  (imp 650C) is much greater than samples exposed to  $650^\circ\text{C}$  RG  $\text{CO}_2$ . The data for graphite weight loss is depicted in Figure 3.17 below. Images showing the surface attack and resulting porosity on the graphite samples is shown in Figure 3.18.

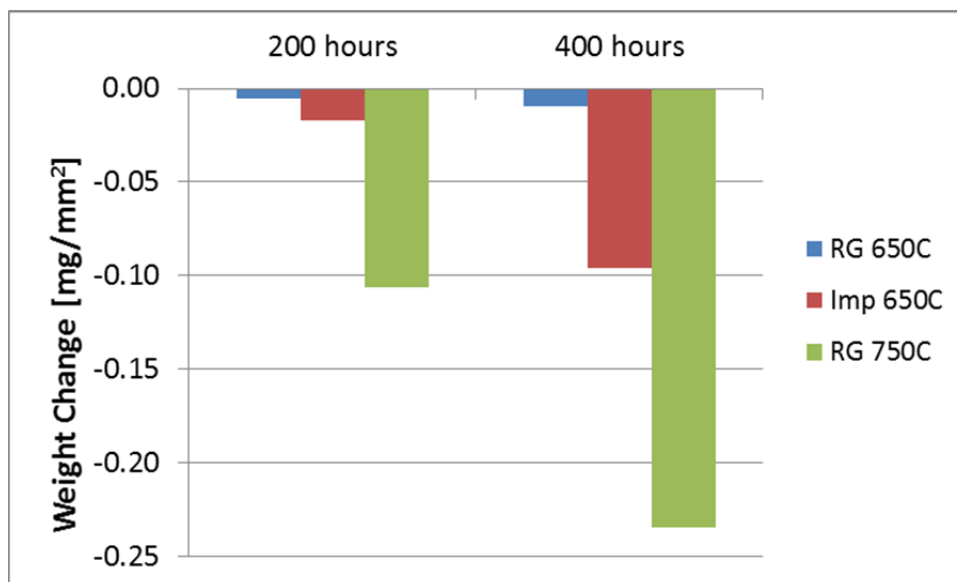


Figure 3.17. Weight loss experienced by graphite exposed to RG SC-CO<sub>2</sub> at 650°C (denoted RG 650C), RG SC-CO<sub>2</sub> at 750°C (denoted RG 750C) for and RG doped with 100 ppm O<sub>2</sub> at 650°C (denoted Imp 650C) at 200 and 400 hours of exposure.

The graphite testing confirms the occurrence of the Bououard reaction at higher temperatures, causing CO<sub>2</sub> to react with carbon, thus dramatically affecting the weight change of the samples. The purpose of the impurities testing with graphite was to demonstrate that in the presence of oxygen, corrosion rates were greater than those samples exposed to environments devoid of oxygen. This is to be expected because oxygen should be the most reactive species in the mixed environment.

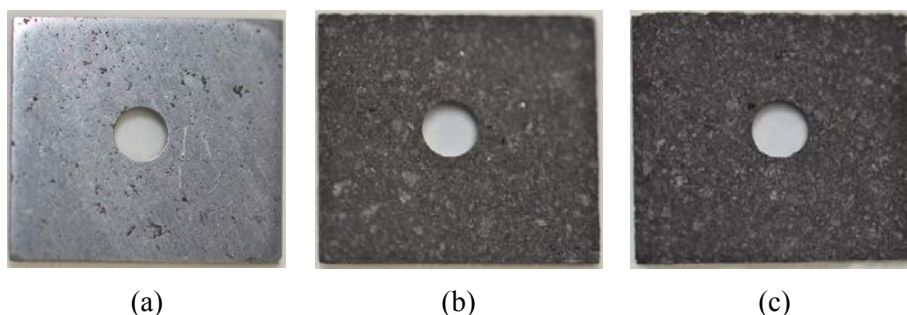


Figure 3.18. Graphite samples exposed to (a) 0 hours, (b) 200 hours, and (c) 400 hours of RG CO<sub>2</sub> at 750°C

The second carbon mechanism hypothesized with SC-CO<sub>2</sub> is the removal of carbon from metal carbides. In order to test this theory, silicon carbide was purchased and tested at 650 and 750°C in RG, IG, and 100 ppm O<sub>2</sub> impurity testing. The weight change data for SiC is plotted in Figure 3.19 below.



Figure 3.19. Weight change data for silicon carbide exposed to SC-CO<sub>2</sub> at various temperatures and gas purity.

All silicon carbide samples had an initial weight loss followed by weight gains. This would indicate the initial removal of carbon from SiC followed by the creation of a SiO<sub>2</sub> oxide layer. Cross sectional SEM and EDS analyses were performed on SiC exposed to 750°C RG SC-CO<sub>2</sub> for 1000 hours and are presented in Figure 3.20 and 3.21, respectively.

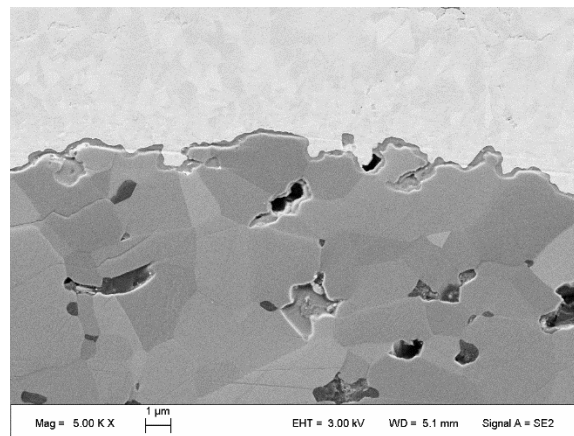


Figure 3.20. SEM cross section micrograph on SiC after exposure to SC-CO<sub>2</sub> at 650°C for 1000 hours.

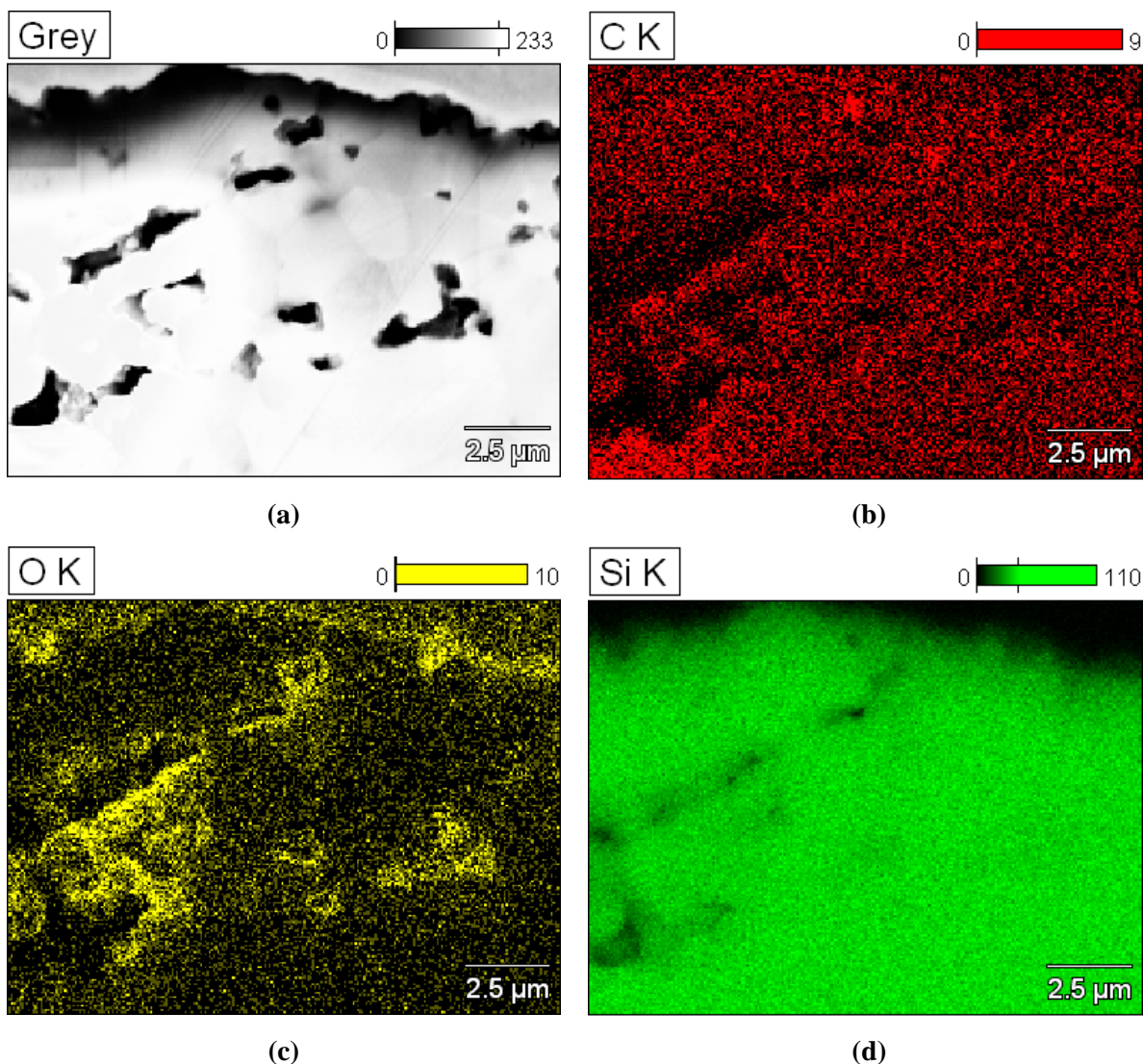
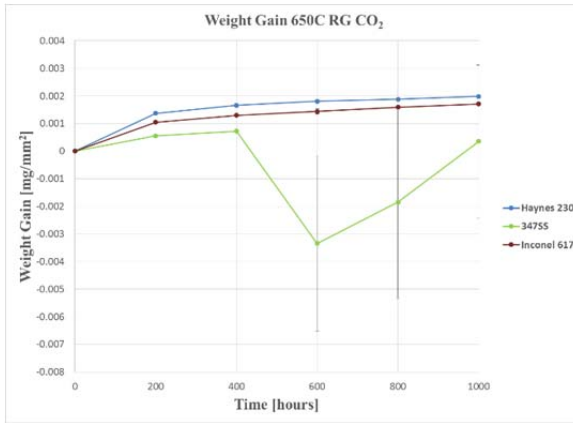


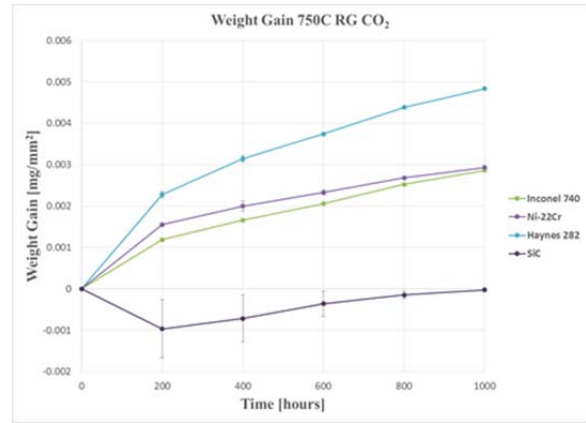
Figure 3.21. SEM cross section micrograph and EDS scan on SiC after exposure to SC-CO<sub>2</sub> at 650°C for 600 hours (a) SEM image, EDS map of (b) Carbon, (c) Oxygen, and (d) Silicon.

As depicted in Figure 3.21, both silicon and oxygen are present within similar regions of the EDS scan, indicating the formation of a silicon oxide both on the surface of SiC and within SiC itself. There are also pits within SiC, potentially corroborating the hypothesis that removal of carbon from the material is occurring. Figure 3.22 is a compilation of all weight gain data tabulated for 650°C and 750°C testing in RG, IG, 100ppm O<sub>2</sub>, and 7ppm O<sub>2</sub> impurity environments.

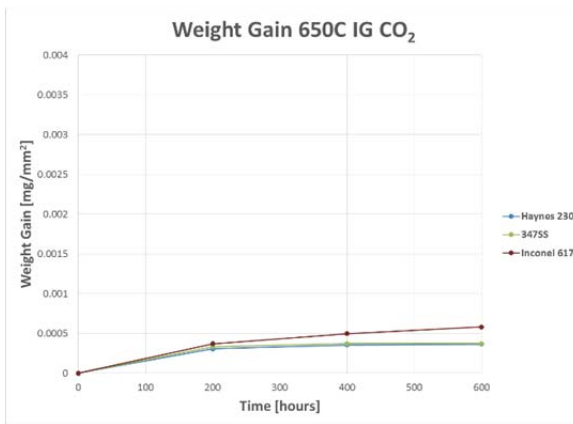




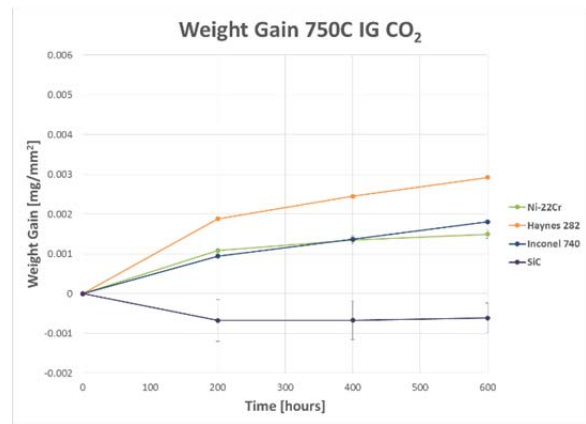
(a)



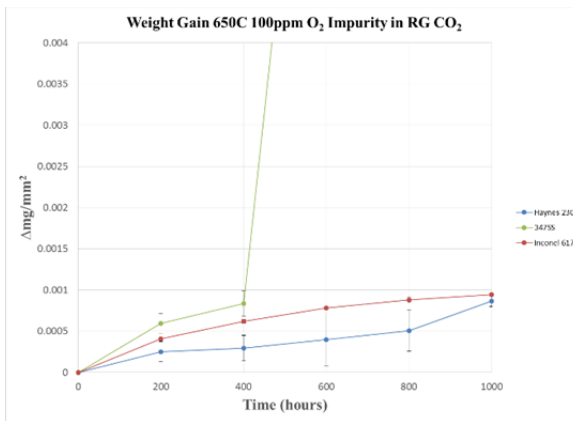
(b)



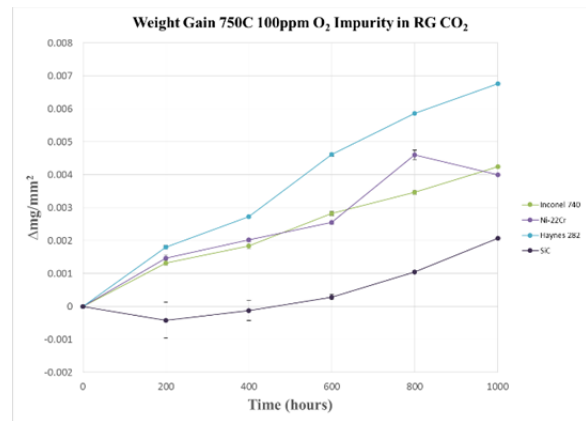
(c)



(d)



(e)



(f)

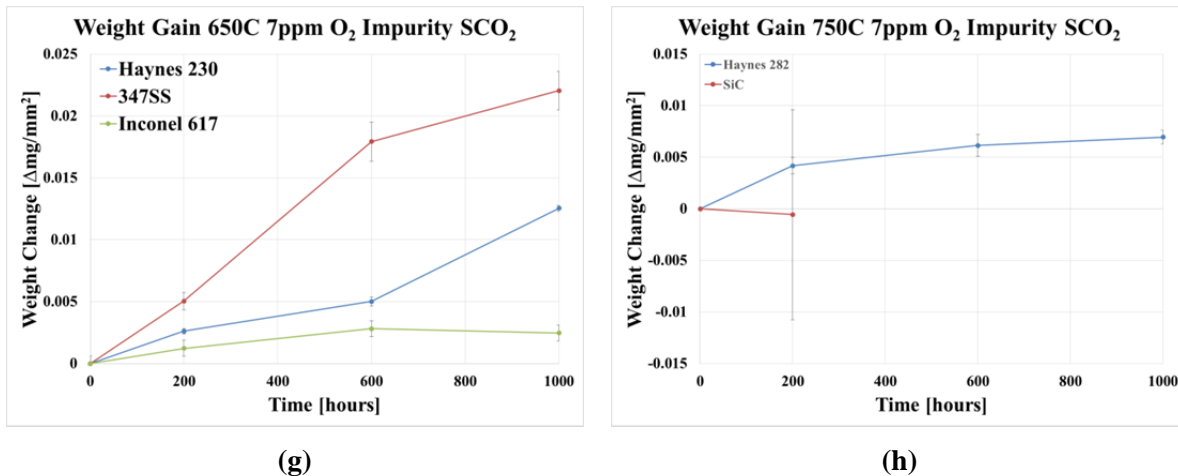


Figure 3.22. Weight change data for materials exposed to (a) 650°C RG CO<sub>2</sub>, (b) 750°C RG CO<sub>2</sub>, (c) 650°C IG CO<sub>2</sub>, (d) 750°C IG CO<sub>2</sub>, (e) 650°C RG CO<sub>2</sub> with 100ppm O<sub>2</sub>, (f) 750°C RG CO<sub>2</sub> with 100ppm O<sub>2</sub>, (g) 650°C RG CO<sub>2</sub> with 7ppm O<sub>2</sub>, (h) 750°C RG CO<sub>2</sub> with 7ppm O<sub>2</sub> as a function of exposure time

The following trends have been observed for weight gain data:

- 650°C
  - Samples exposed to IG SC-CO<sub>2</sub> generally exhibit similar weight gain than samples exposed to RG SC-CO<sub>2</sub>
  - Samples exposed to 100 ppm O<sub>2</sub> in RG SC-CO<sub>2</sub> generally exhibit *less* weight gain than samples exposed to pure RG SC-CO<sub>2</sub>, except for 347SS.
    - Spallation present on 347SS exposed to RG SC-CO<sub>2</sub>
- 750°C
  - Samples exposed to IG SC-CO<sub>2</sub> generally exhibit similar weight gain than samples exposed to RG SC-CO<sub>2</sub>
  - Samples exposed to 100 ppm O<sub>2</sub> in RG SC-CO<sub>2</sub> generally exhibit *more* weight gain than samples exposed to pure RG SC-CO<sub>2</sub>

It is hypothesized that at temperatures less than approximately 700°C, oxygen will react with carbon and carbides to form CO (thus, reduce weight gains); at temperatures greater than 700°C, CO<sub>2</sub> will affect the equilibrium concentration of the reaction described by Boudouard reaction and will not promote the formation of carbon/carbides.

This hypothesis is hampered by the observation that weight gains in 100ppm O<sub>2</sub> RG SC-CO<sub>2</sub> at 750°C are greater than RG SC-CO<sub>2</sub>. It is believed that at 750°C, there are multiple phenomena occurring that account for this trend: carbon is being removed by O<sub>2</sub>, but excess oxygen present is simply allowing for more oxidation to occur after carbon deposits are removed. Figure 3.23 is an expanded version of Figure 3.22(e) that includes the full range of data to show 347SS weight gains in 100ppm O<sub>2</sub> RG SC-CO<sub>2</sub>.



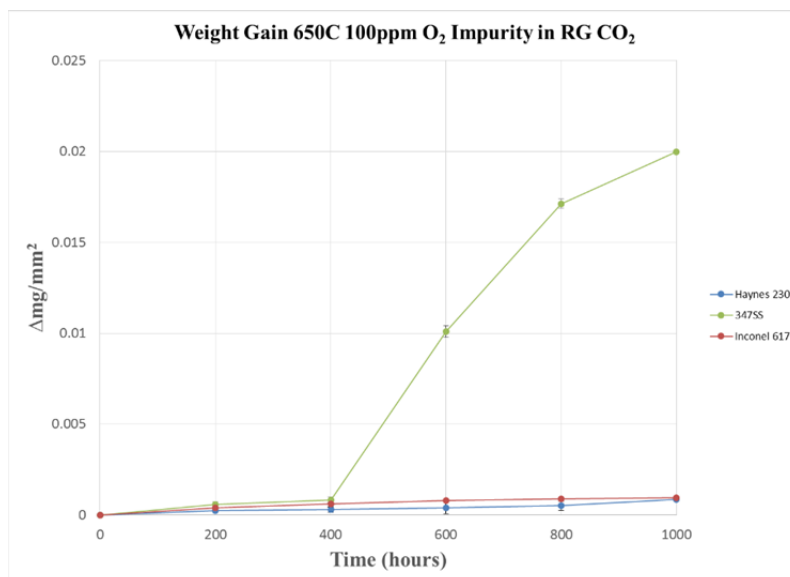


Figure 3.23. Weight change data for materials exposed to 650°C RG CO<sub>2</sub> with 100ppm O<sub>2</sub> as a function of exposure time.

SEM analysis of Haynes 230 exposed to 750C SCO<sub>2</sub>, both RG and 100ppm O<sub>2</sub> doped CO<sub>2</sub> has been conducted, and shown in Figure 3.24. As may be noted the introduction of oxygen impurity increases the oxide layer thickness.

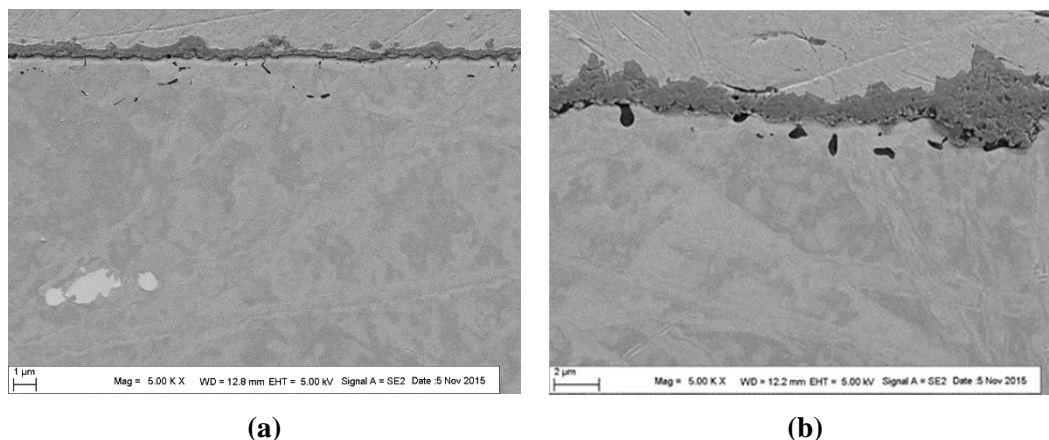


Figure 3.24. Comparison of SEM cross sectional micrographs depicting oxide thicknesses for Haynes 230 after 1000 hours in 750°C (a) RG and (b) 100 ppm O<sub>2</sub> doped CO<sub>2</sub>.

Figure 3.25 compares the SEM micrographs and accompanying EDS linescans of Haynes 230 exposed to 750C SC-CO<sub>2</sub> for 1000 hours in pure RG and doped RG with 100 ppm O<sub>2</sub>. Oxide thicknesses are significantly larger for samples tested in oxygen doped CO<sub>2</sub> which corroborates weight change data depicted in Figure 3.22. Another interesting feature visible in the line scans are larger chromium depletion zones, highlighted with a red box in the line scan, where the chromium composition lowers before increasing for the oxide layer. Chromium depletion can lead to the formation of voids resulting in lower oxide adherence (observed in all oxygen-doped samples above). Chromium depletion zones are more prevalent in oxygen-doped systems than research grade conditions perhaps as a result of chromium diffusion being the rate limiting factor in oxide development in high O<sub>2</sub> concentrations, whereas oxygen availability is the limiting factor in research grade corrosion. Also highlighted in red are peaks in

chromium deep beneath the oxide which could indicate formation of chromium carbides along grain boundaries.

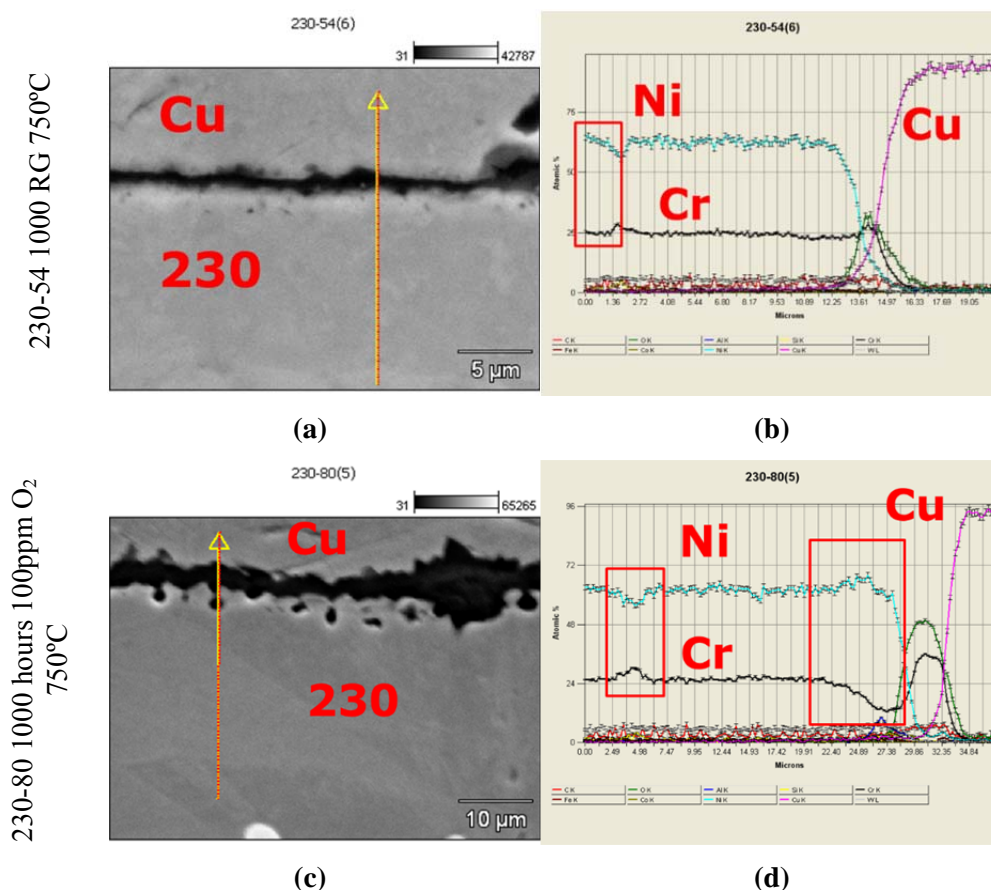


Figure 3.25. SEM micrograph and accompanying EDS linescan of alloy Haynes 230 after 1000 hours of exposure to 750°C (a)(b) RG  $\text{SCO}_2$  and (c)(d) RG  $\text{SCO}_2$  doped with 100 ppm  $\text{O}_2$

Figure 3.26 depicts an EDS cross sectional mapping of alloy Haynes 230 after 1000 hours of exposure to  $\text{CO}_2$  doped with 100 ppm  $\text{O}_2$  at 750°C. An outer layer composed of iron and nickel was observed on top of a chromium rich inner layer. The nickel oxide found on the surface is a result of the higher environmental  $p\text{O}_2$  as discussed for Figure 3.12 above. Nickel rich oxides did not form in the lower  $p\text{O}_2$  environments. A large chromium depletion layer beneath the oxide layer was observed. Another important distinction is the presence of an aluminum rich zone beneath the oxide layer. This suggests the initiation of a protective alumina layer, although at this time exposure, the layer is not fully developed and does not provide additional protection to the base material. The SEM image additionally shows the formation of voids beneath the oxide. This may be caused by rapid diffusion of chromium and other elements out of the base material due to the rapid oxidation at the surface exposed to the oxygen rich environment.

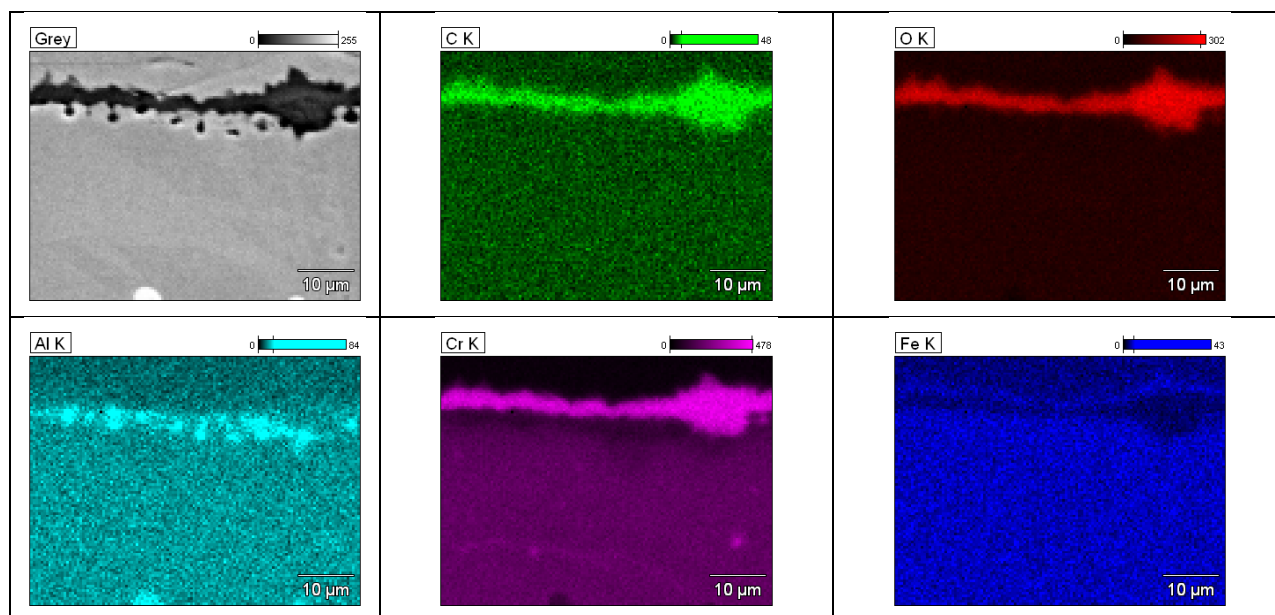


Figure 3.26. 2D EDS cross sectional mapping of alloy Haynes 230 after 1000 hours of exposure to CO<sub>2</sub> doped with 100 ppm O<sub>2</sub> at 750°C

Additionally, further doped RG SCO<sub>2</sub> tests have been conducted through 1000 hours where the impurity level is 7ppm O<sub>2</sub>. Weight gain results are compiled in Figure 3.22. The weight gain trends observed for 7ppm O<sub>2</sub> are larger than other testing conducted, preliminary SEM analysis has been conducted. While no visible spallation was observed on the samples exposed to 100ppm O<sub>2</sub>, it is theorized that the spallation happened during the initial 200 hours on the 7 ppm samples and therefore was not observed. The spallation and future growth of a more uniform oxide for the 7ppm O<sub>2</sub> test is shown for two time exposures in Figure 3.27 below.

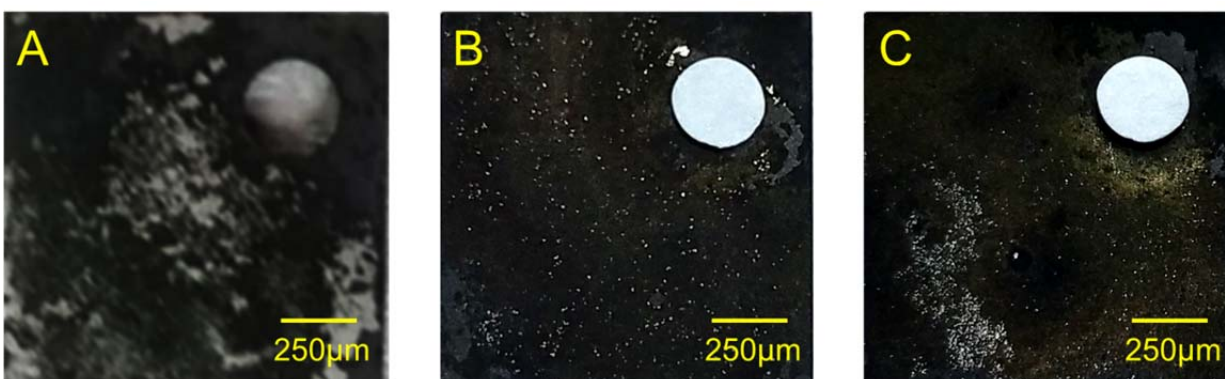


Figure 3.27. Photograph of the entire sample surface showing spallation on exposed to 10ppm O<sub>2</sub> doped CO<sub>2</sub> at 750°C after (a) 200 hours and (b) 600 hours (c) 1,000 hours.

Since visible spallation was observed on the surface, EDS analysis was used to map the surface composition of the sample after 200 hours. The EDS surface mapping in Figure 3.28 shows the different oxides forming on the sample, along with the large spallation regions on the surface of the H230 sample after 200 hours.

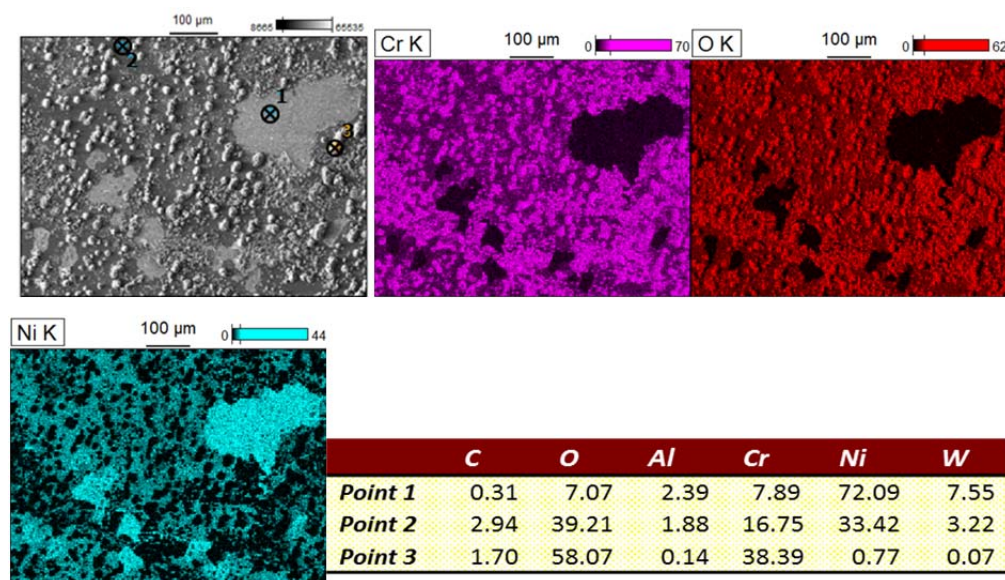


Figure 3.28. EDS surface mapping of H230 exposed to 7ppm CO<sub>2</sub> at 650C after 200 hours.

Based on Figure 3.28, it is theorized that the base layer of oxidation consists of oxides from most of the elements in the base material. These oxides are not thermodynamically allowed when only exposed to CO<sub>2</sub> due to the low associated partial pressure of oxygen ( $\sim 10^{-22}$  atm). Once the oxygen impurity was added, the thermodynamics of these oxides became stable. From the base oxide layer, chromia clusters grow from the surface. Since there is no limit to the amount of oxygen, chromium is able to diffuse very rapidly. This rapid diffusion leads to the formation of voids at the oxide metal interface (SEM images in Figure 3.25). The mixture of the oxides and void formation causes stress in the oxide metal interface that did not exist in the non-doped trials. This stress causes eventual spallation of the oxide. It is observed that the top oxide spalls off, then the inner concentrated chromia layer is left as a protective barrier against the formation of the other oxides. This initial build up and spallation was not found on the H230 samples exposed to 100ppm oxygen. This can be explained by 3.29, which shows the oxygen consumption during the 100ppm doped test. Although an equilibrium was eventually reached at around 7ppm consumed (for 650C), the initial 20 hours consumed as much oxygen as the first 200 hours in the 7ppm test. This means that the buildup and spallation was most likely done before the test was complete, and therefore only the protective chromia layer was left.



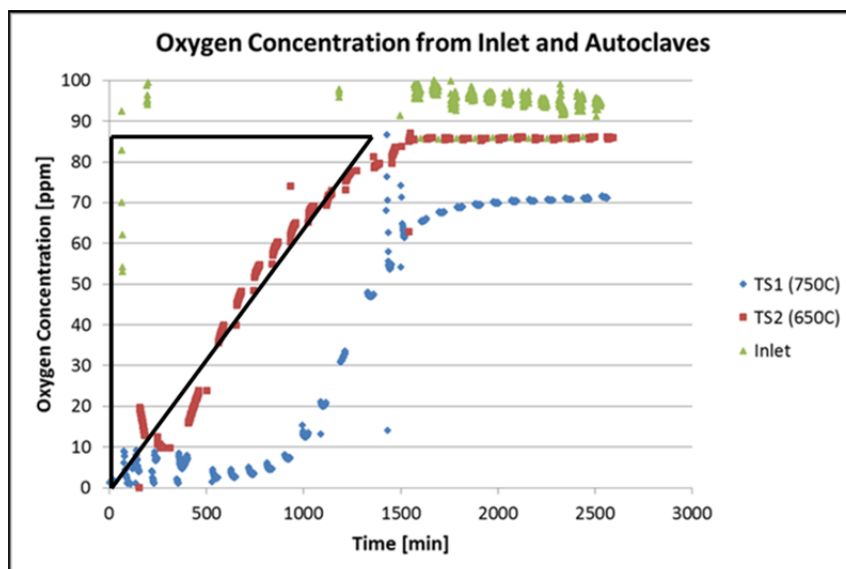


Figure 3.29. Oxygen concentration at inlet and exit lines of the first 200 hours of the 100ppm oxygen doped test.

	H230 (Cross-section)	EDS Line Scan	Thickness [ $\mu\text{m}$ ]
650°C RG			Continuous: <.5 microns
750°C RG			Continuous: .53 $\pm$ .25

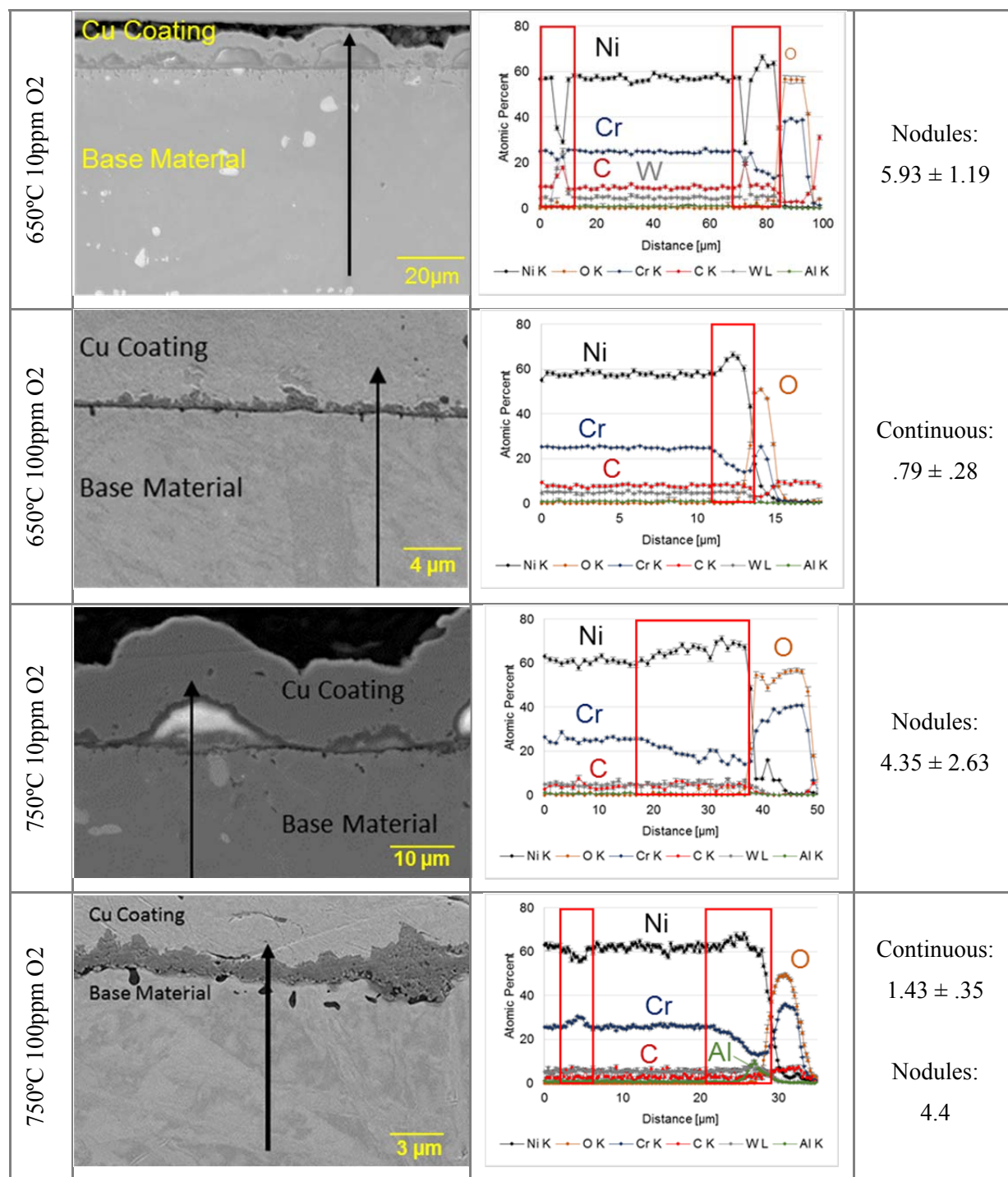


Figure 3.30. SEM cross section images for oxides grown on the surface of Haynes 230 after 1000 hours of exposure to *sCO*<sub>2</sub>

The thickness values presented in Figure 3.30 show that the samples exposed to oxygen impurity containing CO<sub>2</sub> doped cases produced significantly thicker oxides. Thickness values also increased as a function of temperature for the uniform oxides. Due to the nodule formation in the 10ppm oxygen containing tests, the thickness values are only presented for the oxide clusters sampled in the image.



Carbides along grain boundaries have been highlighted on each line scan with red boxes in Figure 3.30. The carbides observed along grain boundaries in the vicinity of the oxidized surface are composed of primarily tungsten and chromium. However, large clusters of tungsten carbides were observed along grain boundaries on unexposed samples which were obviously not a result of  $s\text{CO}_2$  exposure. As a confirmation, an EDS line scan was performed for the unexposed sample as well as throughout the middle of the tested sample to determine if the elevated temperature was the cause of the increased chromium carbide concentration beneath the oxide. The results of the line scans are depicted in figure 3.31, where it appears that significantly less evidence of chromium-rich carbides was observed in non-exposed samples. More analysis on the carburization beneath the oxide is necessary to fully understand the carbon uptake during  $\text{CO}_2$  exposure.

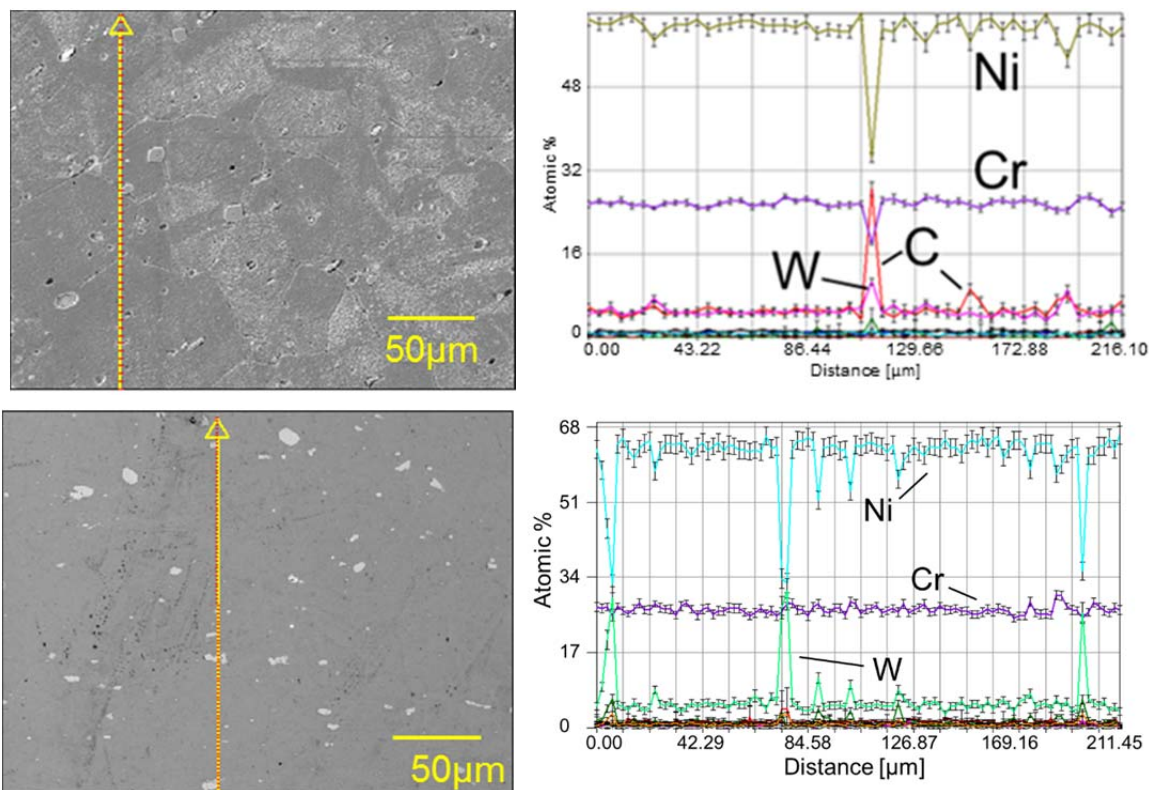


Figure 3.31. EDS line scan of unexposed Haynes230 sample (top), and middle of Haynes 230 sample after exposure at 750°C (bottom) showing presence of tungsten carbide clusters.

Chromium depletion zones were observed for each alloy and are also shown in Figure 3.30 (in red boxes directly beneath oxide). The depletion of chromium is linked to fast outward diffusion of chromium to form the oxide. As the chromium diffuses toward the oxide interface, the chromium from the base material does not diffuse at the same rate producing a lower concentration which is observable in the EDS line scans. The magnitude of the depletion zones for oxygen added  $s\text{CO}_2$  samples was significantly larger than the depletion zones in the RG samples which were non-existent, or very small. EDS elemental mapping analysis was performed to determine the composition of oxide, potential carburization, and chromium depletion beneath the oxide layer and is shown in Figure 3.32.

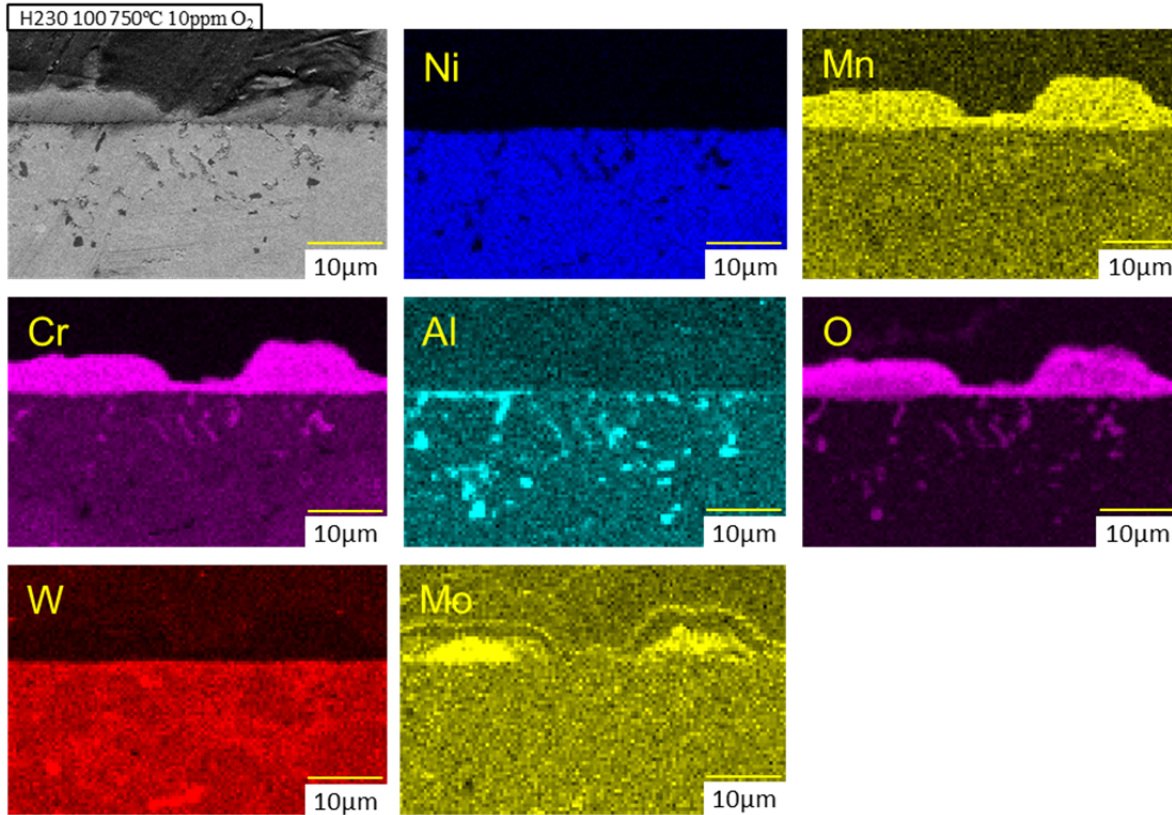
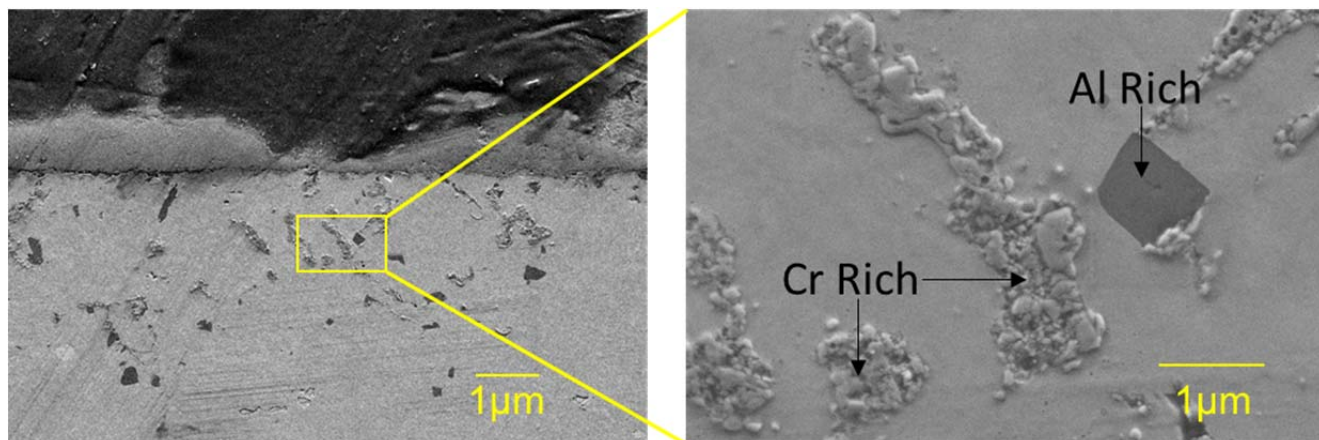


Figure 3.32. Cross-sectional EDS mapping of alloy Haynes 230 after 1000 hours of exposure to  $\text{CO}_2$  with 10 ppm  $\text{O}_2$  at 750°C.

EDS mapping shows a chromium and manganese rich oxide. It also shows nickel and chromium depletion along grain boundaries, as well as aluminum enrichment. The chromium depletion region matches what is observed in figure 3.30. If outward diffusion of chromium is fast enough void formation can occur through the Kirkendall Effect. It is believed that the voids present beneath the oxide layers present in the 750°C and oxygen doped tests are due to this effect (observed in figure 3.30 above). Increased concentration of voids at the oxide interface could potentially initiate oxide spallation. Some voids in the 750°C 100ppm oxygen tests were characterized by very low chromium concentration, and found to have a large enrichment of aluminum. This is more readily observed in Figure 3.32 in which the contrast gradient in the voids is clearly visible. Similar results were observed by Chien and Brown [Chien, 1992]. The composition of the intergranular void region found high concentration of chromium and aluminum rich oxides. It is theorized that these oxides act as pegs which increase the adhesion of subsequent oxide formation by reducing the thermal expansion mismatch of the oxide and base material. SEM of the same region beneath the oxide from figure 3.32 is shown in figure 3.33 below.



*Figure 3.33. SEM imaging showing intergranular chromium and aluminum rich oxides in Haynes 230 sample exposed to CO<sub>2</sub> at 750°C with 10ppm O<sub>2</sub> addition.*

Haynes 230 samples exposed to oxygen-doped CO<sub>2</sub> exhibited growth of large oxygen nodules. These nodules covered almost the entire surface of the samples exposed to CO<sub>2</sub> with 10ppm oxygen, and very few nodules were observed on the surface of samples exposed to 100ppm oxygen. Only samples exposed to 10ppm of oxygen doped CO<sub>2</sub> showed significant surface spallation, and this effect was considerably larger in the first 200 hours than during the following exposure times. A more uniform surface morphology was observed as testing progressed further out to 1000 hours. It is believed that this spallation is a result of the increased stresses that occur during the heating and cooling of the samples during the start and end of each test. In order to obtain bonding information of the different oxides, Raman spectroscopy and XRD was conducted. Raman Spectroscopy was completed on a sample exposed to research grade CO<sub>2</sub> after 800 hours, and grazing incidence XRD analyses was performed on each of the samples after 1000 hours of testing. The Raman spectra were collected using 532nm laser, and compared to the RRUFF database spectrum for chromia in Figure 3.34 below. The XRD spectra was collected using a Co K $\alpha$  target. An incident angle of two degrees was used for each sample, with the results plotted in Figure 3.35 below along with an untested (labeled as “bare”) Haynes 230 sample.

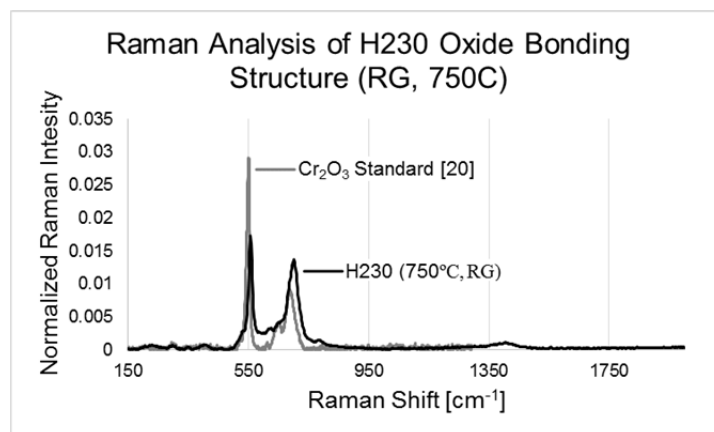


Figure 3.34. Raman spectrum from surface of Haynes 230 sample exposed to RG CO<sub>2</sub> at 750°C after 800 hours, along with standard spectrum for Cr<sub>2</sub>O<sub>3</sub>.

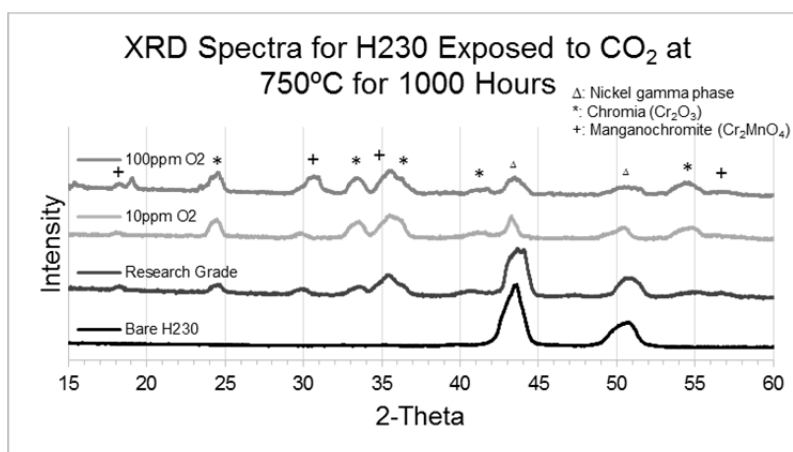


Figure 3.35. X-Ray diffraction patterns from surface of Haynes 230 samples exposed to RG, 10ppm O<sub>2</sub>, and 100ppm O<sub>2</sub> CO<sub>2</sub> at 750°C after 1000 hours.

Both the Raman spectra, as well as the XRD analysis showed the bonding structure of the surface oxide to correspond to Cr<sub>2</sub>O<sub>3</sub>. The XRD spectra also showed the presence of a chromium-manganese spinel (Cr<sub>2</sub>MnO<sub>4</sub>) in the oxide. Since XRD penetrates through the outer oxides, it is believed that the oxides containing other elements were not observed.

### 3.B Modeling of Chromium Oxidation and Carburization in CO<sub>2</sub> Environments

As CO<sub>2</sub> oxidizes metal, carbon monoxide is produced as one potential corrosion product. A gas chromatograph (GC) was used to measure the concentration of carbon monoxide both before and after the autoclave in order to observe the reaction rate of the total system (Figure 3.36). The GC has a lower limit of detection of about 50ppb with an accuracy of +/- 2.5 ppb. The concentration of CO was found to be lower than the detectable limit of the GC before entrance to the autoclave since no reaction has occurred by this point. The CO concentration vs time at the exit of the autoclave has been plotted in figure 2.36 (left). The CO concentration measured at the exit of the autoclave is a function of the flow rate of CO<sub>2</sub> (.1kg/hr), surface area of the samples, and reaction rate of each alloy in the autoclave.

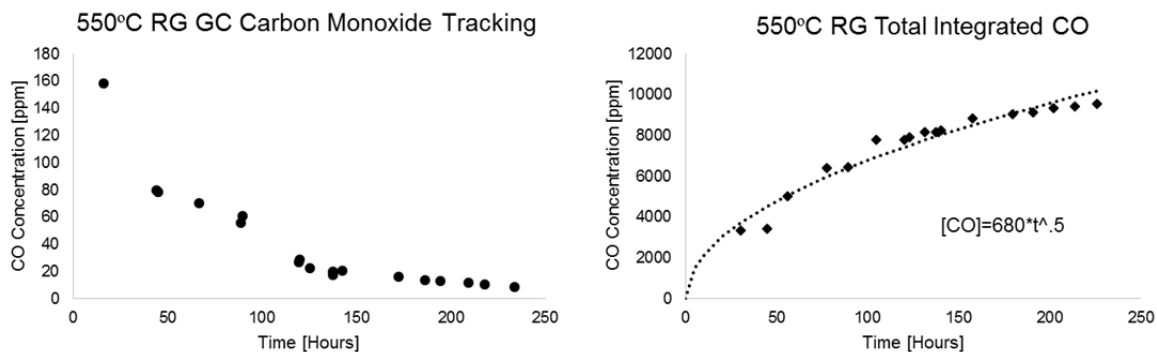


Figure 2.36. CO concentration for the first 240 hours of a SC-CO<sub>2</sub> test conducted at 550°C (Left). Integrated CO concentration vs time for the same test (right).

The CO concentration starts out high, and quickly drops over the first 200 hours before reaching a semi-steady-state condition. This was expected since the alloys exposed to CO<sub>2</sub> in this test all have been shown to produce protective oxides which have a reaction rate of roughly time<sup>.5</sup> power. If the CO concentration vs time graph is integrated, the total CO production from the system can be calculated. This is a useful number since it represents the amount of CO that a closed loop (zero flow) would have as a function of time due to corrosion of the system. The integrated CO data is plotted in figure 2.36 (right), and shows that after around 200 hours, in this test, the total CO concentration was about 1%. It is therefore important to understand the role that CO has on corrosion rates as it may be highly concentrated in the sCO<sub>2</sub> Brayton Cycle.

A large effort has been completed in order to model CO<sub>2</sub> corrosion, and more generally oxidizing and carburizing environments. Initially, it is very surprising to observe carburization in an environment that is highly oxidizing such as CO<sub>2</sub>, but by making assumptions about the oxide interactions with the environment, carbon deposition becomes reasonable. The most prevalent studies in CO<sub>2</sub> corrosion currently support the Available Space Model, which was proposed back during studies on the MAGNOX reactors [Holmes, 1974], and more recently extended by Rouillard and Young [Rouillard, 2016], [Gong, 1974]. This model was proposed for iron-chromium alloys which produce a duplex oxide, and while the nickel-chromium alloys behave different, many similarities arise between the two. One important distinction is that the corrosion rate for nickel chromium alloys is significantly lower, and therefore, the boundary conditions in this study will be solved based on thermodynamics, and not kinetic data (as done for the available space model). The approach being used inherently incorporates the model proposed for the VHTR He corrosion mechanisms set forth by Quadakkers [Quadakkers, 1985]. In order to correlate this model to the CO<sub>2</sub> environment, a few assumptions are made during subsequent calculations:

- Activity coefficients of all species are all equal to 1
- Chromium depletion is neglected (concentration equal to 1)
- Chromium is the only reactive species with oxygen and carbon
- pO<sub>2</sub> at oxide-environment interface is fixed using the testing conditions
- pO<sub>2</sub> at metal-oxide interface is constant, and based on phase equilibrium of Cr and Cr<sub>2</sub>O<sub>3</sub>

The first step was to re-create the Cr-O-C stability diagram observed in the studies above. This was done by using the chemical and equilibrium equations used to form chromia and chromium carbides. An example of the formation of chromia is listed in equations 1-4. All thermodynamic data was acquired using HSC software [Lencka, 1993]. From the chemical balance, the equilibrium equations can be found and are listed next to each chemical equation. At this point, it is usually of interest to look where the two phases are in equilibrium with each other with respect to the reactive species (pO<sub>2</sub> and aC). This is done



for equation 3 by setting  $a_c$  and  $a_{Cr_2O_3}$  equal to one, leaving just  $pO_2$  in the equation. Finally, the equilibrium equation is related to the Gibbs Free Energy shown in equation 4, and solved for the relevant  $pO_2$  and  $a_c$  values. The same method is used for each carbide species as well as the equilibrium between the oxide and carbide. The equilibrium between the oxide and carbide is a slightly more complicated system as the phase equilibrium results in an equation containing both  $a_c$  and  $pO_2$ . The result of these equations produce the volatility diagram given by the left graph in figure 3.37.



$$k_{Cr_2O_3} = \frac{(a_{Cr})^2 (pO_2)^{\frac{3}{2}}}{(a_{Cr_2O_3})} \quad 2$$

$$k_{Cr_2O_3} = \frac{(a_{Cr})^2 (pO_2)^{\frac{3}{2}}}{(a_{Cr_2O_3})} = e^{\frac{-\Delta G}{RT}} \quad 3$$

$$\text{Log}[pO_2] = \frac{2}{3} \text{Log}[k_{Cr_2O_3}] \quad 4$$

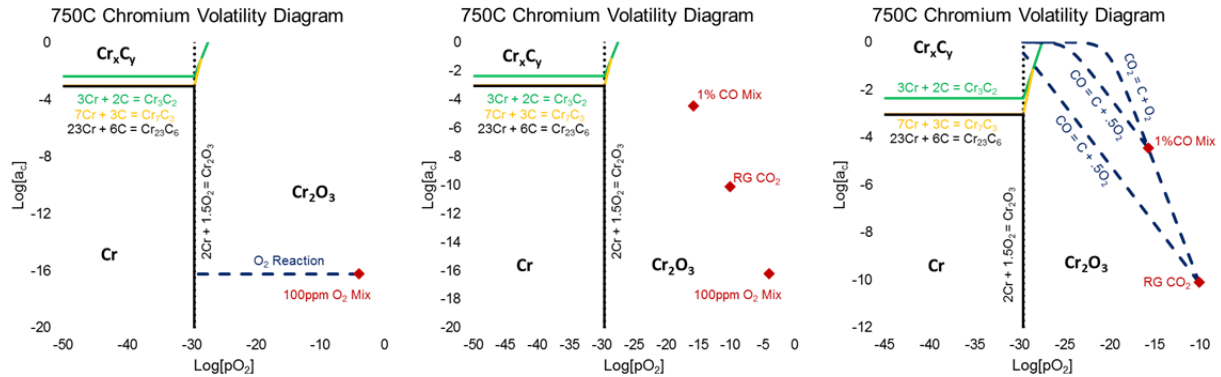


Figure 3.37. Volatility diagram for Cr-C-O phases at 750°C at 1 atm. Left: Basic volatility diagram. Middle: Basic volatility diagram with environmental conditions for RG CO<sub>2</sub>, 100ppm O<sub>2</sub> mixed and 1%CO mixed CO<sub>2</sub>. Right: Basic volatility diagram with environmental conditions with lines representing mass balance of  $pO_2$  and  $a_c$  through the oxide.

The basic volatility diagram in figure 3.37 shows which phases should be present given a partial pressure of oxygen and activity of carbon. This can be expanded explicitly to the CO<sub>2</sub> environments in this study by implementing the gaseous equilibrium given by equations 5 and 6. The environmental conditions of interest are research grade CO<sub>2</sub> (considered 100% pure), 100ppm oxygen mixed RG CO<sub>2</sub>, and 1% CO mixed RG CO<sub>2</sub>. The  $pO_2$  and  $a_c$  values for the environmental dissociation are plotted by red points on the basic volatility diagram in the middle graph of figure 3.37.

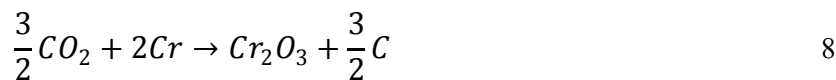


The testing environment sets the boundary condition for the oxide-environment interface. A more important boundary condition is the one between the metal and oxide. This boundary condition controls



the corrosion process, and will determine whether oxidation or carburization occurs. As discussed earlier, the partial pressure of oxygen should be roughly equal to the equilibrium  $pO_2$  calculated between the Cr and  $Cr_2O_3$  phases since both are present at the interface. Since this  $pO_2$  is different from the environmental condition, the activity of carbon must also change in order to maintain the chemical equilibrium. In order to calculate the new  $a_C$ , the most reactive species must be considered. For example, in the 100ppm oxygen doped testing, only oxygen was consumed during oxidation. For this reason, it can be assumed that only  $pO_2$  changes throughout the oxide, and  $a_C$  stays the same. This would result in a horizontal line being drawn on from the environmental condition on the volatility diagram to the Cr- $Cr_2O_3$  vertical line.

The more complicated environments are RG  $CO_2$  and 1%CO mixed environments, in which the activity of carbon is directly linked to the partial pressure of oxygen. In these cases, the oxidation reaction either occurs due to reduction of  $CO_2$  or CO. In either case, oxygen is consumed to form the oxide, resulting in a higher carbon activity. This is observed in equations 7 and 8. Since it is unknown which species is most reactive with the metal, it is useful to consider both reactions in order to create a range of possible carbon activities as a function of partial pressure of oxygen. Equations 7 and 8 can be reduced to 5 and 6 by writing the half reactions, and realizing that the  $pO_2$  and  $a_C$  values are only relevant to the chemical equilibrium of  $CO_2$  and CO. Using the equilibrium equations 4.7 and 4.8, and varying  $pO_2$  values from environmental to oxide-metal interface conditions, the activity of carbon was calculated. This result gives a range of values for the activity of carbon as the partial pressure of oxygen drops through the scale to the value at the oxide interface. This is represented by the dashed blue lines plotted on the right graph in Figure 3.38.



In order to test the thermodynamic model with samples that were tested in these conditions, SIMS analysis was performed by EAG Laboratories. A sputtering technique was used to observe carbon concentration as a function of depth through the oxide, and into the base material. The carbon profile was analyzed on alloy Haynes 625 exposed to RG  $CO_2$ , RG with 1% CO, and RG with 100ppm  $O_2$ . The results are summarized in figure 3.38 (left). The value for the carbon concentration for as received Haynes 625 has also been plotted in figure 3.38. It is observed from the SIMS profile that the max carbon concentration is higher in the 1% CO environment compared to RG. The sample exposed to 100ppm oxygen mixed  $CO_2$  had an oxide that was too thick to penetrate using SIMS, and therefore, the carbon profile is only in the oxide (where carbon should be very low). Another observation is that the carbon profile for the sample exposed to 1% CO mixed  $CO_2$  has a more diffuse profile, indicating that the carbon has diffused further into the sample. Using the SIMS profile, the max value for the concentration of carbon can be obtained. This should be the carbon concentration at the oxide metal interface where thermodynamics predicts that the activity of carbon should be highest. By dividing by the number density of the as received 625 alloy, the atomic percent of carbon at the interface was calculated. As received 625 has roughly .1% carbon, post exposure RG sample showed a max carbon value of .45% , and the 1% CO sample had .8% carbon at the interface. These values were compared to the predicted values and plotted in figure 2.38 (right).

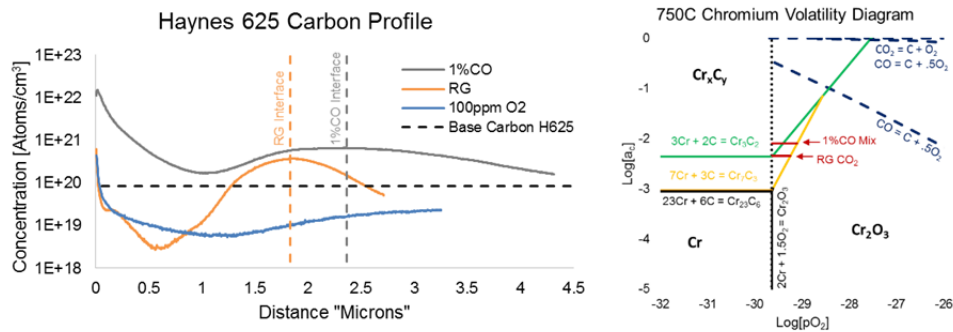
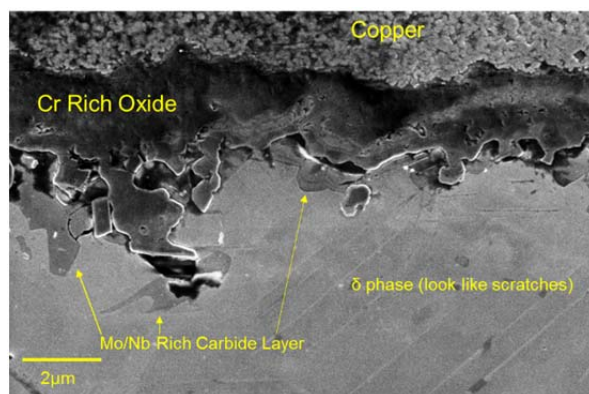


Figure 3.38. Left: SIMS carbon profile for Haynes 625 exposed to CO<sub>2</sub> for 1000 hours at 750°C in RG, RG with 1% CO, and RG with 100ppm O<sub>2</sub>. Right: Volatility diagram for Cr-C-O phases at 750°C, 1 atm for RG and 1%CO mix with SIMS results for carbon activity.

The predicted range for the carbon activity is significantly higher than the observed results from the SIMS testing. A couple possibilities for these deviations are:

- Kinetics have not reached a uniform layer of carburization
- Surface roughness and internal oxidation causes lower a<sub>C</sub> values
- SIMS sputtering plane is not lined up perfectly with metal-oxide interface
- Strong oxidizers such as Aluminum and titanium will cause internal oxidation, which will alter carbon values
- All activity coefficients were assumed to be one, which is not true when concentrations are high enough
- Concentration of chromium was not considered in this model. Haynes 625 starts with 20% chromium, and there was a significant depletion zone from oxidation

Particularly interesting from the SIMS profile is the evidence of carbon throughout the oxide in the 1% CO mixed case. Carbon in the oxide ( $pO_2 > 10^{-29}$ ) should exist as amorphous carbon since it is lower than the a<sub>C</sub> required for carbide formation. Carbon in the base material should form carbides if the pO<sub>2</sub> is set by carbide-oxide limit and pure cr-cr<sub>2</sub>O<sub>3</sub> limit. This is corroborated by the TEM studies presented by KAIST in which they observed amorphous carbon throughout the oxide of the nickel based superalloy, and carbide formation along grain boundaries [Lee, 2016]. As received Haynes 625 contains roughly .1 atomic percent carbon. This exists at an a<sub>C</sub> value of -3 which would indicate precipitation of Cr<sub>7</sub>C<sub>3</sub>/Cr<sub>23</sub>C<sub>6</sub> phases over the Cr<sub>3</sub>C<sub>2</sub> phase. SIMS analysis found the atomic percent of carbon at the interface for the 1% CO and RG cases to be .80 and .45 respectively. If the pO<sub>2</sub> value predicted by the thermodynamic equilibrium is accurate, the carbides that exist at the oxide-metal interface should be a mixture of Cr<sub>3</sub>C<sub>2</sub> and Cr<sub>7</sub>C<sub>3</sub>. In order to check some of these conclusions, SEM/EDS was used in order to look at the Haynes 625 sample exposed to 1%CO mixed CO<sub>2</sub> at 750C for 1,000 hours. Figure 3.39 shows the cross-sectioned SEM image.



*Figure 3.39. Cross-Sectional SEM imaging of Haynes 625 alloy exposed to sCO<sub>2</sub> at 750C, 2900psi for 1,000 hours.*

SEM and EDS showed a chromium manganese rich oxide which is typical for corrosion of nickel based superalloys in these conditions. Figure 3.39 also showed molybdenum and niobium rich carbides beneath the oxide at the interface which was predicted by the thermodynamic model. Figure 3.39 also supports several of the flaws not captured by the model, such as the surface and interfacial roughness of the sample, and the kinetics limited non-uniform carbide layer. In order to continue with the modeling effort, molybdenum and niobium carbides should be considered instead of only chromium rich carbides.

#### **Bibliography Consulted**

- F. Rouillard and T. Furukawa. Corrosion of 9-12Cr ferritic-martensitic steels in high temperature CO<sub>2</sub>. Corrosion Science, (JANUARY), 2016. ISSN 0010938X. doi: 10.1016/j.corsci.2016.01.009.
- D.R. Holmes, R.B. Hill, and L.M. Wyatt. Corrosion of steels in CO<sub>2</sub>. In British Nuclear Energy Society, Reading University, 1974.
- Y Gong, D J Young, P Kontis, Y L Chiu, H Larsson, A Shin, J M Pearson, M P Moody, and R C Reed. On the breakaway oxidation of Fe9Cr1Mo steel in high pressure CO<sub>2</sub>. Acta Materialia, pages 1–14, 2017. ISSN 1359-6454. doi: 10.1016/j.actamat.2017.02.034. <http://dx.doi.org/10.1016/j.actamat.2017.02.034>.
- Korrosion Von Hochtemperaturlegierungen. Corrosion of High Temperature Alloys in the Primary Circuit Helium of High Temperature Gas Cooled Reactors . Part II : Experimental Results. 347:335–347, 1985.
- W J Quadackers and H Schuster. Corrosion of High Temperature Alloys in the Primary Circuit Helium of High Temperature Gas Cooled Reactors. -Part I: Theroetical Background. 150:141–150, 1985.
- Malgorzata M Lencka and Richard E Riman. Thermodynamic Modeling of Hydrothermal Synthesis of. Chemistry Materials, 5(8):61–70, 1993. ISSN 0897-4756. doi: 10.1021/cm00025a014. URL <http://pubs.acs.org/doi/pdf/10.1021/cm00025a014>.
- Ho Jung Lee, Gokul Obulan Subramanian, Sung Hwan Kim, and Changheui Jang. Effect of pressure on the corrosion and carburization behavior of chromia-forming heat resistant alloys in high-temperature carbon dioxide environments. Corrosion Science, 111:649–658, 2016. ISSN 0010938X. doi: 10.1016/j.corsci.2016.06.004. URL <http://dx.doi.org/10.1016/j.corsci.2016.06.004>.
- Chien, F. R., & Brown, R. (1992). Cyclic oxidation of Haynes 230 alloy. Journal of Materials Science, 27(6), 1514–1520. <https://doi.org/10.1007/BF00542912>

## CHAPTER 4: HIGH TEMPERATURE CORROSION OF 316 AND 310 STAINLESS STEELS AND ALLOY 709 IN SC-CO<sub>2</sub>

**4.1. Introduction and Motivation for Alloy 709:** Alloy 709 is receiving considerable attention for implementation into a sodium fast reactor (SFR) but there is interest in the compatibility of alloy 709 in SC-CO<sub>2</sub> because there is interest in using the SC-CO<sub>2</sub> Brayton cycle as the power conversion cycle for the SFR. The alloy has a higher Cr (which promotes chromia formation on the surface) and Ni content than conventional austenitic stainless steel (e.g., 316, 310) and contains a small amount of Mo. Alloy 709 has shown the best overall performance for austenitic stainless steels in terms of yield strength, tensile ductility, thermal aging resistance, resistance to sodium exposure, creep resistance, weldability, and high temperature toughness. Figure 4.1 summarizes some of the attributes of alloy 709.

	316(H) / TP316H	Alloy 709 / TP310MoCbN
Composition (wt%)	18Cr-12Ni-Mn-Mo-C	22Cr-25Ni-Mn-Mo-V-Nb-C-N
Strengthening mechanism	Solution hardening (Mo) + Precipitate hardening (M <sub>23</sub> C <sub>6</sub> )	Solution hardening (Mo) + Precipitate hardening {M(C,N), Z-phase, M <sub>23</sub> C <sub>6</sub> }
Mechanical data	Tensile, creep, toughness: from datasheet (NRI/NIMS)	Tensile, creep, toughness: from datasheet (Nippon Steel)
YS/UTS/EL at RT	205MPa/ 515MPa/ 35%	270MPa/ 640MPa/ 30%
Advantage	<ul style="list-style-type: none"> <li>• Good oxidation resistance</li> <li>• Good weldability</li> <li>• Lower material cost</li> </ul>	<ul style="list-style-type: none"> <li>• Good creep properties</li> <li>• Better oxidation resistance</li> <li>• No problem on welding</li> </ul>
Disadvantage	• Adequate creep properties	• Expensive due to higher Ni

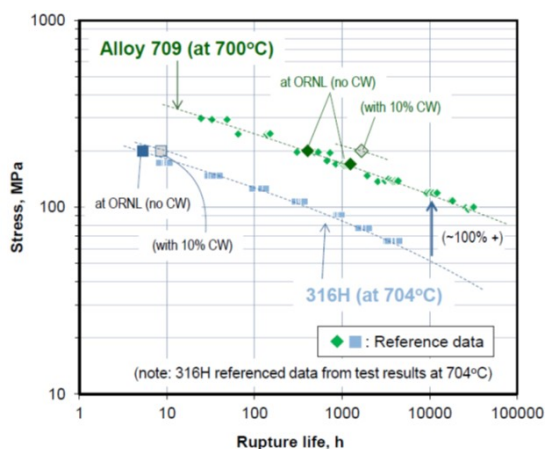
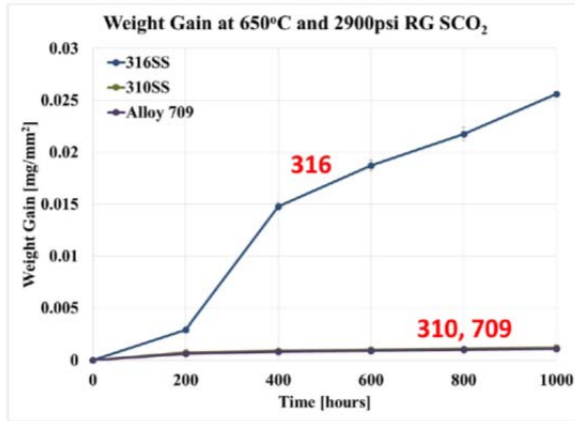


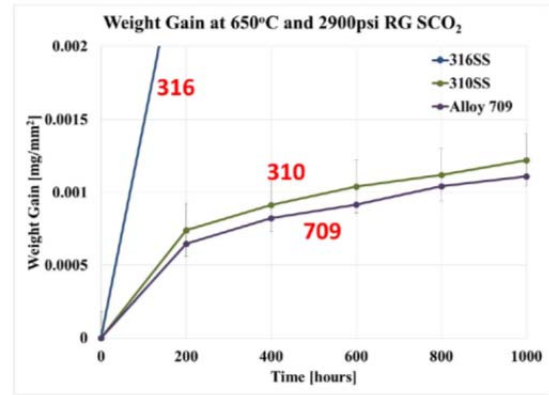
Figure 4.1: (a) General properties of alloy 709, (b) creep rupture life as a function of time at 700°C for alloys 709 and 316SS

In this project, alloy 709 samples procured from Oak Ridge National Laboratory (ORNL) were tested high temperature, high pressure SC-CO<sub>2</sub> and the performance of alloy 709 was benchmarked against 310 and 316 austenitic stainless steels. Tests were performed at 650°C for total exposure duration of 1000 hours in increments of 200 hours in research grade (RG) SC-CO<sub>2</sub> in the autoclave test facility as described earlier. Samples were copper coated before cross sectional analysis to preserve the oxide layer from edge rounding and to provide a distinct separation between the mounting material and the oxide layer.

**4.2. Results and Analysis:** As shown in Figure 4.2a, 316SS exhibited a much greater weight gain than 310SS or alloy 709. This metric indicates that 316SS has significantly lower corrosion resistance than 310SS and alloy 709. Alloy 310SS and alloy 709 perform very similarly and exhibit diffusion-limited protective oxide layer growth, due to the formation of a cohesive, protective chromia oxide layer, while 316SS exhibited para-linear oxidation behavior indicating that excessive oxidation. Figure 4.2b shows an expanded version of Figure 4.2a and shows alloy 709 to have superior in regards to corrosion resistance than 310 stainless steel due to its slightly higher Cr content.



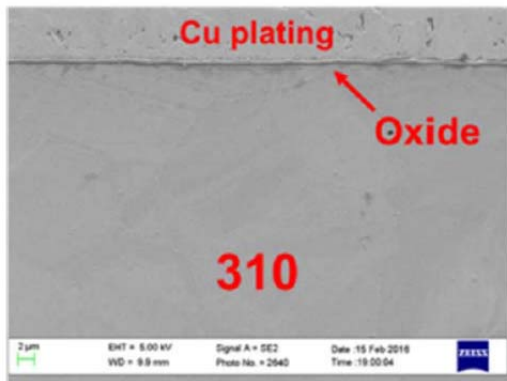
(a)



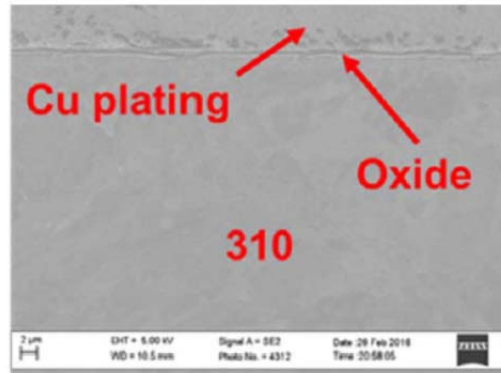
(b)

Figure 4.2: Weight change measurements as a function of exposure time in RG SC-CO<sub>2</sub> at 650°C, (a) compressed scale and (b) expanded scale.

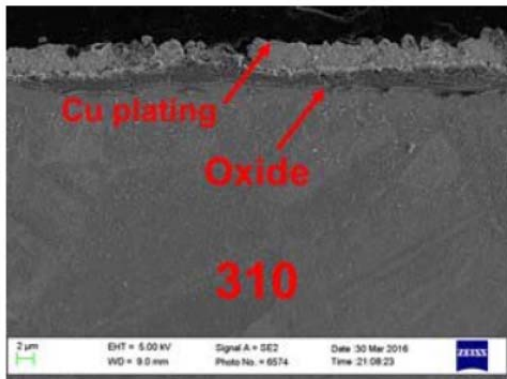
Figure 4.3 shows cross-sectional SEM micrographs of 310SS indicating the progress in after exposure for (a) 200, (b) 600, and (c) 1000 hours at 650°C. The oxide layer thicknesses were measured and determined to be 0.49  $\mu\text{m}$ , 0.76  $\mu\text{m}$ , and 3.00  $\mu\text{m}$ , respectively for 200, 600, and 1000 hours, respectively.



(a)



(b)



(c)

Figure 4.3: Cross-sectional SEM images showing the development of oxide layer on 310 stainless steel as a function of exposure time in RG SC-CO<sub>2</sub> at 650°C, (a) 200 hours, (b) 600 hours, and (c) 1000 hours.

Figure 4.4 shows the cross-sectional SEM micrograph of alloy 310 exposed to SC-CO<sub>2</sub> at 650°C for 1000 hours with a corresponding EDS elemental mapping. The oxide was observed to be an approximately 3.00  $\mu\text{m}$  thick chromium-rich spinel with a region of nickel enrichment and chromium depletion in the substrate directly under the oxide/substrate interface. Oxide cracking is apparent, indicating further oxidation of the metal may readily occur.

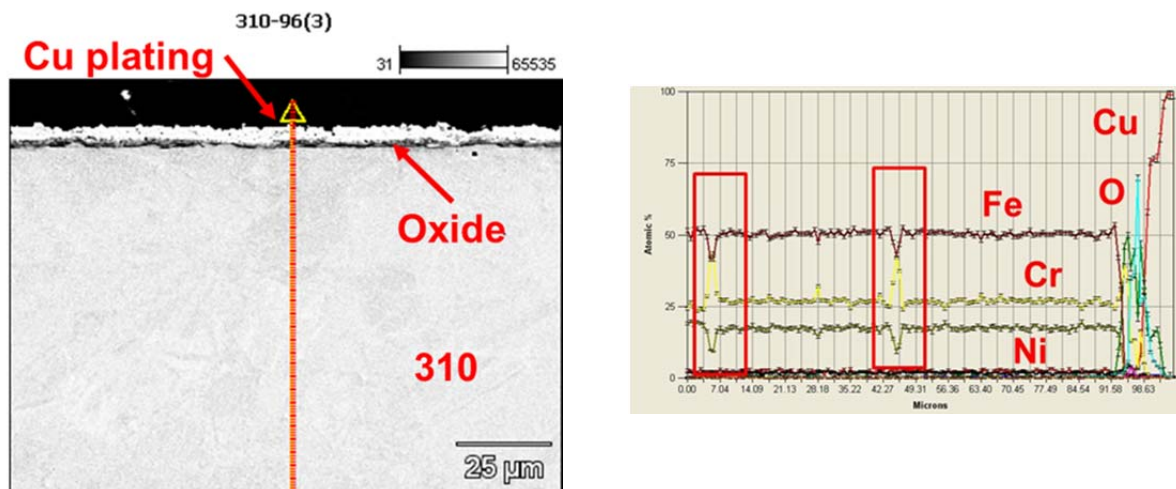


Figure 4.4: (a) Cross-sectional SEM image of oxide layer on 310 stainless steel exposed to RG SC-CO<sub>2</sub> at 650°C for 1000 hours, (b) EDS line-scan across the oxide layer.

Figure 4.5 shows cross-sectional SEM micrographs of 316SS indicating the progress after exposure for (a) 200, (b) 600, and (c) 1000 hours at 650°C. As may be noted 316 SS exhibits a significantly thicker oxide layer than 310SS. The oxide layer formed on 316SS also showed significant spallation as can be seen from plan view images and EDS elemental maps shown in Figure 4.6.



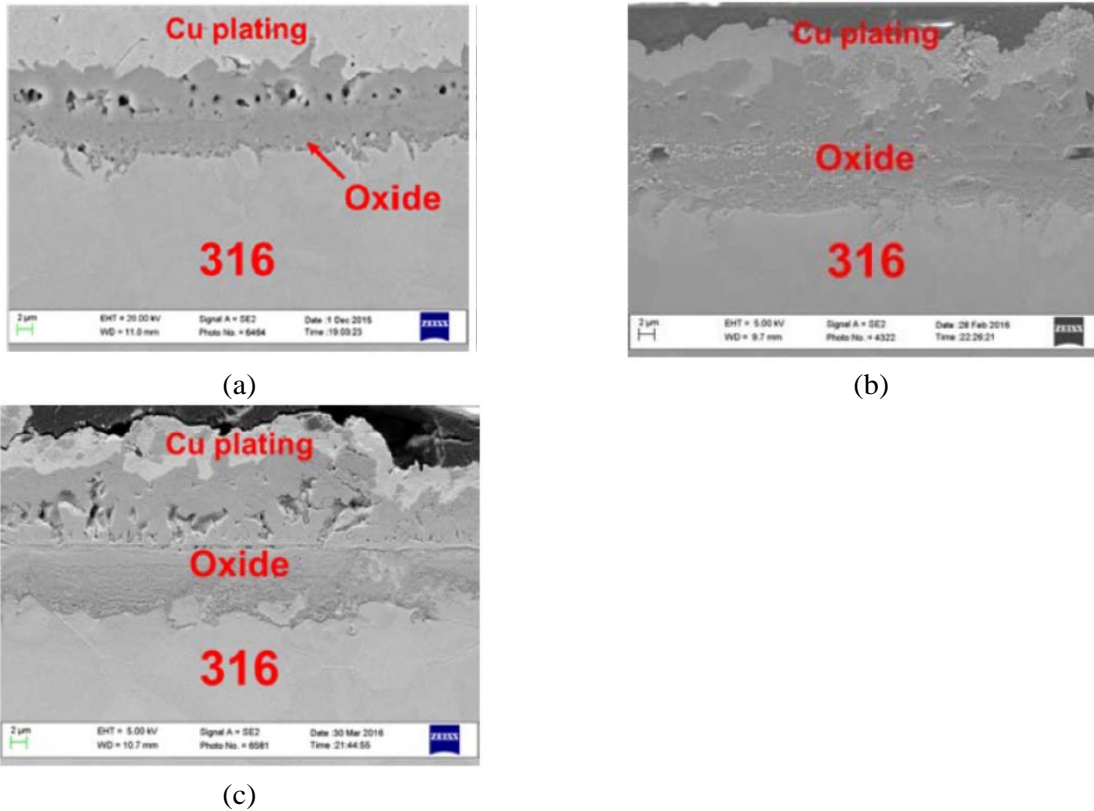


Figure 4.5: Cross-sectional SEM images showing the development of oxide layer on 316 stainless steel as a function of exposure time in RG SC-CO<sub>2</sub> at 650°C, (a) 200 hours, (b) 600 hours, and (c) 1000 hours.

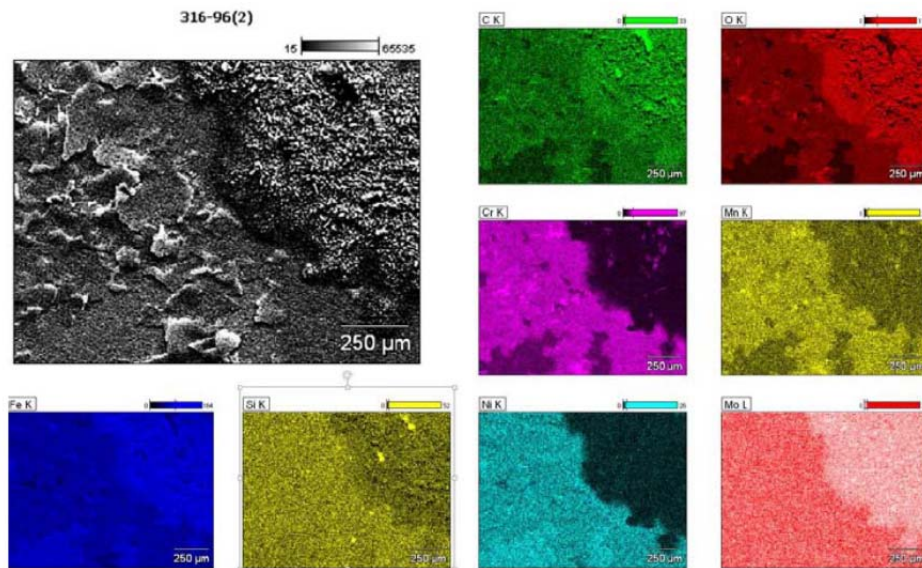


Figure 4.6: SEM plan view images of oxide layer on 316 stainless steel after exposure to just 200 hours in RG SC-CO<sub>2</sub> at 650°C and EDS elemental analysis

Figure 4.7 shows the cross-sectional image of the oxide layer developed on 316SS after exposure to 600 hours in RG SC-CO<sub>2</sub> at 650°C and EDS elemental analysis. The outer layer is a

fragile magnetite layer that may be prone to spallation and an inner spinel (Fe, Cr)-oxide layer.

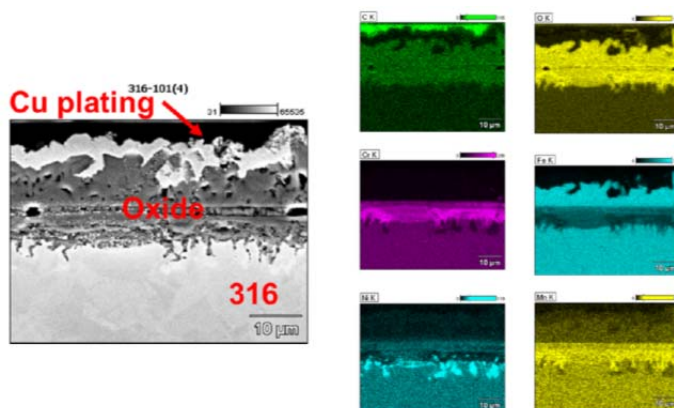


Figure 4.7. SEM cross-sectional image of the oxide layer developed on 316SS after exposure to 600 hours in RG SC-CO<sub>2</sub> at 650°C and EDS elemental analysis showing an outer Fe-oxide magnetite layer and an inner spinel (Fe,Cr)-oxide layer.

Figure 4.8 shows cross-sectional SEM micrographs of alloy 709 indicating the progress in after exposure for (a) 200, (b) 600, and (c) 1000 hours at 650°C. The oxide layer formed on this alloy was substantially thinner than on 316 stainless steel and slightly thinner than the one that formed on 310SS.

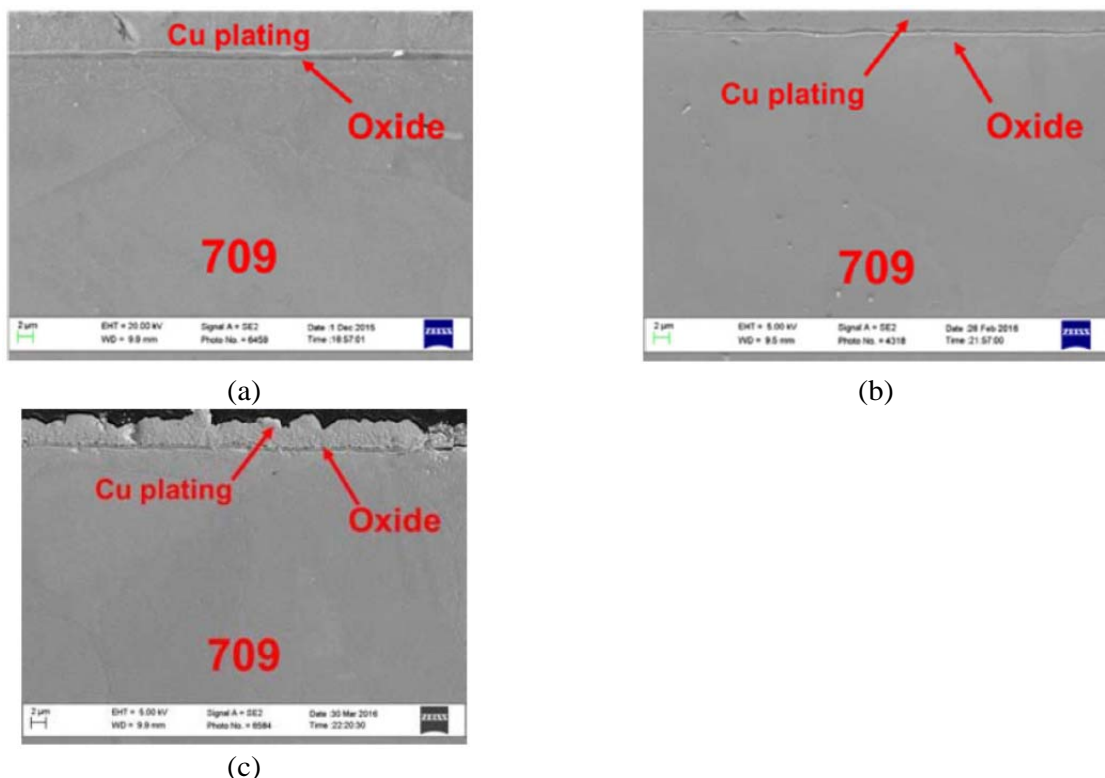


Figure 4.8: Cross-sectional SEM images showing the development of oxide layer on alloy 709 as a function of exposure time in RG SC-CO<sub>2</sub> at 650°C, (a) 200 hours, (b) 600 hours, and (c) 1000 hours.

Figure 4.9 shows a direct comparison of the oxide layer that forms on the three alloys after exposure to RG SC-CO<sub>2</sub> at 650°C for 1000 hours.

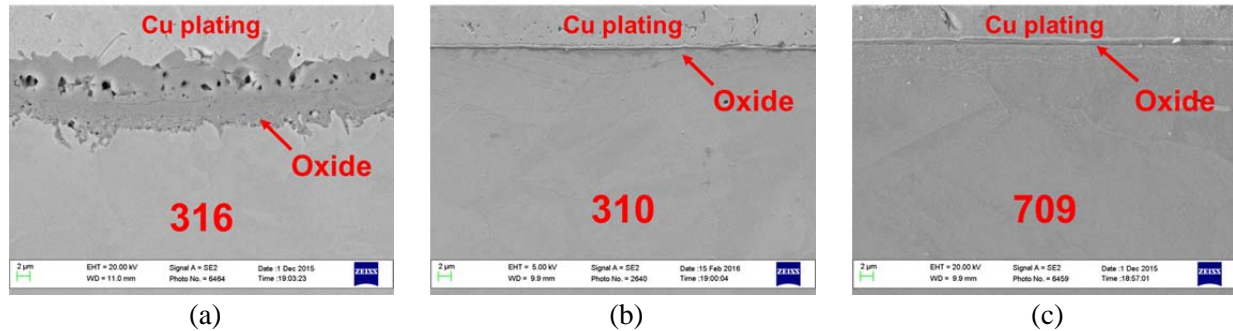


Figure 4.9: Cross-sectional SEM images showing the oxide layer formed after exposure in RG SC- $\text{CO}_2$  at  $650^\circ\text{C}$  for 1000 hours, (a) 316 stainless steel, (b) 310 stainless steel, and (c) alloy 709.

Table 4.1 summarizes the thickness of the oxide layers developed on the three alloys as function of exposure time.

Table 4.1: Measured Oxide Thicknesses for Alloys Investigated. [ $\mu\text{m}$ ].

	310	316	709
200 hours	0.49	11.39	0.61
600 hours	0.76	19.64	0.66
1000 hours	3.00	17.94	0.66

Figure 4.10 shows the x-ray diffraction patterns of the oxide layers that form on 310SS. A brief description of phases observed is as follows:

- *Untested 310SS*: As expected, peaks from the base material austenite phase.
- *400 hours*: Chromium rich spinel,  $\text{Cr}_{2-x}\text{Fe}_x\text{O}_3$ , and manganese-iron spinel,  $\text{Mn}_{2-x}\text{Fe}_x\text{O}_4$ , and chromium manganese spinel,  $\text{CrMn}_2\text{O}_4$  observed. Contributions from the austenite base material were observed since the oxide layer is very thin.
  - *1000 hours*: Chromium rich spinel,  $\text{Cr}_{2-x}\text{Fe}_x\text{O}_3$ , and manganese-iron spinel  $\text{Mn}_{2-x}\text{Fe}_x\text{O}_4$  observed. Contributions from the austenite base material were also detected but the intensity of the peaks was smaller than the 400 hour sample due to thicker oxide layer.

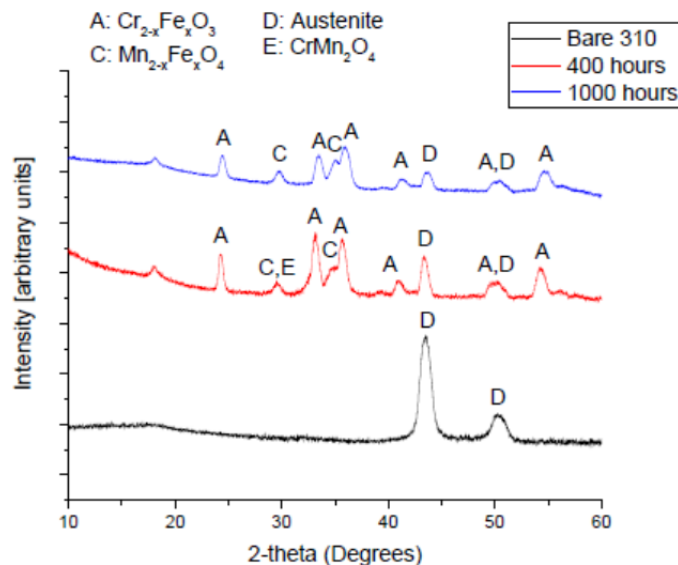


Figure 4.10: XRD patterns for 310SS for bare, untested sample and after exposure to 400 hour, and 1000 hours.

Figure 4.11 shows the XRD patterns for 316SS. Peaks identified include:

- *Untested sample:* As expected, peaks from the austenite phase base material.
- *400 hours:* Primarily Cr, Mn, and Fe based oxide species were observed, including (Cr,Mn,Fe)O<sub>4</sub>, Mn<sub>2</sub>NiO<sub>4</sub>, (Mn,Fe)O<sub>3</sub>. Base material austenite peaks were not observed due to the thick oxide layer.
- *1000 hours:* Hematite and magnetite oxide phases are now observed including Fe<sub>2</sub>O<sub>3</sub> and Fe<sub>3</sub>O<sub>4</sub>. Other Cr-, Mn-, Fe-, and Ni-oxide phases observed including, (Cr,Mn,Fe)O<sub>4</sub>, Mn<sub>2</sub>NiO<sub>4</sub>, NiCr<sub>2</sub>O<sub>4</sub>, Mn<sub>2</sub>O<sub>3</sub>.

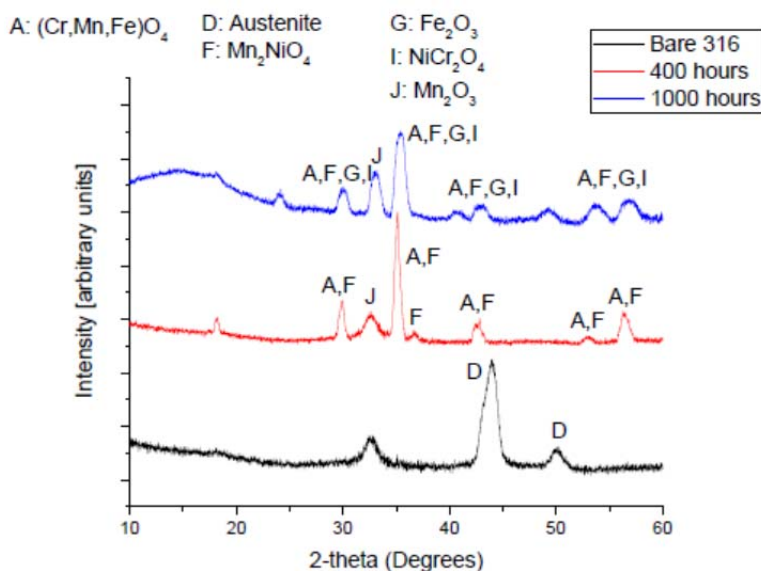


Figure 4.11: XRD patterns for 316SS for bare, untested sample and after exposure to 400 hour, and 1000 hours.

Figure 4.12 shows the XRD peaks for alloy 709.

- *Untested alloy*: Base material austenite phase.
- *400 hours*: Cr-rich  $\text{Cr}_{2-x}\text{Fe}_x\text{O}_3$  spinel peaks were observed alongside with contributions from the austenite base material due the small thickness of the oxide layer.
- *1000 hours*: Cr-rich spinel,  $\text{Cr}_{2-x}\text{Fe}_x\text{O}_3$ , manganese-iron spinel,  $\text{Mn}_{2-x}\text{Fe}_x\text{O}_4$ , and chromium manganese spinel,  $\text{CrMn}_2\text{O}_4$  were observed. Contributions from the austenite base material were still detected.

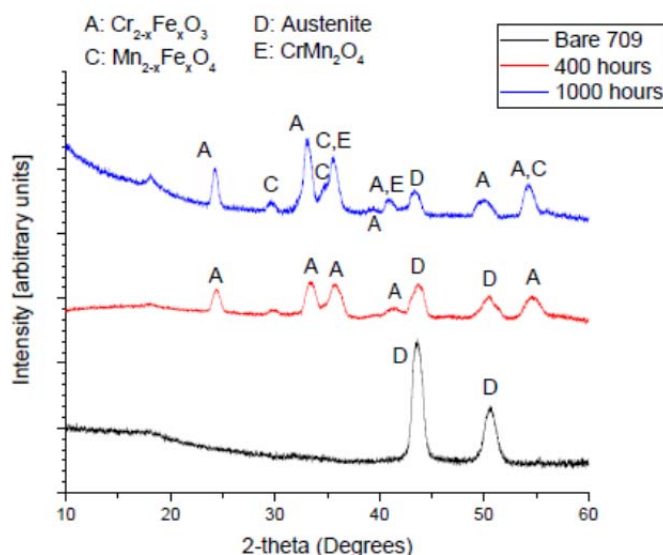
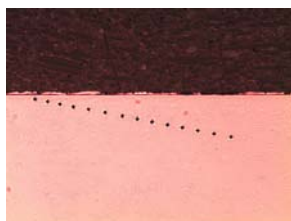
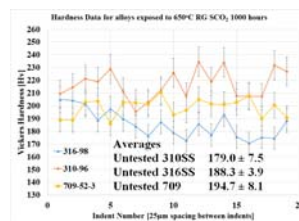


Figure 4.12: XRD patterns for alloy 709 for bare, untested sample and after exposure to 400 hour, and 1000 hours.

Microhardness testing was conducted on 1000 hour exposed samples to investigate the possibility of carburization during SC- $\text{CO}_2$  exposure at  $650^\circ\text{C}$ . Tests were performed using the Vickers hardness test (Wilson Tukon 1202) with an applied load of 50g. Indents were laterally spaced 75 microns apart from one another and 25 microns vertically. An optical micrograph of a microhardness measurement pattern is shown in Figure 4.13a. Average microhardness values for untested samples were also measured and the hardness profiles are presented in Figure 4.13b. No significant increase in hardness was observed indicating that carburization does not occur to any significant degree given that carburization increases the hardness.



(a)



(b)

Figure 4.13: (a) optical microscopy image of typical microhardness measurement pattern and (b) pattern. Microhardness test results on 310, 316, and 709 and accompanying average hardness values for untested samples.

#### Bibliography Consulted



Robert Hill. Overview of us fast reactor technology program. 2013.

Sam Sham. Advanced reactor concepts program materials development - accomplishments and plans. 2013.  
URL <http://www.energy.gov/sites/prod/files/2013/09/f2/ARC-Matls-CrossCut-2013.pdf>.

A Moiseyev, Y Tang, S Majumdar, C Grandy, and K Natesan. Impact from the adoption of advanced materials on a sodium fast reactor design. *Nuclear Technology*, 175(2):468–479, 2011.

Philip J Maziasz, Bruce A Pint, John P Shingledecker, Karren L More, Neal D Evans, and Edgar Lara-Curzio. Austenitic stainless steels and alloys with improved high- temperature performance for advanced microturbine recuperators. In *ASME Turbo Expo 2004: Power for Land, Sea, and Air*, pages 131–143. American Society of Mechanical Engineers, 2004.

RW Swindeman. Stainless steels with improved strength for service at 760 c and above. Technical report, Oak Ridge National Lab., TN (United States), 1998.

CD Lundin and CYP Qiao. Comparative evaluations of the weldability of modified 800h and other advanced austenitic stainless steels. Technical report, Oak Ridge National Lab., TN (United States), 1993.

Todd R Allen, Kumar Sridharan, Yun Chen, Lizhen Tan, Xiaowei Ren, and Alan Krutzenga. Research and development on materials corrosion issues in supercritical water environment. *ICPWS XV, Berlin, Germany*, pages 1–12, 2008.

Stephen Osgerby and A Tony Fry. Steam oxidation resistance of selected austenitic steels. In *Materials Science Forum*, volume 461, pages 1023–1030. Trans Tech Publ, 2004.

K Natesan, A Purohit, and DL Rink. Fireside corrosion of alloys for combustion power plants. *POWERPLANT CHEMISTRY*, 4:549–556, 2002.

TC Totemeier, H Lian, DE Clark, and JA Simpson. Microstructure and strength characteristics of alloy 617 welds. *INL/EXT-05-00488*, 2005.

Ho Jung Lee, Gokul Obulan Subramanian, Sung Hwan Kim, and Changheui Jang. Effect of pressure on the corrosion and carburization behavior of chromia-forming heat- resistant alloys in high-temperature carbon dioxide environments. *Corrosion Science*, 2016.



## CHAPTER 5: CORROSION STABILITY OF SOLID STATE DIFFUSION BONDS IN SC-CO<sub>2</sub> ENVIRONMENT

**5.1. Introduction:** Diffusion bonding (DB) is a high temperature, high pressure solid state metal joining process that is attractive for the fabrication of heat exchangers for the SC-CO<sub>2</sub> Brayton cycle. Diffusion bonding is defined as the process that make permanent joints by establishing interatomic bonds between workpieces through the action of local or general heating or plastic deformation, or both. The process obviates the need for liquation-base processes such as welding, which leave behind a gradient a microstructure and properties from the fusion zone to the heat-affected zone (HAZ) to the base material. In order for the diffusion bonding process to be effective, and the materials involved must be amenable to interdiffusion of atoms of the two mating surfaces. Important parameters in diffusion bonding include:

*Pressure:* The applied loads are great enough to cause slight micro-plastic deformation (1-2%) but not cause macro-deformation of the material.

*Temperature:* The temperatures applied are generally 50-80% of the absolute melting temperature of the materials being bonded.

*Time:* The time for the bonding process can range up to 60 minutes and greater.

*Surface Finish:* The surface finish of the material is very important because it influences how the materials being bonded interact with each other on an atomic scale. The surface roughness determines the extent of initial surface contact, the size of the voids and ultimately influences the efficacy of the bonding. The presence of oxides and other debris can lead to a poor bonding.

*Environment:* The bonds are most often fabricated in a vacuum (i.e., at low base pressures).

*Interlayer Materials:* Interlayer materials are often used when bonding dissimilar materials in order to enhance contact and reduce residual stresses or thermal expansion mismatch developed at the dissimilar material interfaces.

Figure 5.1 schematically illustrates the microstructural evolution of the diffusion bond. In the first stages of diffusion bonding, initial asperities of the materials come into contact with one another. Plastic deformation of the asperities occurs and the contact areas consequently increase. Large, irregularly shaped voids are then removed and the grain boundaries migrate. Lastly, isolated voids are removed by diffusion and the grain boundaries coalesce and volume diffusion occurs.

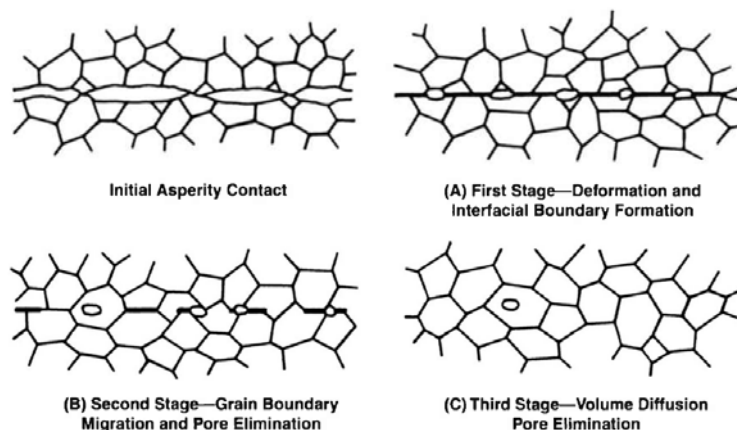


Figure 5.1: Mechanism of diffusion bonding.

Printed Circuit Heat Exchangers (PCHE) are being considered for heat exchangers for the SC-CO<sub>2</sub> Brayton cycle because PCHE maximizes the available surface area for effective heat transfer. Because of the small channel sizes of PCHE, diffusion bonding is emerging as an ideal fabrication technique for this type of a heat exchanger. Figure 5.2 shows an example of PCHE, where flow channels are etched chemically onto metal plates and the plates are then stacked and combined into a single block using diffusion bonding processes to create the heat exchanger.

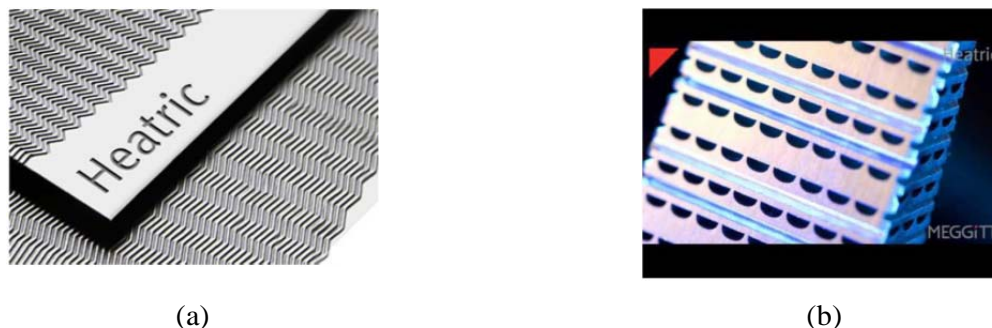


Figure 5.2: (a) Etched plates for PCHE and (b) bonded PCHE cross-section depicting flow channels.

**6.2. Experimental:** The following material couple systems were investigated in this project for diffusion bonding experiments: (i) mutual bonding between 310 stainless steel, (ii) mutual bonding between 316 stainless steel, and (c) mutual bonding between Haynes 230. The diffusion bond work was performed at a private company Vacuum Process Engineering. The diffusion bonding parameters used are as follows (more specific parameters could not be provided by the company due to proprietary reasons): (i) *Temperature:* 900-1200°C, (ii) *Pressure:* 500-1000 psi, (iii) *Physical Deformation:* 1-2%, and (iv) *Time:* 1-2 hours

Testing was conducted in the experimental facility described earlier in the report, at 20 MPa pressure, 650°C RG SC-CO<sub>2</sub> for exposure durations of 200, 600, and 1000 hours. Samples were prepared to ensure that edge effects were minimized which is particularly important for examining the performance of the diffusion bonding.

In order to more fully understand the effect of high temperature SC-CO<sub>2</sub> corrosion on diffusion bonds, detailed characterization was performed of the materials before bonding, after diffusion bonding, and after corrosion testing. It should be noted that there are multiple sources of stress that the diffusion bonds experience including:

- Thermal and physical stress from diffusion bonding process,
- Heat from autoclave environment (in effect, heat treating the materials)
- Ingress of CO<sub>2</sub> into substrate material which may affect the integrity of the bond, for example through carburization.
- Of most importance in this work was the ingress of SC-CO<sub>2</sub> into the material and how it affects the bonds integrity by way of corrosion. Therefore, extensive characterization was must performed at various stages to most effectively identify the effects of SC-CO<sub>2</sub> corrosion on the diffusion bond line. The following samples were systematically evaluated:
- As-received material
- As-received diffusion bond
- Along diffusion bond interface, near edge exposed to SC-CO<sub>2</sub>
- Along diffusion bond interface, away from edge exposed to SC-CO<sub>2</sub>

- Bulk material (to identify the changes in bulk material due to thermal effects).
- Diffusion bond exposed to SC-CO<sub>2</sub>

**5.3. Evaluation Techniques:** In order to assess the response of the diffusion bond to SC-CO<sub>2</sub> environment, optical microscopy, SEM, EDS, and microhardness testing were performed. The etchant used for 310 and 316 were Glyceregia (15 mL HCl, 10 mL glycerol, 5 mL HNO<sub>3</sub>), etched for approximately 2-3 minutes by immersion. The etchant used on the Haynes 230 was Kallings reagent (40 mL HCl, 40 mL HNO<sub>3</sub>, and 2g CuCl<sub>2</sub>) etched for approximately 2 minutes by immersion. Optical microscopy was used to evaluate the quality of etching. Figure 5.3 depicts microstructure after etching along the bond interface near the surface of the diffusion bonded 310 stainless steel sample exposed to RG SC-CO<sub>2</sub>.

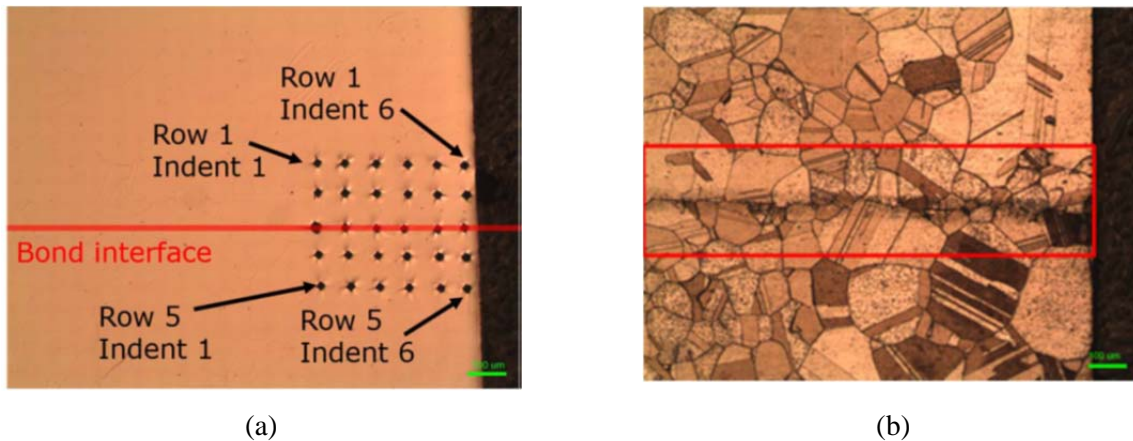


*Figure 5.3: (a) near edge microhardness and (b) microstructure for 310 stainless steel-310 stainless steel couple after exposure to RG SC-CO<sub>2</sub> at 650°C after 200 hours exposure.*

Microhardness testing was performed to evaluate the degree of carburization within the samples to examine if the diffusion bond acts as a conduit for carbon ingress. Figure 5.3(a) depicts typical microhardness indents made along the bond interface near the diffusion bond line, while Figure 5.4 depicts typical microhardness results. Microhardness indents are made in rows along the bond interface and parallel to the bond interface to compare differences. Results plotted are indents specific to each row and averaged along each row, and compared to as-received DB and non-DB as received material samples. SEM and EDS were primarily used to obtain high resolution images of the region where potential carburization could have occurred and led to an increased concentration of carbides.

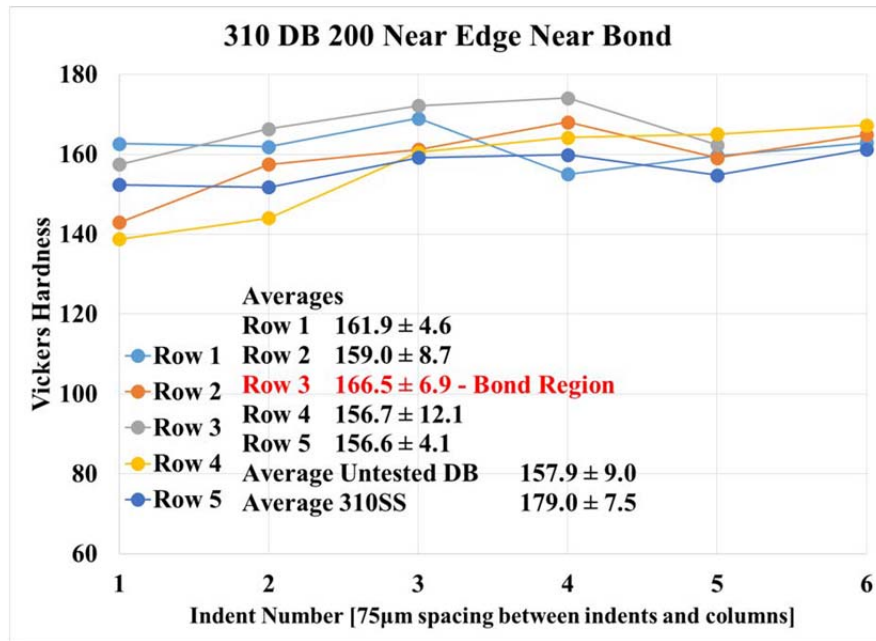
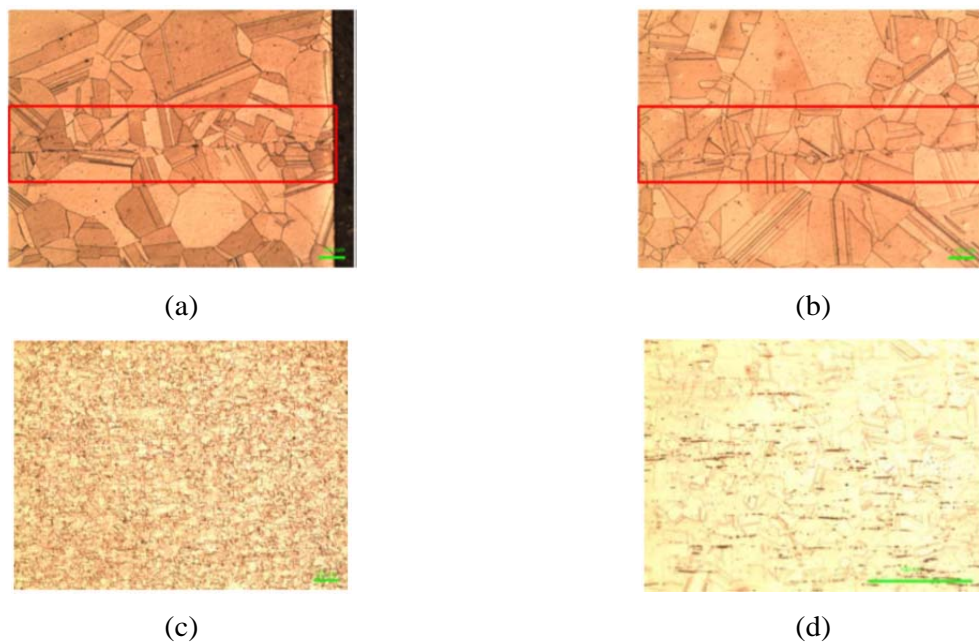
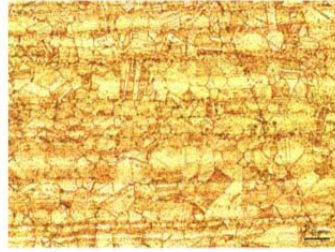


Figure 5.4: Vickers hardness testing results on 310 stainless steel-310 stainless steel couple sample near the edge.

**5.4. Results and Analysis:** Figures 5.5 and 5.6 show etched 310SS samples to ascertain the behavior of diffusion bonded samples in the SC-CO<sub>2</sub> environment. Figure 5.5 shows an etched, as received, untested 310SS diffusion bond (a) along diffusion bond (DB) interface near the edge exposed to SC-CO<sub>2</sub> and (b) along DB interface near the center of sample which is not exposed to SC-CO<sub>2</sub>. Figure 5.5(c) and (d) low and high magnification optical images of etched, as received, non-diffusion bonded, untested 310SS to compare the microstructure of the diffusion bonded material and as-received, untested material. Figure 5.5(e) shows a non-DB, etched 310SS exposed to 650°C RG SC-CO<sub>2</sub> for 1000 hours.





(e)

(f)

*Figure 5.5: Etched optical microscopy images of as-received 310 stainless steel: (a) untested 310DB near edge, (b) untested 310 DB near center of sample, (c) untested 310, non-DB low magnification, (d) untested 310, non-DB high magnification, and (e) etched 310SS exposed for 1000 hours at 650°C RG SC-CO<sub>2</sub>.*

Figure 5.6 (a) and (b) depict similar images to Figure 5.5(a) and (b) except they have been aged in the SC-CO<sub>2</sub> environment for 200 hours; Figure 5.6(c) and (d) show similar images except they have been aged in the SC-CO<sub>2</sub> environment for 600 hours, and Figure 5.6 (e) and (f) show similar images except they have been aged in the SC-CO<sub>2</sub> environment for 1000 hours. The bond region is highlighted in red. In outlined area, the following observations are made about 310SS diffusion bonded samples:

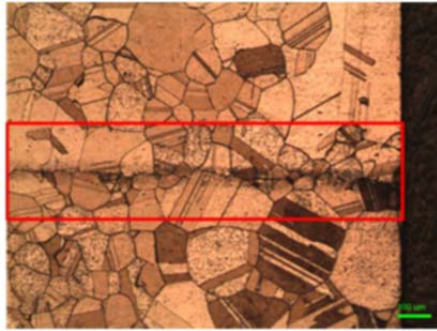
The initial bond quality is not as good and the grains do not appear to coalesce around the bond interface, indicating that the two joined materials have not necessarily thoroughly bonded. The grain size of the material dramatically increases as a result of the diffusion bonding process. This is expected because the material is exposed to 1000-1200°C for a few hours during the diffusion bonding process. This observation is consistent with previous studies.

As a consequence of the material not being perfectly bonded, after 200 hours of exposure to SC-CO<sub>2</sub>, there is significant carburization along the bond line nearest to the edge exposed to SC-CO<sub>2</sub> indicating that CO<sub>2</sub> was able to ingress into the bond initially. After 600 hours of exposure to SC-CO<sub>2</sub>, the carbides near the bond interface are not present; carburization occurs very slightly along grain boundaries. The degree of carburization along grain boundaries is slightly greater on the edge exposed to SC-CO<sub>2</sub>. The grains appear not nearly as separated as the initial bond indicating that the grains may begin to coalesce. After 1000 hours of exposure to SC-CO<sub>2</sub>, the carbide near the bond interface are present again but only near the edge exposed to SC-CO<sub>2</sub>. The grain size appears to be smaller near the bond interface, indicating that the two materials have joined effectively to form one material. The grain size of the material dramatically increases as a result of the diffusion bonding process. This is expected because the material is exposed to 1000-1200°C for a few hours during the diffusion bonding process. After 200 hours of exposure to SC-CO<sub>2</sub>, there is slight carbide formation along bond line nearest the edge exposed to SC-CO<sub>2</sub> indicating that SC-CO<sub>2</sub> may be able to ingress into the bond initially. This does not appear to be present in the center of the sample, indicating the diffusion of CO<sub>2</sub> into the material is limited to near the edge exposed to SC-CO<sub>2</sub>.

After 600 hours of exposure to SC-CO<sub>2</sub>, the carbides near the bond interface are not present but carburization occurs along grain boundaries. The degree of carburization along grain boundaries is greater on the edge near the sample exposed to SC-CO<sub>2</sub>.

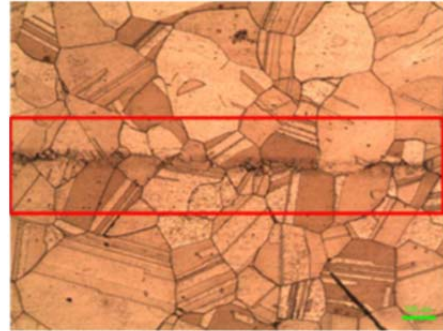
After 1000 hours of exposure to SC-CO<sub>2</sub>, carbides are observed to preferentially form along grain boundaries and are most densely located near the edge exposed to SC-CO<sub>2</sub>; however, clustered carbides are still observed near the center of the sample both near the diffusion bond interface and in the bulk material.





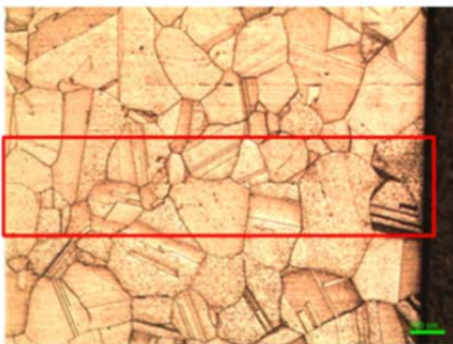
(a) 310 DB near edge exposed to 650°C RG S-CO<sub>2</sub> for 200 hours

(a)



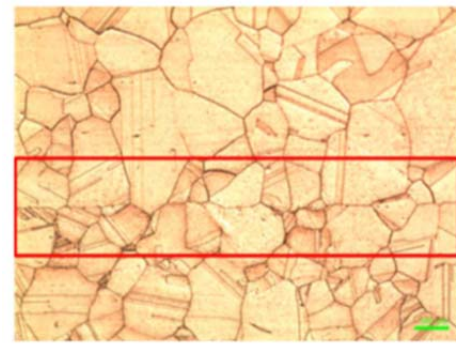
(b) 310 DB near center exposed to 650°C RG S-CO<sub>2</sub> for 200 hours

(b)



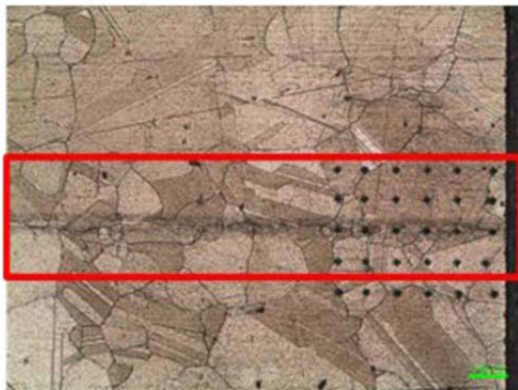
(c) 310 DB near edge exposed to 650°C RG S-CO<sub>2</sub> for 600 hours

(c)



(d) 310 DB near center exposed to 650°C RG S-CO<sub>2</sub> for 600 hours

(d)



(e) 310 DB near edge exposed to 650°C RG S-CO<sub>2</sub> for 1000 hours

(e)



(f) 310 DB near center exposed to 650°C RG S-CO<sub>2</sub> for 1000 hours

(f)

Figure 5.6: Etched optical images of diffusion bonded 310SS exposed to RG SC-CO<sub>2</sub> at 650°C.



Figures 5.7 and 5.8 show etched 316SS samples to evaluate the stability of diffusion bonded samples in the SC-CO<sub>2</sub> environment. Figure 5.8 depicts an etched, as received, untested 316SS diffusion bond (a) along DB interface near the edge exposed to S-CO<sub>2</sub> and (b) along DB interface near the center of sample which is not exposed to S-CO<sub>2</sub>. Figure 5.7(c) and (d) show low and high magnification optical images of etched, as received, non-diffusion bonded, untested 316SS to compare the microstructure between the diffusion bonded material and as-received, untested material. Figure 5.7(e) shows a non-DB, etched 316SS exposed to 650°C RG SC-CO<sub>2</sub> for 1000 hours. Figure 5.8 (a) and (b) depict images similar to Figure 5.7 (a) and (b), except that they have been aged in the SC-CO<sub>2</sub> environment for 200 hours; Figure 5.8(c) and (d) show similar images but with the samples aged in the SC-CO<sub>2</sub> environment for 600 hours, and Figure 5.8(e) and (f) show similar images with the samples aged in the SC-CO<sub>2</sub> environment for 1000 hours. The area where the bond is located is highlighted in red. The initial bond quality is good. The grains appear to coalesce around the bond.

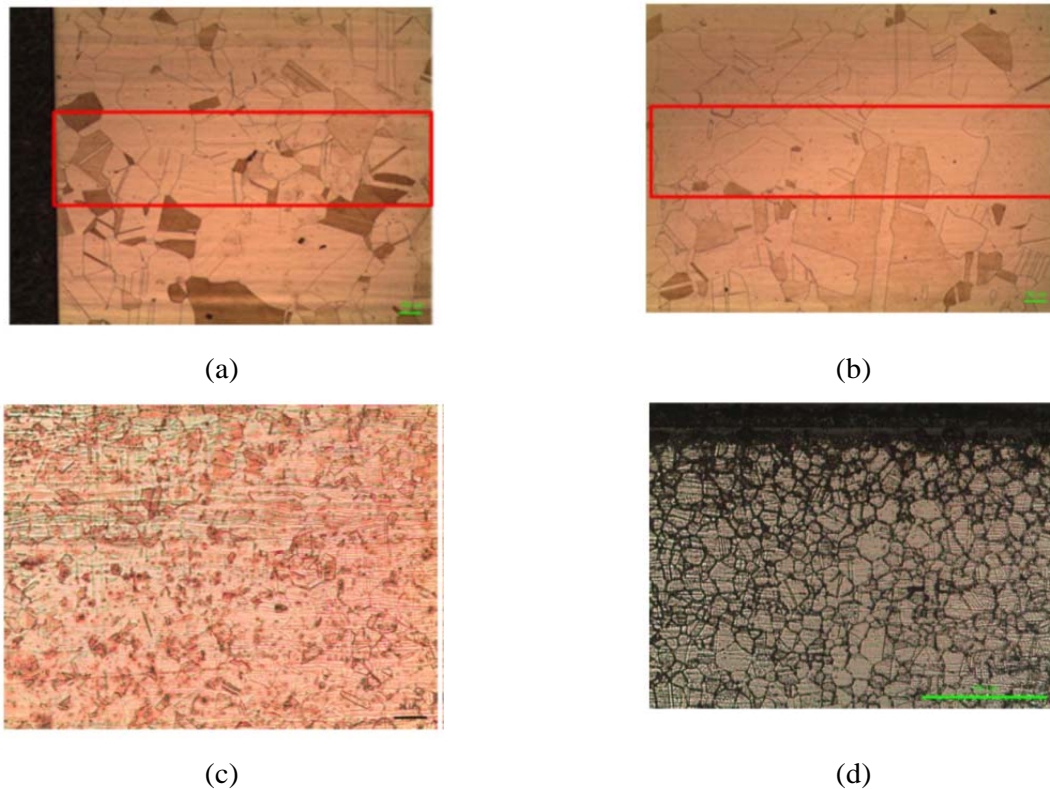
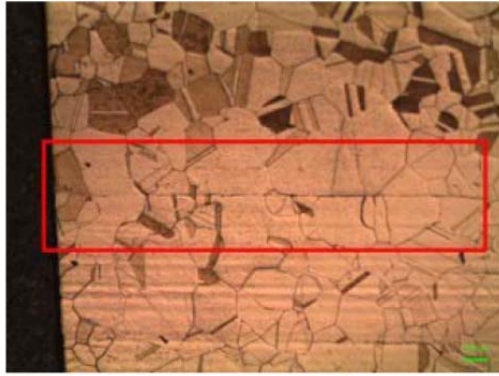
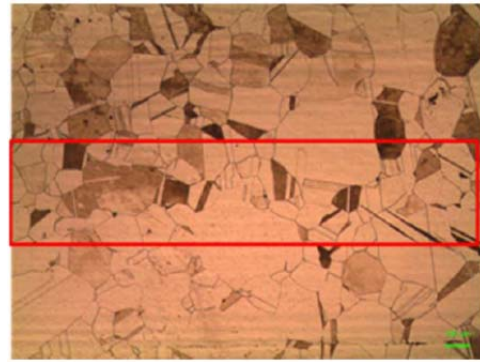


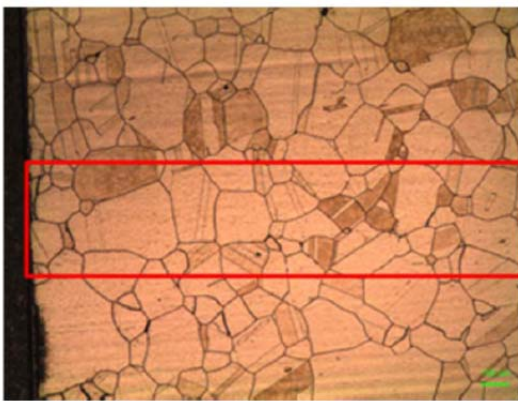
*Figure 5.7: Etched optical images of etched, as received 316SS; DB and non-DB.: (a) Untested 316 DB near edge, (b) Untested 316 DB near center of sample, (c) untested 316, non-DB, and (d) etched 316SS exposed to 650°C RG S- CO<sub>2</sub> for 1000 hours.*



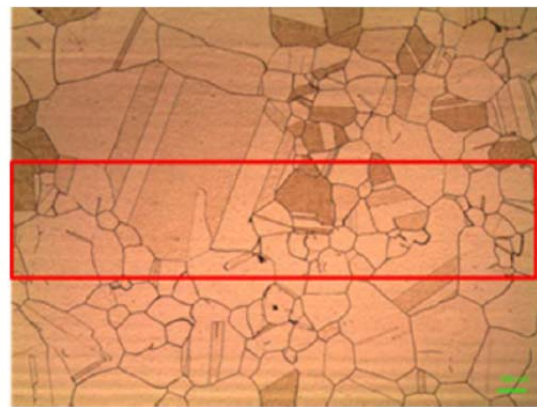
(a) 316 DB near edge exposed to 650°C RG S-CO<sub>2</sub> for 200 hours



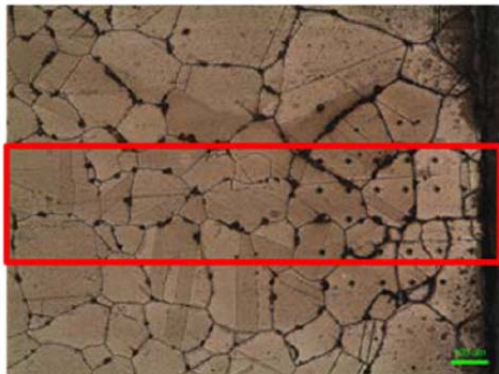
(b) 316 DB near center exposed to 650°C RG S-CO<sub>2</sub> for 200 hours



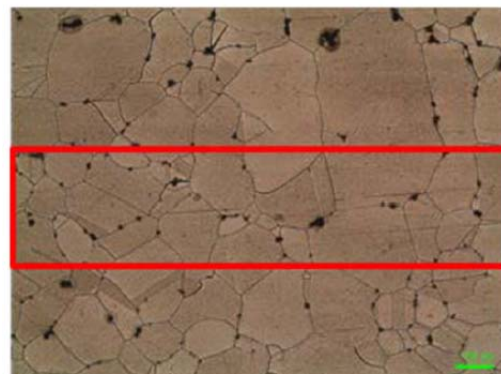
(c) 316 DB near edge exposed to 650°C RG S-CO<sub>2</sub> for 600 hours



(d) 316 DB near center exposed to 650°C RG S-CO<sub>2</sub> for 600 hours



(e) 316 DB near edge exposed to 650°C RG S-CO<sub>2</sub> for 1000 hours



316 DB near center exposed to 650°C RG S-CO<sub>2</sub> for 1000 hours

*Figure 5.8: Etched optical microscopy images of diffusion bonded 316 stainless steel after exposure to SC-CO<sub>2</sub>.*

Figures 5.9 and 5.10 depict etched Haynes 230 samples to ascertain the behavior of diffusion bonded samples in the S-CO<sub>2</sub> environment. Figure 5.9 depicts an etched, as received, untested Haynes 230 diffusion bond (a) along DB interface near the edge exposed to SC-CO<sub>2</sub> and (b) along DB interface near the center of sample which is not exposed to SC-CO<sub>2</sub>. Figure 5.9 c and d show low and high magnification optical images of etched, as received, non-diffusion bonded, untested Haynes 230 to compare the microstructure between the diffusion bonded material and as received, untested material. Figure 5.9e shows a non-DB, etched Haynes 230 sample exposed to 650°C RG SC-CO<sub>2</sub> for 600 hours.

Figure 5.10 a and b show similar images to Figure 5.9 a and b except they have been aged in the S-CO<sub>2</sub> environment for 200 hours; Figure 5.10 (c) and (d) show similar images except they have been aged in the S-CO<sub>2</sub> environment for 600 hours, and Figure 5.10 (e) and (f) show similar images except they have been aged in the S-CO<sub>2</sub> environment for 1000 hours. The area where the bond is located is highlighted in red. The following observations are made about Haynes 230 diffusion bonded samples:

The initial bond quality is not as good as for the 316SS but better than the 310SS. The grains appear to coalesce around the bond interface, indicating that the two joined materials have combined to form one material. There is still secondary carbide formation along the bond interface as the result of the diffusion bonding process. The grain size of the material increases as a result of the diffusion bonding process yet not nearly to the degree as the grain growth observed in the 310SS and 316SS, but secondary carbide formation is observed. After 200 hours of exposure to SC-CO<sub>2</sub> the secondary carbides were observed to be less present than in the as-received material, but more than the as-received, untested Haynes 230. The carbides phases are still observed bond interface.

After 600 hours of exposure to SC-CO<sub>2</sub> secondary carbides were observed to be less present than in the as received material, but more than the as-received, untested Haynes 230. The carbides present at the bond interface are still observed but much less readily than in the bonded, as received diffusion bonds or the 200 hours tested bonds. This may be an artifact of the etching process. There are still more secondary carbides present than in the as received, untested, unbonded material.

The concentration of secondary carbides appears to be smaller in the 1000 hour sample as compared to the 600 hours tested samples. It is possible that the exposure to 650°C is heat treating the material and removing most of the secondary carbides that resulted from the diffusion bonding process.

Secondary carbides are present at the surface of the unbonded, tested Haynes 230 at 650°C for 600 hours, indicating that carbon ingress may be possible; however, this behavior was not observed on the DB samples. Carburization tends to be initiated at grain boundaries on the surface of the non-DB sample.



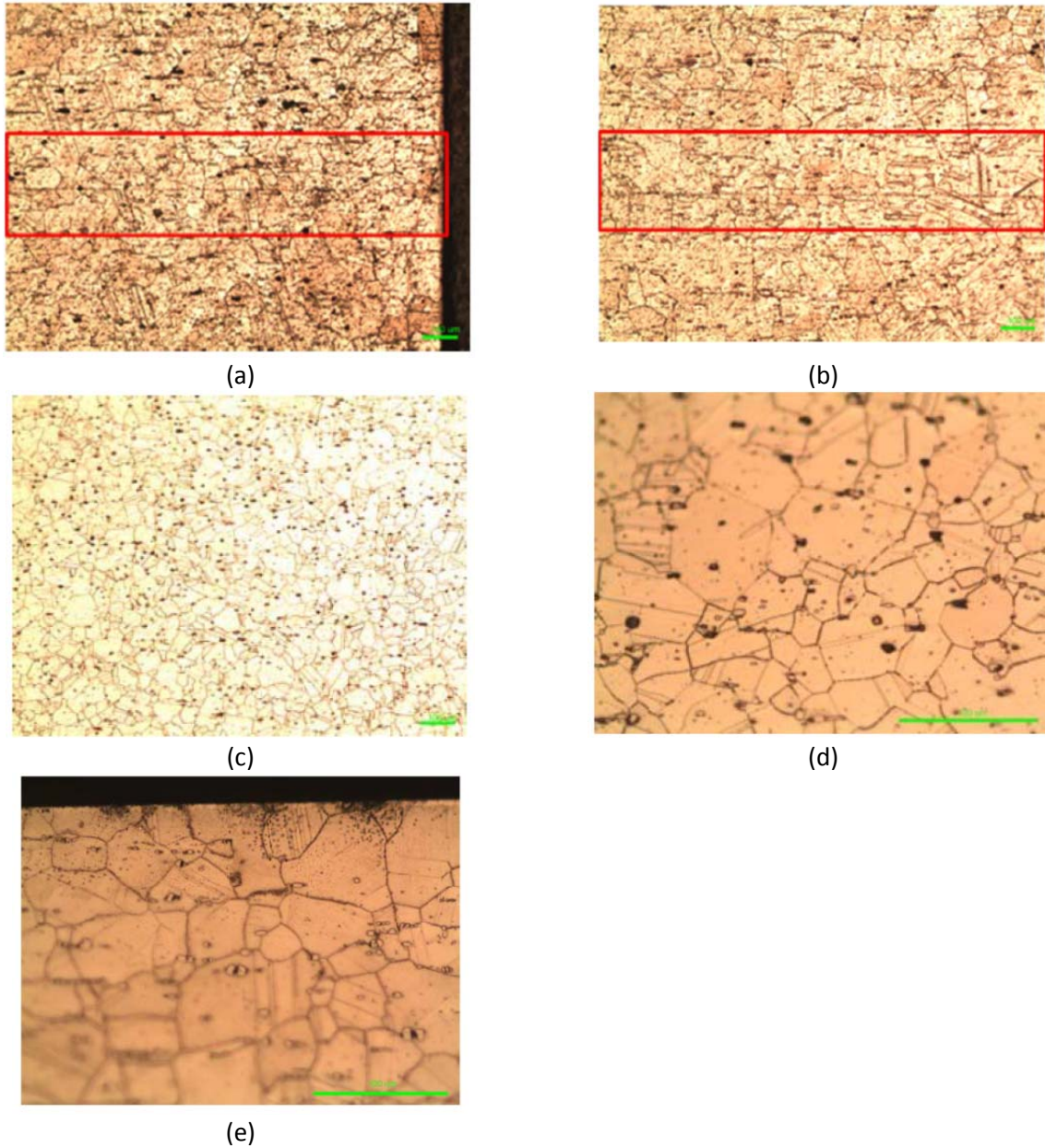


*Figure 5.9: Etched optical images of etched, as received Haynes 230; DB and non-DB: (a) untested DB near edge, (b) untested DB in the center of the sample, (c) untested DB sample away from DB, low magnification, (d) untested DB sample away from DB, high magnification, (e) etched after exposure to SC-CO<sub>2</sub> at 650°C for 600 hours.*

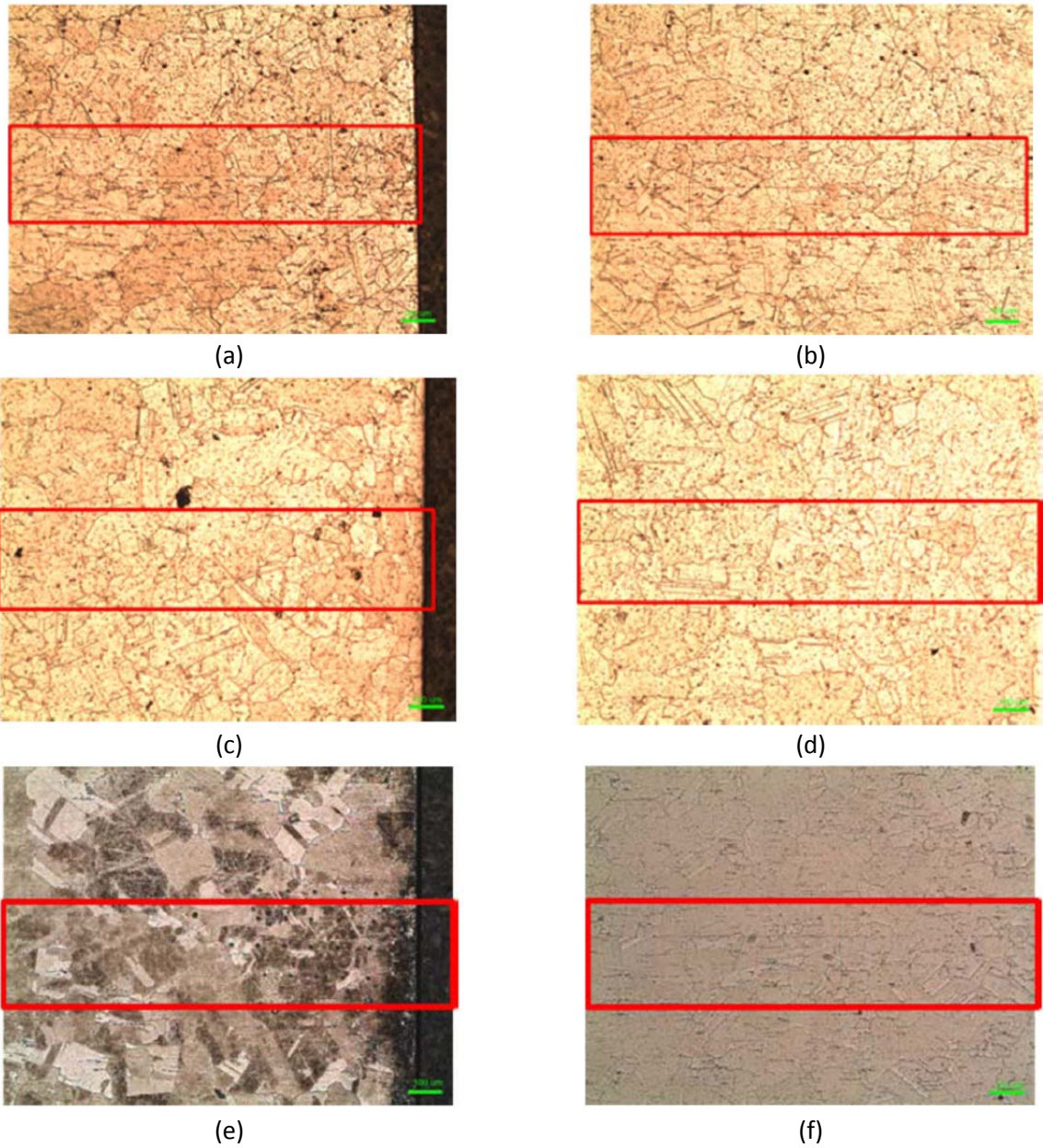


*Figure 5.10: Optical images of etched diffusion bonded Haynes 230 exposed to S-CO<sub>2</sub> (a) DB near-edge, 200 hours exposure at 650°C, (b) DB center of sample, 200 hours exposure at 650°C, (c) DB near-edge, 600 hours exposure at 650°C, (d) DB center of sample, 400 hours exposure at 650°C, (e) DB center of sample, 1000 hours exposure at 650°C, and (f) DB center of sample, 1000 hours exposure at 650°C,*



**6.4. Microhardness Testing:** Microhardness measurements were conducted to evaluate the extent of carburization (if any) within DB samples exposed to SC-CO<sub>2</sub>. Although, this may not be a fully confirmatory test to establish if carburization has occurred (particularly at low carburized layer thickness), it has been used as a sensitive indicator of microstructural changes. Extensive carburization will likely result in an increase in hardness. Figure 5.11(a), 5.12(a), and 5.14(a) show the minimum, maximum, and average Vickers hardness values made on 310, 316, and 230 samples, respectively. Figure 5.11(b), 5.12(b), and 5.14(b) show the average Vickers hardness values made on sets of rows on 310, 316, and 230 samples, respectively to evaluate if the diffusion bond interface acts as a conduit for carburization. Hardness measurements were made near the bond interface on the edge to SC-CO<sub>2</sub> and away from the edge exposed to SC-CO<sub>2</sub>, on samples exposed to SC-CO<sub>2</sub> for 1000 hours, as-received DB samples, and as-received, non-DB, untested samples to understand if diffusion bond process facilitates carburization.

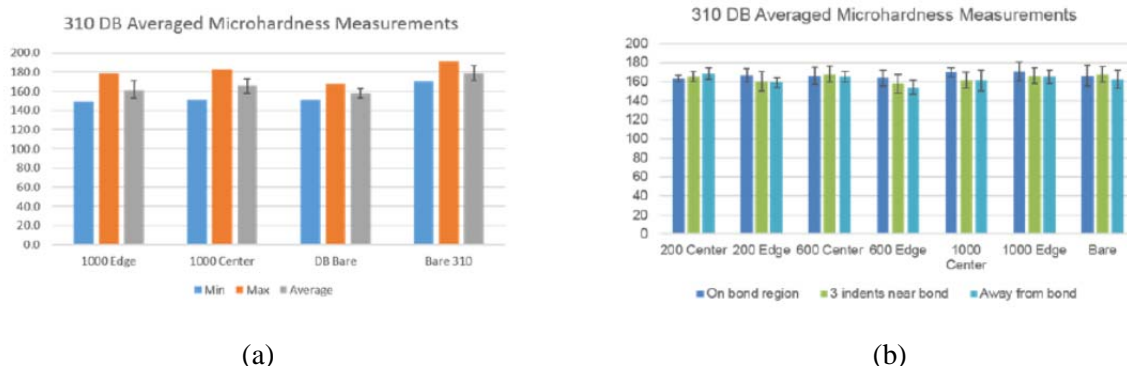


Figure 5.11: Averaged microhardness measurements for diffusion bonded 310SS, (a) minimum, maximum, and averaged microhardness measurements, (b) averaged microhardness measurements along rows.

As shown in Figure 5.11, the overall hardness of the material decreases after the diffusion bonding process. There is a slight increase in hardness after exposure to SC-CO<sub>2</sub>, but there is no overall trend indicating that the bond acts as a significant conduit for carburization. No statistically significant conclusions can be made based on hardness measurements for 310SS in regards to effect of carburization on diffusion bond, indicating that no significant carburization occurred.

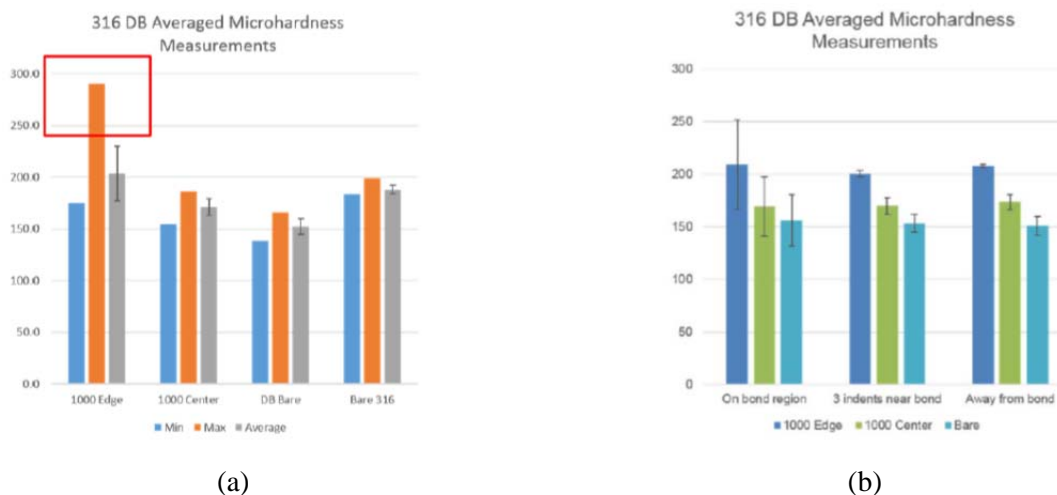


Figure 5.12: Averaged microhardness measurements for diffusion bonded 316SS, (a) untested DB near edge, (b) untested DB near center of sample.



As depicted in Figure 5.12, the overall hardness of the 316SS decreases after the diffusion bonding process. 316SS DB samples exhibited the most significant evidence for carburization. There is a slight increase in hardness on the surface exposed to SC-CO<sub>2</sub>, but there is no overall trend indicating that the bond acts as a significant conduit for carburization; if carburization were to occur it would occur within the first 10  $\mu$ m. No statistically significant conclusions could be made from hardness measurements for 316SS, in regards to carburization effecting the bond after 1000 hours of SC-CO<sub>2</sub> exposure.

As depicted in Figure 5.14, the overall hardness of the Hhaynes decreases after the diffusion bonding process. Haynes 230 DB samples exhibited the most variability in the microhardness measurements. This is the result of the W<sub>6</sub>C solid solution carbide strengtheners present in the matrix. A large microhardness value is attributable to indents placed on carbide rich regions. There is no statistically significant hardness measurements made on Haynes 230, indicating that no significant carburization occurred after 1000 hours of SC-CO<sub>2</sub> exposure.

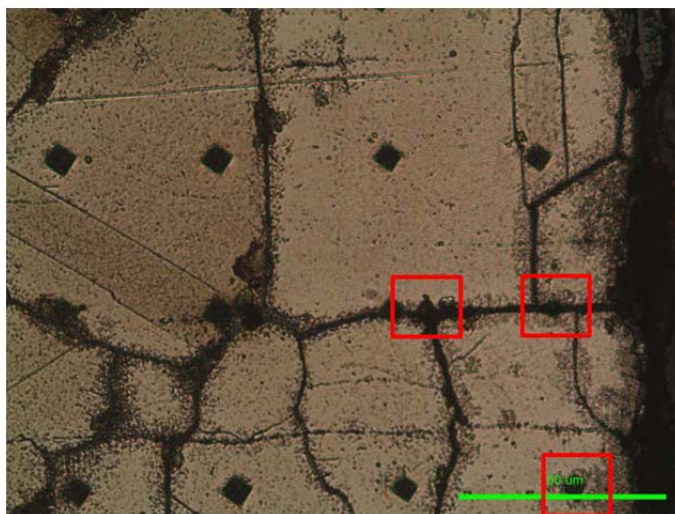


Figure 5.13: Optical image of Vickers hardness testing indents on 316 DB sample near edge exposed to 650°C RG SC-CO<sub>2</sub> for 1000 hours.

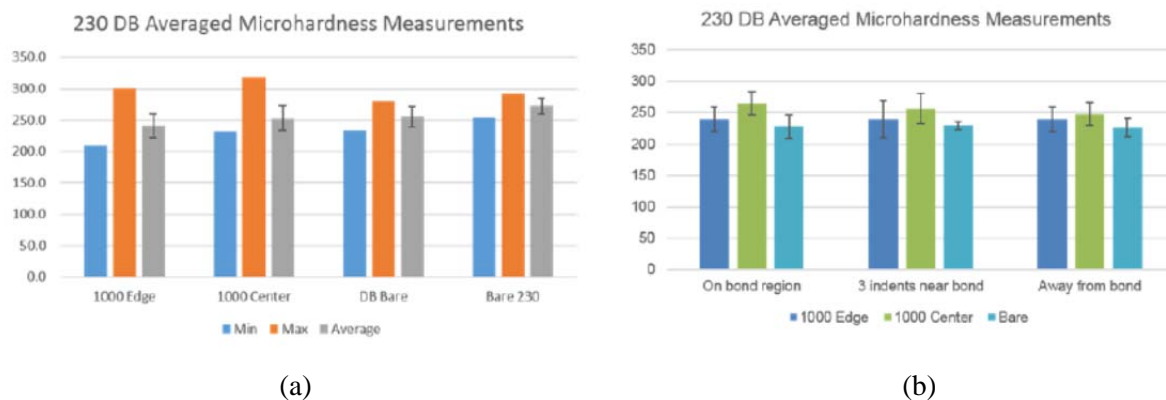


Figure 5.14: Averaged microhardness measurements for diffusion bonded Haynes 230, (a) untested DB near edge and (b) untested DB near center of sample.

**5.5. Summary:** Solid state diffusion bonding has been identified as a technique for manufacturing printed circuit heat exchangers that have considerable potential applications for use in the SC-CO<sub>2</sub> Brayton cycle. Diffusion bonding was performed on three alloys 310SS, 316SS, and Haynes 230 to create similarly bonded joints (i.e. 310 bonded to 310, 316 bonded to 316, and 230 bonded to 230)

by a commercial company. The changes in microstructure due to high temperature used for diffusion bonding, and initial bond quality and its subsequent degradation in the SC-CO<sub>2</sub> environment was evaluated using microhardness testing, and SEM/EDS. The diffusion bonding process itself was found to promote grain growth in 310 and 316, while generating a large amount of secondary carbides in Haynes 230. Diffusion bonds in 310SS and Haynes 230 exhibited good resistance to corrosion attack in SC-CO<sub>2</sub> environment and did not show evidence of bond facilitated degradation of the material whereas 316SS was observed to form intergranular carbides closest to the edge of the sample exposed to SC-CO<sub>2</sub>, indicating that the diffusion bond interface may facilitate material degradation.

## Bibliography Consulted

- [1] G.C. Wood. Some observations on the break-through of protective oxide films on iron- chromium alloys. *Corrosion Science*, 2(4):255 – 268, 1962. ISSN 0010-938X. doi: [http://dx.doi.org/10.1016/0010-938X\(62\)90030-6](http://dx.doi.org/10.1016/0010-938X(62)90030-6). URL <http://www.sciencedirect.com/science/article/pii/0010938X62900306>.
- [2] G.C. Wood and D.P. Whittle. The mechanism of breakthrough of protective chromium oxide scales on Fe-Cr alloys. *Corrosion Science*, 7(11):763 – 782, 1967. ISSN 0010- 938X. doi: [http://dx.doi.org/10.1016/S0010-938X\(67\)80003-9](http://dx.doi.org/10.1016/S0010-938X(67)80003-9). URL <http://www.sciencedirect.com/science/article/pii/S0010938X67800039>.
- [3] HJ Yearian, WD Derbyshire, and JF Radavich. The formation of oxide films on chromium and 18 cr-8 ni steels. *Corrosion*, 13(9):65–75, 1957.
- [4] G Cao, V Firouzdar, K Sridharan, M Anderson, and TR Allen. Corrosion of austenitic alloys in high temperature supercritical carbon dioxide. *Corrosion Science*, 60:246–255, 2012.
- [5] F Rouillard, G Moine, M Tabarant, and JC Ruiz. Corrosion of 9cr steel in CO<sub>2</sub> at intermediate temperature ii: Mechanism of carburization. *Oxidation of Metals*, 77(1-2): 57–70, 2012.
- [6] ASTM Standard. G99-05, 2010, ". *Standard Test Method for Wear Testing with a Pin- on-Disk Apparatus*," ASTM International, West Conshohocken, PA, 2010.
- [7] ASTM G30-97. Standard practice for making and using u-bend stress-corrosion test specimens. 2000.
- [8] Robert Hill. Overview of us fast reactor technology program. 2013.
- [9] Sam Sham. Advanced reactor concepts program materials development - accomplishments and plans. 2013. URL <http://www.energy.gov/sites/prod/files/2013/09/f2/ARC-Matls-CrossCut-2013.pdf>.
- [10] A Moiseyev, Y Tang, S Majumdar, C Grandy, and K Natesan. Impact from the adoption of advanced materials on a sodium fast reactor design. *Nuclear Technology*, 175(2):468–479, 2011.
- [11] Philip J Maziasz, Bruce A Pint, John P Shingledecker, Karren L More, Neal D Evans, and Edgar Lara-Curzio. Austenitic stainless steels and alloys with improved high- temperature performance for advanced microturbine recuperators. In *ASME Turbo Expo 2004: Power for Land, Sea, and Air*, pages 131–143. American Society of Mechanical Engineers, 2004.
- [12] RW Swindeman. Stainless steels with improved strength for service at 760 c and above. Technical report, Oak Ridge National Lab., TN (United States), 1998.
- [13] CD Lundin and CYP Qiao. Comparative evaluations of the weldability of modified 800h and other advanced austenitic stainless steels. Technical report, Oak Ridge National Lab., TN (United States), 1993.
- [14] Todd R Allen, Kumar Sridharan, Yun Chen, Lizhen Tan, Xiaowei Ren, and Alan Kruienza. Research and development on materials corrosion issues in supercritical water environment. *ICPWS XV, Berlin, Germany*, pages 1–12, 2008.
- [15] Stephen Osgerby and A Tony Fry. Steam oxidation resistance of selected austenitic steels. In

*Materials Science Forum*, volume 461, pages 1023–1030. Trans Tech Publ, 2004.

- [16] K Natesan, A Purohit, and DL Rink. Fireside corrosion of alloys for combustion powerplants. *POWERPLANT CHEMISTRY*, 4:549–556, 2002.
- [17] Joseph R Davis et al. *ASM specialty handbook: heat-resistant materials*. Asm International, 1997.
- [18] TC Totemeier, H Lian, DE Clark, and JA Simpson. Microstructure and strength characteristics of alloy 617 welds. *INL/EXT-05-00488*, 2005.
- [19] F Rouillard, G Moine, L Martinelli, and JC Ruiz. Corrosion of 9cr steel in co<sub>2</sub> at intermediate temperature i: Mechanism of void-induced duplex oxide formation. *Oxidation of metals*, 77(1-2):27–55, 2012.
- [20] F Rouillard and L Martinelli. Corrosion of 9cr steel in co<sub>2</sub> at intermediate temperatureiii: Modelling and simulation of void-induced duplex oxide growth. *Oxidation of metals*, 77(1-2):71–83, 2012.
- [21] F Rouillard and T Furukawa. Corrosion of 9-12cr ferritic–martensitic steels in high- temperature co<sub>2</sub>. *Corrosion Science*, 105:120–132, 2016.
- [22] Ling-Feng He, Paul Roman, Bin Leng, Kumar Sridharan, Mark Anderson, and Todd R Allen. Corrosion behavior of an alumina forming austenitic steel exposed to supercritical carbon dioxide. *Corrosion Science*, 82:67–76, 2014.
- [23] Ho Jung Lee, Hyunmyung Kim, Sung Hwan Kim, and Changheui Jang. Corrosion and carburization behavior of chromia-forming heat resistant alloys in a high-temperature supercritical-carbon dioxide environment. *Corrosion Science*, 99:227–239, 2015.
- [24] Ho Jung Lee, Gokul Obulan Subramanian, Sung Hwan Kim, and Changheui Jang. Effect of pressure on the corrosion and carburization behavior of chromia-forming heat-resistant alloys in high-temperature carbon dioxide environments. *Corrosion Science*, 2016.
- [25] SB Dunkerton. Diffusion bonding overview. In *Diffusion Bonding 2*, pages 1–12. Springer, 1991.
- [26] Nobuyoshi Tsuzuki, Yasuyoshi Kato, and Takao Ishiduka. High performance printed circuit heat exchanger. *Applied Thermal Engineering*, 27(10):1702 – 1707, 2007. ISSN 1359-4311. doi: <http://dx.doi.org/10.1016/j.applthermaleng.2006.07.007>. URL <http://www.sciencedirect.com/science/article/pii/S1359431106002493>. Heat transfer and sustainable energy technologies.
- [27] Konstantin Nikitin, Yasuyoshi Kato, and Lam Ngo. Printed circuit heat exchanger thermalhydraulic performance in supercritical {CO<sub>2</sub>} experimental loop. *International Journal of Refrigeration*, 29(5):807 – 814, 2006. ISSN 0140-7007. doi: <http://dx.doi.org/10.1016/j.ijrefrig.2005.11.005>. URL <http://www.sciencedirect.com/science/article/pii/S0140700705002483>.
- [28] N.F. Kazakov. 1 - an outline of diffusion bonding in vacuum. In N.F. Kazakov, editor, *Diffusion Bonding of Materials*, pages 10 – 16. Pergamon, 1985. ISBN 978-0-08-032550-7. doi: <http://dx.doi.org/10.1016/B978-0-08-032550-7.50005-9>. URL <http://www.sciencedirect.com/science/article/pii/B9780080325507500059>.
- [29] Denis Clark, Ronald Mizia, and Piyush Sabharwall. Diffusion welding of alloys for molten salt service-status report. Technical report, Idaho National Laboratory (INL), 2012.
- [30] K Bhanumurthy, D Joyson, SB Jawale, A Laik, and GK Dey. Diffusion bonding of nuclear materials. *BARC*, 2:19, 2013.
- [31] Shu-Xin Li, Lei Li, Shu-Rong Yu, R. Akid, and Hong-Bo Xia. Investigation of intergranular corrosion of 316l stainless steel diffusion bonded joint by electrochemical potentiokinetic reactivation. *Corrosion Science*, 53(1):99 – 104, 2011. ISSN 0010-938X. doi: <http://dx.doi.org/10.1016/j.corsci.2010.09.027>. URL <http://www>.

sciencedirect.com/science/article/pii/S0010938X10004580.

[32] Piyush Sabharwall, Denis Clark, Michael Glazoff, Guiqiu Zheng, Kumar Sridharan, and Mark Anderson. Advanced heat exchanger development for molten salts. *Nuclear Engineering and Design*, 280:42–56, 2014.

[33] Bulent Kurt and Adnan alik. Interface structure of diffusion bonded duplex stainless steel and medium carbon steel couple. *Materials Characterization*, 60(9):1035 – 1040, 2009. ISSN 1044-5803. doi: <http://dx.doi.org/10.1016/j.matchar.2009.04.011>. URL <http://www.sciencedirect.com/science/article/pii/S104458030900151X>.

[34] M.F Islam and N Ridley. Isostatic diffusion bonding of a microduplex stainless steel. *Scripta Materialia*, 38(8):1187 – 1193, 1998. ISSN 1359-6462. doi: [http://dx.doi.org/10.1016/S1359-6462\(98\)00037-2](http://dx.doi.org/10.1016/S1359-6462(98)00037-2). URL <http://www.sciencedirect.com/science/article/pii/S1359646298000372>.

[35] P He. Diffusion bonding of titanium alloy to stainless steel wire mesh. *Materials science and technology*, 17(9):1158–1162, 2001.

[36] Amir Abbas Shirzadi Ghoshouni. *Diffusion Bonding Aluminium Alloys and Composites: New Approaches and Modelling*. PhD thesis, University of Cambridge, 1998.

[37] Shu Xin Li, Fu Zhen Xuan, Shan Tung Tu, and Shu Rong Yu. Interfacial failure mechanism of 316L diffusion bonded joints. In *ICF12, Ottawa 2009*, 2013.

[38] Widodo Widjaja Basuki, Oliver Kraft, and Jarir Aktaa. Optimization of solid-state diffusion bonding of hastelloy c-22 for micro heat exchanger applications by coupling of experiments and simulations. *Materials Science and Engineering: A*, 538:340–348, 2012.

[39] Injin Sah, Donghoon Kim, Ho Jung Lee, and Changheui Jang. The recovery of tensile ductility in diffusion-bonded ni-base alloys by post-bond heat treatments. *Materials & Design*, 47:581–589, 2013.

[40] Xiuqing Li, David Kininmont, Renaud Le Pierres, and Stephen John Dewson. Alloy 617 for the high temperature diffusion-bonded compact heat exchangers. *Proceedings of ICAPP08, Anaheim, CA, Paper*, (8008), 2008.

[41] U Kamachi Mudali, BM Ananda Rao, K Shanmugam, R Natarajan, and Baldev Raj. Corrosion and microstructural aspects of dissimilar joints of titanium and type 304L stainless steel. *Journal of Nuclear Materials*, 321(1):40–48, 2003.

[42] S.M. Shushan, E.A. Charles, and J. Congleton. The environment assisted crack-ing of diffusion bonded stainless to carbon steel joints in an aqueous chloride so- lution. *Corrosion Science*, 38(5):673 – 686, 1996. ISSN 0010-938X. doi: [http://dx.doi.org/10.1016/0010-938X\(96\)00158-8](http://dx.doi.org/10.1016/0010-938X(96)00158-8). URL <http://www.sciencedirect.com/science/article/pii/0010938X96001588>.

[43] JW Prybylowski, S Floreen, WJ Sherwood, and RW Wittmeier. The stress corrosion performance of diffusion-bonded nickel-base alloys. *Corrosion*, 47(3):210–215, 1991.

[44] Shaily M. Bhola, Sukumar Kundu, Rahul Bhola, Brajendra Mishra, and Subrata Chatterjee. Electrochemical study of diffusion bonded joints between micro-duplex stainless steel and Ti6Al4V alloy. *Journal of Materials Science I & Technology*, 30(2):163 – 171, 2014. ISSN 1005-0302. doi: <http://dx.doi.org/10.1016/j.jmst.2013.09.017>. URL <http://www.sciencedirect.com/science/article/pii/S1005030213002168>.

[45] Monica Kapoor, Omer Dogan, Kyle Rozman, Jeffrey Hawk, Aaron Wilson, Thomas L'Estrange, and Vinod Narayanan. Diffusion bonding of ni-based superalloys for microchannel heat exchanger for application in supercritical CO<sub>2</sub> cycles. *The 5th International Symposium - Supercritical CO<sub>2</sub> Power Cycles, Paper*, (075), 2016.

[46] JP Campbell, RO Ritchie, and KT Venkateswara Rao. The effect of microstructure on fracture toughness and fatigue crack growth behavior in  $\gamma$ -titanium aluminide based intermetallics.

*Metallurgical and Materials Transactions A*, 30(3):563–577, 1999

## CHAPTER 6: WEAR AND SPALLATION OF OXIDE LAYERS ON STRUCTURAL ALLOYS FORMED IN HIGH TEMPERATURE SC-CO<sub>2</sub> ENVIRONMENT

**6.1. Introduction:** The mechanical fragility of the protective oxide layer that forms during corrosion in SC-CO<sub>2</sub> is of considerable significance in the Brayton cycle application given the high flow rates of CO<sub>2</sub> in this application. The removal of protective oxide layer can lead to enhanced corrosion, and more importantly the detachment of hard oxide particulates can lead to three-body wear in turbomachinery and other components. This facet of the project has therefore focused on evaluating wear performance of various oxide layers formed on various structural materials in SC-CO<sub>2</sub> Brayton cycle, using a pin-on-disk wear testing apparatus.

**6.2. Experimental Technique:** In an attempt to simulate erosion-corrosion effects on materials exposed to SC-CO<sub>2</sub>, pin-on-disk wear tests were conducted in accordance with ASTM Standard G99-05 “Standard Test Method for Wear Testing with a Pin-on-Disk Apparatus. In this test, the disc (i.e., the test sample) is affixed to a horizontal platform which rotates in the horizontal plane. A pin, with a spherical tip, is impressed against the disk with a specified load. The test is conducted for a specific time with a specific rotational speed (i.e., revolutions per-minute, rpm) to describe a circular wear track on the sample surface. The wear track was then evaluated for wear magnitude and mechanisms using an SEM and the dimensions of the wear track were measured using an optical profilometer. The SEM and profilometry analysis were coupled with image analysis codes to evaluate further refined dimensional measurements and evaluate spallation. A well-defined wear track with sharp boundaries is indicative of an oxide that would be resistant to spallation and wide wear track would be indicative of an oxide layer with poor wear resistance. The two effects are somewhat exclusive, in that an oxide layer exhibiting a large wear track may exhibit relatively low spallation if it possesses a cohesive microstructure. The pin material is a variable, however in this project, 3mm alumina balls (aluminum oxide Al<sub>2</sub>O<sub>3</sub>: synthetic ruby ball from the company Small Parts, Inc., Florida) were used as a pin material based on the high hardness and chemical inertness of this material. Figure 6.1 shows the pin-on-disk wear tester used in this study.



*Figure 6.1: Photograph of the pin-on-disk testing apparatus used in this project.*

As an example, the SEM image of a wear track on oxide layer developed on alloy Haynes 282 after exposure to RG SC-CO<sub>2</sub> at 750°C for 600 hours, along with our image processing approach is shown in Figure 6.2.



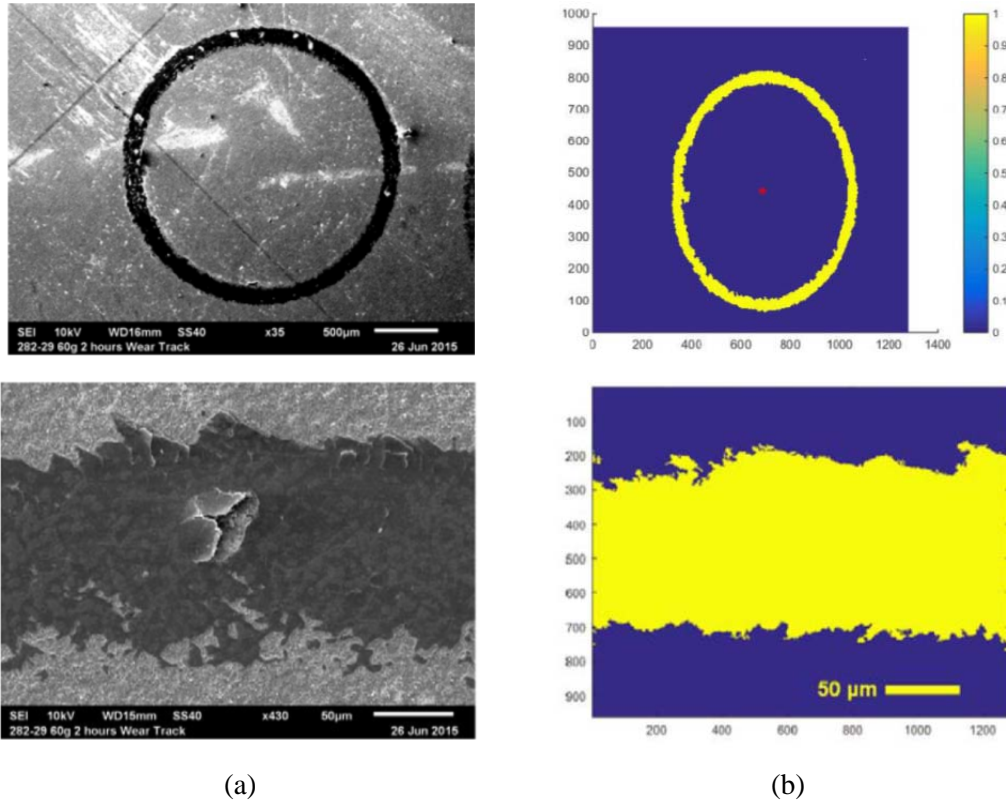


Figure 6.2. (a) Low and high magnification SEM micrographs and (b) accompanying processed images of wear track on Haynes 282 after exposure to RG SC-CO<sub>2</sub> at 750°C for 600 hours subjected to two hours of pin on disc wear testing at 60g load.

Additional measurements and analysis using profilometry and SEM imaging was used to calculate the wear track depth and uniformity. The wear track depth was measured using profilometry scans. Figure 6.3a shows a typical profilometry scan and of the wear track on the oxide layer formed on Haynes 282, while Figure 6.3b depicts the depth profile of the wear track as measured by the profilometer. Figure 6.3c shows a curve-fit to the depth profile assuming an elliptical Hertzian contact by the ruby ball on the oxide layer. Multiple profilometry scans were taken in order to provide statistical evidence of average depth profiles. Image processing was also used to calculate the statistical variability of the width of the wear track which may be regarded as a measure of spallation. The variability of the wear track was determined by calculating the area of the actual wear track and comparing it to the area of the idealized wear track. A value of unity indicates that the actual wear track mimics the behavior of an idealized wear track; deviations from this behavior (smaller or larger area) indicate variability of the wear track due to spallation or fragmentation of the oxide layer. Calculations are presented as a ratio of the actual wear track area to the idealized wear track is simply given by,

$$\text{Variability} = \frac{\text{Area of Oxide Layer}}{\text{Area of Idealized WearTrack}}$$

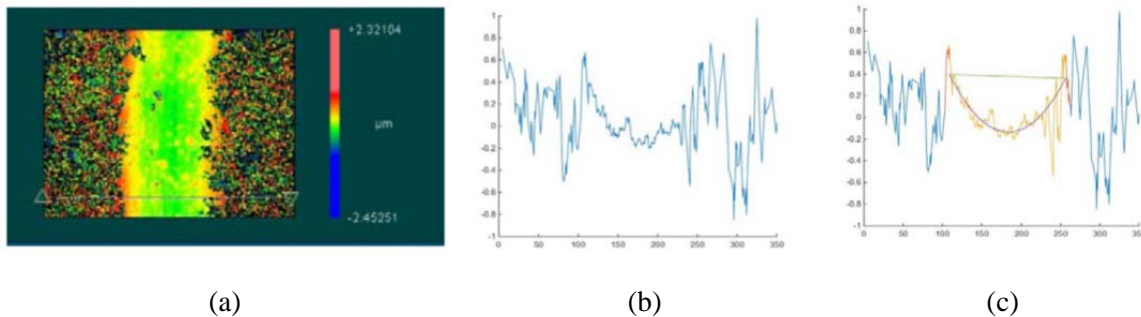


Figure 6.3: Profilometry scan of wear track on Haynes 282 after exposure to RG SC-CO<sub>2</sub> at 750°C for 600 hours subjected to two hours of pin on disc wear testing at 60g load, (b) corresponding extracted depth profile, and (c) curve fit of the depth profile.

The image processing method is given below and makes extensive use of the Image Processing Toolbox included in MATLAB v2015a. Figures 6.4 and 6.5 show each step of the image processing methodology used in the wear track analysis. Figure 6.4 depicts the original image pixel intensity filter using the MATLAB utility 'imagesc.' The utility is used to highlight contrast using the full color range instead of grey scale.

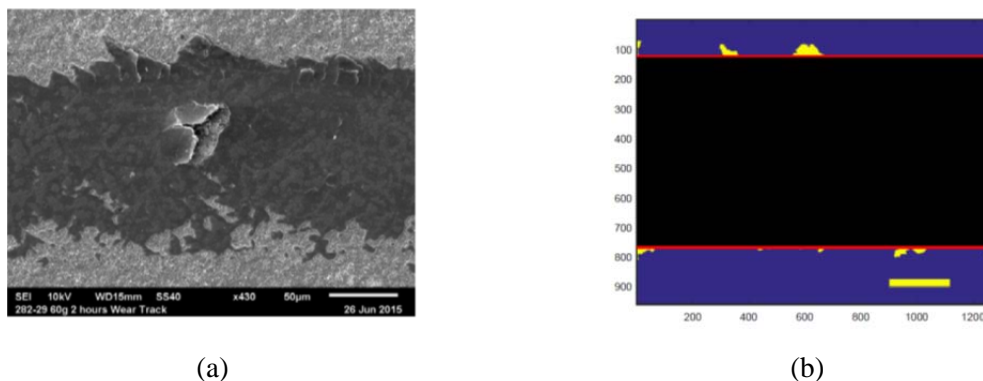
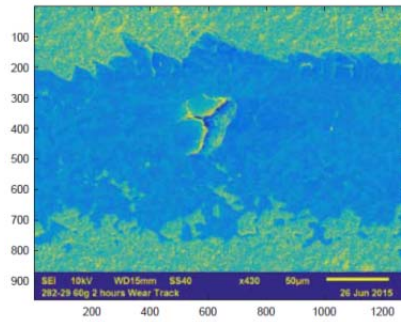


Figure 6.4: (a) High magnification SEM image and (b) processed image of a wear track formed on Haynes 282 after exposure to RG SC-CO<sub>2</sub> at 750°C for 600 hours after being subjected to two hours of pin on disc wear testing at 60g load.

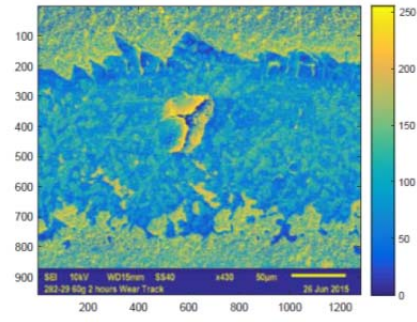
Figure 6.5b depicts the enhancement of contrast using MATLAB's 'adapthisteq' utility. The 'adapthisteq' utility uses "contrast-limited adaptive histogram equalization." The purpose of the utility is to enhance the contrast of the image to more readily isolate the wear track from the background.

Figure 6.5c depicts the use of MATLAB's median filter 'medfilt2' utility used to smooth out and remove noise from the image to further isolate the wear track from the background image.

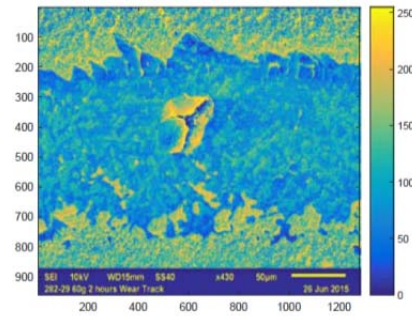
Figure 6.5.d depicts where the modified grayscale image is turned into a binary image using MATLAB's 'im2bw' utility that makes use of a global threshold calculation. By this point the wear track edge should be sufficiently defined such that further operations on the grayscale image are unnecessary and the edges retained in the binary image are sufficient for further processing.



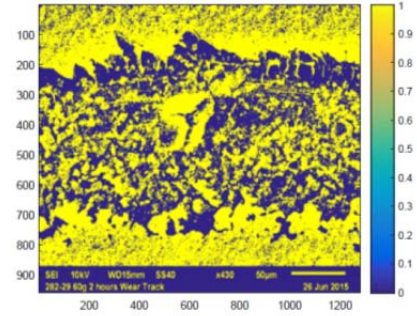
(a)



(b)



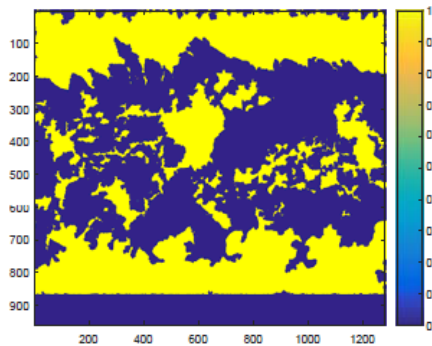
(c)



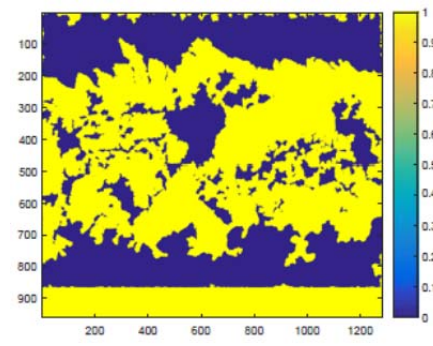
(d)

*Figure 6.5. Image processing methodology used to isolate wear tracks for thickness measurements in MATLAB.*

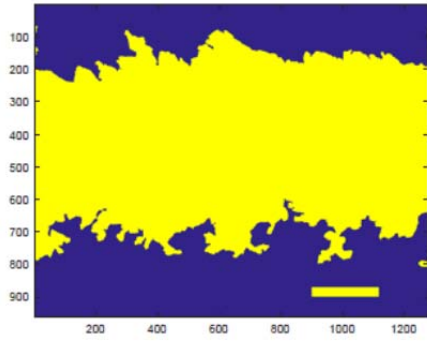
Figure 6.6 depicts the procedure for image processing of the wear track as follows; Figure 6.6a shows the use of morphological operators to remove unwanted artifacts from the binary image. Figure 6.6b shows the inversion of the image (i.e. 1's are turned to 0's and vice versa). Figure 6.6c depicts the final clean-up of the image using the MATLAB utility 'imfill, holes' to remove any regions in the image that have pixels that do not touch the background. A scale bar is also placed. Figure 6.6d depicts the superposition of the ideal wear track measured from profilometry measurements and the associated deviation from the idealized behavior.



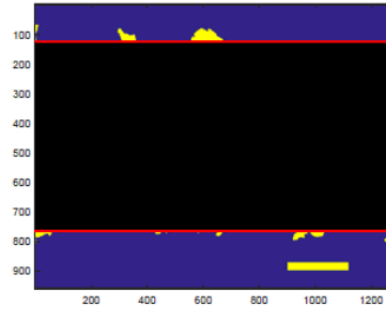
(a)



(b)



(c)

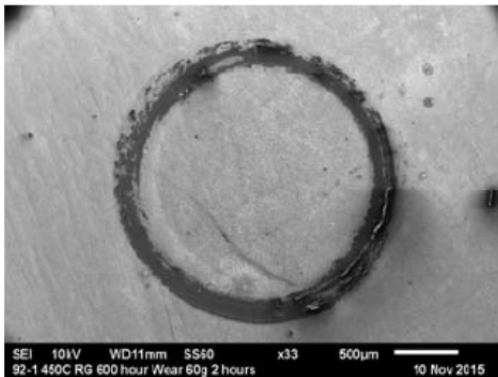


(d)

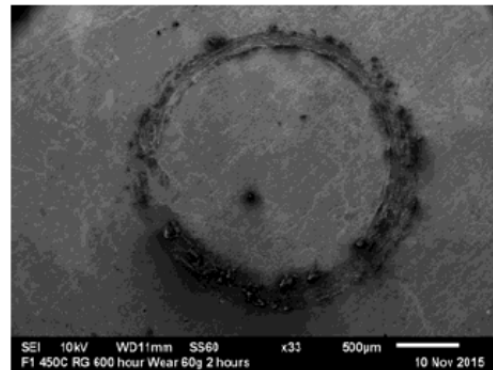
Figure 6.6: Image processing methodology used to isolate wear track width measurements in MATLAB: (a) morphological operator applied, (b) inverted image, (c) image is cleaned up and scale bar is placed, and (d) idealized wear track and deviation is superimposed on the processed image

**6.3. Results and Analysis for ferritic steels:** Wear testing was performed on two ferritic alloys, T92 steel and a model Fe12%Cr alloy exposed to 450°C RG SC-CO<sub>2</sub> for 600, 800, and 1000 hours. Samples were subjected to a 60g load for 2 hours at a constant 150 rpm. The wear phenomena observed in the wear track included: (a) compacting of oxide layer, (b) pushing/ploughing of oxide layer, (c) fragmentation of the oxide layer, and (d) formation of wear related debris. The outer magnetite layer formed on ferritic steels is particularly susceptible to these effects.

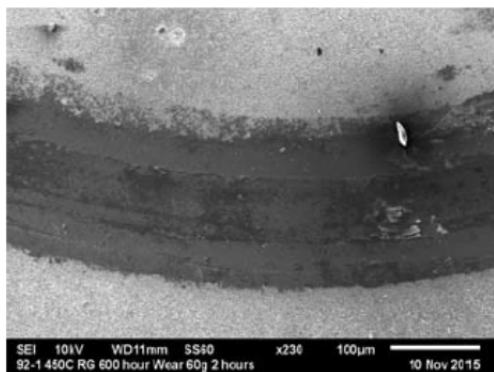
Figure 6.7 show low magnification SEMs micrographs of wear tracks on T92 steel and Fe12%Cr alloy exposed to 450°C RG SC-CO<sub>2</sub> for 600 hours. T92 exhibits a more well-defined uniform wear track and less debris generation than Fe-12%Cr alloy. The Fe12%Cr wear track is much less uniform, appears to fragment more readily off of the substrate, and generates much more debris than compared to the T92 wear track. Oxide cracking is apparent on sections of the wear track for T92 and Fe12Cr. The region of non-uniformity on the Fe12%Cr is postulated to be the result of nodular oxide growth observed on many Fe-Cr binary alloys. The T92 600 hour exposed sample appears to be relatively coherent and comparatively devoid of voids and cracks when compared to the 800 hour test sample.



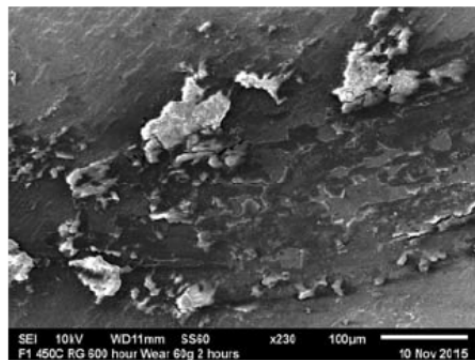
(a)



(b)



(c)



(d)

Figure 6.7: SEM plan view micrographs of wear tracks formed on T92 steel and Fe-12%Cr alloy after exposure to RG SC-CO<sub>2</sub> at 450°C for 600 hours subjected to two hours of pin on disc wear testing at 60 grams load: (a) and (c) T92 steel and (b) and (d) Fe-12%Cr alloy.

Figure 6.8 shows the results of the wear track uniformity for the ferritic alloys. Almost all test conditions result area ratios less than unity the exception being T92 exposed to S-CO<sub>2</sub> for 800 hours. The previous high magnification images of the plan view wear tracks illustrate this in that a fair amount of oxide tearing and cracking within the inner portion of the wear track. The T92 800 hour sample exhibits the most uniform wear of the ferritic alloy conditions tested. The 1000 hour Fe12Cr sample exhibits the lowest ratio of the alloys; this is due to the nodular oxide growth present where chromia extrudes from the surface of the sample and more readily protects the sample from wear as compared to magnetite. The 800 hour Fe12Cr sample exhibits intermediate behavior in that the wear depth is substantially reduced in comparison to the 600 hour sample but the wear track width and material removed are similar in magnitude to the 600 hour sample.

Figure 6.9 provides an overall summary of wear testing of ferritic steels as depicted in a radar plot. The radar plot depicts the normalized results of the wear track thickness, wear depth, material removed, and wear track uniformity. Larger values (and a greater overall area) indicate poor performance. Highlighted in Figure 6.9, Fe12%Cr at 600 hours performs worst in terms of the wear track width, wear depth, and the overall material removed and Fe12Cr at 1000 hours performs worst in terms of the wear track uniformity metric due to the nodular growth of chromia which effectively protects the alloy substrate better. In comparison, the T92 600 hour sample performs best of the T92 samples, followed by the 1000 hour sample and the 800 hour sample performs worst. The 600 hour and 1000 hour sample perform similarly; oxide cracking was observed in the 800 hour sample and is believed to be the primary reason for the poor wear resistance of the oxide.



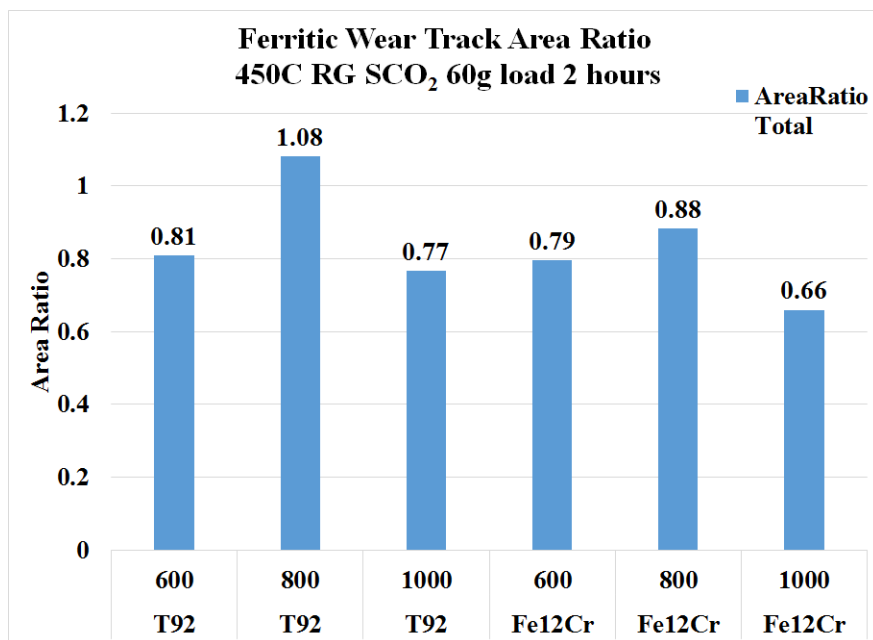


Figure 6.8: Calculated wear track uniformity area ratio for T92 steel and Fe-12%Cr alloy tested in RG SC-CO<sub>2</sub> environment at 450°C.

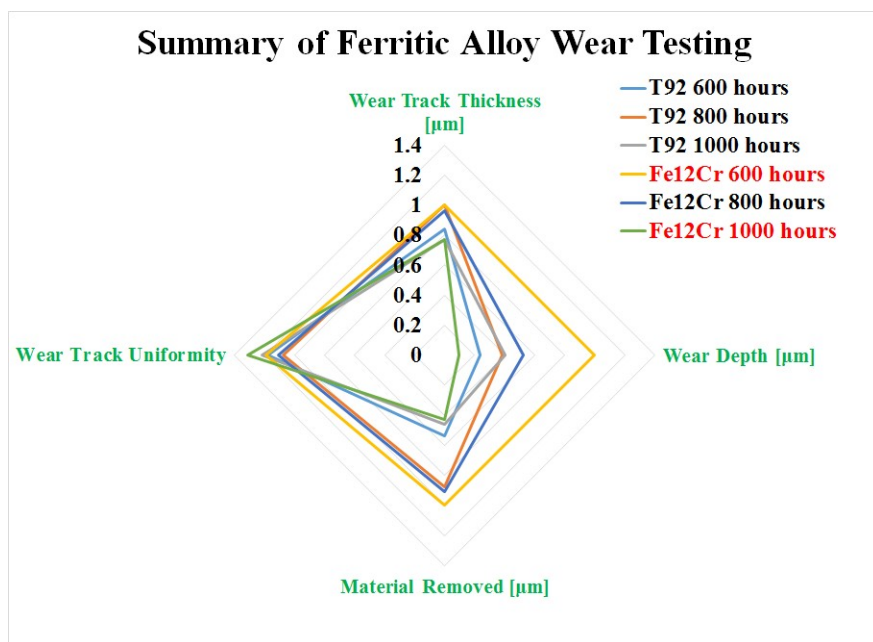
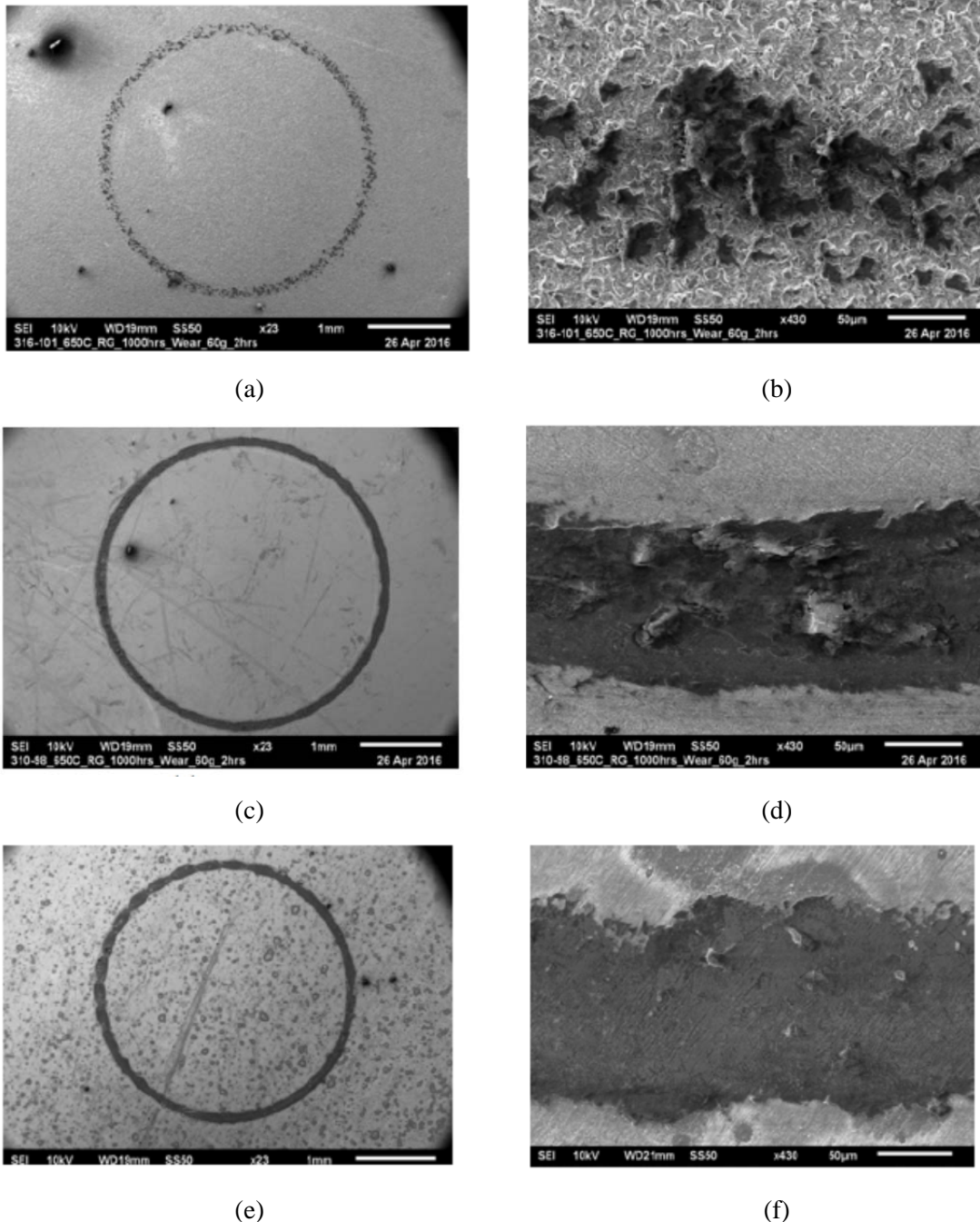


Figure 6.9: Overall assessment of oxide wear behavior for T92 ferritic steel and Fe-12%Cr alloy.

**6.3. Results and Analysis for austenitic alloys:** Three austenitic alloys, 316 and 310 stainless steel, and alloy 709 exposed to 650°C RG SC-CO<sub>2</sub> for 400 and 1000 hours were tested in the pin-on-disk wear testing apparatus. Samples were subjected to a 60g load for 2 hours at 150 rpm. Wear track analysis for various exposures was performed but only results from 1000 hours exposure is presented in Figure 6.10. 316SS exhibited the highest wear of the three alloys tested. While 310SS exhibited the smallest wear track it also suffered from oxide cracking during testing but alloy 709 exhibited a slightly larger and less uniform wear track.



From the discussion of oxide layer analysis for 310SS, 316SS, and alloy 709 presented earlier in the report the composition of the oxide layers on 310SS and alloy 709 were chromia-rich spinels while the composition of the outer regions of oxide layer on 316SS was composed on iron-rich magnetite which is porous and more prone to wear and erosion. Overwhelmingly, the alloy 709 and 310SS performed very similarly and exhibited very low wear rates whereas the 316SS exhibited much higher wear rates.



*Figure 6.10: Low and high magnification images of wear tracks formed after exposure to SC-CO<sub>2</sub> at 650°C for 1000 hours: (a) and (b) 316 stainless steel, (c) and (d) 310 stainless steel, and (e) and (f) alloy 709.*

Figure 6.11 shows the calculated volume removed from each sample and test condition. 316SS exhibited much greater wear rates on the 400 hour sample in comparison to the 1000 hour sample. The

400 hour sample exhibited large amounts of micro-tears of the oxide layer, ostensibly due to a fragile outer magnetite layer. Chromia nodules were observed on the surface of the 1000 hour sample which provides greater wear resistance than magnetite. The wear rates for 310SS and alloy 709 were very similar for both time intervals. However, the morphology of the wear tracks differed between the two alloys. For example, the 1000 hour-test 709 sample exhibited primarily oxide compression and small amounts of tears. Little oxide related debris was formed. Alloy 310SS exhibited similar behavior but not nearly to the magnitude exhibited on the alloy 709. Figure 6.12 shows the results of the wear track uniformity for the austenitic alloys. Most of the austenitic alloys exhibited uniform wear tracks with the exception of 316SS exposed to S-CO<sub>2</sub> for 1000 hours. As mentioned earlier, this is the result of chromia phase extruding out of the surface of the alloy, and providing wear protection.

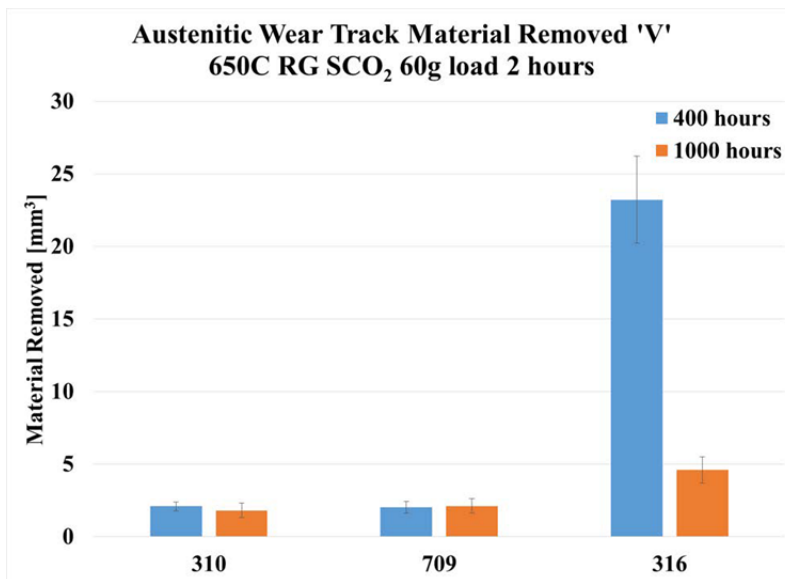


Figure 6.11: Calculated material removed during wear tests for austenitic alloys.

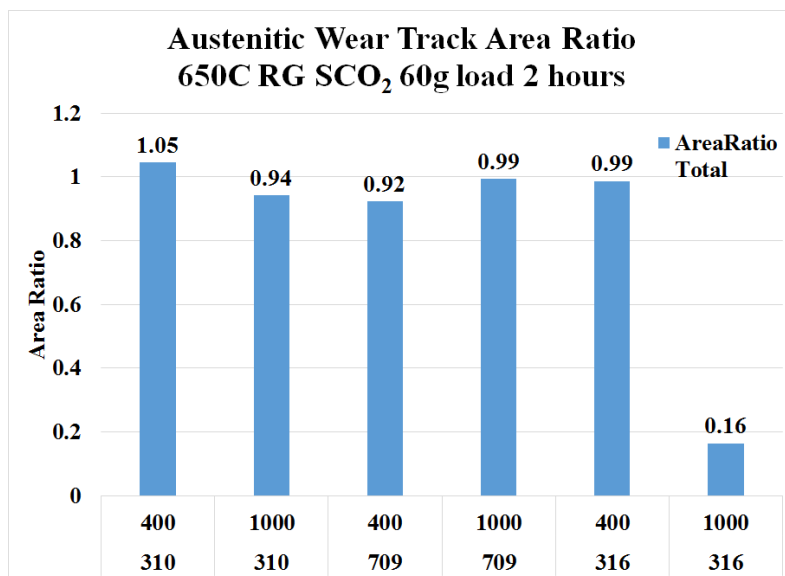


Figure 6.12: Calculated wear track area ratio for assessing uniformity of wear tracks for austenitic alloys, as a measure of spallation.

Figure 6.13 depicts the overall summary of austenitic wear testing as depicted in a radar plot. The radar plot depicts the normalized results of the wear track thickness, wear depth, material removed, and wear track uniformity. Larger values (and a greater overall area) indicate poor performance. Overwhelmingly 316SS performed worst for most metrics. 310SS at 1000 hours performed best, followed closely by 709 at 1000 hours, 709 at 600 hours, and 310SS at 600 hours. The 1000 hour test alloys generally performed better than the 600 hour test samples due to the development of a more cohesive and wear and erosion resistant oxide layer.

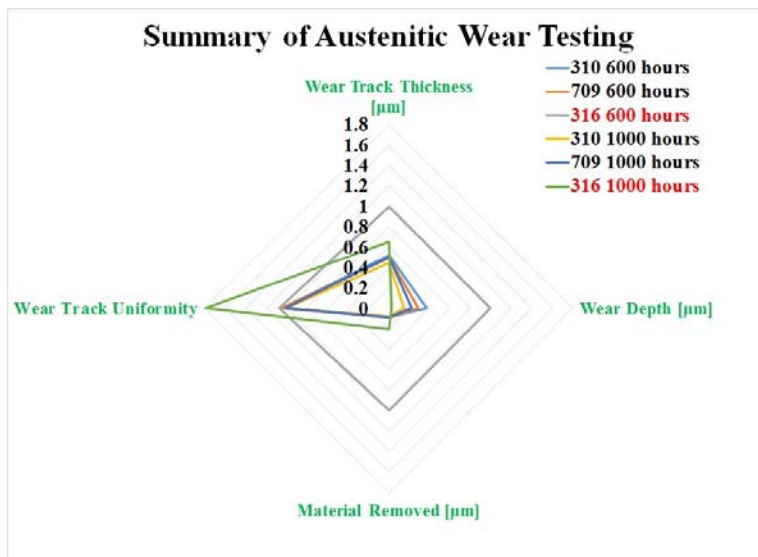
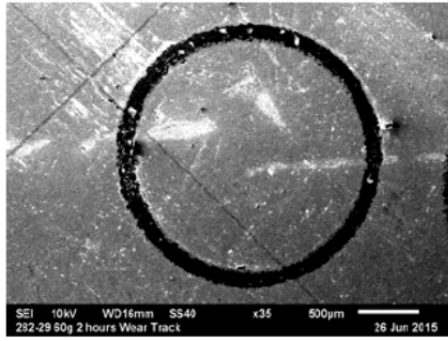


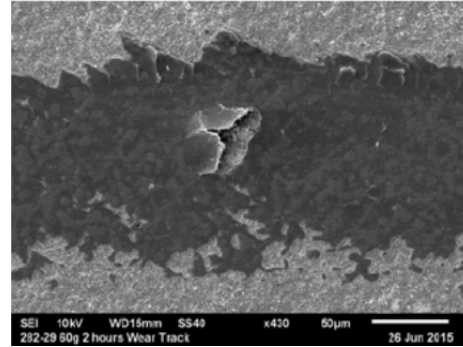
Figure 6.13: Overall assessment of wear and erosion resistance of oxides formed on austenitic alloys.

**6.3. Results and Analysis for Ni-based alloys:** Wear testing was performed on Haynes 282, Inconel 740, and binary alloy Ni-22Cr after exposure to 750°C RG SC-CO<sub>2</sub> for 600 and 1000 hours. Similar to previous alloys, these Ni-based alloy samples were also subjected to a 60g load for 2 hours at a constant 150 rpm. SEM images of the wear tracks formed on these alloys after 600 hours exposure is shown in Figure 6.14. The surface oxide layers for all Ni-base alloys was a very thin ( $< 1\mu\text{m}$ ) chromia rich spinel. As chromia is a very hard material (Mohs hardness 8 to 8.5), the expected wear rate is very low. Examination of the wear tracks shows the oxide layer formed on Haynes 282 to be more wear resistant but also more prone to spallation than Inconel 740, while the oxide layer on Ni-22%Cr shows the most spallation.

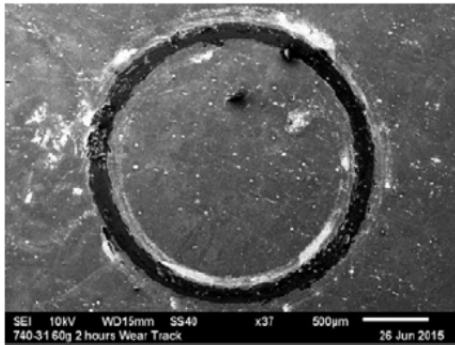
Figure 6.15 shows the calculated wear volume for the alloys (the wear performance of 347 stainless steel is tested under similar conditions is also shown for comparison). For the 600 hour samples, 347SS exhibits the poorest wear resistance in that any oxide removed by the wear testing apparatus is removed by catastrophic ploughing and spallation of the oxide. The binary alloy, Ni-22Cr, exhibits a more well-defined wear track in the low magnification micrograph but spallation and tearing of the oxide is readily apparent at high magnifications. Of the alloys wear tested, Haynes 282 and Inconel 740 exhibit the best wear resistance. Haynes 282 appears to exhibit slightly better wear resistance because the thickness of the wear track is smaller than that of Inconel 740. In terms of the calculated material removed, Haynes 282 and Inconel 740 perform very similarly; Ni-22Cr exhibits a higher wear rate.



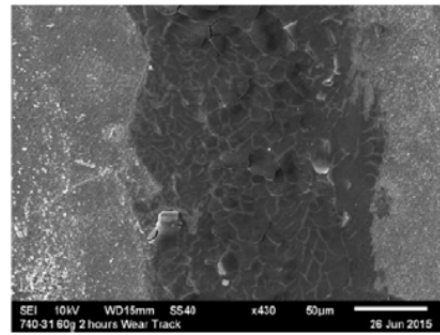
(a)



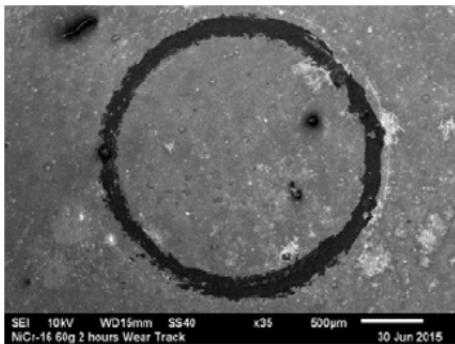
(b)



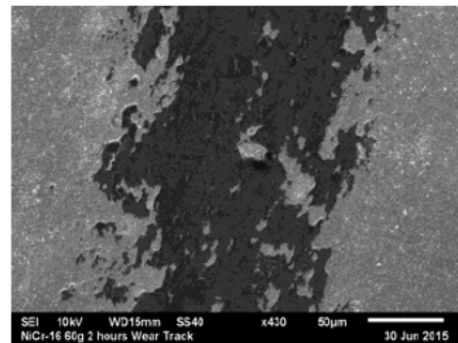
(c)



(d)



(e)



(f)

*Figure 6.14: Low and high magnification images of wear tracks formed after exposure to SC-CO<sub>2</sub> at 750°C for 600 hours: (a) and (b) Haynes282, (c) and (d) Inconel 740, and (e) and (f) binary alloy Ni-22%Cr.*

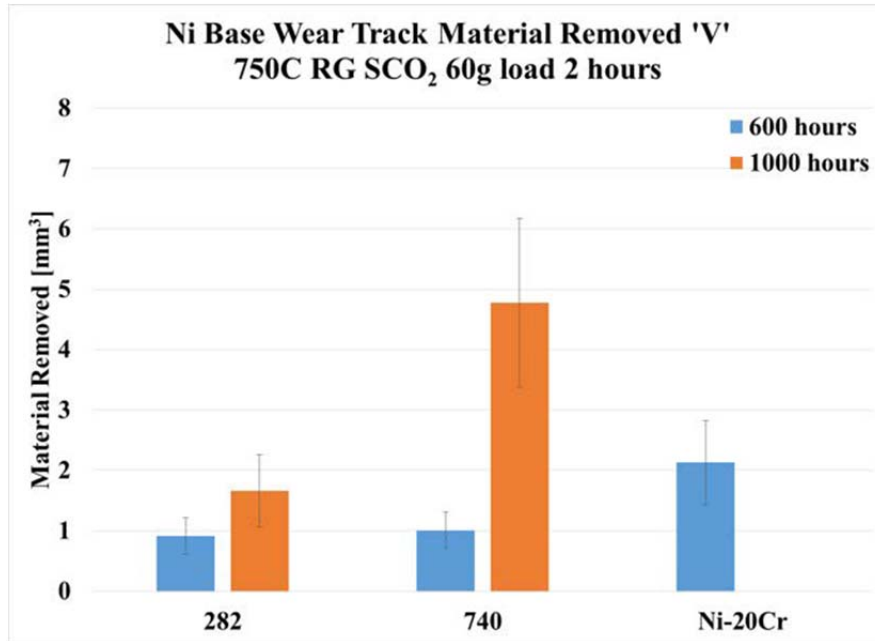


Figure 6.15: Calculated wear volume from nickel-based alloys tested.

Figure 6.16 shows the results of the wear track uniformity for the nickel base alloys. The nickel-base alloys exhibit greater uniformity in comparison to the ferritic alloys. In many of the samples there is evidence of influence of wear outside of the wear track (as opposed to debris from spalled oxide) and this is believed to be the result of a microscopically non-uniform oxide. This is most readily apparent in the wear track of the Ni-22Cr. In general, alloys Haynes 282 and Inconel 740 performed best in terms of the wear track variability measurement.

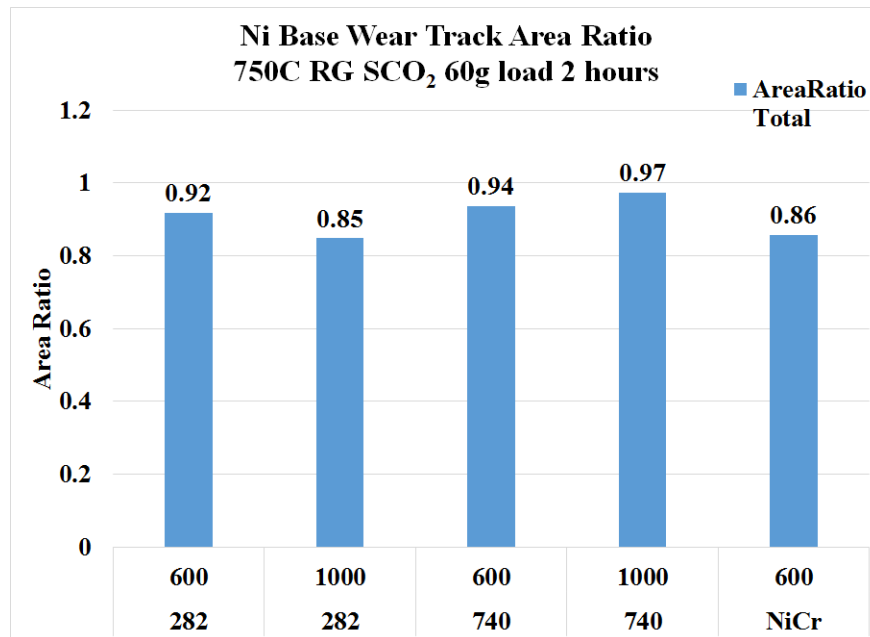


Figure 6.16: Calculated wear track uniformity area ratio for nickel base alloys.

Figure 6.17 depicts the overall summary of wear testing of Ni-based alloys as depicted in a radar plot. The overall best performing alloy was the Haynes 282 exposed for 600 hours. In general terms the Haynes 282 outperformed the Inconel 740 samples. Overall, in comparison to the austenitic stainless steels and ferritic alloys, the nickel base alloys perform much better due to the formation of a uniform, hard, dense chromia layer.

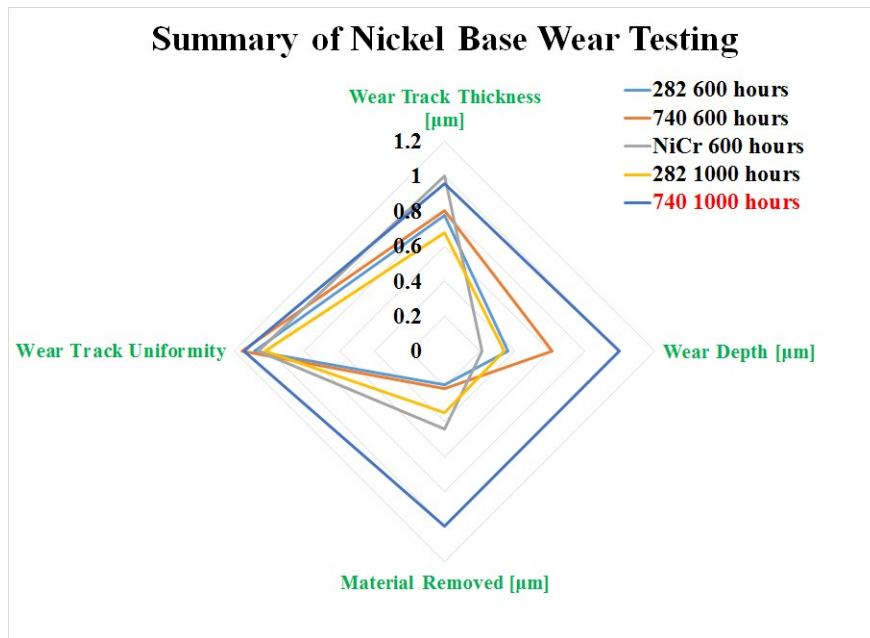


Figure 6.17: Overall assessment of wear performance of oxide layers formed on nickel-based alloys.

#### Bibliography Consulted

Alan V Levy. *Solid particle erosion and erosion-corrosion of materials*. Asm International, 1995.

Inga Bargmann, Anne Neville, Xinming Hu, Staffan Hertzman, and Faisal Reza. Erosion-corrosion in oil and gas stainless steel under de-aerated slurry impingement attack, 2009.

D.M Rishel, F.S Pettit, and N Birks. Structural materials: Properties, microstructure and processing some principal mechanisms in the simultaneous erosion and corrosion attack of metals at high temperatures. *Materials Science and Engineering: A*, 143(1):197 – 211, 1991. ISSN 0921-5093. doi: [http://dx.doi.org/10.1016/0921-5093\(91\)90739-A](http://dx.doi.org/10.1016/0921-5093(91)90739-A). URL <http://www.sciencedirect.com/science/article/pii/092150939190739A>.

IG Wright, V Nagarajan, and J Stringer. Observations on the role of oxide scales in high-temperature erosion-corrosion of alloys. *Oxidation of Metals*, 25(3-4):175–199, 1986.

N Birks, FS Pettit, and DM Rishel. Erosion-corrosion and wear. *Le Journal de Physique IV*, 3(C9):C9–667, 1993.

J.L. Li, H.X. Ma, S.D. Zhu, C.T. Qu, and Z.F. Yin. Erosion resistance of {CO<sub>2</sub>} corrosion scales formed on {API} {P110} carbon steel. *Corrosion Science*, 86:101 – 107, 2014. ISSN 0010-938X. doi: <http://dx.doi.org/10.1016/j.corsci.2014.04.051>. URL <http://www.sciencedirect.com/science/article/pii/S0010938X14002224>.

K Natesan. Corrosion-erosion behavior of materials in a coal-gasification environment.

*Corrosion*, 32(9):364–370, 1976.

Luis Efrain Sanchez-Caldera, P Griffith, and E Rabinowicz. The mechanism of corrosion–erosion in steam extraction lines of power stations. *Journal of engineering for gas turbines and*



*power*, 110(2):180–184, 1988.

PC Wu. Erosion/corrosion-induced pipe wall thinning in us nuclear power plants. Technical report, Nuclear Regulatory Commission, Washington, DC (USA). Div. of Engineering and Systems Technology, 1989.

Darryn D Fleming and Alan Michael Kruienza. Identified corrosion and erosion mechanisms in sco2 brayton cycles. Technical report, Sandia National Laboratories (SNL- NM), Albuquerque, NM (United States); Sandia National Laboratories, Livermore, CA, 2014.

M. Gwodzik and Z. Nitkiewicz. Studies on the adhesion of oxide layer formed on x10crmovnb9-1 steel. *Archives of Civil and Mechanical Engineering*, 14(3):335 – 341, 2014. ISSN 1644-9665. doi: <http://dx.doi.org/10.1016/j.acme.2013.10.005>. URL <http://www.sciencedirect.com/science/article/pii/S1644966513001362>.

W. Tabakoff and B.V.R. Vittal. High temperature erosion study of inco 600 metal. *Wear*, 86(1):89–99, 1983. ISSN 0043-1648. doi: [http://dx.doi.org/10.1016/0043-1648\(83\)90091-1](http://dx.doi.org/10.1016/0043-1648(83)90091-1). URL: <http://www.sciencedirect.com/science/article/pii/0043164883900911>.

John Ernest Garnham. *The wear of bainitic and pearlitic steels*. PhD thesis, University of Leicester, 1995.

Bharat Bhushan. *Modern tribology handbook, two volume set*. CRC press, 2000.

F.H. Stott. The role of oxidation in the wear of alloys. *Tribology International*, 31(13):61–71, 1998. ISSN 0301-679X. doi: [http://dx.doi.org/10.1016/0301-679X\(98\)00008-5](http://dx.doi.org/10.1016/0301-679X(98)00008-5). URL <http://www.sciencedirect.com/science/article/pii/S0301679X98000085>.

R. Liu, J.H. Yao, Q.L. Zhang, M.X. Yao, and R. Collier. Sliding wear and solid-particle erosion resistance of a novel high-tungsten stellite alloy. *Wear*, 322323:41 – 50, 2015. ISSN 0043-1648. doi: <http://dx.doi.org/10.1016/j.wear.2014.10.012>.

A.R. Rastkar and T. Bell. Characterization and tribological performance of oxide layers on a gamma based titanium aluminide. *Wear*, 258(1112):1616 – 1624, 2005. ISSN 0043-1648. doi: <http://dx.doi.org/10.1016/j.wear.2004.11.014>. URL <http://www.sciencedirect.com/science/article/pii/S0043164804004272>.

Sunniva R Collins, Arthur H Heuer, and Vinod K Sikka. Low temperature surface carburization of stainless steels. Technical report, Swagelok Company, Solon, OH, 2007.

Michelle C.S. Duarte, Cristina Godoy, and J.C. Avelar-Batista Wilson. Analysis of sliding wear tests of plasma processed {AISI} 316l steel. *Surface and Coatings Technology*, 260:316 – 325, 2014. ISSN 0257-8972. doi: <http://dx.doi.org/10.1016/j.surfcoat.2014.07.094>. URL <http://www.sciencedirect.com/science/article/pii/S0257897214007142>. The 41st International Conference on Metallurgical Coatings and Thin Films.

JM Oh. Effect of alloying elements on oxidation of low-chromium alloys. *Rep. of investigations/US Bureau of mines*.

## CHAPTER 7: STRESS CORROSION CRACKING IN HIGH TEMPERATURE SC-CO<sub>2</sub> ENVIRONMENT – A BRIEF SURVEY

**7.1. Introduction:** As shown in figure 7.1, stress corrosion cracking (SCC) can occur if there is a simultaneous presence of tensile stresses, a corrosive environment, and susceptible material/microstructure. Austenitic stainless steels are particularly prone to SCC.

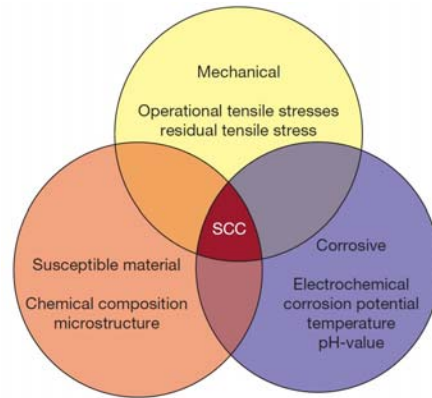
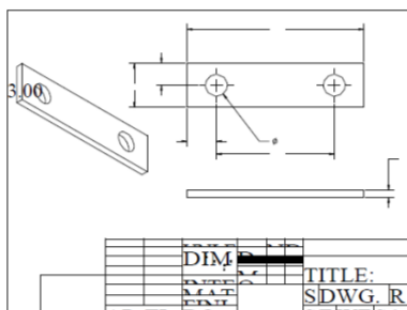


*Figure 7.1: Schematic illustration depicting the need for confluence of tensile stresses, corrosive environment, material/microstructural susceptibility for SCC to occur.*

**7.2. Experimental:** The SCC work in this project was not focused on pinpointing the mechanisms of SCC in SC-CO<sub>2</sub> but rather to make an initial assessment of propensity for SCC in this environment. 316 austenitic stainless steel and Haynes 230 were investigated for SCC testing in this project, and U-bend samples of these materials were used for this study. Figure 7.2a schematically shows the dimensions of the SCC samples and Figure 7.2b shows a photograph of a SCC sample that was fabricated in accordance with ASTM Standard G30-97, “Standard Practice for making and Using U-Bend Stress-Corrosion Test Specimens.” Flat, unbent samples were water-jet cut from sheet material to dimensions of 3” x 0.75” x 0.625” and bent around a 0.625” diameter mandrel. 316 stainless steel screws were used to hold the bent samples in place and alumina washers were used to electrically isolate the U-bend samples from these screws to avoid galvanic corrosion. As in the case of test flat samples discussed in the previous sections, the U-bend samples were placed in the SC-CO<sub>2</sub> autoclaves and testing was performed at 650°C for various exposure durations up to 1000 hours. Additionally, similarly prepared samples were exposed in ambient air (as a non-carbon bearing oxidizing environment) at the same temperature for the same durations.



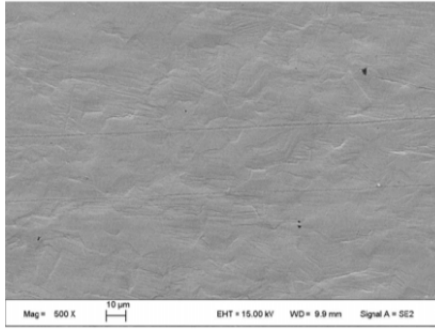
(a)



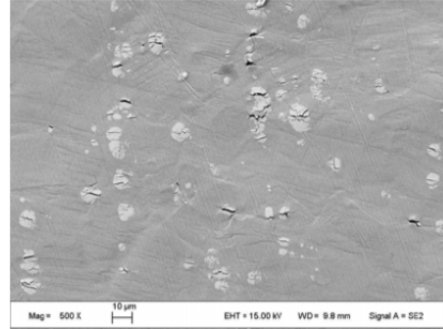
(b)

*Figure 7.2: SCC sample used in this project, (a) schematic diagram of the plate material from which the U-bend samples prepared, (b) photograph of the actual SCC sample (prepared according to ASTM Standard G30-97).*

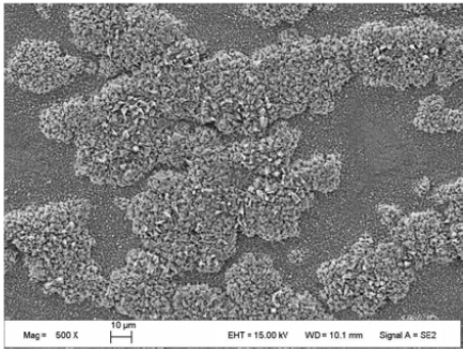
**7.3. Results and Analysis:** Figure 7.3 shows plan view SEM micrographs of the untested and tested samples exposed to both air and SC-CO<sub>2</sub> for 200 hours on the apex of the U-bend sample. Unfortunately, slight cracking was observed in the samples on both Haynes 230 and 316 stainless steel. Cracking appeared to initiate along brittle W<sub>6</sub>C carbides for Haynes 230 whereas cracking initiated randomly on the 316SS. After testing in both air and SC-CO<sub>2</sub>, cracking was not observed on 316SS as it was obscured by the formation of an oxide layer. For Haynes 230, cracking did not discernibly progress as a result of testing. Figure 7.4 depicts cross sectional SEM micrographs of the untested and tested samples exposed to both air and S-CO<sub>2</sub> for 600 hours. No discernible cracking was observed in these cross-sectional images. The oxide layer remained intact on the 316 stainless steel samples exposed to SC-CO<sub>2</sub> for 600 hours and was very similar to the oxide layer developed on test flat samples (discussed earlier), indicating that the applied stress of the U-bend did not facilitate SCC or change the oxidation behavior. The oxide layer on the Haynes 230 samples is too thin and was not apparent on the samples. No significant propagation of pre-existing cracks in either was observed during the tests.



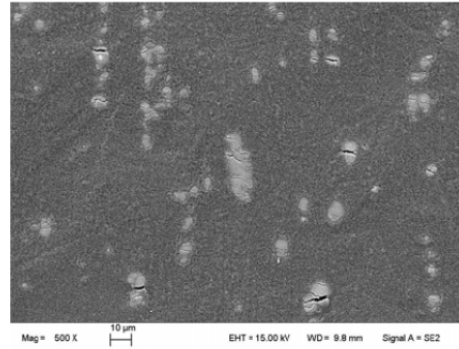
(a)



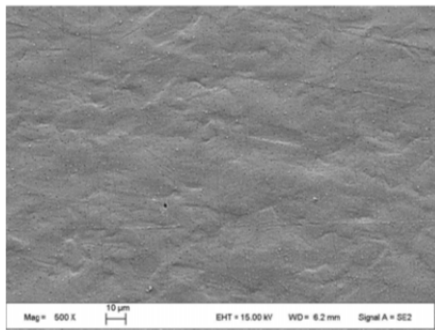
(b)



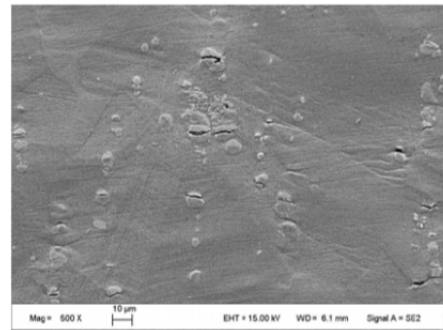
(c)



(d)

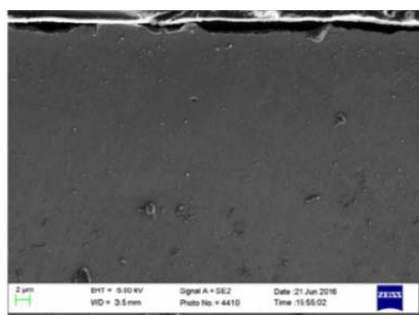


(e)

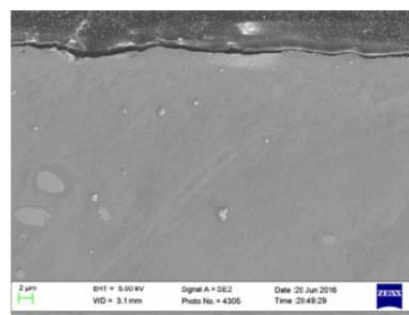


(f)

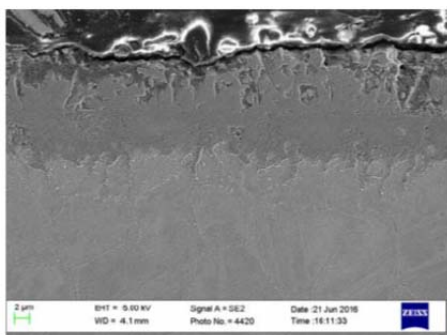
*Figure 7.3: Low magnification SEM plan view micrographs of the surface of apex of U-bend samples exposed to 650°C air or SC-CO<sub>2</sub> for 200 hours, (a) as-received, untested 316SS, (b) as-received, untested Haynes 230, (c) 316SS tested in SC-CO<sub>2</sub>, (d) Haynes 230 tested in SC-CO<sub>2</sub>, (e) 316SS tested in air, (f) Haynes 230 tested in air.*



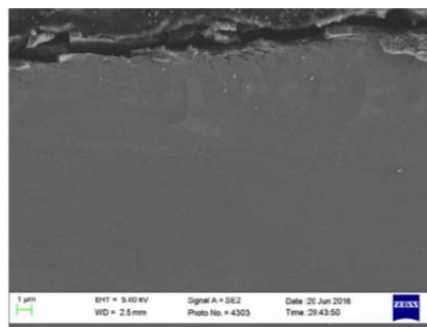
(a)



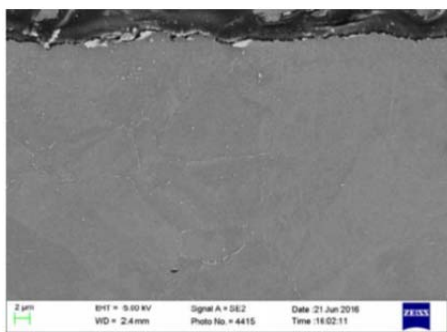
(b)



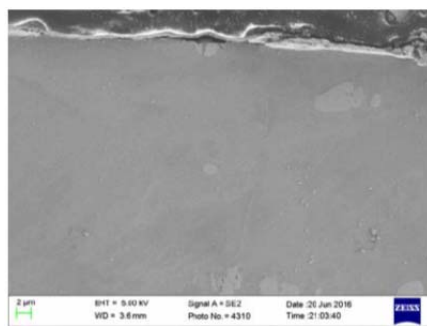
(c)



(d)



(e)



(f)

Figure 7.4: Low magnification SEM cross-sectional view micrographs of the surface of apex of U-bend samples exposed to 650°C air or SC-CO<sub>2</sub> for 600 hours, (a) as-received, untested 316SS, (b) as-received, untested Haynes 230, (c) 316SS tested in SC-CO<sub>2</sub>, (d) Haynes 230 tested in SC-CO<sub>2</sub>, (e) 316SS tested in air, (f) Haynes 230 tested in air.

**7.4. Summary:** Preliminary tests were conducted to evaluate the propensity for stress corrosion cracking (SCC) in SC-CO<sub>2</sub> environments using U-bend tests of 316 stainless steel and Haynes 230 alloy. A comparison was made between SCC samples tested in air (as a non-carbon bearing environment) and in SC-CO<sub>2</sub> environments. No detectable cracking was observed in the samples exposed to SC-CO<sub>2</sub> environment. However, the testing procedure had many limitations and points to the need for performing thin sample tensile tests after SC-CO<sub>2</sub> corrosion testing or still better, *in situ* tensile testing in SC-CO<sub>2</sub> environment.



## Bibliography Consulted

- HJ Russell. Stress-corrosion cracking materials performance and evaluation. *USA: ASM International*, pages 1–40, 1992.
- S. Fyfe. 5.04 - corrosion and stress corrosion cracking of ni-base alloys. In Rudy J.M. Konings, editor, *Comprehensive Nuclear Materials*, pages 69 – 92. Elsevier, Oxford, 2012. ISBN 978-0-08-056033-5. doi: <http://dx.doi.org/10.1016/B978-0-08-056033-5.00079-3>. URL <http://www.sciencedirect.com/science/article/pii/B9780080560335000793>.
- Roger W. Staehle. *Quantitative Micro-Nano (QMN) Approach to SCC Mechanism and Prediction-Starting a Third Meeting*, pages 1535–1625. John Wiley & Sons, Inc., 2012. ISBN 9781118456835. doi: 10.1002/9781118456835.ch161. URL <http://dx.doi.org/10.1002/9781118456835.ch161>.
- Mohammed Al-Rabie. Observations of stress corrosion cracking behaviour in super duplex stainless steel. 2011.
- W Dietzel, P Bala Srinivasan, and A Atrens. Testing and evaluation methods for stress corrosion cracking (scc) in metals. *Stress Corrosion Cracking: Theory and Practice., 1st edition*. Woodhead Publishing, pages 133–166, 2011.
- James R Keiser, Douglas L Singbeil, Gorti B Sarma, Joseph R Kish, Kimberly A Choudhury, Laurie A Frederick, J Peter Gorog, François R Jetté, Camden R Hubbard, Robert W Swindeman, et al. Cracking and corrosion of composite tubes in black liquor recovery boilers. *40 Years Recovery Boiler Co-operation in Finland*, pages 12–14, 2001.
- TR Allen, Y Chen, X Ren, K Sridharan, L Tan, GS Was, E West, and D Guzonas. Material performance in supercritical water. *Comprehensive nuclear materials*, 5:279, 2012.
- L Caseres and Todd S Mintz. *Atmospheric Stress Corrosion Cracking Susceptibility of Welded and Unwelded 304, 304L, and 316L Austenitic Stainless Steels Commonly Used for Dry Cask Storage Containers Exposed to Marine Environments*. Southwest Research Institute, 2010.
- U Ehrnstrén. Corrosion and stress corrosion cracking of austenitic stainless steels. *Comprehensive Nuclear Materials, Elsevier, Amsterdam*, pages 93–104, 2012.
- RB Setterlund. Stress-corrosion cracking of high-strength alloys. Technical report, DTIC Document, 1964.
- JB Cai, C Yu, RK Shiue, and LW Tsay. Stress corrosion cracking of austenitic weld deposits in a salt spray environment. *Journal of Nuclear Materials*, 465:774–783, 2015.
- Tad Dee Clark. An analysis of microstructure and corrosion resistance in underwater friction stir welded 304L stainless steel. 2005.
- T Abraham, H Jain, and P Soo. Stress corrosion cracking tests on high-level- waste container materials in simulated tuff repository environments. Technical report, Brookhaven National Lab., Upton, NY (United States), 1986.
- Joseph Rogelio Fernandez. Stress corrosion cracking evaluation of candidate high strength stainless steels for prestressed concrete. 2011.
- Phani P Gudipati. Stress corrosion cracking resistance of martensitic stainless steels for transmutation applications. 2004.

- Lieutenant JK Lewis. *An Investigation of Stress Corrosion Cracking in High Strength Aluminum AUoys-The Development of New Test Method*. PhD thesis, Royal Military College of Canada, 1998.
- SJ Pawel. Corrosion assessment of candidate materials for the shine subcritical assembly vessel and components–2015 report. *Oak Ridge National Laboratory Technical Memorandum ORNL/TM-2015/704*, 2015.
- TS Gendron, PM Scott, SM Bruemmer, and LE Thomas. Internal oxidation as a mechanism for steam generator tube degradation. *Canadian Nuclear Society Societe Nucleaire Canadienne*, page 390, 1998.
- PL Andresen, FP Ford, K Gott, RL Jones, PM Scott, T Shoji, RW Staehle, and RL Tapping. Expert panel report on proactive materials degradation assessment, (nureg/cr-6923, bnl-nureg-77111-2006). *Brookhaven National Laboratory, US Nuclear Regulatory Commission, Office of Nuclear Regulatory Research, Washington, DC*, 2007.
- ASTM G30-97. Standard practice for making and using u-bend stress-corrosion test specimens. 2000.
- Stephen M Bruemmer and Gary S Was. Microstructural and microchemical mechanisms controlling intergranular stress corrosion cracking in light-water-reactor systems. *Journal of Nuclear Materials*, 216:348–363, 1994.
- Seong Sik Hwang, Yun Soo Lim, Sung Woo Kim, Dong Jin Kim, and Hong Pyo Kim. Role of grain boundary carbides in cracking behavior of ni base alloys. *Nuclear Engineering and Technology*, 45(1):73–80, 2013.

## CHAPTER 8: EXPERIMENTS-SUPPORTED MODELING OF CORROSION OF FERRITIC STEELS IN HIGH TEMPERATURE SC-CO<sub>2</sub> ENVIRONMENT

### 8.1. Alloys Tested

This section of the report focuses on the work performed on corrosion performance of ferritic steels which are being deemed as candidate materials for the lower temperature end of S-CO<sub>2</sub> Brayton cycle (up to about 450 °C) because they lack high temperature strength of stainless steel and Ni-based alloys, but at the same time are more cost-effective because they do not contain Ni. Furthermore, although ferritic and ferritic-martensitic steels have lower high temperature strength and corrosion resistance than austenitic alloys, they exhibit lower swelling under radiation compared to austenitic alloys. They are therefore attractive candidate structural materials for nuclear reactors. The ferritic-martensitic steels investigated in this study have therefore been studied by previous researchers quite widely for nuclear reactor applications. Although the S-CO<sub>2</sub> Brayton cycle application does not involve radiation, the incentive to use already code certified materials makes these alloys viable candidates for SC-CO<sub>2</sub> Brayton cycle for nuclear reactors.

In this research, corrosion behavior of ferritic steels T22, T92, and T122 along with pure Fe and Fe12Cr binary alloy were evaluated at 450°C and 20MPa research grade (RG) CO<sub>2</sub> were evaluated. Oxidation of ferritic/martensitic steels at 450 °C and 20 MPa research grade SC-CO<sub>2</sub> were performed for exposure durations of up to 1000 hours, with samples being removed at intervals of 200 hours for analysis. Table 8.1 summarizes the composition of these alloys.

*Table 8.1: Materials tested at 450 °C and 200 bar research grade SC-CO<sub>2</sub> in this research.*

<i>Tested Alloys</i>		<i>Nominal Composition (wt. %)</i>								
		<i>C</i>	<i>Al</i>	<i>Si</i>	<i>V</i>	<i>Cr</i>	<i>Fe</i>	<i>Ni</i>	<i>Mo</i>	<i>W</i>
<i>Ferritic Steels</i>	<i>T22</i>	0.1	-	0.5	-	2.25	<i>Bal.</i>	-	1	-
	<i>T92</i>	0.11	0.02	0.1	0.2	8.94	<i>Bal.</i>	0.21	0.5	1.91
	<i>T122</i>	0.12	0.01	0.27	0.2	10.7	<i>Bal.</i>	0.41	0.35	1.9
<i>Model Alloys</i>	<i>Fe12Cr</i>	-	-	-	-	12	<i>Bal.</i>	-	-	-
	<i>Fe</i>	-	-	-	-	-	1000	-	-	-

### 8.2. Oxide Morphology

#### 8.2.1. Oxidation of Pure Fe in SC-CO<sub>2</sub>

The surface of the samples after exposures at 200 and 400 hours showed considerable spallation of the oxide. Figure 8.1 shows surface image of the sample after 200 hour exposure and corresponding EDS analysis. These EDS results must be deemed qualitative given the limitations of EDS method for detection of light elements such as oxygen and carbon. Carbon contamination at the surface also cannot be ruled out.

<i>% Atom</i>	<i>C</i>	<i>O</i>	<i>Si</i>	<i>Fe</i>
<i>Pure Fe(3)_pt1</i>	4.33	50.71		44.96
<i>Pure Fe(3)_pt2</i>	4.39	56.08	0.53	39.00
<i>Pure Fe(3)_pt3</i>	4.42	52.41	1.06	42.11

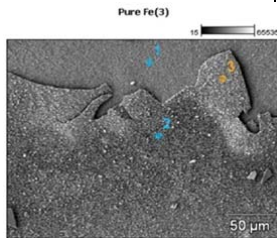
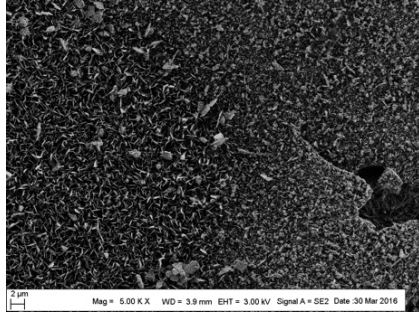
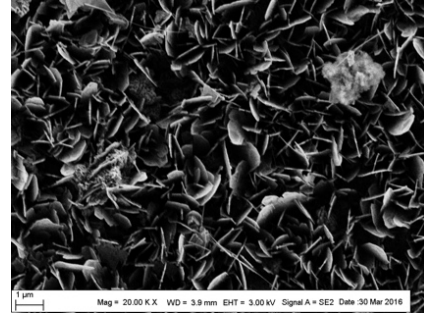


*Figure 8.1: SEM-EDS point analyses performed on various regions of surface oxide layer.*

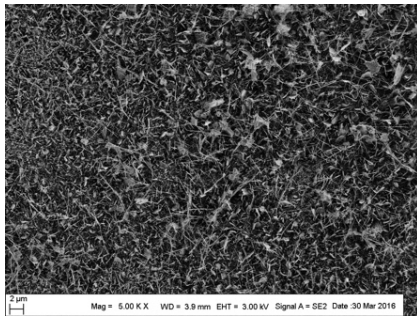
Different types of surface morphologies of the oxide corrosion product were detected for the 400 hour exposed samples, and are documented in figure 8.2. Figure 8.2a features a cracked region indicating susceptibility to spallation. Figure 8.2b shows a lamellar morphology. In addition, whisker-type morphological formation as small in size-scale as 1 µm was also observed as shown in figure 8.2c&d. This whisker and lamellar formation could play an important role in the surface reactions with CO<sub>2</sub> due to increased surface area leading to accelerated weight gain. This whisker morphology was not associated with cracks, leading to the speculation that the formation of lamellar or whisker type morphology require uninterrupted Fe outward diffusion.



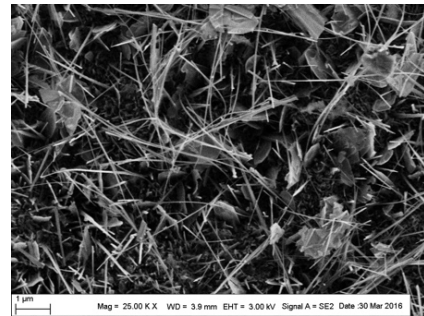
*a) 5KX SEM micrograph featuring a crack region*



*b) 20KX SEM micrograph featuring a lamellar type growth*



*c) 5KX SEM micrograph featuring whisker formation*



*d) 25KX SEM micrograph featuring whisker formation*

*Figure 8.2: SEM micrographs of 400h exposed pure Fe sample featuring (a) cracking, (b) lamellar morphology, and (c, d) whisker type morphology.*

Cross-sectional examination of oxide layer by SEM indicated the formation of a duplex oxide formation. Figure 8.3 presents the cross-sectional SEM observations in 200h exposed sample, where a continuous oxide scale separation from base Fe, and a continuous interface within the the oxide was observed.

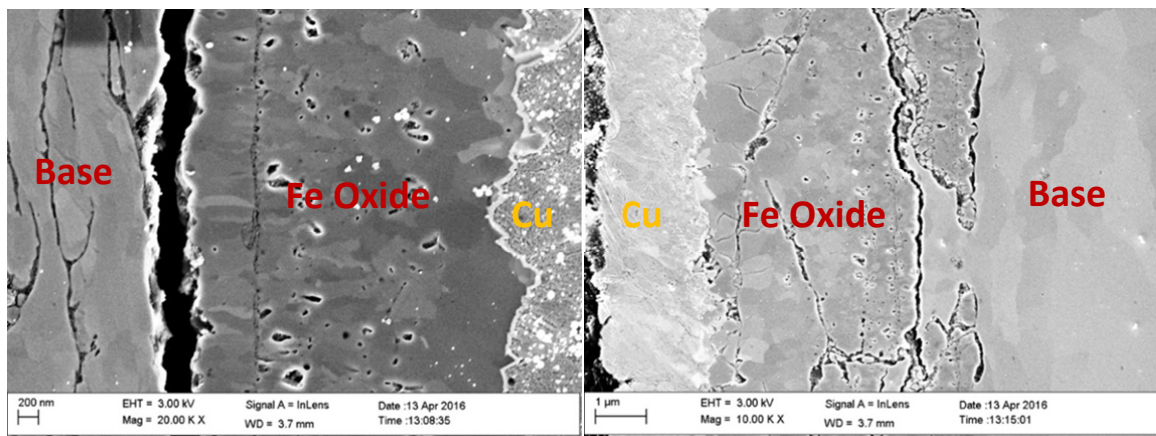


*Figure 8.3: Cross-sectional SEM micrographs of 200h exposed pure Fe samples showing spallation of the oxide layer and (left) a continuous interface inside the oxide and internal attack of Fe are observed (right).*



For the 1000h exposed sample, scale separation of base Fe and oxide was still present as expected. For more accurate iron oxide stoichiometry determination, 1000h exposed sample was subjected to the EPMA-WDS analyses. The sample was first mirror polished and plasma cleaned for 40min prior to this analysis. The results shown in figure 8.4 indicate all the oxide to be of  $\text{Fe}_3\text{O}_4$  stoichiometry.

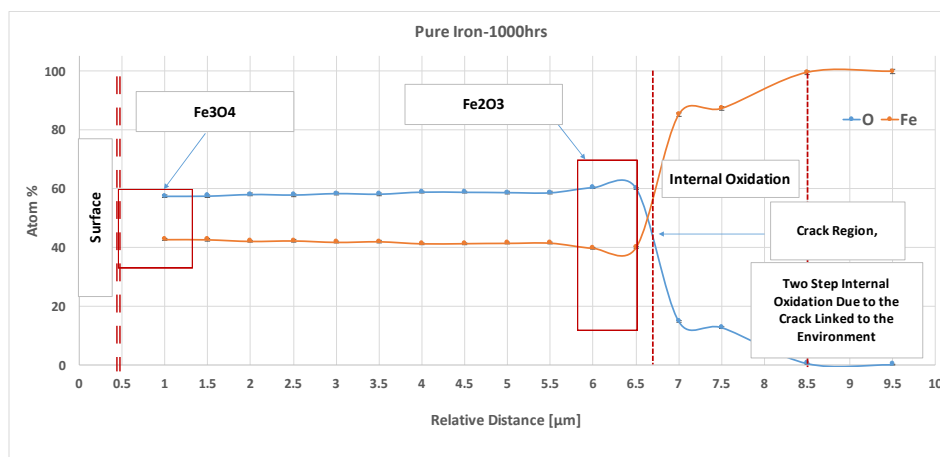


Figure 8.4: EPMA-WDS analyses performed on the cross-section of 1000h exposed iron sample featuring iron and oxygen distribution from the oxide surface to the base Fe.

XRD analyses of oxide surface formed on the pure-Fe after its 1000h exposure, (figure 8.4) shows magnetite and base iron peaks. No patterns of hematite phase were observed. This result is in agreement with the result by EMPA-WDS where ratio of atomic percentages of O and Fe indicated the presence of magnetite.

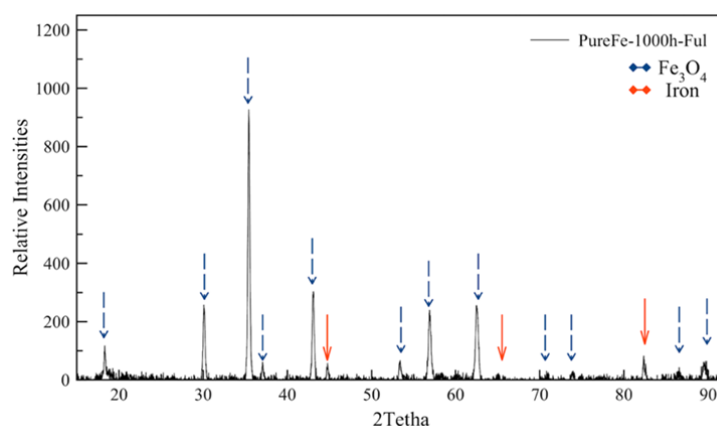
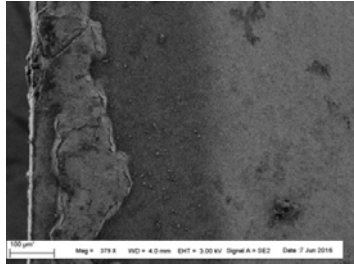


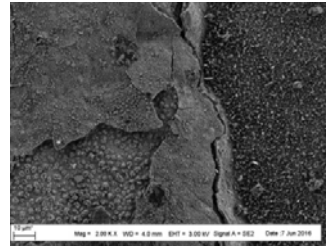
Figure 8.5: XRD analysis for the 1000 hour exposed samples showing magnetite and base Fe patterns.

### 8.2.2 Oxidation of T22 in SC- $\text{CO}_2$

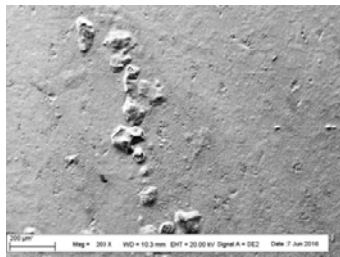
As a preliminary assessment of the oxidation behavior of T22 in SC- $\text{CO}_2$ , plain view SEM observations were performed and presented in figure 8.6 for 200, 400, and 1000h exposed samples.



*a)379X SEM micrograph of 200h exposed sample featuring a crack region at the edge of the sample*



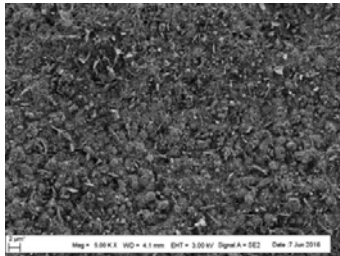
*b)2KX SEM micrograph of 200h exposed sample featuring a crack region at the edge of the sample*



*c)200X SEM micrograph of 200h exposed sample featuring blister formation in the middle of the sample*



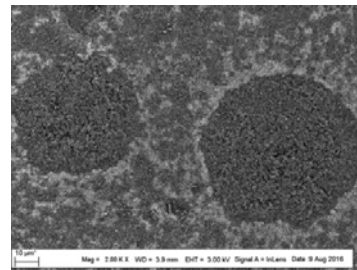
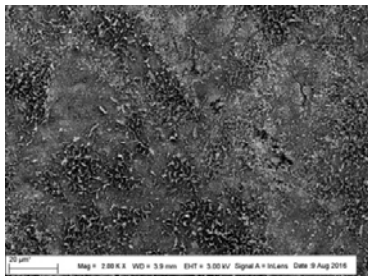
*d)1KX SEM micrograph of 200h exposed sample featuring blister formation in the middle of the sample*



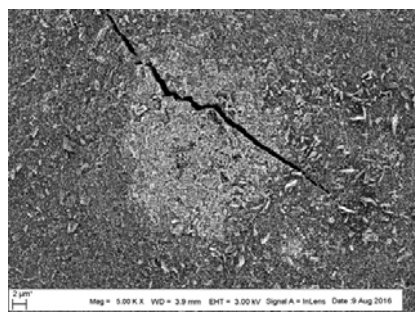
*e)5KX SEM micrograph of 400h exposed sample featuring in the middle of the sample*



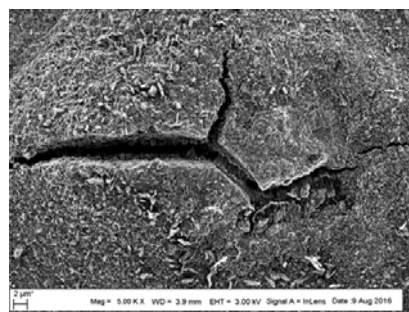
*f)40KX SEM micrograph of 400h exposed sample featuring whisker in the middle of the sample*



*g) 2KX SEM micrograph of 1000h exposed sample featuring in the edge of the sample with lamellar oxide growth and surface cracks*



*h) 2KX SEM micrograph of 1000h exposed sample featuring in the middle of the sample with compositional differences*



*k) 5KX SEM micrograph of 1000h exposed sample featuring whisker in the middle of the sample with a crack formation*

*l) 5KX SEM micrograph of 1000h exposed sample featuring blister and crack formation on top in the middle of the sample*

*Figure 8.6: SEM plain views of T22 exposed for 200h (a-d), 400hr(e-f), and 1000h (g-l) showing oxide surface morphology.*

The figures (8.6 a-d) were taken with the 200h exposed sample for which increased attack at the edges were visible with the partial spalling of the oxide flakes. The observation on the mid-section of the sample, in addition, revealed blister-like oxide formation with surface cracks. For 400h exposed sample, plan view images taken on the mid-section of the sample showed a moderately uniform oxide formation with small amount of approximately 1  $\mu\text{m}$  whiskers. The oxide on the 1000h exposed sample (see figures (8.6 g-l)) was found to be formed irregularly having whisker and lamellar structures, compositional irregularities, surface cracks, and blister formations. Further analyses on the plain oxide surfaces were performed. Figure (8.7) shows surface EDS elemental mapping and point analyses on the locations of interests. The surface appears to predominantly consist of Fe-oxide with some Si enrichment.

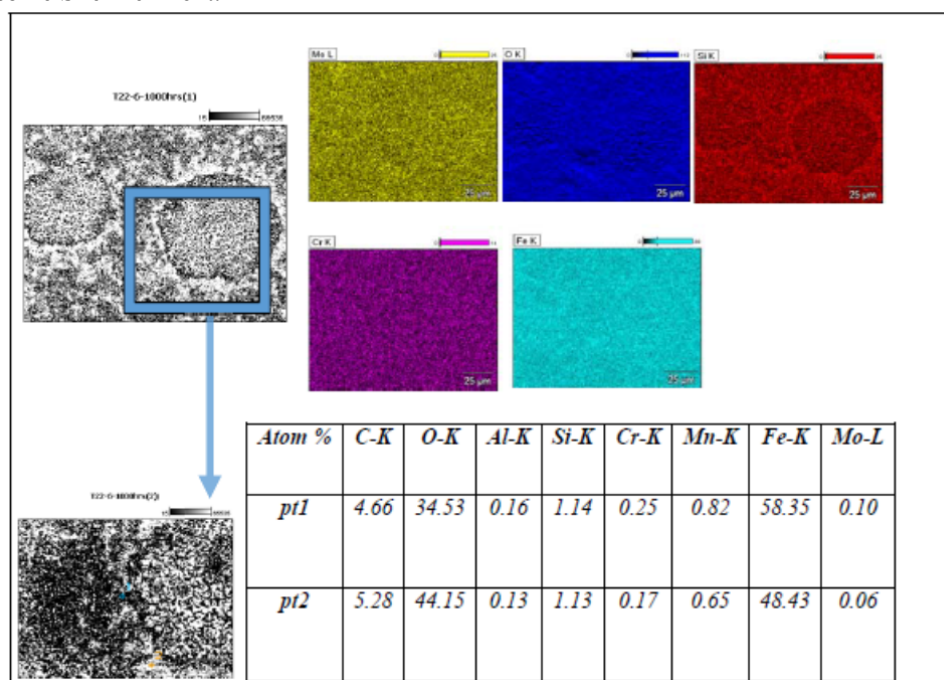


*Figure 8.7: SEM-EDS analyses on the locations of interest for 1000hr exposed T22.*

Figure 8.8 shows the EDS elemental analysis of the oxide layer in cross-section of a samples exposed for 1000hours. The oxide layer formed is duplex in nature with outer Fe-rich and an inner Cr-rich oxide layers.

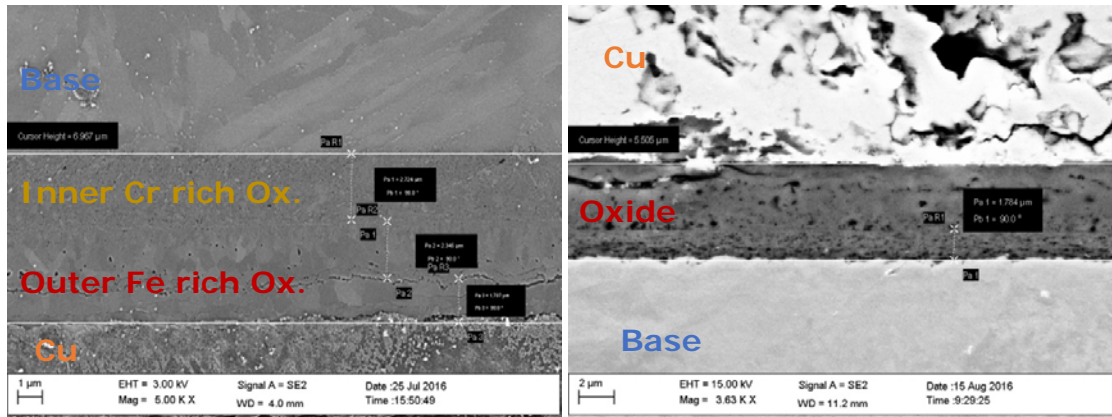


Figure 8.8: SEM micrographs taken on the cross-sectioned 1000hr exposed T22 sample featuring inner and outer oxide thickness measurements.

It was further observed that the ratio of thicknesses of inner and outer layer varied within the sample. As shown in figure 8.8 the ratio of the thickness of inner and outer layers range between 0.64 and 0.48, respectively. To improve accuracy further analysis of thickness was performed using EDS line scans. SEM observations indicated a generally porous oxide scale which would allow  $\text{CO}_2$  transport into the inner oxide and oxide/metal interface. A continuous stable interface between the outer and inner oxide layers is assumed to be the original metal surface before testing. With this assumption, it became clear that the oxidation occurs in both directions, outward and inward. This assumption is based on the fact that the Cr does not necessarily diffuse out with respect to iron outward diffusion. The inward oxygen diffusion is also very low with respect to iron diffusion leading the assumption that the inner oxidation must occur with the local presence of  $\text{CO}_2$  as dictated by the available space model to be discussed later. Figure 8.9 shows the result of EDS line scan where overall Cr content, blue line, is approximately as same as in the base alloy and in the inner oxide layer.

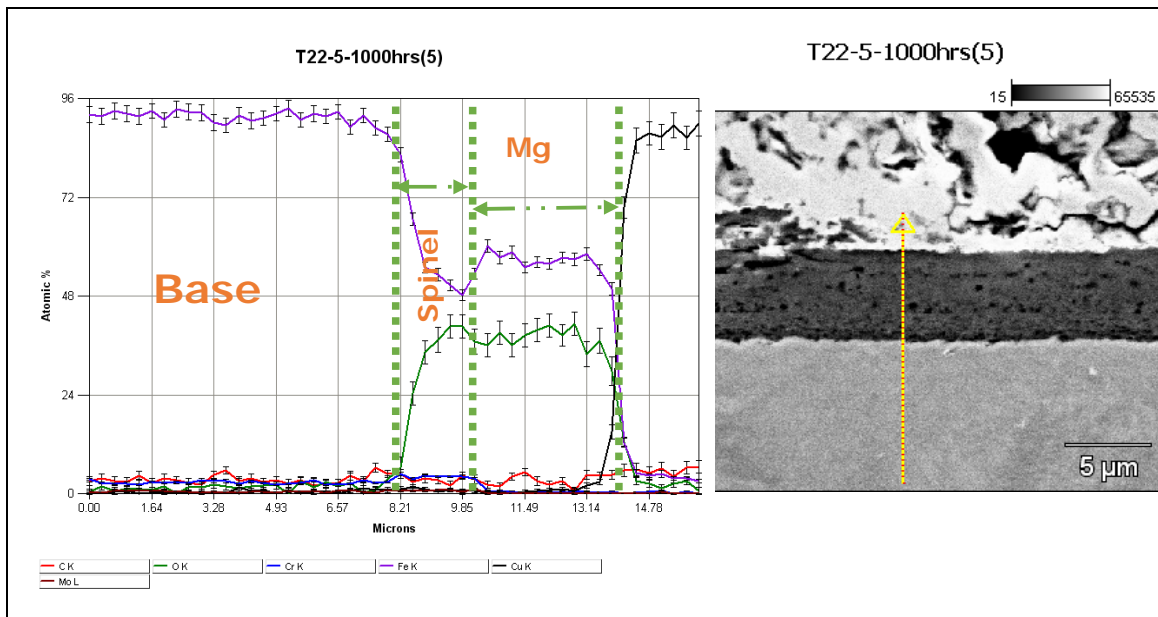


Figure 8.9: SEM-EDS line scan across the oxide cross-section of 1000h exposed T22 showing compositional variations as a function of near-surface depth.

In order to determine the oxide stoichiometries, XRD analyses were performed on the 1000h exposed sample. The results shown in figure 8.9, indicate magnetite and spinel type oxide structures. Specifically, the oxide phases determined were magnetite and chrome spinel of the form  $\text{Cr}_x\text{Fe}_{(3-x)}\text{O}_4$  for which value of  $x$  as obtained from literature database was 0.1. However, this is not quantitatively conclusive since the diffraction signal emanates from a large body of Cr-Fe-O oxide in which the distribution of those atoms will no doubt vary. A more quantitative (as an averaged value) assessment can be made by EPMA-WDS analyses and through a mass balance. In terms of inner and outer oxide stoichiometries, an approach based on the global mass balance between the oxide layers were thus employed. The result of this approach will be provided later in context of the results for 9-12Cr alloys.

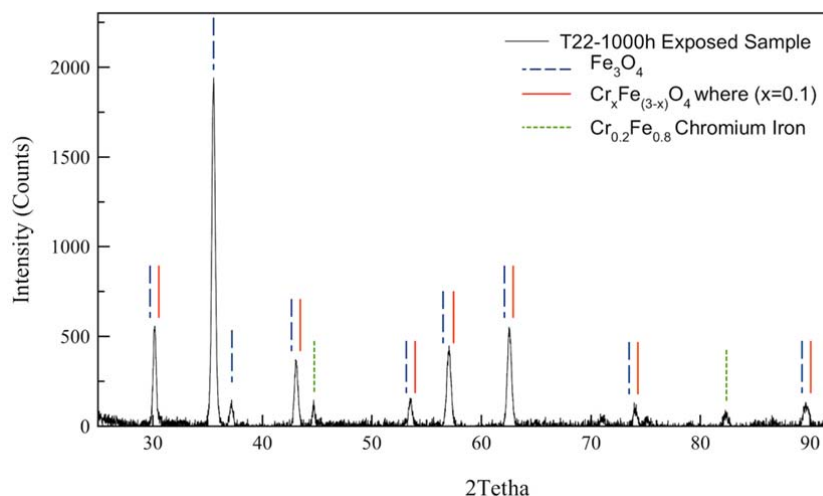
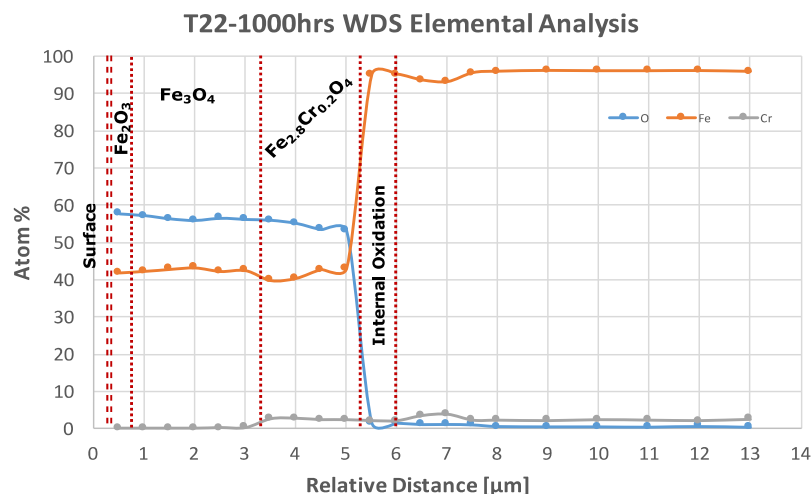


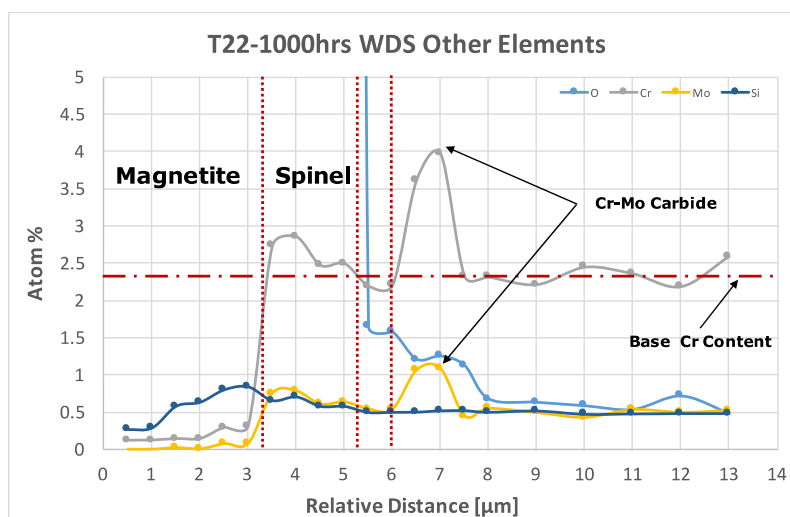
Figure 8.9: XRD analysis of 1000 hour exposed T22 sample indicating the formation of Fe-oxide magnetite and Cr-rich spinel oxide phase.

EPMA analysis was performed on the 1000 hour exposed T22 sample. A cross-sectioned, mirror polished, and plasma cleaned sample was used and EPMA analysis with  $1\mu\text{m}$  spot size and  $0.5\mu\text{m}$  intervals was performed. The results are presented in figure 8.10. Analysis of these results revealed that Cr, while enriched in the spinel layer does not diffuse outward notably. This enrichment could either be due to the relative decrease in Fe content or Cr diffusion from the unaffected base-steel. In the case of Cr diffusion from the base steel, there should be a depletion zone for Cr, which however is not the case. In regards to the outer Fe-rich oxide layer, two stoichiometries, hematite and magnetite, were observed. The hematite was detected based on a small increase in O content. However, both  $\text{Fe}_2\text{O}_3$  and  $\text{Fe}_3\text{O}_4$  were found to be non-stoichiometric but data from the very surface of oxide closely matched with the  $\text{Fe}_2\text{O}_3$  while underneath the oxide phase was the  $\text{Fe}_3\text{O}_4$ . In addition, this study showed evidence of Si outward diffusion and an increase in Mo content inside the spinel was observed (figure 8.10b). Also, there seems to be a simultaneous increase in both Cr and Mo content inside the base material most likely due to the presence of Cr-Mo carbides. Finally, the EPMA analysis also sheds light on the composition of the spinel compound – the value of  $x$  in the compound  $\text{Cr}_x\text{Fe}_{(3-x)}\text{O}_4$  was determined to be approximately 0.2 (with data given in figure 8.10c).





a) EPMA-WDS elemental analyses performed on the 1000h exposed T22 featuring major elements O-Fe-Cr



b) EPMA-WDS elemental analyses performed on the 1000h exposed T22 featuring minor alloying elements Mo-Ni-W-Si and outer diffusion of Si

<i>Element</i>	<i>Oxygen</i>	<i>Fe</i>	<i>Cr</i>	<i>x in (Fe,Cr)<sub>x</sub>O<sub>4</sub></i>
<i>Stoichiometric Values from Focused Beam</i>	<sup>4</sup> <i>Assumed Value</i>	2.67	0.19	2.86
<i>Stoichiometric Values from Readings Inside the Spinel</i>	<sup>4</sup> <i>Assumed Value</i>	3.05	0.19	3.25
<i>Averages</i>	<sup>4</sup> <i>Assumed Value</i>	2.86	0.19	3.05
<i>Stdevs</i>	-	0.27	-	0.28
<i>Err</i>	-	0.19	-	0.20

*c) Stoichiometric Calculations based on the atomic % of Fe,Cr and O readings inside the spinel layer for T22*

Figure 8.10: EPMA-WDS analyses performed on the oxide cross-section of 1000h exposed T22 featuring compositional change from the base steel and through the oxide layer.

### 8.2.3. Oxidation of 9-12Cr Steels in SC-CO<sub>2</sub>

T92 (~9%Cr) and T122 (~12%Cr) were subjected to corrosion tests at 450 °C and 20MPa CO<sub>2</sub>. A model binary alloy, Fe-12Cr, was also tested in order to establish a base line for the corrosion performance of these third generation ferritic-martensitic steels. Initial analysis of the samples was performed by SEM-EDS. Figures (8.11-13) show SEM micrographs at various magnifications for this analysis for Fe-12%Cr alloy.

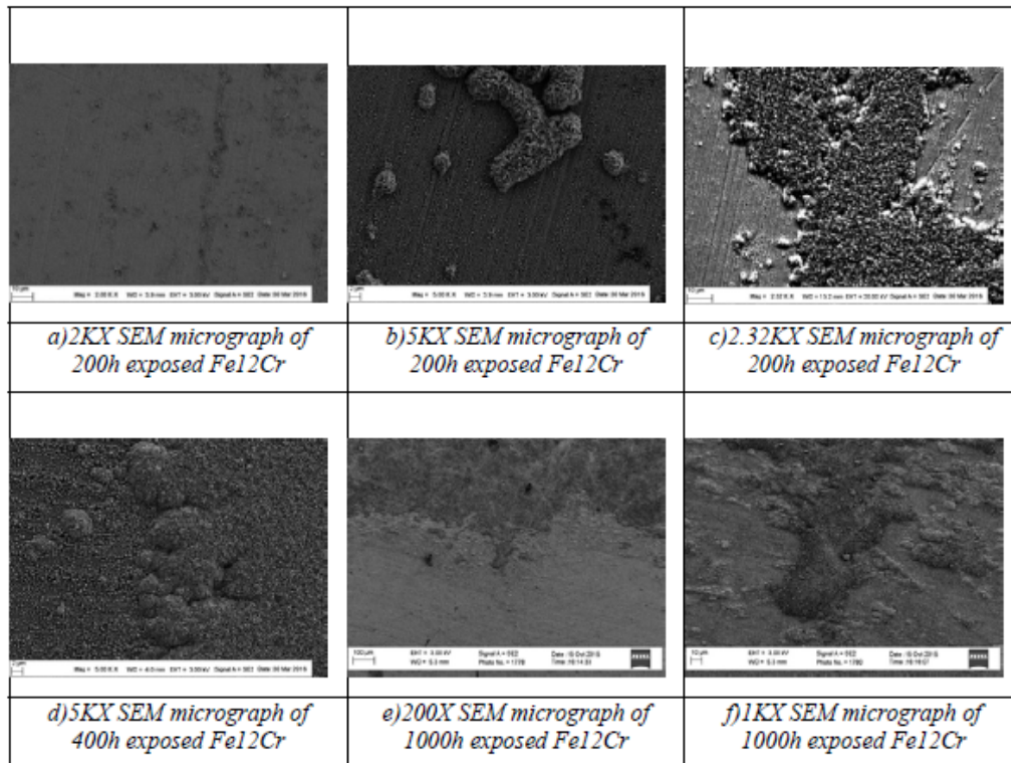
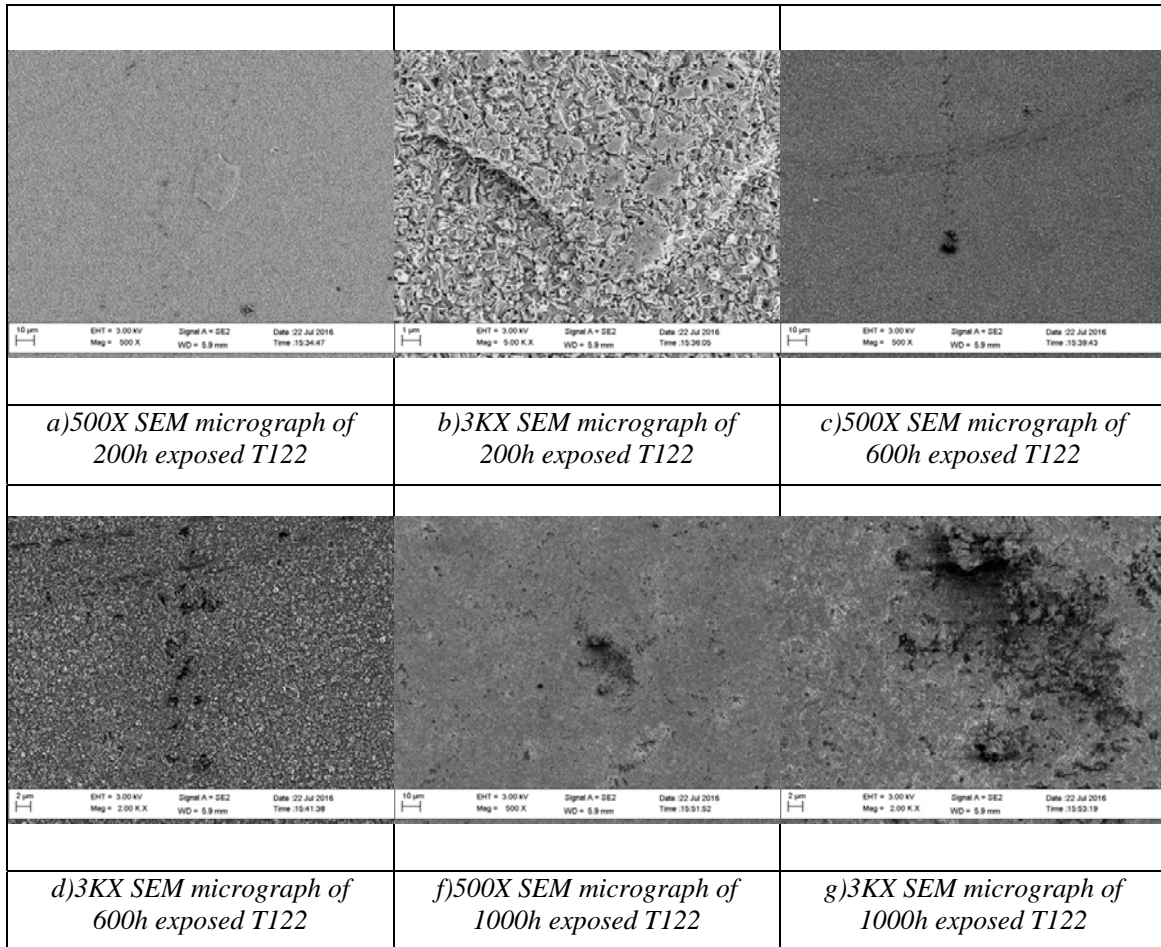


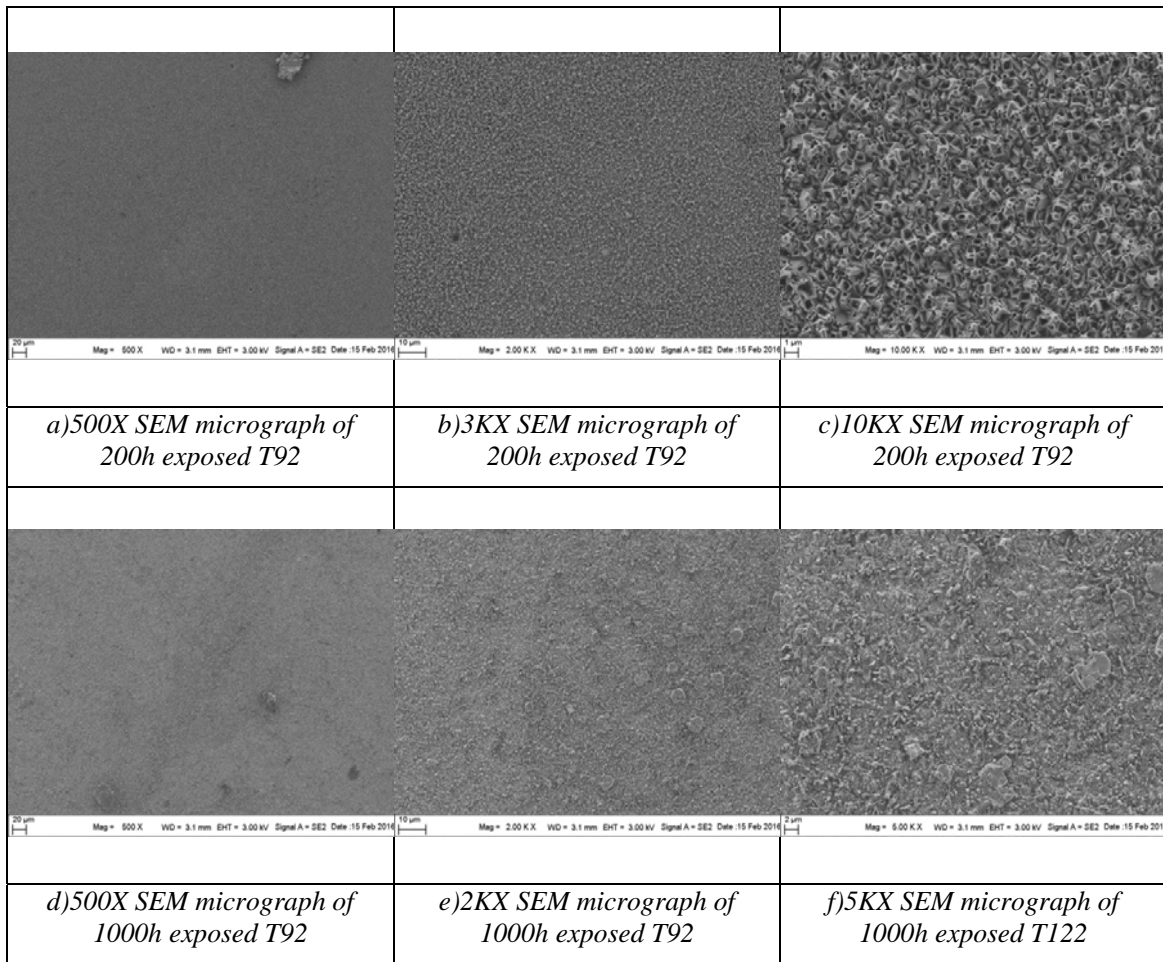
Figure 8.11: SEM plan view micrographs of Fe-12Cr alloy exposed for up to 1000h featuring nodular oxide formation on the surface.

Figure 8.12 shows oxide formation on the surface of T122 steel after exposure up to 1000h. In contrast to oxidation behavior of Fe-12Cr alloy, the oxide formation is more uniform. There were some small irregularities (2-10  $\mu\text{m}$ ) found on the samples surfaces. However, the overall plan view observations indicated no inconsistencies in terms of oxide species on the surface. This was later confirmed by SEM-EDS analysis.



*Figure 8.12: SEM plain view micrographs of T122 steel after exposures for up to 1000h featuring a more uniform oxide layer formation.*

Figure (8.13) shows plan view images of T92 steel after exposures for up to 1000 hours. Similar to T122 steel the oxide layer is quite uniform and dense even after 200 hours exposure and this uniformity persists all the way up to 1000 hours.



*Figure 8.13: SEM plain view micrographs of T92 steel exposed for up to 1000h featuring uniform oxide layer formation on the surface.*

The SEM-EDS analyses performed on the Fe12Cr samples after corrosion tests showed that the nodules are Fe-rich oxides, most likely  $\text{Fe}_3\text{O}_4$ , and the rest is very thin protective oxide Cr-rich oxide. The quantitative analyses on the nodules and protective portion of the surface oxide are presented in the figure (8.14).

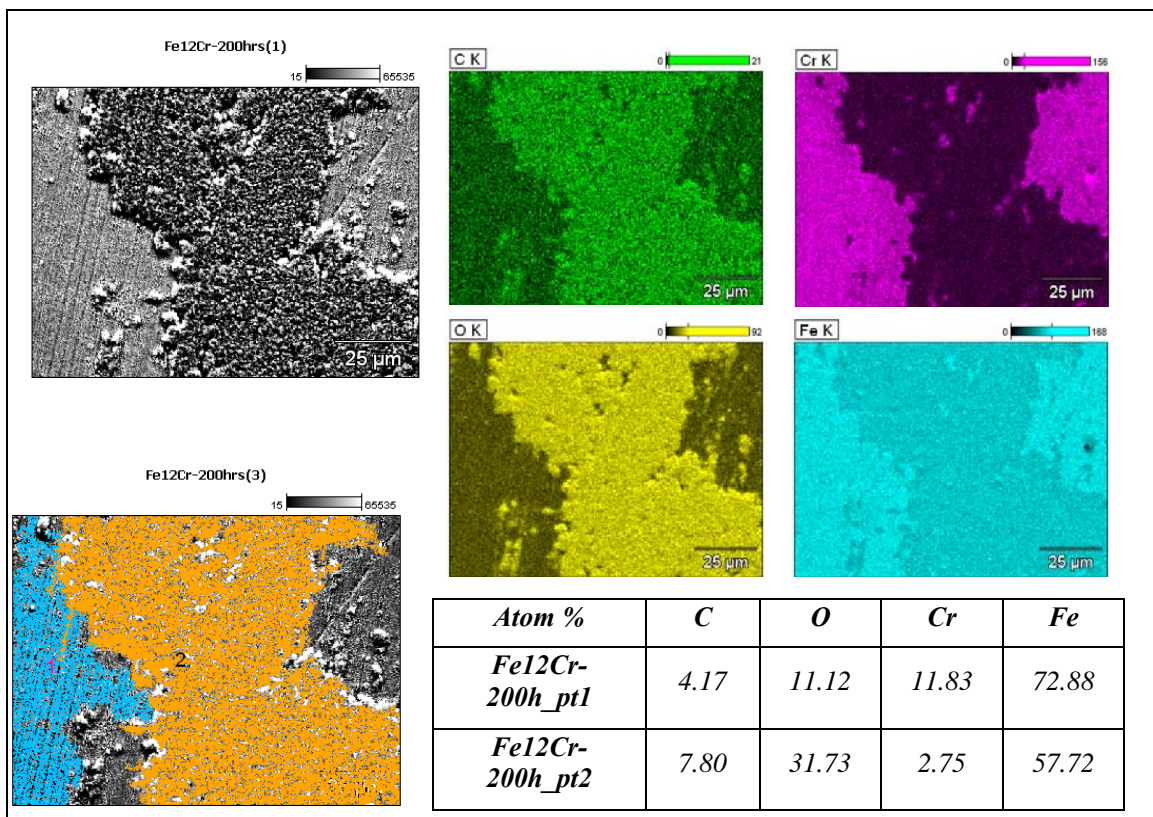


Figure 8.14: SEM-EDS analyses performed on the surface of the 200h exposed Fe-12Cr alloy.

The oxide nodule does not necessarily include Cr. The Cr signal most likely came from an underlying duplex oxide layer or from the base alloy. Regarding the carbon signals, both elemental distribution mapping (figure 8.14) and semi-quantitative data indicate that the carbon intake is higher in the nodular regions with respect to the thin surface oxide (carbon analyses is not reliable by SEM-EDS analysis). This could be an indication that oxidation and carbon uptake are interlinked.



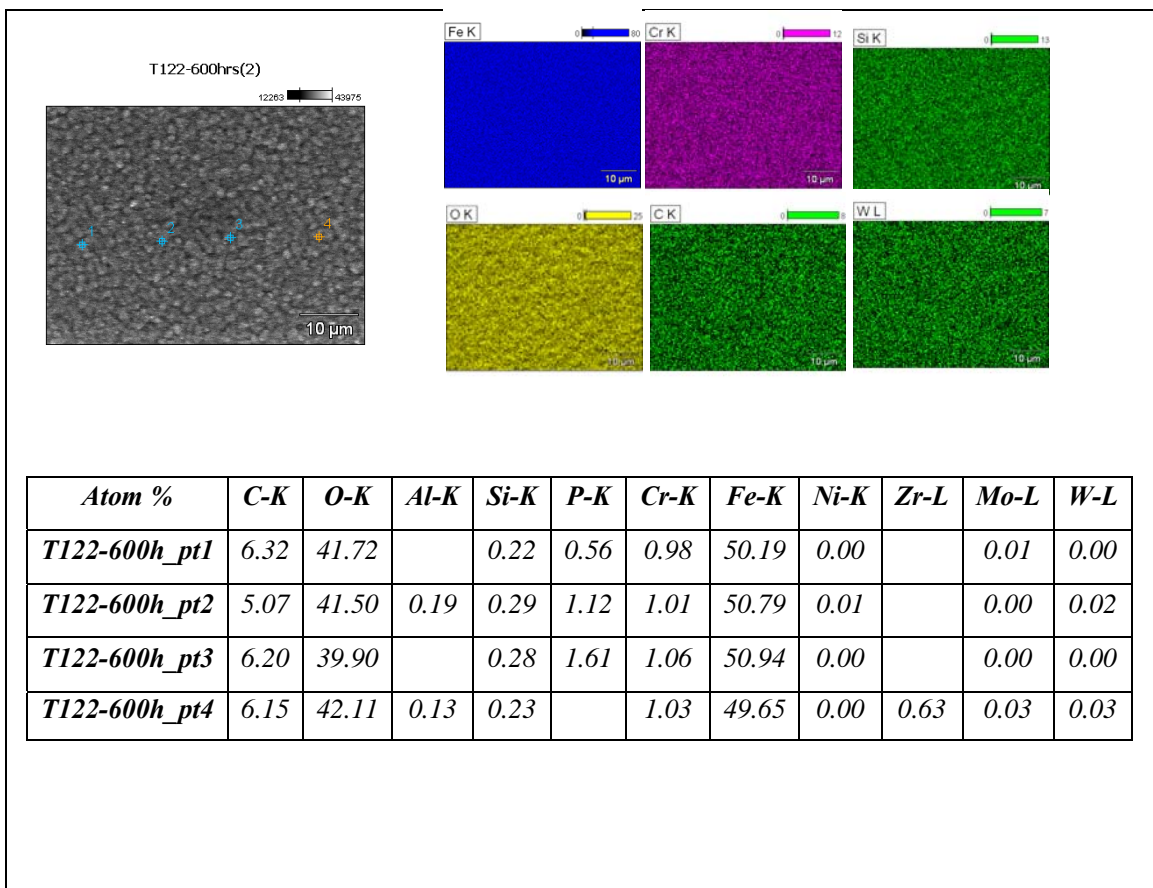
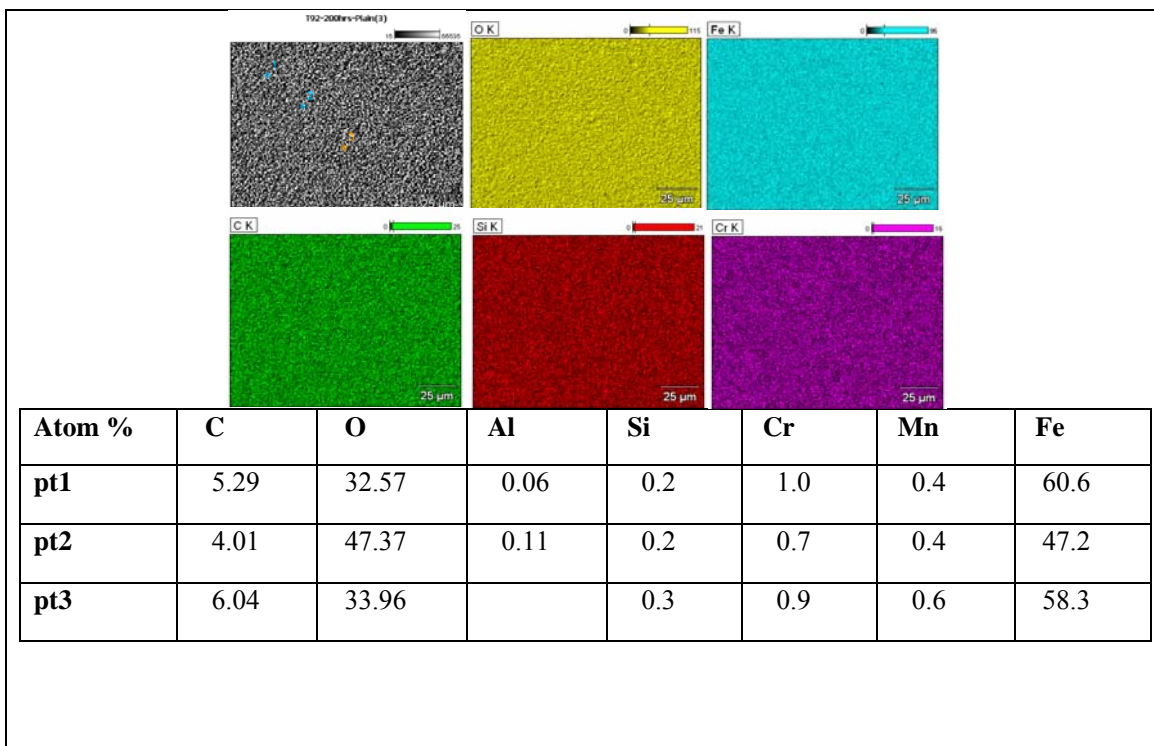


Figure 8.15: SEM-EDS analyses performed of the surface of the 600h exposed T122 steel.

The SEM-EDS analyses performed on the surface of 600h exposed T122 sample is shown in figure 8.15, where uniform oxide formation can be seen using elemental mapping. In addition, point analyses performed in the same region indicates that the oxide surface is mainly composed of iron-oxide. The relative signals of major alloying elements such as Cr, Mo, W found to be suppressed in multiple points of analysis. Si, P, and Zr signal at one of the points is an artifact of the analysis. Again a carbon content is reported and should be deemed qualitative.

SEM-EDS analyses performed on the surface of 200h exposed T92 steel is shown in the figure 8.16. As it was the case for T122 steel, relative signals of alloying elements are largely absent indicating the presence of Fe-rich oxide at the surface. However, there are some inconsistencies in atomic oxygen and iron quantity suggesting different stoichiometric iron oxide formation. However, this initial conclusion needs to be further confirmed since EDS is not an effective tool for quantitative analyses of oxygen. Again carbon content is reported noting that its detection by EDS is purely qualitative.



**Figure 8.16: SEM–EDS analyses performed on the surface of the 200h exposed T92 steel.**

Further analysis of the oxide and corrosion product layer was performed by mounting the tested samples in cross-section. SEM micrographs of oxide layer on Fe12Cr binary alloy is shown in in the following figure (8.17 a-g).

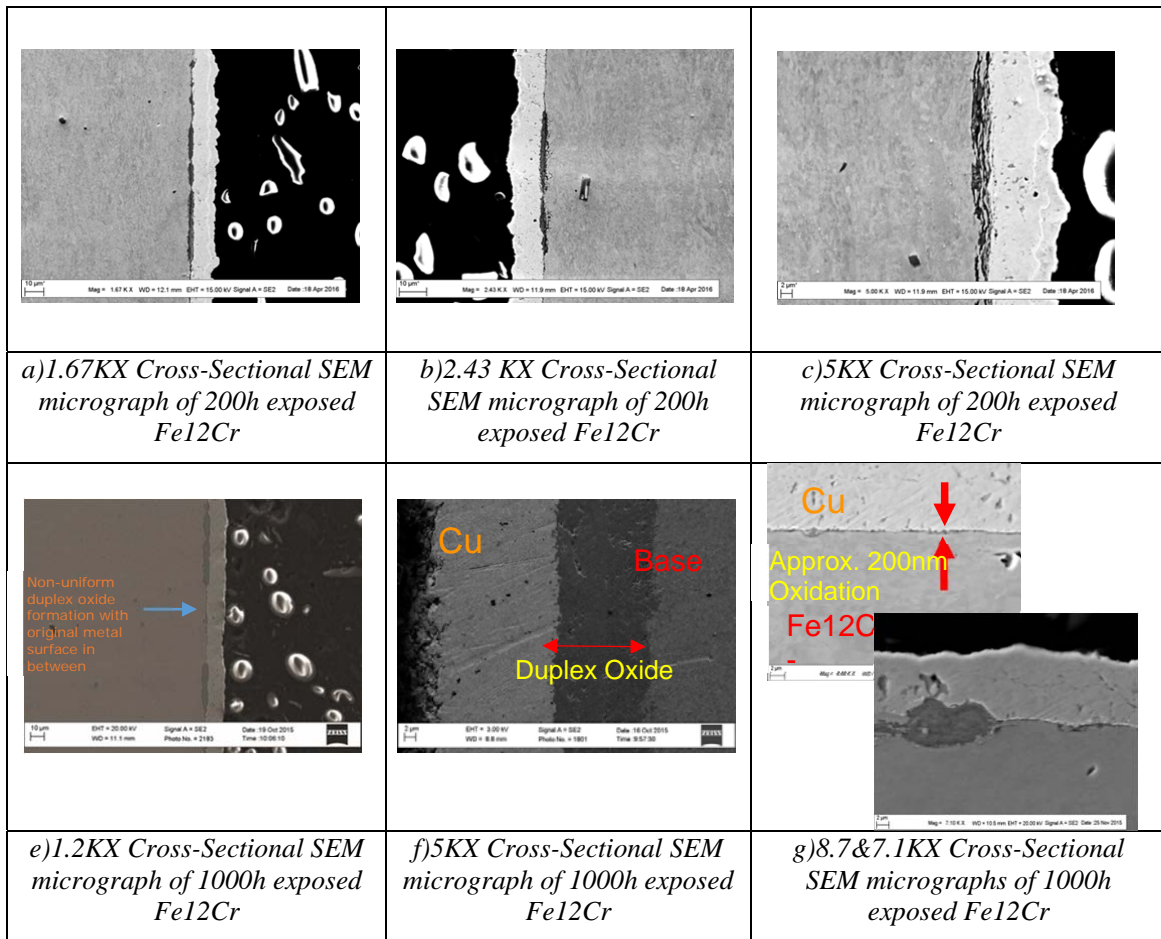
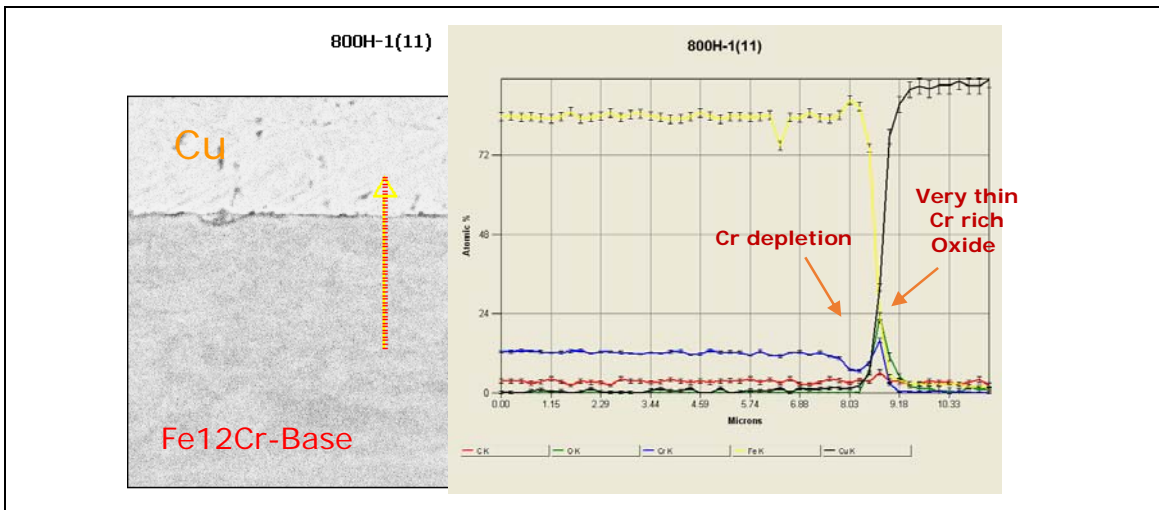


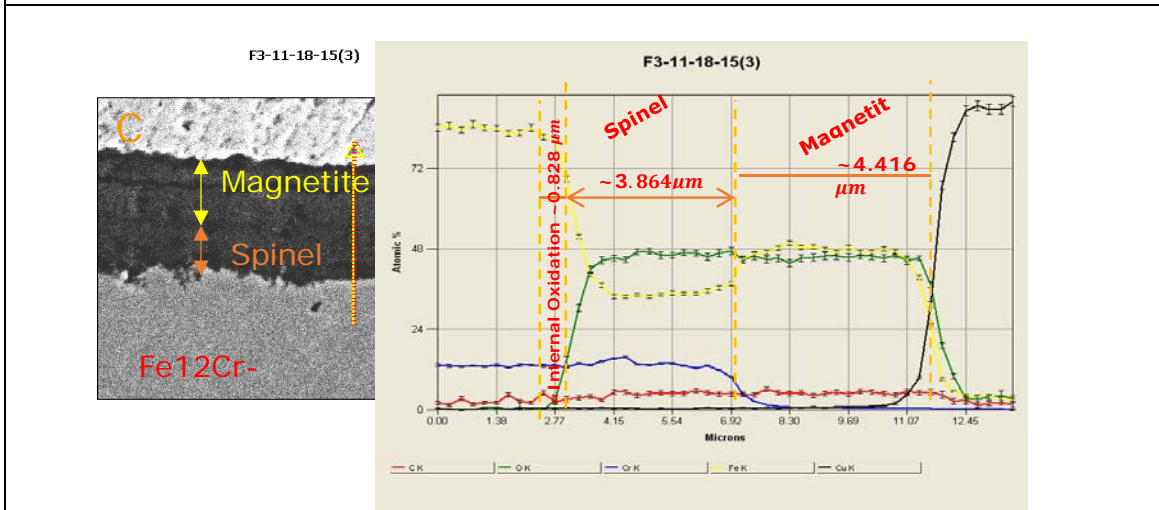
Figure 8.17: Cross-sectional SEM observations on oxide layer formed on Fe-12Cr alloy exposed for 1000h.

In figure 8.17 a-c) features initial stages (200 hours) of oxide formation as well as very thin protective oxide of Fe12Cr. For longer exposure durations (up to 1000h), in the regions adjacent to the base steel a very thin (approx. 200nm) oxide layer was observed which is most likely chromia while other regions exhibited a duplex oxide scale formation (figure 8.17f)).

EDS line scans were also performed in order to observe behavior of individual elements in the protective and duplex oxide regions. Figure 8.18 shows the SEM-EDS line-scan analyses performed on the regions with protective and duplex oxide scale formation. EDS line scan on the protective oxide region (figure 8.18-a) suggested a Cr depletion zone underneath a very thin surface oxide. The surface oxide was observed to be correspondingly very Cr rich. However, the EDS line scan performed across the regular oxide scale indicated duplex inner oxide layer that was Cr-rich. Thus the outer oxide layer was Fe-rich while the inner oxide layer was Cr-rich that the outer layer formed by the outward diffusion of Fe. The observations in figure 8.18e and Cr content in the sub-oxide layer (figure 8.18b), suggest that the inner layer was in the base steel.



a) Cross-Sectional SEM-EDS analyses on the protective regions of 600h exposed Fe12Cr steel.



b) Cross-Sectional SEM-EDS analyses on the duplex oxide regions of 1000h exposed Fe12Cr steel.

Figure 8.18: SEM-EDS line scan compositional analysis taken across the cross-section of the oxide layer for 1000h exposed T22 steel.

Results of cross-sectional analysis (by SEM, SEM-EDS, XRD, EPMA-WDS) of oxide corrosion product layers 9-12Cr alloys, T92 and T122, are shown in figure (8.19). Figure 8.19 presents the SEM micrographs and EDS analysis of 200 and 1000h exposed T122 samples. Figure 8.19a was taken on the two opposite surfaces of 200h exposed T122 where the oxide formation exhibits some difference in terms of oxide thicknesses. The main reason of this approximately 0.5 micrometer thickness variance, could be because the thicker surface interacts with the CO<sub>2</sub> first. EDS elemental mapping shown in figure 8.19b for 200h exposed sample shows duplex oxide formation, as expected. With longer exposure, the variance in oxide thicknesses of two opposite surface appears to decrease figure 8.19c, possibly due to the system achieving equilibrium in which the oxygen potentials are same on all the surfaces. The EDS line scan shown in figure figure 8.19c illustrates the duplex oxide formation where inner (spinel) layer is Cr-rich whereas outer layer (magnetite) is Fe rich.

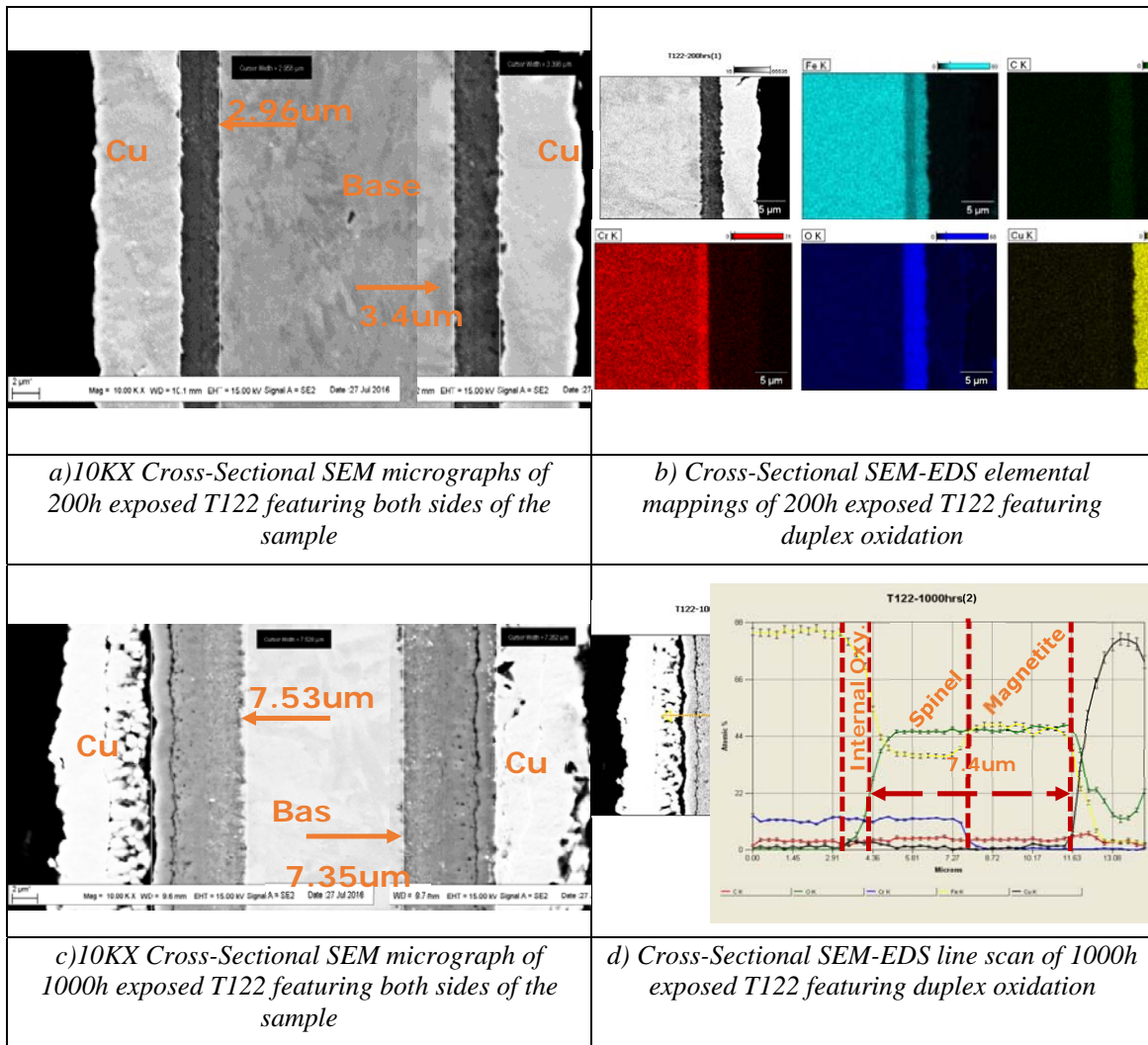


Figure 8.19: SEM and SEM-EDS analyses of 200 and 1000h exposed T122 featuring duplex oxide layer formation.

The figure 8.20 presents the SEM micrographs taken with 3kV and 10kV accelerating voltage on 600h exposed T92 steel along with EDS elemental analysis. The image taken with 3kV electron beam (figure (8.20a)) features the oxide surface in detail such that voids in the outer Fe-rich layer can be seen in addition to the interfaces between the oxide layers and even some oxide grains. Images taken with 15kV electron beam (figure 8.20b) presents compositional changes across base-alloy and the oxide.



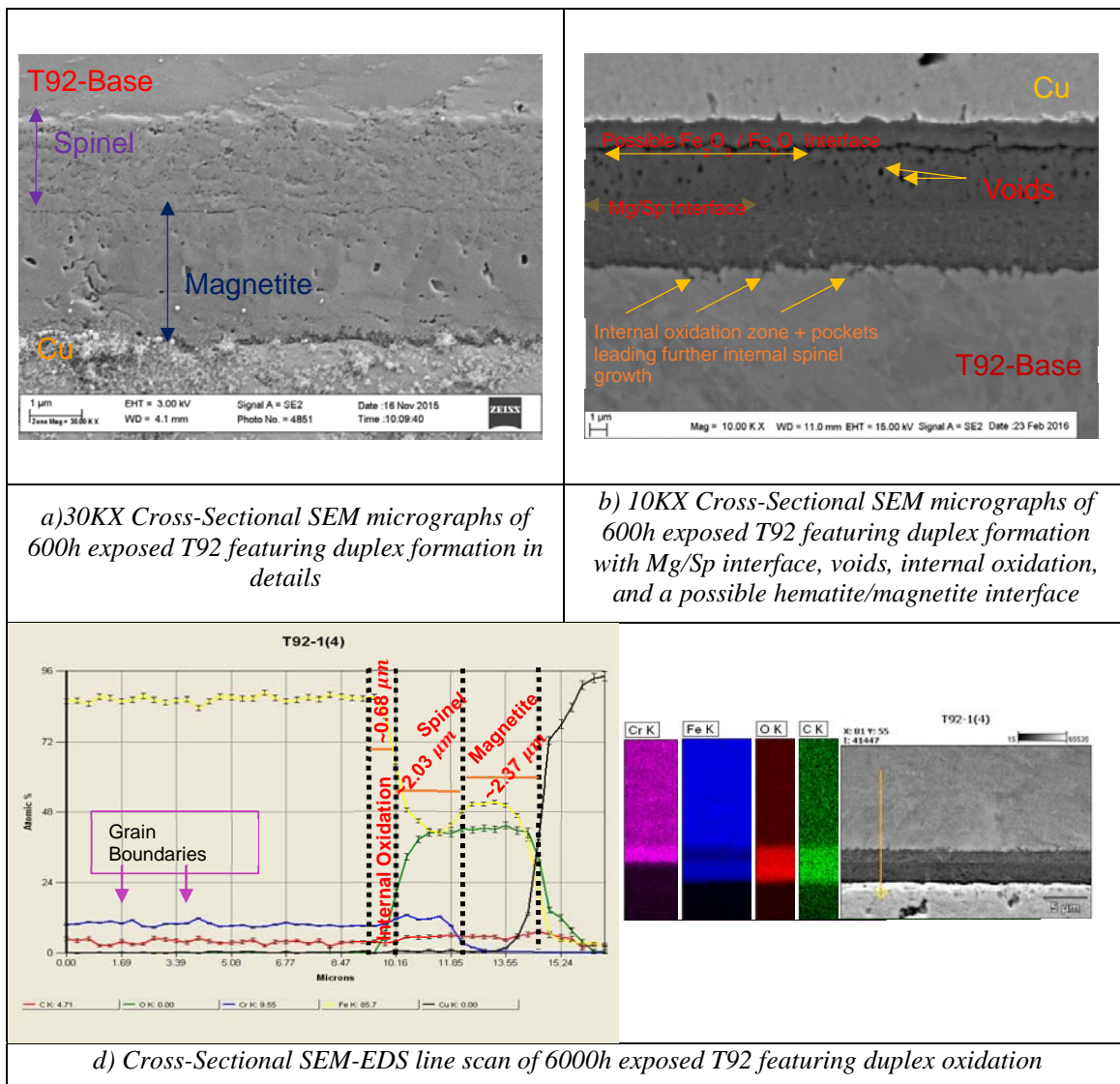


Figure 8.20: SEM and SEM-EDS analyses of 600h exposed T92 steel showing duplex oxide layer formation.

In addition, this image presents an additional interface within the outer oxide layer leading to the possibility of an outermost hematite layer (hematite can form as a result of reduction of magnetite). However, both EDS elemental mappings and line scan did not confirm any  $\text{Fe}_2\text{O}_3$  layer. Yet, further analyses were also performed since EDS is a semi-quantitative instrument. Regarding the oxide thickness variances on opposite surfaces, T92 steel showed results similar to pure Fe, and T122. The figure (8.21) presents the SEM micrographs taken on the opposite surfaces of 600 and 800h exposed samples. Significant differences in thicknesses were observed. This difference in thickness decreased with the increased exposure time.

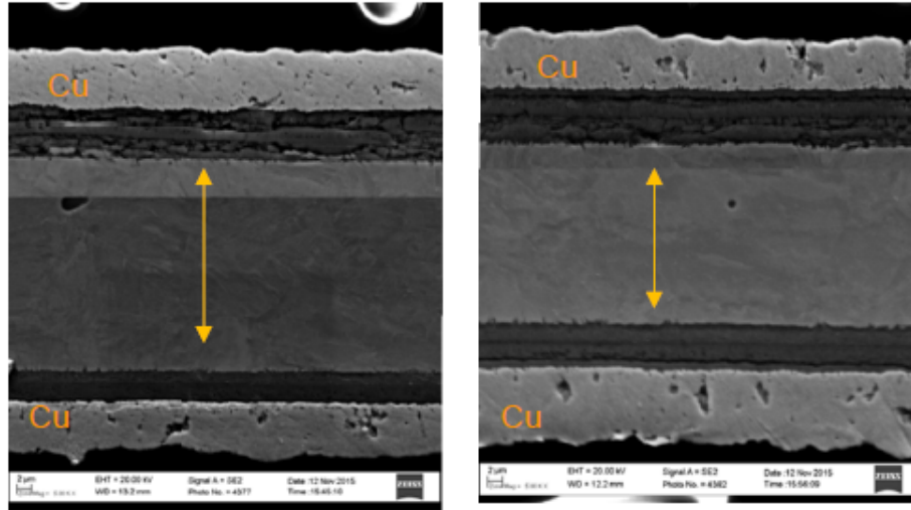


Figure 8.21: 5KX SEM micrographs of opposite surfaces of T92 samples (left is after 600h and right is after 800h exposure) featuring oxide thickness variances in opposite sides of the samples.

XRD analyses of T92 and T122 steels were also performed and presented in the following figures (8.22-23). For the case of T122, grazing incident small angle scattering of x-rays technique as well as full 2theta scans were employed. In order to present the relative locations, the XRD pattern by 2 and 4-degree incident beams are presented in the top section of the figure (8.22) where no spinel structure is evident based on Bragg angle. However, as the incident beam angle increased (in return the depth of penetration increases), the spinel phase appears. The magnetite peaks start to increase as the incident beam angle increases indicating that the magnetite layer is underneath an uppermost hematite layer. Regarding the spinel phase formations, both XRD patterns of T92 (Fig. 8.22) and T122 indicated  $\text{Cr}_x\text{Fe}_{(3-x)}\text{O}_4$  type formation with  $x=1.2$ . However, the more accurate value of  $x$  was determined later by means of EPMA-WDS analyses and mass balance calculations.

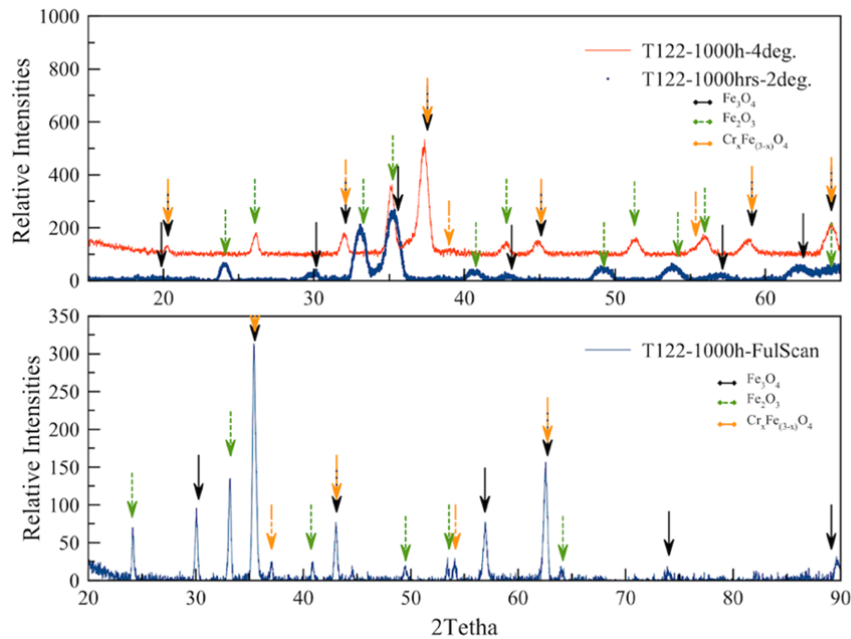


Figure 8.22: Grazing incident x-ray (top) and full range scan (bottom) results showing oxide phases that form on T122 steel surface.

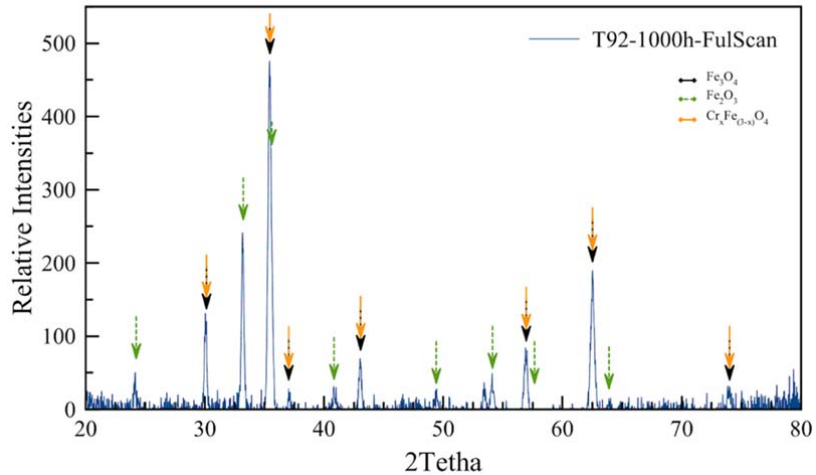
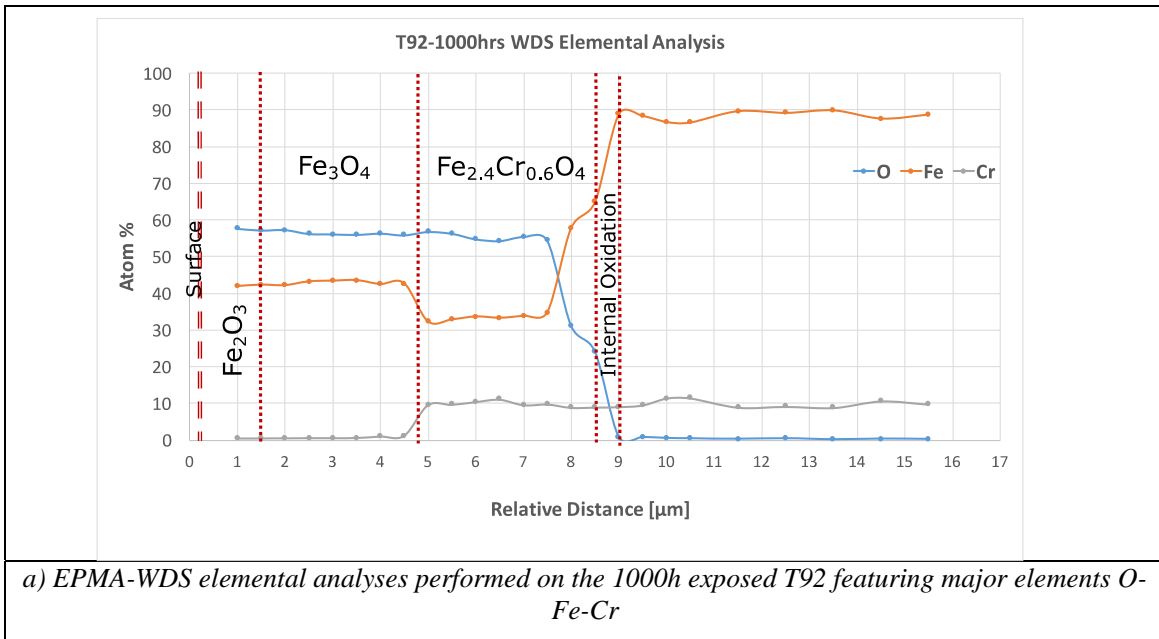
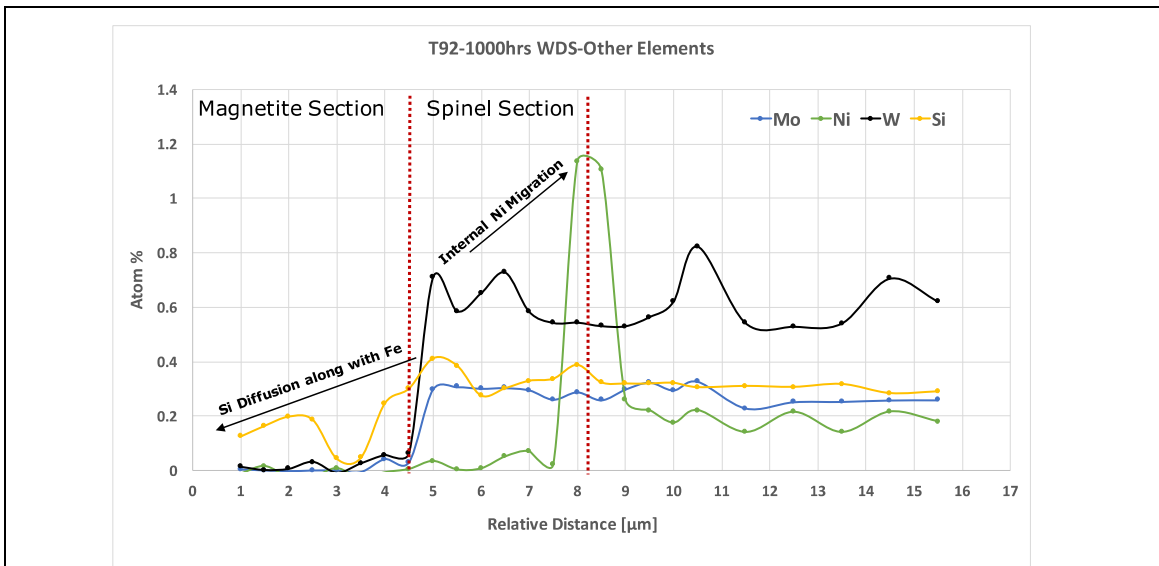


Figure 8.23: XRD full range scan results featuring showing oxide structures on T92 steel surface.

In order to acquire more quantitative data and determine the spinel stoichiometries formed on the inner oxide layer formed on T92 and T122 steel, EPMA-WDS analysis was employed, using 1000 hour exposed samples. The elemental distribution across the base steel to the oxide surface and the stoichiometric yields for each oxide layers, are given in the figures (8.24-25), respectively for T92 and T122. The WDS elemental profile on the T92-1000h exposed sample (figure (8.24a)) revealed that the inner Cr level is approximate as same as the original base metal content and, in addition, no Cr was detected in the outer oxide layer led the assumption that no Cr diffuses out and the inner oxide layer forms within the base metal.





b) EPMA-WDS elemental analyses performed on the 1000h exposed T92 featuring minor alloying elements Mo-Ni-W-Si

Element	Oxygen	Fe	Cr	$x$ in $(Fe,Cr)_xO_4$
Stoichiometric Values from Focused Beam	4 Assumed Value	2.23	0.57	2.80
Stoichiometric Values from Readings Inside the Spinel	4 Assumed Value	2.51	0.60	3.12
Averages	4 Assumed Value	2.37	0.59	2.96
Stdevs	-	0.20	0.03	0.23
Err	-	0.14	0.02	0.16

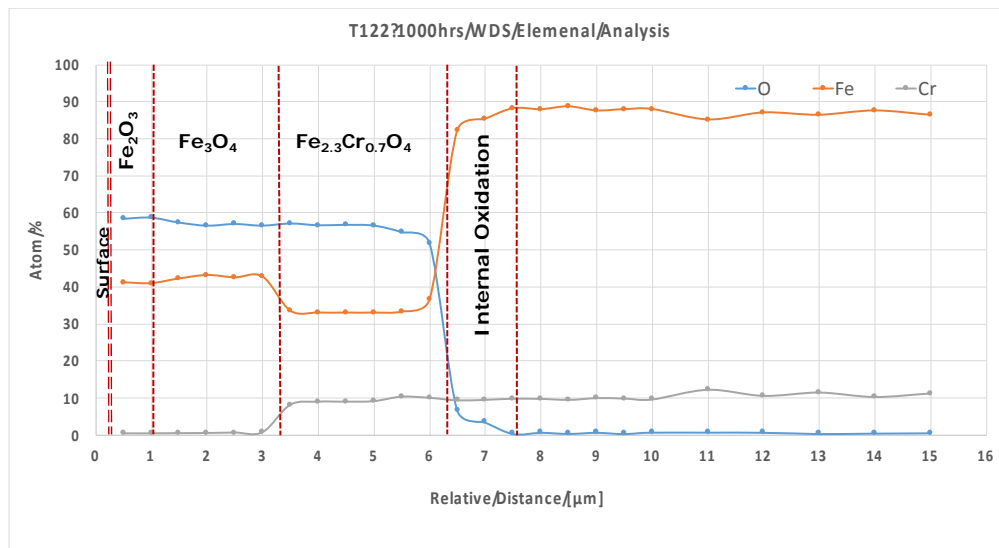
c) Stoichiometric Calculations based on the atomic % of Fe,Cr and O readings inside the spinel layer

Figure 8.24: EPMA-WDS analyses performed on the oxide cross-section of 1000h exposed T92 featuring compositional change through base steel to the oxide surface and spinel stoichiometry.

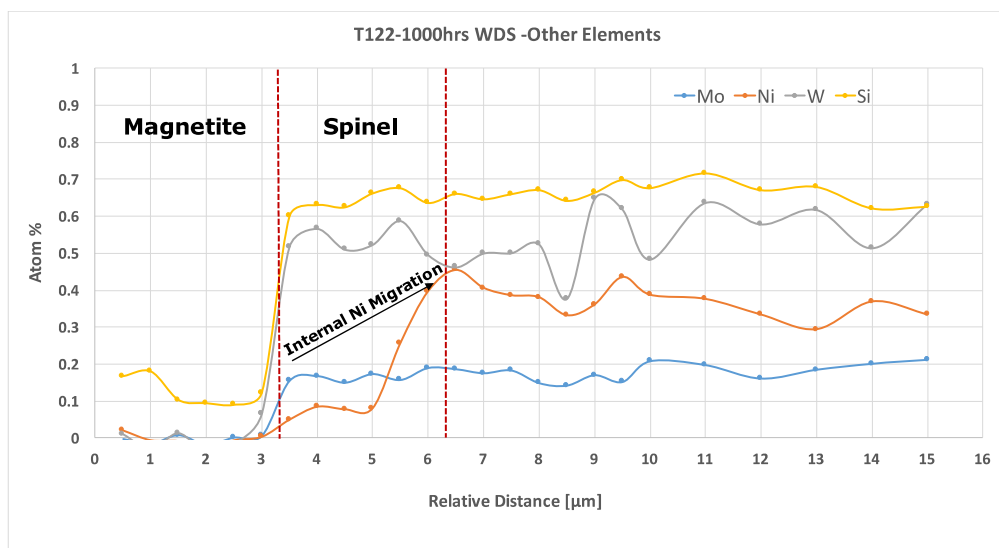
Referring to figure (8.24b), it was found that W, Mo, and Ni did not diffuse out and the concentrations of W and Mo in the inner oxide layer were approximately same as in the base steel. Ni content was found to accumulate at the oxide/metal interface. Si was detected in the outer magnetite layer indicating outer Si diffusion along with Fe. Regarding the stoichiometric assumptions, spinel with  $Cr_xFe_{(3-x)}O_4$  was previously detected by means of XRD. With the quantitative analysis of Cr, Fe and O data by means of WDS, the  $x$  value was further determined using obtained data in the inner spinel layer (data presented with figure 8.24-c). The total contents of Cr and Fe were approximated to be a quarter of the oxygen content. Therefore, the  $x$  value in  $Cr_xFe_{(3-x)}O_4$  was found 0.59 and approximated as 0.6. In terms of outer oxide layer, Fe/O ratio indicated the outermost layer to be hematite with a magnetite layer underneath.

The EPMA-WDS for the 1000h exposed T122 is shown in figure 8.25 with major alloying elements and oxygen (figure 8.25a)) and minor elements (figure 8.25b), and the data obtained on the spinel layer (figure 8.25c). As for T92 and other Fe-Cr ferritic steel, the Cr content in the inner spinel layer was found to be the same as the base alloy with no Cr outward diffusion. The outer layer was

again found to consist of an outermost hematite layer with a magnetite layer underneath.



*a) EPMA-WDS elemental analyses performed on the 1000h exposed T122 featuring major elements O-Fe-Cr*



*b) EPMA-WDS elemental analyses performed on the 1000h exposed T122 featuring minor alloying elements Mo-Ni-W-Si*



<i>Element</i>	<i>Oxygen</i>	<i>Fe</i>	<i>Cr</i>	<i>x in (Fe,Cr)<sub>x</sub>O<sub>4</sub></i>
<i>Stoichiometric Values from Focused Beam</i>	<i>4 Assumed Value</i>	<i>2.09</i>	<i>0.78</i>	<i>2.80</i>
<i>Stoichiometric Values from Readings Inside the Spinel</i>	<i>4 Assumed Value</i>	<i>2.43</i>	<i>0.67</i>	<i>3.12</i>
<i>Averages</i>	<i>4 Assumed Value</i>	<i>2.26</i>	<i>0.73</i>	<i>2.96</i>
<i>Stdevs</i>	<i>-</i>	<i>0.24</i>	<i>0.08</i>	<i>0.23</i>
<i>Err</i>	<i>-</i>	<i>0.17</i>	<i>0.06</i>	<i>0.16</i>

*c) Stoichiometric Calculations based on the atomic % of Fe,Cr and O readings inside the spinel layer*

*Figure 8.25: EPMA-WDS analyses performed on the oxide cross-section of 1000h exposed T122 featuring compositional change across the base steel and the oxide layer and the spinel stoichiometry.*

Regarding distribution of the minor elements in base steel and oxide layers, no outward diffusion of elements except Si was detected. This was observed for the T92 steel. In addition, an inward Ni migration was also observed for T122 steel. The stoichiometry of the inner spinel layer was identified to be  $\text{Cr}_x\text{Fe}_{(3-x)}\text{O}_4$  with x value determined to be 0.73 and approximated as 0.7.

#### **8.2.4. Oxide Thickness Measurements by Means of SEM-EDS Observations**

For all alloys containing Cr, an inner oxide Cr-rich oxide layer and an outer Fe-rich oxide layer(s) were observed. Even though pure Fe displayed inner oxidation, there were no significant compositional changes detected that would be indicative of a clear interface. Oxide layer thickness measurements were then performed using SEM-EDS line scan through which compositional changes were observed. The thickness measurements were performed with some assumptions which were also supported by the detailed visual inspection of the cross-section image by SEM. It was assumed that the magnetite layer begins where approximately no Cr present (less than approximately half of the initial content since the incoming characteristic x-ray signal volume is not perfectly controlled and always includes signals from rear and front of the intended location). Internal oxidation is marked by the region between where the Fe composition increases and where Cr composition begins to decrease (about half-way up of down these gradients, respectively) and where oxygen values decrease to below detection limits. Spinel layer is assumed to begin when the atomic oxygen content reaches approximately 20-25%. The gas/metal interface where outer magnetite layer ends, is marked by visual observations on the SEM-EDS micrographs where the bright oxide contrast ends and the Cu plating begins. As an example, these regions are shown for T92 steel from 600 hours exposure tests (Fig. 8.26)

Using data from figure 8.26, the total oxide layer thickness was determined to be 4.4  $\mu\text{m}$  composed of 2.37  $\mu\text{m}$  outer magnetite layer, 2.03  $\mu\text{m}$  spinel layer, and 0.68  $\mu\text{m}$  internal oxidation layer. With these assumptions, all the thickness measurements were performed at, at least 5-7 different locations. To maintain consistency, regions with crack-blister formation or oxide spallation were avoided. A sample data for the thickness measurements on 400h exposed T92 steel is presented in Table (8.1)

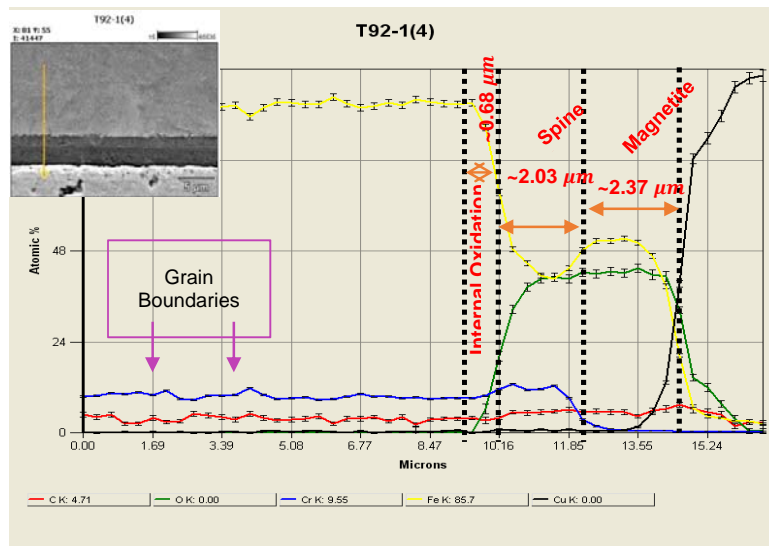


Figure 8.26: Various oxide layer regimes as measured by SEM EDS analysis for 600h tested T92 steel.

Table 8.1: Sample oxide thickness measurements using SEM-EDS for 400hour exposure T92 steel.

<b>T92-5 400hrs</b>	<b>EDS 1 μm</b>	<b>EDS 2 μm</b>	<b>EDS 3 μm</b>	<b>EDS 4 μm</b>	<b>EDS 5 μm</b>	<b>EDS 6 μm</b>	<b>EDS 7 μm</b>	<b>Average μm</b>	<b>SDEV μm</b>	<b>St.Err μm</b>
<b>Spinel</b>	2.30	2.55	2.38	2.63	2.75	2.49	2.68	2.54	0.16	0.06
<b>Magnetite</b>	3.07	2.72	2.89	2.88	2.88	2.62	3.09	2.88	0.17	0.06
<b>Total (except internal)</b>	5.38	5.27	5.27	5.51	5.63	5.11	5.77	5.42	0.23	0.09
<b>Internal Oxidation</b>	0.58	0.51	0.68	0.66	0.92	0.66	0.82	0.69	0.14	0.05
<b>Spnl/Mgnt Ratio</b>	0.75	0.94	0.82	0.91	0.95	0.95	0.87	0.89	0.08	0.03

Figures 8.27 presents the total oxide thicknesses formed during testing at 450 °C in 20 MPa CO<sub>2</sub>. The oxide thickness development of T92 steel, showed a slight dip after 600 hours exposure however no spallation was observed in this sample. Generally, the overall trend, excluding 600h, presented in the figure 8.27 indicates a parabolic growth for all Cr-containing steels. Based on data for oxide thickness measurements, T122 steel exhibits the best corrosion resistance. T22 steel exhibits a slight decrease in oxide thickness which is assumed to be due to spallation.

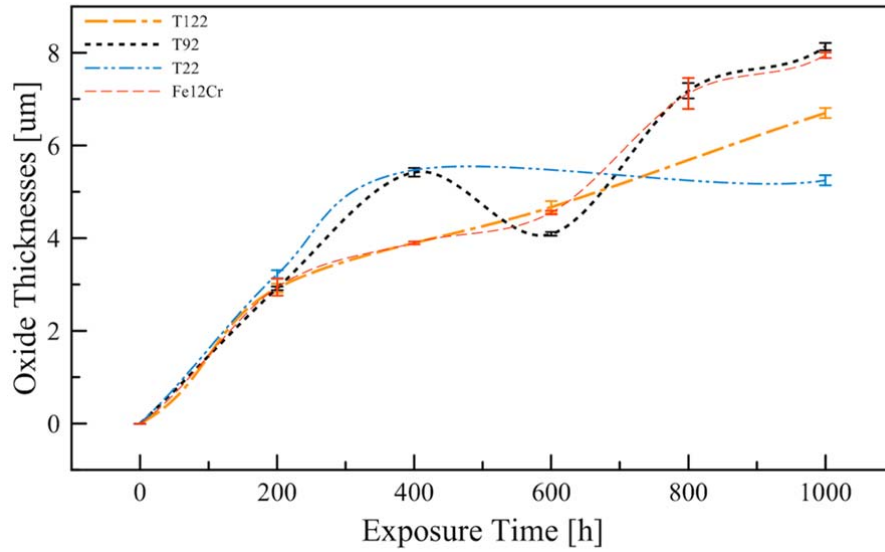


Figure 8.27: Oxide thickness development on ferritic-martensitic steels tested at 450 °C in 20Mpa CO<sub>2</sub> for up to 1000h.

As discussed earlier, the inner layer growth is governed by the available space model discussed earlier. However, recently Martinelli L et. al., reviewed the formation mechanism of inner spinel oxide formation using a global mass balance approach through outer Fe cation diffusion in a three-part publication titled as “Oxidation mechanism of an Fe–9Cr–1Mo steel by liquid Pb–Bi eutectic alloy at 470 °C”. This approach was adapted in this study to further develop a theory for oxide growth mechanisms. Using mass balance between inner and outer oxide layers the stoichiometric value of Cr is determined as:

$$x = 3 \frac{\left(1 + \frac{h_{\text{Magnetite}}}{h_{\text{Spinel}}}\right)}{\left(1 + \frac{C_{\text{Fe}}^{\text{Base}}}{C_{\text{Cr}}^{\text{Base}}}\right)} \quad (8.1)$$

where  $C_{\text{Fe-Cr}}^{\text{Base}}$  denotes the molar concentration of labeled species in the base steel, and  $h$  denotes the individual thicknesses of oxide layers.  $x$  is the stoichiometric value of Cr in  $\text{Cr}_x\text{Fe}_{(3-x)}\text{O}_4$  spinel compound which determined by XRD analyses.

For the materials tested in this study, the individual oxide layer thicknesses were measured and the spinel-to-magnetite ratios were recorded. Figure 8.28 presents these ratios and their averaged values through 1000h of exposure. The important observation from this figure is that the spinel-to-magnetite ratios (Sp/Mg), increased as the initial Cr content of the base alloy and this ratio remains reasonably constant as a function of exposure time.

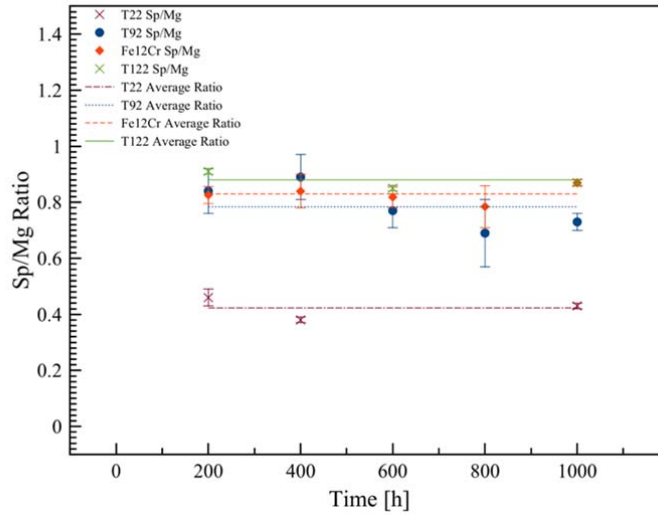


Figure 8.28: Measured Sp/Mg ratios of ferritic-martensitic steels tested at 450 °C and 20Mpa CO<sub>2</sub> as a function of exposure time.

The average values of ratios were found as 0.42, 0.78, 0.83, 0.88 with respect to T22(2Cr), T92(9Cr) Fe12Cr, and T122(12Cr). For these steels with varying Cr and Fe molar concentrations, the x value in the spinel stoichiometry of Cr<sub>x</sub>Fe<sub>(3-x)</sub>O<sub>4</sub> were determined using the equation (8.1) to be approximately 0.15, 0.6, 0.78, 0.7 for T22, T92, Fe12Cr, and T122 respectively.

The global mass balance, for which the molar volume of magnetite  $V_{Fe_3O_4}$  and  $V_{Cr_xFe_{(3-x)}O_4}$  (cm<sup>3</sup>/mol) are similar, indicates the following:

$$h_{\text{Consumed}} = \frac{1}{C_{\text{Fe}}^{\text{Base}} V_{Fe_3O_4}} \{ (3 - x) h_{\text{Spinel}} + 3 h_{\text{Magnetite}} \} \quad (8.2)$$

where the consumed metal thickness can be represented in terms of measured spinel and magnetite thicknesses. With the further assumption that  $h_{\text{Consumed}} = h_{\text{Spinel}}$  the following relation, just in terms alloy composition, is approximated as follows:

$$h_{\text{Spinel}} = \frac{C_{\text{Fe}}^{\text{Magnetite}}}{C_{\text{Fe}}^{\text{Base}} - C_{\text{Fe}}^{\text{Spinel}}} h_{\text{Magnetite}} \quad (8.3)$$

with above equations (8.3), the spinel thickness calculated and compared with measured values by SEM-EDS. Figure 8.29 presents all three of these measurements/calculations with for each experimental data available.

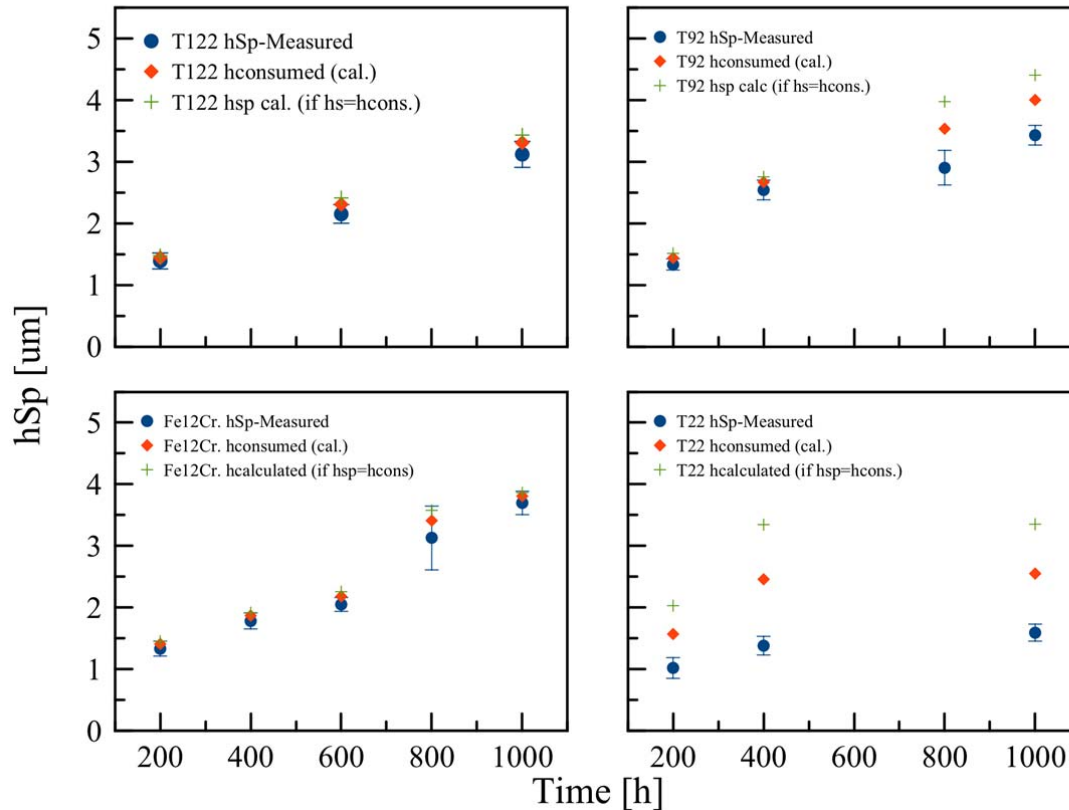


Figure 8.29: Spinel oxide layer thickness measurements and calculations of each duplex oxide forming steels investigated in this study.

The close agreement between values obtained from equation (8.3) and experimental values obtained by SEM-EDS measurements indicates that oxidation is indeed occurring through the available space model. The figure 8.29 indicates that for T122 and Fe12Cr, the agreement is very close, however, T92 steel displayed some deviations from expected values, particularly for 800h and 1000h exposure an effect that may be attributed to some cracking. However, the other three data point showed perfect match indicating oxidation occurs through available space for T92 as well. As for the comparison of the values obtained for T22, no match for all the available data points were found indicating no global mass balance between the inner and outer oxide layers. In terms of the validity of the global mass balance between the layers, other approaches employed will be discussed in the next chapter.

### 8.2.5 Weight Gain Measurements of Ferritic-Martensitic Alloys in S-CO<sub>2</sub>

Figure 8.30 shows the weight gain measurements for the steels as a function of exposure time.



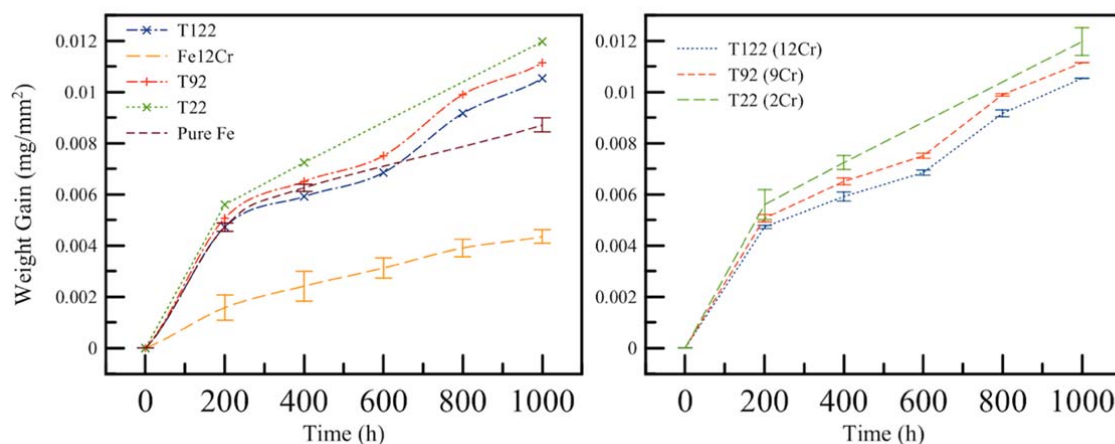


Figure 8.30: Weight gain measurements for ferritic-martensitic alloys investigated in this study.

In order to understand the oxidation behavior of T22, T92, and T122 steels with increasing Cr content, a separate plot is presented in the right side of the figure 8.30 where decreasing weight gain with respect to increased Cr content can be seen. The T22 steel which contains the least amount of Cr exhibited the highest weight gain while the T122 alloy which has the highest Cr content exhibited the least gain. The Fe12Cr binary alloy, exhibited the least weight gain even compared to T122 steel which contains about the same amount of Cr. The reason for this could be the nodular oxide formation observed on the Fe12Cr surfaces. A very thin (as low as 200 nm) protective chromia layer was observed to form adjacent to these nodules. Also, the standard deviation of the weight gain measurements of Fe12Cr was higher and tended to decrease with the increased exposure time indicating both decrease trend in the protective portion of the surface and variation in the formation of nodules sample to sample. One important observation is that the weight gain of pure Fe in S-CO<sub>2</sub> is lower than all engineering alloys tested. These results may be regarded as an artifact and likely caused by oxide spallation observed in pure Fe.

### 8.2.6. Summary of the Chapter

In this chapter, experimental observations of oxidation behavior of ferritic-martensitic steels of interest in 450 °C 20Mpa CO<sub>2</sub> along with theoretical approaches to predict oxidation were presented. The oxide layers developed were characterized in detail using SEM-EDS analysis, XRD, and EPMA-WDS techniques. All Cr containing alloys exhibited a duplex oxide layer structure with an outer Fe-rich magnetite oxide layer and an inner Cr-rich spinel oxide layer. The ratio of thickness of the spinel-and-magnetite remained constant over the range of exposure times over which the tests were performed. This ratio also increased with Cr content of the alloy. Very good agreement was observed between the experimentally measured values and those predicted using the mass balances and the available space model.

### 8.3. Modeling of Duplex Oxide Growth on Ferritic-Martensitic Steels using Available Space Model

As demonstrated the previous chapter, the oxide growth on ferritic-martensitic steels are duplex in nature made up of the outer Fe-oxide (mostly magnetite) layer and in inner Cr-rich spinel oxide layer. Nano channels play an important role in the development of these layers by providing a path for the environmental oxidant species to the base steel substrate. The outer layer forms by outward Fe-cation diffusion and surface reactions. Previous literature has shown that in many oxidizing environments such a duplex oxide layer formation is supported mass balance calculations, between the outer and inner layers. Furthermore, it has been shown that this global mass balance persists throughout the oxidation process once an equilibrium is established with the rate limiting step being the diffusion of

iron cations from the spinel layer to the outer layer.

### 8.3.1 Extrapolation of Iron Diffusion Coefficients in Magnetite and Spinel

Since there is a fixed global mass balance between the layers, spinel oxide layer thickness can be estimated as a function of magnetite layer thickness according to the following equation:

$$h_{\text{Spinel}} = \frac{C_{\text{Fe}}^{\text{Magnetite}}}{C_{\text{Fe}}^{\text{Base}} - C_{\text{Fe}}^{\text{Spinel}}} h_{\text{Magnetite}} \quad (8.4)$$

The magnetite layer growth is controlled by iron diffusion through the oxide scale first through the spinel layer and then the magnetite layer. Therefore, the iron diffusion coefficients in spinel and magnetite are required for the modeling of oxide growth.

Iron diffusion coefficient in magnetite in the temperature range 900 and 1400 °C has been discussed by Ricoult B. M. and Dieckmann R.. In addition, Atkinson A. et al., have shown successful extrapolation of the relationship to lower temperatures. Therefore, the extrapolation results by Atkinson A. et al., of the relationship provided by Ricoult B. M. and Dieckmann R. for the iron diffusion in magnetite will be used for modeling our results at 450°C.

$$D_{\text{Fe}}^{\text{Mg}}(T) = \frac{A a_{\text{O}_2}^{2/3}}{12(1 + 2K_V a_{\text{O}_2}^{2/3})} + \frac{4B}{3} a_{\text{O}_2}^{2/3} \quad (8.5)$$

In above relationship,  $A = D_V K_V$  and  $B = D_I K_I$  where  $D [cm^2 s^{-1}]$  denotes the diffusion coefficients for vacancy and interstitial according to sub-labels V and I, respectively and  $K$  with the same sub-labels denotes the equilibrium constants for formation of vacancy and interstitial sites.

In terms of temperature dependence,  $D_V$ ,  $D_I$ ,  $K_V$  and  $K_I$  are expressed as:

$$D_V = 0.177\eta \exp\left(\frac{-14000}{T(K)}\right) + 1.16 \times 10^{-3}(1 - \eta) \exp\left(\frac{-8760}{T(K)}\right) \quad (8.6)$$

where  $T(K)$  is temperature in Kelvin degree and  $\eta$  is provided with the following relation:

$$\eta = \left( \frac{1}{1 + 3 \times 10^{-3} \exp\left(\frac{11900}{T(K)}\right)} \right) \quad (8.7)$$

$$D_I = \frac{1.22 \times 10^6 \exp\left(\frac{-27700}{T(K)}\right)}{[1 + 1.56 \times 10^6 \exp\left(\frac{-20100}{T(K)}\right)]} \quad (8.8)$$

$$K_V = 2.04 \times 10^{-7} \exp\left(\frac{27100}{T(K)}\right) \quad (8.9)$$

$$K_I = 1.93 \times 10^3 \exp\left(\frac{-43140}{T(K)}\right) + 3.01 \times 10^9 \exp\left(\frac{-63270}{T(K)}\right) \quad (8.10)$$

where  $a_{\text{O}_2}^0 = \frac{P_{\text{O}_2}}{P_{\text{O}_2}^0}$  and  $P_{\text{O}_2}^0 = 1 \text{ bar}$ .

Regarding the nature of duplex oxide formation, one can see that the iron flux in magnetite is strongly related to the iron flux in spinel and therefore iron diffusion in spinel. This dependence can be discussed in the context of experimental measurements of iron diffusion coefficient in spinel performed by Topfer J. et al. Using radioactive isotopes, Topfer J. et al. have determined the cation diffusion coefficients in  $(\text{Cr}_x\text{Fe}_{(1-x)})_{3-8}\text{O}_4$  for  $x=0.1, 0.2, 0.33, 0.4$ , and  $0.5$ . From our experimental studies of spinel formation for T22, T92, T122, and Fe12Cr presented in the previous chapter,  $x=0.2$  value was determined to be is an exact match for the oxidation results of T92 alloy. However, it is possible to extrapolate the experimental data for various  $x$  values ( $x$  in spinel stoichiometry) by using the experimental data by Topfer J. et al. The following table presents this data of partial tracer diffusion coefficients at 1200 °C.

Table 8.2: Partial tracer diffusion coefficients obtained at 1200 °C for various spinel stoichiometry [Topfer et al].

<i>Experimental Data by Topfer J. et al.</i>						
$x$ in $(Cr_xFe_{(1-x)})_3O_4$	0	0.1	0.2	0.33	0.4	0.5
$3x$	0	0.3	0.6	0.99	1.2	1.5
$\log [V]^o$	0.699	0.644	0.649	0.544	0.467	0.487
$\log [I]^o$	-8.495	-9.38	-9.65	-10.5	-10.65	-10.49
$\log [D_{Fe}^o] [V]$	-5.44	-4.94	-5.67	-5.77	-5.31	-
$\log [D_{Fe}^o] [I]$	-14	-14.9	-14.58	-15.56	-15.65	-
$\log [D_{Cr}^o] [V]$	-8.06	-7.71	-8.14	-8.38	-8.41	-
$\log [D_{Cr}^o] [I]$	-16.9	-17.16	-17.76	-18.5	-18.78	-

Where  $D_{Fe}^o$  are the partial tracer diffusion coefficients normalized to  $a_{O_2} = 1$ . The oxygen dependence of  $D_{Fe}$  can be determined by the following equation:

$$D_{Fe} = D_{Fe[V]} + D_{Fe[I]} = D_{Fe[V]}^o a_{O_2}^{2/3} + D_{Fe[I]}^o a_{O_2}^{-2/3} \quad (8.11)$$

By using the equation (8.11), the iron diffusion coefficient in various spinel stoichiometry can be plotted as a function of oxygen activity.

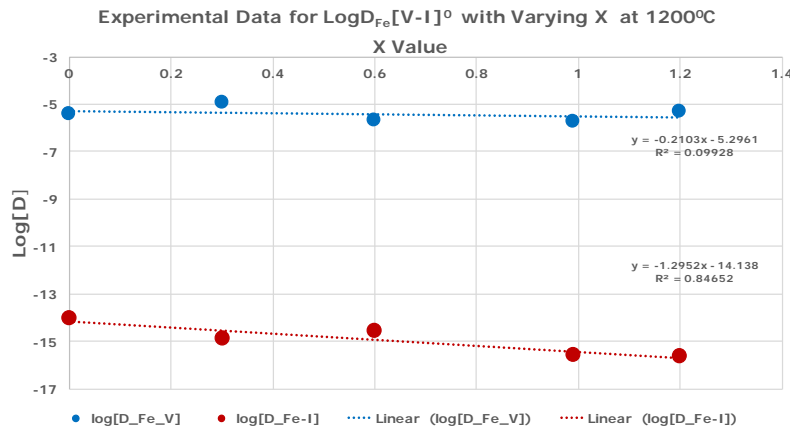


Figure 8.31: Partial iron diffusion coefficients for various spinel stoichiometry at 1200 °C.

It is further noted that the deviations from the stoichiometry,  $\delta$ , will be ignored despite its oxygen activity dependence since its value is very small (approx.  $10^{-3}$ ) and tends to further decline in lower oxygen activities. Regarding partial diffusion coefficients as a function of  $x$  (i.e., in  $Cr_xFe_{(3-x)}O_4$ ) a linear relation is observed from the data presented in Table 8.2 and plotted in figure 8.31. This linear fit approximates well the diffusion through interstitials. Despite the lower confidence of the fit for diffusion through vacancies, this stoichiometric dependence along with the oxygen activity dependence have been used to establish the partial diffusion relationships as a function of both spinel stoichiometry and oxygen activity.

As presented in figure 8.32, the extrapolation is valid for the diffusion via interstitials rather than the diffusion via vacancies. The extrapolated values for  $x=0.7$  spinel is located between the experimental values for  $x=0.6$  and  $x=0.99$ . Despite over estimation for diffusion via vacancies (due to lower confidence of fit), the difference can be ignored. One other observation is that for decreasing values of  $x$ , the diffusion coefficient of iron in spinel approaches the diffusion coefficient of iron in magnetite (i.e. as spinel composition in theory converges to magnetite composition).

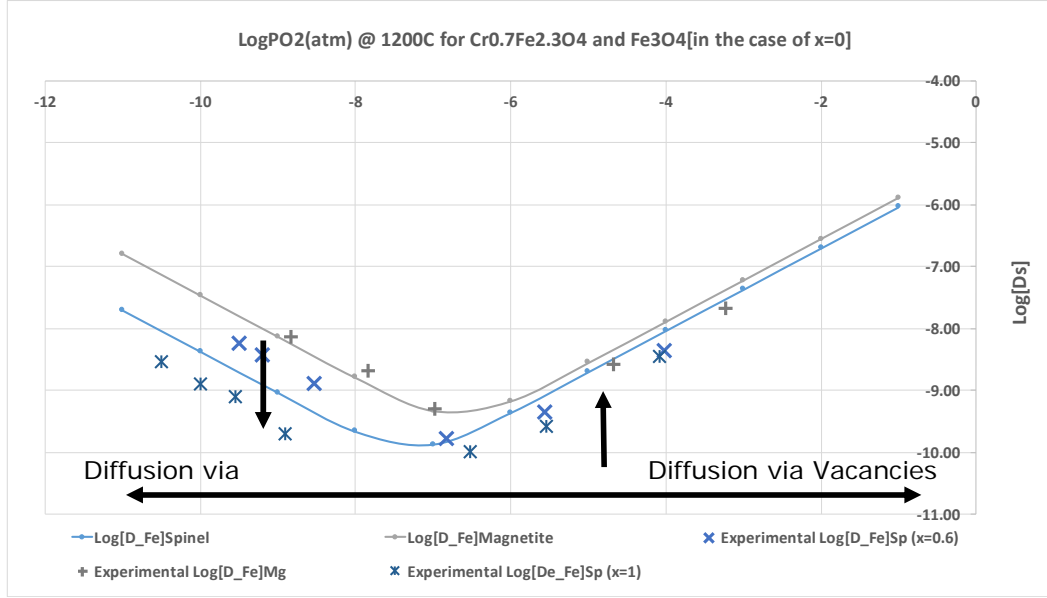


Figure 8.32: Calculated and experimentally determined partial iron diffusion coefficients via interstitials and vacancies at 1200 °C.

From equation 8.6 and the experimental values by Topfer J. et al, it is obvious that there are diffusion mechanisms through vacancies and through interstitials since  $A = D_V K_V$  and  $B = D_I K_I$ . However, what is more important is that the linear relationship exists between diffusion coefficients of iron in magnetite and spinel for both interstitial and vacancy approaches. This relationship has been shown to be promising in modeling of Fe-Cr steel corrosion with the assumption that the relationship has no temperature dependence. In other words, the relationship is assumed to be conserved in the case of extrapolation of iron diffusion in magnetite to lower temperatures such as 450 °C by equation 8.6. The relation is given as:

$$D_{Fe}^{Sp}(T) = \frac{D_{Fe}^{Sp}(V, 1200\text{ }^{\circ}\text{C})}{D_{Fe}^{Mg}(V, 1200\text{ }^{\circ}\text{C})} D_{Fe}^{Mg}(V, T) + \frac{D_{Fe}^{Sp}(I, 1200\text{ }^{\circ}\text{C})}{D_{Fe}^{Mg}(I, 1200\text{ }^{\circ}\text{C})} D_{Fe}^{Mg}(I, T) \quad (8.12)$$

where  $\frac{D_{Fe}^{Sp}(V, 1200\text{ }^{\circ}\text{C})}{D_{Fe}^{Mg}(V, 1200\text{ }^{\circ}\text{C})} = bV$  and  $\frac{D_{Fe}^{Sp}(I, 1200\text{ }^{\circ}\text{C})}{D_{Fe}^{Mg}(I, 1200\text{ }^{\circ}\text{C})} = bI a_{O_2}^{aI}$  are the ratio of iron diffusion coefficient through vacancies and interstitials in spinel with respect to magnetite respectively based on the experimental results by Topfer J. et al., at 1200 °C. According to this relation (equation (8.12)), the iron diffusion in  $x=0.6$  spinel, based on the experimental data points, is the following:

$$D_{Fe}^{Sp}(T) = 0.7 D_{Fe}^{Mg}(V, T) + 0.71 a_{O_2}^{0.04} D_{Fe}^{Mg}(I, T) \quad [81] \quad (8.13)$$

For the purposes of modeling oxidation for T92 this relation may be employed since the calculated and experimental spinel stoichiometries matches with the experimental data given by Töpfer J. et al. For the other alloys, T22 and T122, and Fe12Cr different stoichiometric spinel structures are present and there are no experimental values for our knowledge literature. Thus, previously presented fit obtained from tracer diffusion experiments by Töpfer J et al., will be used. In addition, comparisons will be made for the experimental relations and the relations obtained from the fit. Using the fit presented in figure (8.31), the following relationships have been obtained for T22, T92, and T122 with  $x=0.2$ ,  $0.6$ ,  $0.7$  respectively. Note that since the  $x$  values for Fe12Cr and T92 are the same (from P-B relations), the relationships are also identical.

$$D_{Fe}^{Sp(x=0.2)}(T) = 0.9 D_{Fe}^{Mg}(V, T) + 0.59 a_{O_2}^{1.32e-2} D_{Fe}^{Mg}(I, T) \quad (8.14)$$

$$D_{Fe}^{Sp(x=0.6)}(T) = 0.71 D_{Fe}^{Mg}(V, T) + 0.22 a_{O_2}^{5.55e-2} D_{Fe}^{Mg}(I, T) \quad (8.15)$$

$$D_{Fe}^{Sp(x=0.7)}(T) = 0.81D_{Fe}^{Mg}(V, T) + 0.18a_{O_2}^{7.91e-2}D_{Fe}^{Mg}(I, T) \quad (8.16)$$

In order to obtain the above relationships, the following fits were used while noting the oxygen activity dependence for the interstitial part. The linear relations for each case ( $x=0.2$ ,  $0.6$ , and  $0.7$ ) is present in figure 8.33-36.

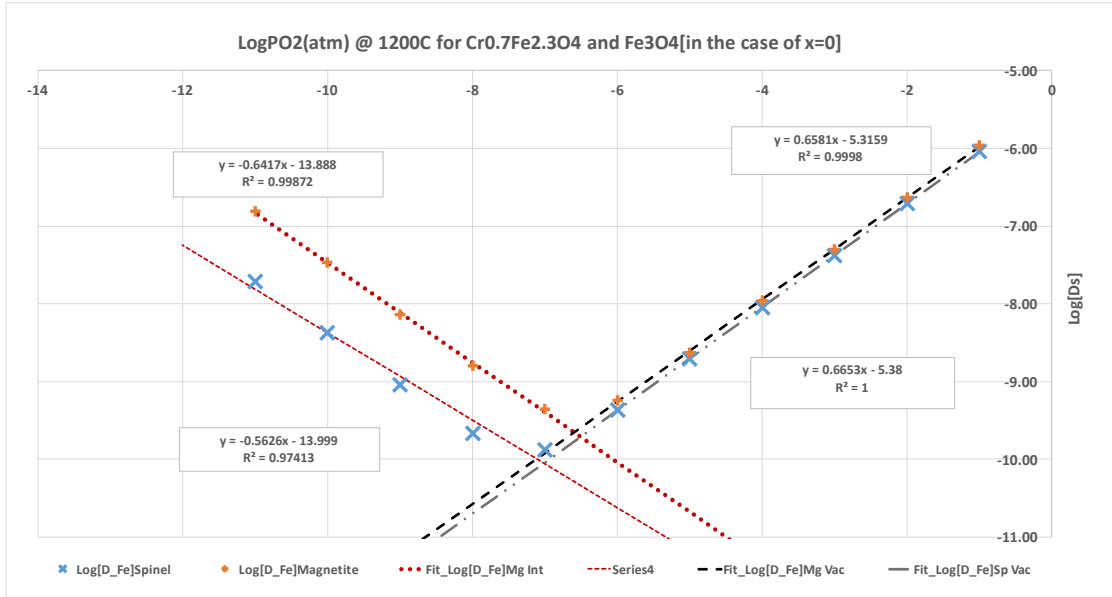


Figure 8.33: Linear relationships of vacancy and interstitial diffusion coefficients for  $x=0.7$  at  $1200^\circ\text{C}$ .

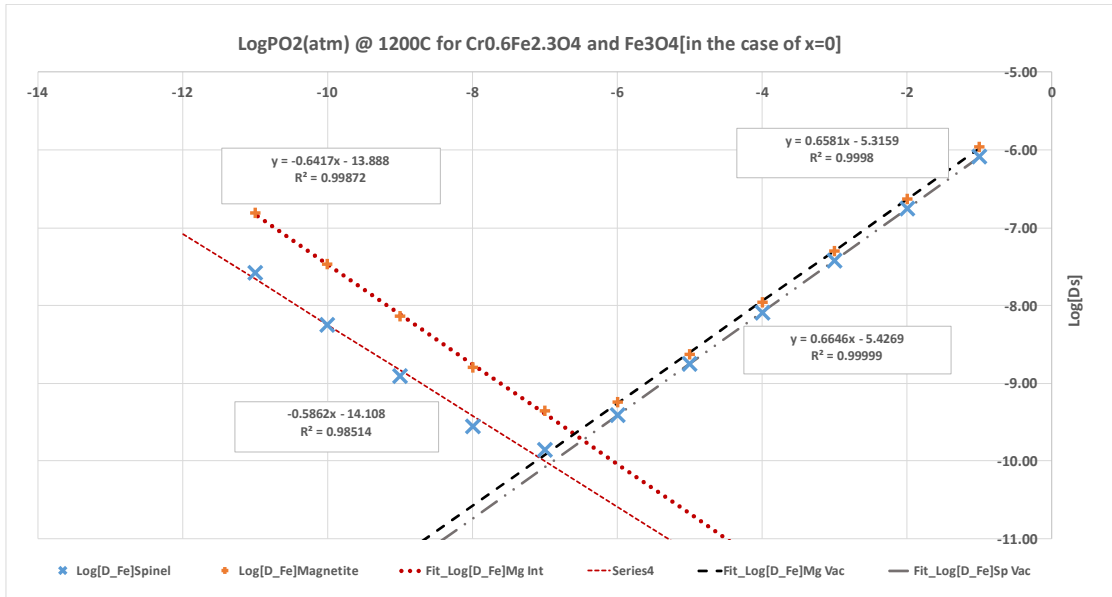


Figure 8.34: Linear relationships of vacancy and interstitial diffusion coefficients for  $x=0.6$  at  $1200^\circ\text{C}$ .



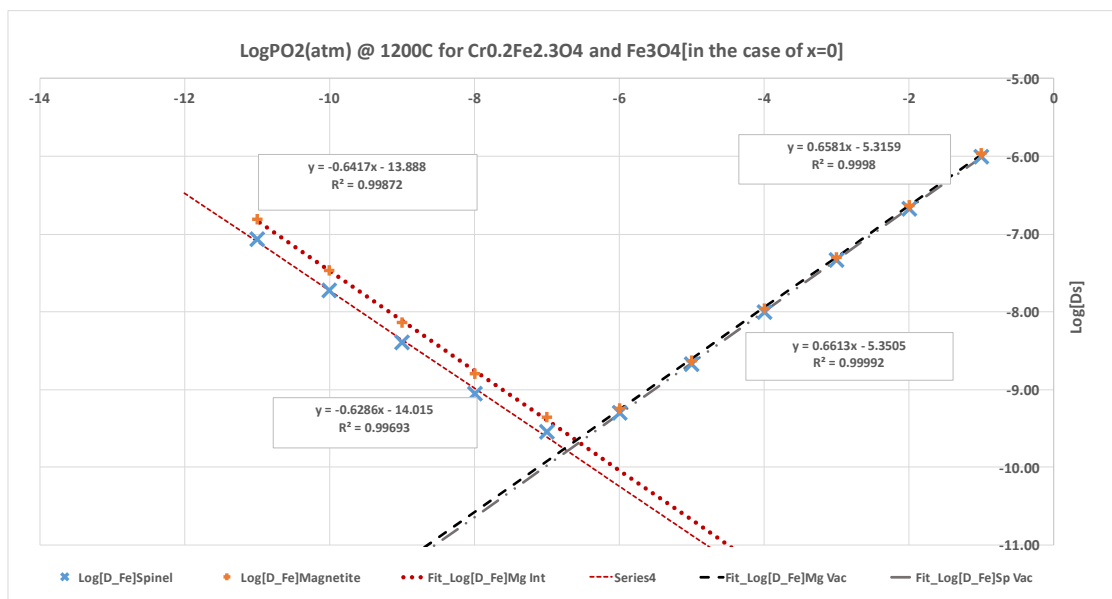


Figure 8.35: Linear relationships of vacancy and interstitial diffusion coefficients for  $x=0.2$  at  $1200^{\circ}\text{C}$ .

Once the relationships are obtained, the iron diffusion coefficients in spinel with  $x=0.6$  from the experimental values by Topfer J. et al., were compared with the result obtained from the equation 8.15 for  $x=0.6$  spinel. The results given in figure (8.32) present a perfect match for the diffusion via interstitials. However, as the fit in figure 8.31 demonstrated lack of confidence for the vacancy part, diffusion via vacancies are deemed as overestimations.

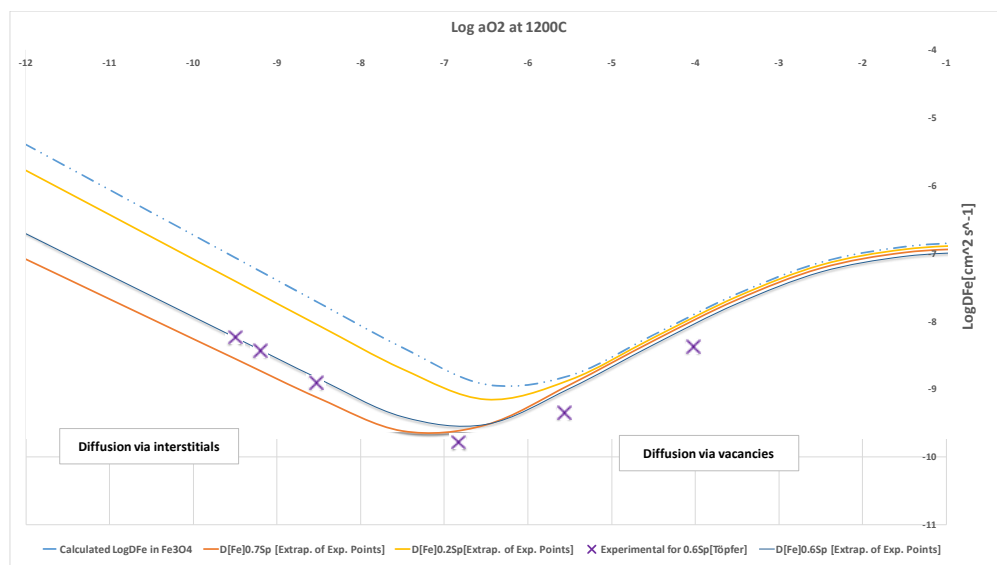


Figure 8.36: Extrapolated diffusion coefficients of iron in spinel with various stoichiometry based on calculated iron diffusion in magnetite (equation (4.1.1.)) at  $1200^{\circ}\text{C}$ .

### 8.3.2. Modeling of Oxide Growth

Since the diffusion coefficients of iron in spinel and magnetite are available for the target temperature for each alloy with different spinel stoichiometry, the modeling of oxide growth based global mass balance can be performed since the growth of outer magnetite layer follows a parabolic kinetic based on Wagner's theory of thick oxide growth ( $x^2 = 2k_p t = k_p t$ ). As presented in the first

chapter, the chemical potential for the magnetite formation reaches a constant (0) value when the  $3\text{Fe}+2\text{O}_2=\text{Fe}_3\text{O}_4$  reaction reaches it equilibrium state. In this regard, the following relationship can be deduced:

$$d\mu_{\text{Fe}} = -\frac{2}{3} (RT d\ln P_{\text{O}_2}) \quad (8.17)$$

For the magnetite formation, the iron flux can be written as follows:

$$J_{\text{Fe}} = -\frac{D_{\text{Fe}} C_{\text{Fe}}}{RT} \frac{\partial \mu_{\text{Fe}}}{\partial x_{\text{Mg}}} \quad (8.18)$$

Based on equations (4.2.1) and (4.2.2), the flux can be represented as:

$$J_{\text{Fe}} = \frac{2}{3} \frac{D_{\text{Fe}} C_{\text{Fe}}}{a_{\text{O}_2}} \frac{\partial a_{\text{O}_2}}{\partial x_{\text{Mg}}} \quad (8.19)$$

where

$$D_{\text{Fe}} C_{\text{Fe}} = \sum_V D_V C_I + \sum_I D_I C_I = D_{\text{Fe}}^{\text{Mg}} C_{\text{Fe}}(T) \quad (8.20)$$

and as the scale grows the following assumptions can be made:

$$x_{\text{Mg}} = h_{\text{Mg}} \quad (4.2.5)$$

with

$$\frac{dn}{dt} = C_{\text{Fe}} S \frac{dx_{\text{Mg}}}{dt} = S J_{\text{Mg}}(h_{\text{Mg}}) = S J_{\text{Fe}}(h_{\text{Mg}}) \quad (8.21)$$

where  $n$  is the iron content (mol) and  $S$  is the surface area ( $\text{cm}^2$ )

and thus, the growth with respect to time and oxygen activity is as follows:

$$\frac{dx_{\text{Mg}}}{dt} = \frac{2}{3} \frac{D_{\text{Fe}}^{\text{Mg}}(T)}{a_{\text{O}_2}} \frac{\partial a_{\text{O}_2}}{\partial x_{\text{Mg}}} \quad (8.22)$$

where  $x_{\text{Mg}} = y$  and  $y = \frac{x_{\text{Mg}}}{h_{\text{Mg}}}$  and oxygen activity is independent of time. Therefore, the assumption is  $\frac{\partial a_{\text{O}_2}}{\partial x_{\text{Mg}}} = \frac{da_{\text{O}_2}}{dy}$ . With all the above assumptions, the following relationship emerges:

$$\frac{dx_{\text{Mg}}}{dt} = \frac{2}{3} \frac{D_{\text{Fe}}^{\text{Mg}}(T)}{a_{\text{O}_2}} \frac{1}{h_{\text{Mg}}} \frac{da_{\text{O}_2}}{dy} \quad (8.23)$$

with respect to  $\int_{h_{\text{Mg}}} dh_{\text{Mg}}$  and  $\int_t dt$ , the equation (4.2.8) yields as:

$$h_{\text{Mg}}^2 = \frac{2}{3} t \int_{a_{\text{O}_2}^{\text{Int}}}^{a_{\text{O}_2}^{\text{Ext}}} \frac{D_{\text{Fe}}^{\text{Mg}}(T)}{a_{\text{O}_2}} da_{\text{O}_2} \quad (8.24)$$

note that above  $a_{\text{O}_2}^{\text{Int}}$  represents the oxygen activity at which the magnetite starts to form. Therefore  $a_{\text{O}_2}^{\text{Int}}$  is the  $a_{\text{O}_2}^{M/S}$  in figure 8.37.

In regards to the global mass balance between spinel and magnetite layer and magnetite growth relationship (equation (8.24) the modeling can be p with adopting some other assumptions. To illustrate this, a schematic illustration of oxide layer growth is presented in Fig. 8.37 is presented featuring the scale growth according to available space mode. The assumptions are as follows:

- Since the experimental setup was not capable of tracking the oxygen activities (or its partial pressure) in the system, the surface oxygen activity,  $a_{O_2}^{ext}$ , is assumed to be as same as the oxygen activities required for the formation of  $Fe_2O_3$  through reduction of  $Fe_3O_4$ .
- $a_{O_2}^{int}$  is the oxygen activity between  $Fe_3O_4$  and metallic base steel. This will be approximated as the oxygen activity required for the oxidation of Fe to  $Fe_3O_4$ .

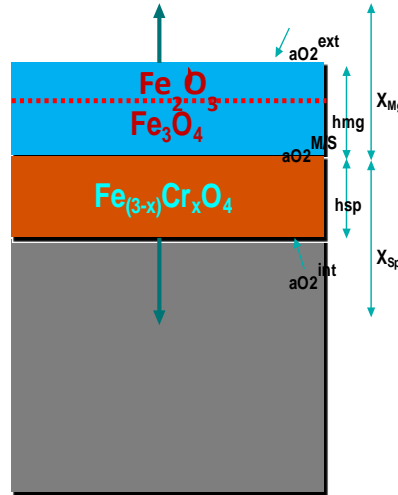


Figure 8.37: Schematic illustration of scale growth according to available space

- Oxygen activities are independent of time.
- No accumulation of elements at the boundaries or loss at the scale.
- The iron flux in spinel is equal to the iron flux in magnetite at all the times as such:

$$J_{Fe} = \frac{2}{3} \frac{D_{Fe} C_{Fe}}{a_{O_2}} \frac{\partial a_{O_2}}{\partial x_{Mg}}$$

$$J_{Fe}^{Sp} = \frac{2}{(3-x)} \frac{D_{Fe}^{Sp} C_{Fe}^{Sp}}{a_{O_2}} \frac{\partial a_{O_2}}{\partial x_{Sp}}$$

$$\Rightarrow \text{where } (3-x)Fe + xCr + 2O_2 = Fe_{(3-x)}Cr_xO_4 \text{ and } (3-x)d\mu_{Fe} + 2\mu_{O_2} = 0$$

Regarding modeling with above assumptions, the magnetite growth can be simulated by using both the iron flux in magnetite and the iron flux in spinel. However, there is one unknown value for both cases which is the oxygen activity between two oxide layer,  $a_{O_2}^{M/S}$ . Therefore, two flux relation can be employed for the calculation of  $a_{O_2}^{M/S}$ . The following relations are thus presented in regards to the magnetite growth through iron flux in spinel,  $(Fe_{(3-x)}Cr_xO_4)$ :

$$d\mu_{Fe} = -\frac{2}{(3-x)} (RT d\ln P_{O_2}) \quad (8.25)$$

$$J_{Sp} = -\frac{D_{Fe}^{Sp} C_{Fe}^{Sp}}{RT} \frac{\partial \mu_{Fe}}{\partial x_{Sp}} \quad (8.26)$$

$$J_{Sp} = \frac{2}{(3-x)} \frac{D_{Fe}^{Sp} C_{Fe}^{Sp}}{a_{O_2}} \frac{\partial a_{O_2}}{\partial x_{Sp}} \quad (8.27)$$

$$\frac{dn}{dt} = C_{Fe}^{Mg} S \frac{dx_{Mg}}{dt} = J_{Mg}(h_{Mg})S \quad (8.28)$$

Since the assumption is based on equal fluxes of iron in spinel and magnetite, the following relation is adopted:

$$J_{Mg}(h_{Mg})S = J_{Mg}(x_{Mg})S = J_{Sp}(h_{Sp})S \quad (8.29)$$

thus:

$$\frac{dx_{Mg}}{dt} = \frac{2}{(3-x)} \frac{D_{Fe}^{Sp} C_{Fe}^{Sp}}{C_{Fe}^{Mg} a_{O_2}} \frac{\partial a_{O_2}}{\partial x_{Sp}} \quad (8.30)$$

where  $x_{Sp} = y$  and  $y = \frac{x_{Sp}}{h_{Sp}}$  and oxygen activity is independent of time. Therefore, the assumption is  $\frac{\partial a_{O_2}}{\partial x_{Sp}} = \frac{da_{O_2}}{dy}$ . Therefore, the above relation becomes:

$$C_{Fe}^{Mg} \frac{dh_{Mg}}{dt} = \frac{2}{(3-x)} \frac{D_{Fe}^{Sp} C_{Fe}^{Sp}}{a_{O_2}} \frac{1}{h_{Sp}} \frac{da_{O_2}}{dy} \quad (8.31)$$

where  $h_{Spinel} = \frac{C_{Fe}^{Magnetite}}{C_{Fe}^{Base} - C_{Fe}^{Spinel}} h_{Magnetite}$  and thus with respect to  $\int_{h_{Mg}} dh_{Mg}$  and  $\int_t dt$ , the equation (4.2.16) yields as:

$$h_{Mg}^2 = \frac{2}{(3-x)} \frac{C_{Fe}^{Sp} (C_{Fe}^{Base} - C_{Fe}^{Sp})}{C_{Fe}^{Mg^2}} t \int_{a_{O_2}^{Int}}^{a_{O_2}^{Ext}} \frac{D_{Fe}^{Sp}}{a_{O_2}} da_{O_2} \quad (8.32)$$

According to equation (4.2.17) and (4.2.9), there are two available calculations for magnetite growth. With respect the boundaries presented in the figure (4.7) the following balance equations can be presented:

$$\frac{2}{(3-x)} \frac{C_{Fe}^{Sp} (C_{Fe}^{Base} - C_{Fe}^{Sp})}{C_{Fe}^{Mg^2}} t \int_{a_{O_2}^{Int}}^{a_{O_2}^{Mg/Sp}} \frac{D_{Fe}^{Sp}}{a_{O_2}} da_{O_2} = \frac{2}{3} t \int_{a_{O_2}^{Mg/Sp}}^{a_{O_2}^{Ext}} \frac{D_{Fe}^{Mg}(T)}{a_{O_2}} da_{O_2} \quad (8.33)$$

where  $D_{Fe}^{Mg}(T) = \frac{A a_{O_2}^{2/3}}{12(1+2K_V a_{O_2}^{2/3})} + \frac{4B}{3} a_{O_2}^{2/3}$  (the first and second parts present  $D_{Fe}^{Mg}(V, T)$  and  $D_{Fe}^{Mg}(I, T)$  respectively) and  $D_{Fe}^{Sp} = bV \cdot D_{Fe}^{Mg}(V, T) + bI \cdot a_{O_2}^{aI} \cdot D_{Fe}^{Mg}(I, T)$ .

Therefore, the final equation is the following:

$$\begin{aligned} & \frac{2}{(3-x)} \frac{C_{Fe}^{Sp} (C_{Fe}^{Base} - C_{Fe}^{Sp})}{C_{Fe}^{Mg^2}} t \left\{ \frac{AbV}{16K_V} \ln \left[ \frac{1+2K_V a_{O_2}^{Sp/Mg^{2/3}}}{1+2K_V a_{O_2}^{Int^{2/3}}} \right] + \frac{4B}{3aI-2} \left[ a_{O_2}^{Sp/Mg^{aI-2/3}} - a_{O_2}^{Int^{aI-2/3}} \right] \right\} \\ & = t \left\{ \frac{A}{24K_V} \ln \left[ \frac{1+2K_V a_{O_2}^{Ext^{2/3}}}{1+2K_V a_{O_2}^{Sp/Mg^{2/3}}} \right] + \frac{4B}{3} \left[ a_{O_2}^{Sp/Mg^{-2/3}} - a_{O_2}^{Ext^{-2/3}} \right] \right\} \quad (8.34) \end{aligned}$$

The above model (presented as the equation (4.2.19)) has only one unknown,  $a_{O_2}^{Sp/Mg}$  with two equations. Once  $a_{O_2}^{Sp/Mg}$  is available, the global oxide growth simulation can be performed by using either of the iron fluxes with subsequent use of the global mass relation for various temperatures and alloys with different spinel structures.

### 8.3.3 Validity of Available Space for Ferritic Steels of Interest

There are three manifestation of available space model in terms of global mass balance. First comes with the assumption that  $h_{Consumed}^{Base} = h_{Sp}$  since the inner growth becomes possible with outward diffusion of iron cations. With this assumption the flowing relation is given:

$$\frac{h_{Sp}}{h_{Mg}} = \frac{C_{Fe}^{Magnetite}}{C_{Fe}^{Base} - C_{Fe}^{Spinel}} \quad (8.35)$$

if the comparison of the ratio  $\frac{h_{Sp}}{h_{Mg}}$  from the SEM-EDS measurements with the ratio  $\frac{C_{Fe}^{Magnetite}}{C_{Fe}^{Base} - C_{Fe}^{Spinel}}$  from the alloy composition is small or none, it can be stated that the oxidation occurs via available space

mechanism.

Table 8.3: Calculated and measured  $h_{Sp}/h_{Mg}$  ratios for alloys of interest.

<i>Alloys</i>	<i>Ratios from SEM-EDS Measurements</i>	<i>Ratios Calculated from the Alloy Specifications</i>
<i>T22 (2Cr)</i>	0.42	0.91
<i>T92 (9Cr)</i>	0.78	0.95
<i>T122 (12Cr)</i>	0.88	0.96
<i>Fe12Cr Binary</i>	0.83	0.96

As presented in the above table, the difference of ratios from calculation and SEM-EDS measurements seems to be within 8 to 12% difference for all the alloys except T22 for which approximately 54% difference exist.

The second approach to validating of model is based on the Pilling-Bedworth ratio and the relation between magnetite volume and nano-cavity volume on which spinel forms. The Pilling-Bedworth relation is given as:

$$P - B_{Ratio} = \frac{V_{Oxide}}{V_{Metal}} = \frac{M_{Oxide} \times d_{Metal}}{M_{Metal} \times n \times d_{Oxide}} \quad (8.36)$$

where  $V_{Oxide-Metal}$  is the volume of the scale ( $cm^3$ );  $d_{Oxide-Metal}$  is the density notation ( $g/cm^3$ );  $M_{Oxide-Metal}$  is the atomic or molecular weight notation ( $g/mol$ );  $n$  is the number of metal atoms per one molecule of the oxide.

Considering the vacancy accumulation approach, the spinel volume can be presented as:

$$V_{Spinel} = V_{Consumed}^{Fe} + V_{Nano-Vacancies} \quad (8.37)$$

where  $V_{Spinel}$  is presented with the volume of metallic atoms ( $V_{Consumed}^{Fe}$ ) diffused out used to form spinel-like oxides along with the volume of cationic vacancies ( $V_{Nano-Vacancies}$ ) created inside. In terms of P-B ratio, the spinel volume can be also presented as:

$$V_{Spinel} = P - B_{Spinel} \cdot V_{Consumed}^{Fe} \quad (8.38)$$

Using both equation (4.3.3 & 4.3.4), the spinel volume can be represented as the volume of nano vacancies created upon outward iron diffusion as follows:

$$V_{Spinel} = \frac{P - B_{Spinel}}{P - B_{Spinel} - 1} \cdot V_{Nano-Vacancies} \quad (8.39)$$

where  $P - B_{Spinel}$  is the Pilling-Bedworth ratio for  $Cr_xFe_{(3-x)}O_4$  type spinel formation. Since the magnetite growth is a function of total nano vacancies created, the volume of Fe in magnetite,  $V_{Magnetite}^{Fe}$ , is approximately same as the volume of nano vacancies in the base steel:

$$V_{Magnetite}^{Fe} \cong V_{Nano-Vacancies} \quad (8.40)$$

with the Pilling-Bedworth approach, the magnetite volume is then approximated as:

$$V_{Magnetite} = P - B_{Magnetite} \cdot V_{Nano-Vacancies} \quad (8.41)$$

therefore, the following relation in terms of thickness ratio of spinel to magnetite can be established:

$$\frac{V_{Spinel}}{V_{Magnetite}} = \frac{h_{Sp}}{h_{Mg}} = \frac{P - B_{Spinel} \times P - B_{Magnetite}}{P - B_{Spinel} - 1} \quad (8.42)$$

Where, the  $P - B_{Spinel}$  is a strong function of the  $x$  stoichiometric value in  $Cr_xFe_{(3-x)}O_4$ . Assuming that of  $x=0$  to  $x=3$  and using the equation (8.42), the  $P - B_{Spinel}$  can be calculated as function of  $x$  for which  $d_{Sp}$  assumed as in between  $5.18$  ( $g/cm^3$ ) and  $6.1$  ( $g/cm^3$ ) [118]. For the calculations of equation



(4.3.8),  $P - B_{Magnetite}$  is further found to be 2.1 with respect to  $d_{Mg}$  (5.1-5.2) [119] taken as 5.18 ( $\text{g}/\text{cm}^3$ ). Figure 8.38 is presented as the result of these calculations with respect to the ratios calculated assuming  $C_{Fe}^{Spinel}$  is also a function of  $x$  as  $\frac{3-x}{V_{Magnetite}}$ .

As presented, the ratios calculated based on aforementioned theory are indicative of  $x=0.15$ , 0.6, and 0.7 (Fig. (8.39)). However, further comparison of  $P - B_{Ratio}$  assumptions with experimentally (SEM-EDS) obtained  $h_{Sp}/h_{Mg}$  yields with some differences of  $x$  values especially for T22. The experimental consideration for T122, for instance, yielded a  $h_{Sp}/h_{Mg}$  value 7% different than the  $h_{Sp}/h_{Mg}$  with  $P - B_{Ratio}$  assumptions while  $x$  values were found to be the same (0.7). Note that the internal oxidation as a part of spinel was not considered in which case  $h_{Sp}/h_{Mg}$  will increase. However, this difference for T22 was found to be approximately 63% in terms ratio comparisons with a different  $x$  value (0.15 vs 0.23) which is a clear indication that the available space model is not valid for for T22 steel (2Cr alloy). Same, approx. 7%, differences were also found for T92 and Fe12Cr alloys with no significant difference in  $x$  values.

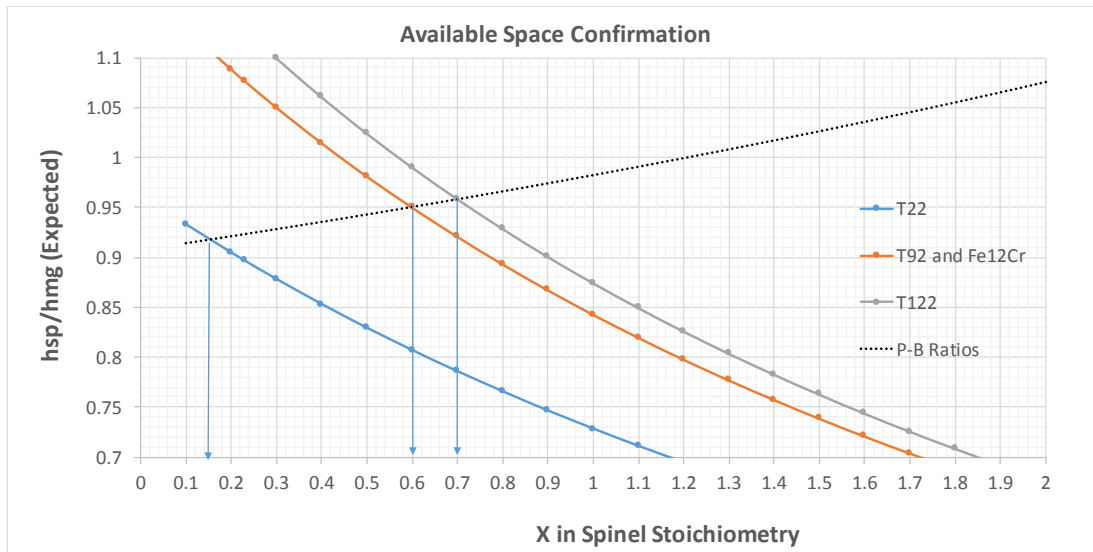


Figure 8.38: Expected  $h_{Sp}/h_{Mg}$  ratio with  $P - B_{Ratio}$  assumptions for the steels investigated.

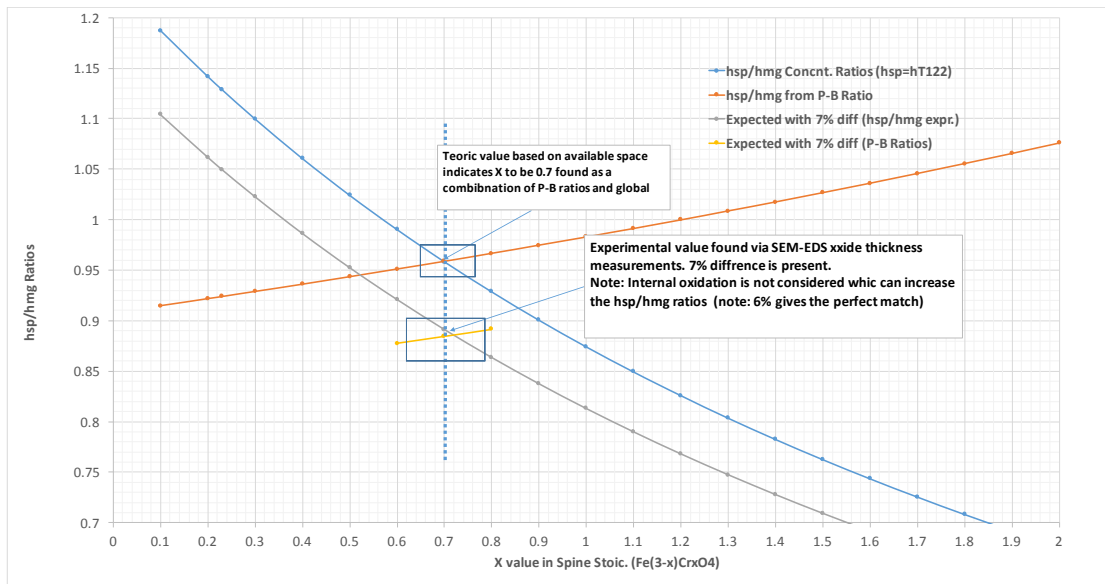


Figure 8.39: Expected  $h_{Sp}/h_{Mg}$  with  $P - B_{Ratio}$  assumptions and with global mass balance for T122.

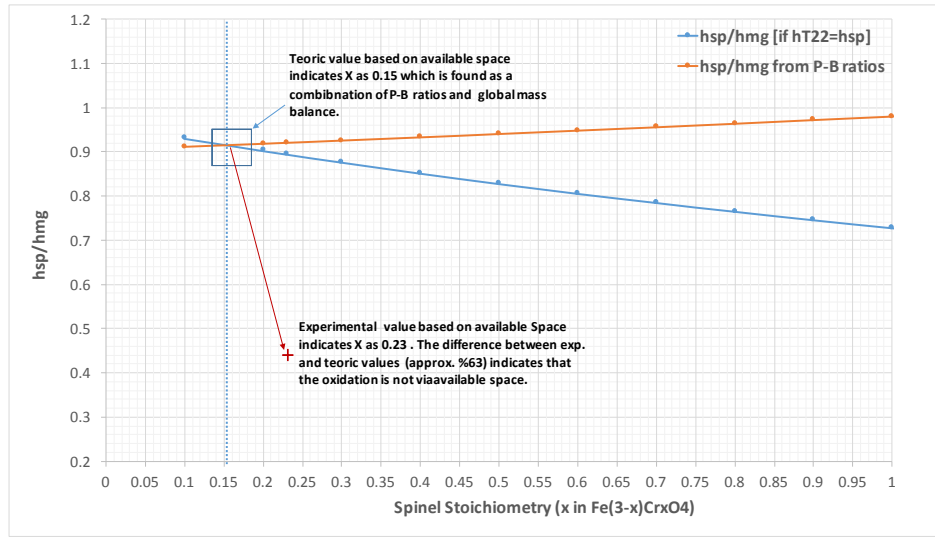


Figure 8.40: Expected  $h_{Sp}/h_{Mg}$  with  $P - B_{Ratio}$  assumptions and with global mass balance for T22.

The above figures 8.39 and 8.40 feature the resulted difference between  $P - B_{Ratio}$  assumptions and with global mass balance for T22 and T122. Note that for T22 not only are the ratios different but the x values are also different. As a last validity test, the x values from the calculations and the measurements from the EPMA analyses were compared. The calculated x values are based on both alloy specifications and the  $h_{Sp}/h_{Mg}$  values obtained from SEM-EDS measurements. The equation indicating x in spinel stoichiometry is as following:

$$X = 3 \frac{\left(1 + \frac{h_{Magnetite}}{h_{Spinel}}\right)}{\left(1 + \frac{C_{Fe}^{Base}}{C_{Cr}^{Base}}\right)} \quad (8.43)$$

By employing this above equation, the x values for all the alloys of interest were calculated. The results were then compared with the results from EPMA. The results were only different for alloy T22.

With respect to all the measurements and calculations performed regarding validity of available space for the alloys of interest, table (8.4) is presented below,

Table 8.4: Measurements and calculations performed to test the validity of available space model.

<i>Alloys</i>	<i>Ratios from SEM-EDS Measurements</i>	<i>Ratios Calculated from the Alloy Specifications</i>	<i>Ratios from P-B Ratio Calculations</i>	<i>X Values from P-B Ratios</i>	<i>X Values Calculated with Equation (4.1.3.9)</i>	<i>X Values from EPMA Analyses</i>
<b>T22 (2Cr)</b>	0.42	0.91	0.92	0.15	0.23	0.19
<b>T92 (9Cr)</b>	0.78	0.95	0.95	0.6	0.61	0.59
<b>T122 (12Cr)</b>	0.88	0.96	0.95	0.7	0.7	0.73
<b>Fe12Cr Binary</b>	0.83	0.96	0.96	0.6	0.78	Not Performed

Regarding the calculated (from P-B and alloy composition.) and measured ratios (from SEM-EDS) of 9-12Cr alloys, it can be said that the differences are not necessarily an indication of a deviation from the model especially noting that internal oxidations were not taken into account. In the case of assumption that internal oxidation is a part of spinel, the difference between measurement and calculations would approach zero. However, the assessment of internal oxidation based on EDS measurements with some assumptions were not perfect. For this reason, the spinel measurements were performed as independent of internal oxidation. Further, considering the x values of spinel stoichiometry for 9-12Cr alloys from P-Bs, global mass balance calculations (equation (4.1.3.9)), and EPMA results there are no significant differences present. With respect to  $h_{Sp}/h_{Mg}$  ratio and x findings, it can be concluded that the oxidation for 9-12Cr steels in this study oxidized via available space and a global mass balance exists. However, with the same considerations, available space model seems to not apply perfectly for the oxidation of T22 in S-CO<sub>2</sub> at 450 °C especially regarding the mass balance. Therefore, the simulation of T22 by just comparing above presented values, in table (4.1.3.2), will possibly fail. However, considering the mechanism of oxide formation on T22, the void-induced oxide mechanism (available space) still takes place since the oxide formed is duplex in oxide is composed of an outer magnetite and an inner spinel layer, which in this case seems to be not stable.

#### 8.3.4. Simulation of Oxide Growth on Ferritic Alloys Tested in S-CO<sub>2</sub> at 450 °C and 200 bar.

The alloys of interest in our tests have been tested in research grade S-CO<sub>2</sub> at 450 °C and 200 bar with coupons as being removed every 200h for thickness measurements and other analyses. The nature of the oxidation has been assessed as parabolic as described by the Wagner's law and duplex. The available space model then provided a basis for global mass balance. With respect to mass balance approach, the validity of model has been tested for all the ferritic alloys within the scope of this thesis and it was concluded that all the ferritic steels but T22 seems to present a valid global mass balance.

By referring the following equation once more:

$$\frac{2}{(3-x)} \frac{C_{Fe}^{Sp}(C_{Fe}^{Base} - C_{Fe}^{Sp})}{C_{Fe}^{Mg^2}} t \left\{ \frac{AbV}{16K_V} \ln \left[ \frac{1+2K_V a_{O_2}^{Sp/Mg^{2/3}}}{1+2K_V a_{O_2}^{Int^{2/3}}} \right] + \frac{4B}{3a-2} \left[ a_{O_2}^{Sp/Mg^{a-2/3}} - a_{O_2}^{Int^{a-2/3}} \right] \right\} \\ = t \left\{ \frac{A}{24K_V} \ln \left[ \frac{1+2K_V a_{O_2}^{Ext^{2/3}}}{1+2K_V a_{O_2}^{Sp/Mg^{2/3}}} \right] + \frac{4B}{3} \left[ a_{O_2}^{Sp/Mg^{-2/3}} - a_{O_2}^{Ext^{-2/3}} \right] \right\} \quad (8.44)$$

the following equation can be written:

$$H = f \left[ T, D_{Fe}^{Mg}, D_{Fe}^{Sp}(x), a_{O_2}^{Int}, a_{O_2}^{Sp/Mg}, a_{O_2}^{Ext} \right] \quad (8.45)$$

where the total oxide thickness,  $H$ , is a function of iron diffusion in magnetite and spinel and the oxygen activities at boundaries of the oxide scale. As previously assumed,  $a_{O_2}^{Int}$  and  $a_{O_2}^{Ext}$  are fixed values for all the cases determined as [121]:

$$\log a_{O_2}^{Int}(Fe/Fe_3O_4) = -\frac{28930}{T(K)} + 8.460 \quad (8.46)$$

$$\log a_{O_2}^{Ext}(Fe_3O_4/Fe_2O_3) = -\frac{24660}{T(K)} + 5.84 + 2.592 \cdot \log T(K) \quad (8.47)$$

where  $a_{O_2}^{Int}$  and  $a_{O_2}^{Ext}$  at 450 °C are  $1.46 \cdot 10^{-21}$  and  $2.85 \cdot 10^{-32}$  respectively. The value of  $D_{Fe}^{Mg}$  at 450 °C determined is also a function determined by  $a_{O_2}^{Int}$  and  $a_{O_2}^{Ext}$  and assumed to be same for all the alloys. However,  $D_{Fe}^{Sp}(x)$  is a function of  $D_{Fe}^{Mg}$  depending upon the spinel stoichiometry and has been shown to be different for the steels tested. With the calculation of  $D_{Fe}^{Sp}(x)$ ,  $D_{Fe}^{Mg}$ ,  $a_{O_2}^{Int}$  and  $a_{O_2}^{Ext}$  at 450 °C, the  $a_{O_2}^{Sp/Mg}$  values were determined by employing the equation 8.34 for each alloy with a specific spinel stoichiometry. Once the  $a_{O_2}^{Sp/Mg}$  values for each steel were determined, individual scale thicknesses of  $h_{Mg}$  evaluated using the one part of the equation 8.34 and of  $h_{Sp}$  by using equation (8.4). Consequently, the oxidation rates,  $k_p$  [cm<sup>2</sup>s<sup>-1</sup>], for each alloy were determined for the

comparison with the experimentally obtained values. The values obtained are presented in the table (8.5)

Table 8.5: Specific values obtained for the oxidation in S-CO<sub>2</sub> at 450 °C and 200 bar for various steels.

Alloys	$a_{O_2}^{Int}$	$a_{O_2}^{Ext}$	$a_{O_2}^{Sp/Mg}$	$k_p \text{ for } H^2 = k_p \cdot t \text{ [cm}^2\text{s}^{-1}\text{]}$	
				Experimental	Model
<b>T22</b>	$1.46 \cdot 10^{-21}$	$2.85 \cdot 10^{-32}$	$4.67 \cdot 10^{-22}$	$7.61 \cdot 10^{-14}$	$6.36 \cdot 10^{-14}$
<b>T92</b>			$6.28 \cdot 10^{-22}$	$1.71 \cdot 10^{-13}$	$5.36 \cdot 10^{-14}$
<b>T122</b>			$5.79 \cdot 10^{-22}$	$1.15 \cdot 10^{-13}$	$5.80 \cdot 10^{-14}$
<b>Fe12Cr</b>			$6.31 \cdot 10^{-22}$	$1.36 \cdot 10^{-13}$	$5.37 \cdot 10^{-14}$

It can be seen from the table 8.5 that the model underestimates the oxidation with respect to experimental oxidation rates. The calculated values of oxygen activity at 450 °C, the  $a_{O_2}^{Sp/Mg}$  are consistent with previous findings in the 470 to 620 °C temperature range. Thus, the underestimated simulation results are thought to be due to  $D_{Fe}^{Sp}(x)$  and  $D_{Fe}^{Mg}$  values used. These values, represent diffusion through bulk lattice and one can argue, that grain boundaries which are high diffusion pathways leading  $D_{gb} \gg D_{bulk}$  (usually four to six orders of magnitude larger) may be responsible for this effect. With this consideration, it is clear that if  $D_{gb}$  is used, the model will also fail by over estimating the kinetics. Even though the grain boundaries provide the high diffusion pathways, the global diffusion occurs through both lattice and grain boundaries. Thus, an effective diffusion for a system exist including both  $D_{Gb}$  and  $D_{Bulk}$ . The following relation by Hart provides the effective diffusion coefficient:

$$D_{eff} = g \cdot D_{Gb} + (1 - g)D_{Bulk} \quad (8.48)$$

where  $g$  present the fraction of atomic sites in a grain boundary as:

$$g = \frac{q \times \delta}{d} \quad (4.1.4.6)$$

where  $\delta$  and  $d$  are grain boundary width, in general assumed to be a constant  $\delta = 0.5 \text{ nm}$ , and the size of the grain respectively. The quantity  $q$  is a factor depending on grain shape such as 1 for parallel and 3 for cubic grains. Considering the parallel structure of magnetite and 50 nm spinel grains sizes,  $g$  becomes equal to 0.01, thus  $D_{eff} = 0.01 \cdot D_{Gb} + (0.99)D_{Bulk}$ . Regarding the grain boundary diffusion of iron in magnetite,  $D_{Gb} = 600D_{bulk}$  has been provided in literature.

By assuming these values, the effective diffusion coefficient for the system becomes as  $D_{eff} = 6.99 \cdot D_{Bulk}$ .

For the calculation of  $D_{eff}$  in a system involving both diffusion via vacancies and interstitials the following relation is assumed:

$$D_{eff} \propto (A_{eff} + B_{eff}) \quad (8.49)$$

and thus:

$$D_{eff} \propto 6.99 \cdot (D_V + D_I) \quad (8.50)$$

Subsequently,  $D_{Fe}^{Sp}(x)_{eff}$  and  $D_{Fe}^{Mg}_{eff}$  values were evaluated and since the  $a_{O_2}^{Sp/Mg}$  values are independent of oxidation kinetics, the  $k_p$  values for each alloy were then calculated as explained previously regarding the new  $D_{eff}$ . The new  $k_p$  calculation results are presented in the following table with the previous cases.

Table 8.6:  $k_p$  values obtained for the oxidation of ferritic alloys in  $S\text{-CO}_2$  at  $450^\circ\text{C}$  and 200 bar via experimental observations and simulations by  $D_{\text{Bulk}}$  and  $D_{\text{eff}}$ .

Alloys	$k_p \text{ for } H^2 = k_p \cdot t \text{ [cm}^2\text{s}^{-1}\text{]}$		
	Experimental	Modeling with $D_{\text{Bulk}}$	Modeling with $D_{\text{eff}}$
T22	$7.61 \cdot 10^{-14}$	$6.36 \cdot 10^{-14}$	$4.45 \cdot 10^{-13}$
T92	$1.71 \cdot 10^{-13}$	$5.36 \cdot 10^{-14}$	$3.75 \cdot 10^{-13}$
T122	$1.15 \cdot 10^{-13}$	$5.80 \cdot 10^{-14}$	$4.01 \cdot 10^{-13}$
Fe12Cr	$1.36 \cdot 10^{-13}$	$5.37 \cdot 10^{-14}$	$3.75 \cdot 10^{-13}$

As shown in table 8.6, it is clear that the simulation using  $D_{\text{eff}}$  also fails to predict the actual kinetics observed. Therefore, either the spinel grain size or  $D_{\text{Gb}} = 600D_{\text{bulk}}$  assumptions are not perfect for the steel systems being studied. Nonetheless, the calculated oxygen activities provide information indicating how the diffusion occurs such as via vacancies or interstitials or both. In this regard, figure 8.41 is presented for T92 with  $a_{\text{O}_2}^{\text{Sp/Mg}} = 6.28 \cdot 10^{-22}$ . Regarding the location of  $\log a_{\text{O}_2}$ 's in this figure, it is clear that the growth of magnetite is due to diffusion via vacancies while the spinel growth region occurs by a combination of diffusion via interstitials and vacancies. Once the iron cations are at the spinel/magnetite boundary, their diffusion throughout the outer magnetite scale occurs only diffusion via vacancies. For this case, the following equation can be written for magnetite formation rate as follows:

$$k_p^{\text{Mg}} = t \left\{ \frac{A}{24K_V} \ln \left[ \frac{1+2K_V a_{\text{O}_2}^{\text{Ext}^{2/3}}}{1+2K_V a_{\text{O}_2}^{\text{Sp/Mg}^{2/3}}} \right] + \frac{4B}{3} \left[ a_{\text{O}_2}^{\text{Sp/Mg}^{-2/3}} - a_{\text{O}_2}^{\text{Ext}^{-2/3}} \right] \right\} \quad (8.51)$$

$$k_p^{\text{Mg}} = t \left\{ \frac{A}{24K_V} \ln \left[ \frac{1+2K_V a_{\text{O}_2}^{\text{Ext}^{2/3}}}{1+2K_V a_{\text{O}_2}^{\text{Sp/Mg}^{2/3}}} \right] \right\} \quad (8.52)$$

where  $k_p^{\text{Mg}}$  is the rate constants for the magnetite scale formation in case of  $D_{\text{Bulk}}$  use. By comparing this equation with the experimentally obtained  $k_p^{\text{Mg}}$ , the following relation can be written.

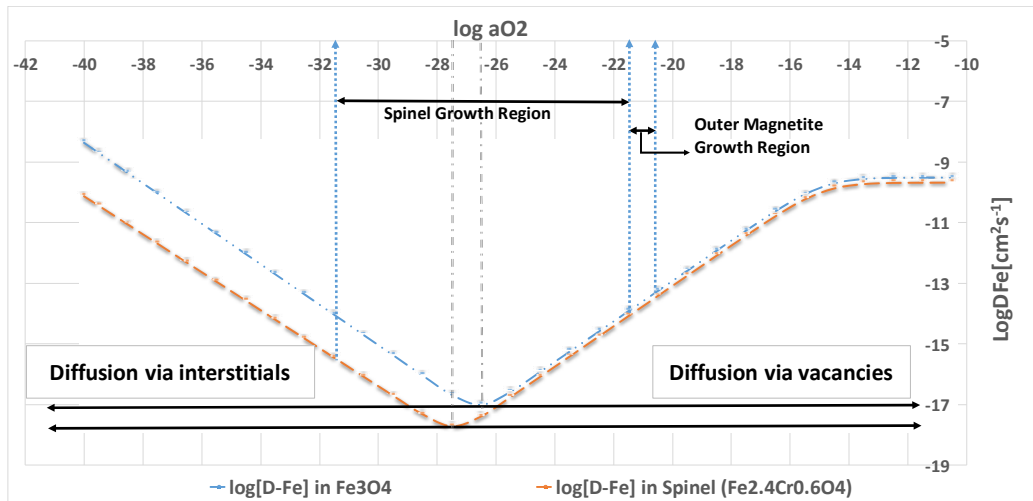


Figure 8.41: The dominant regimes of diffusion mechanisms for the oxide scale formation on T92; note that all other alloys exhibit the same behavior regarding magnetite and spinel growth regimes.

$$k_p^{Mg}(\text{exp}) = t \left\{ \frac{A_{eff}^{Exp}}{24K_V} \ln \left[ \frac{1+2K_V a_{O_2}^{Ext^{2/3}}}{1+2K_V a_{O_2}^{Sp/Mg^{2/3}}} \right] \right\} \quad (8.53)$$

where  $A_{eff}^{Exp}$  determines the effective diffusion via vacancies. Therefore, the following relation can be written:

$$\frac{k_p^{Mg}(\text{exp})}{k_p^{Mg}} = \frac{A_{eff}^{Exp}}{A} = D_V^{eff} = f \cdot D_V \quad (8.54)$$

Where,  $f$  is the constant defining the relationship between  $D_{eff}$  and  $D_{Bulk}$ .  $f$  is the same for both diffusions via vacancies and via interstitials as presented below.

$$\frac{A_{eff}^{Exp}}{A} = \frac{B_{eff}^{Exp}}{B} = f \quad (8.55)$$

The assumption presented in this equation has been first tested by assuming the  $f$  values obtained from magnetite kinetics are same as for the spinel kinetics. The figure 8.42 presents the spinel simulation for which the growth is based on diffusion via both interstitials and vacancies as presented in figure (8.41).

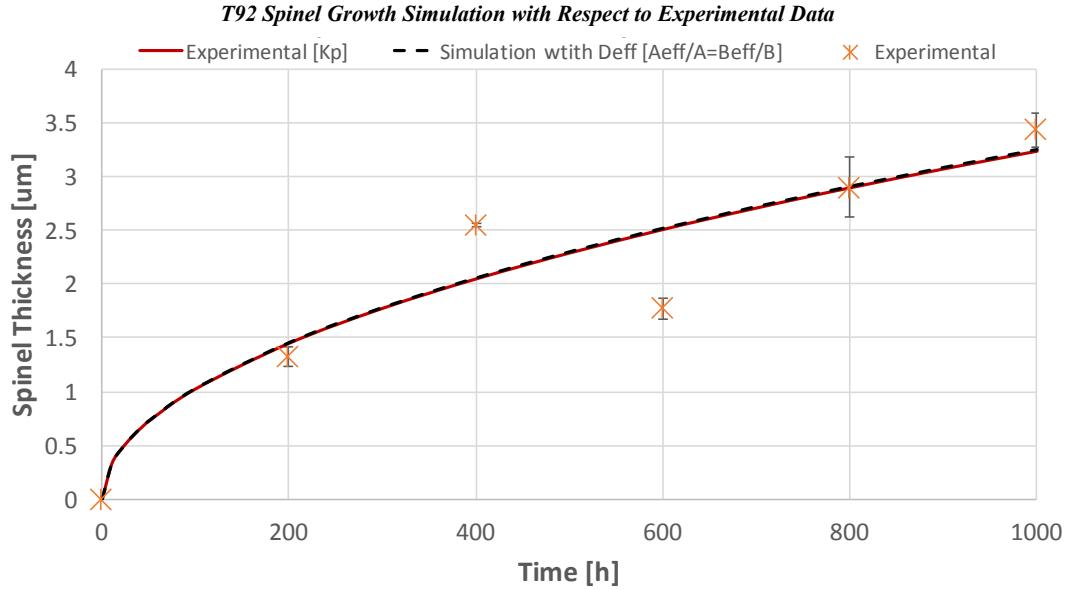


Figure 8.42: The simulation of spinel oxide growth on T92 with respect to experimental data points.

For the above spinel growth simulation, first the magnetite growth was simulated by using the iron flux in spinel layer for which diffusion via both interstitials and vacancies occur (figure (8.41)). Then using the experimentally obtained  $h_{Sp}/h_{Mg}$  ratio, the spinel growth was deduced. The above plot presents the spinel growth by experimental  $k_p$  and by simulated  $k_p$  values with respect to experimental data points. With respect to presented results,  $\frac{A_{eff}^{Exp}}{A} = \frac{B_{eff}^{Exp}}{B}$  seem to be a reasonable assumption. Therefore, the ratio  $f$  were evaluated for all the alloys using experimentally obtained magnetite growth rates, and then global oxide growth for each alloy were performed. The following table and figures are presented with the all the results of simulations with different diffusion coefficients.



Table 8.7:  $k_p$  values obtained for the oxidation of ferritic steels via experimental observations and simulations using  $D_{Bulk}$  and  $D_{eff}$  and  $D_{eff}^{Exp}$  values.

Alloys	$k_p \text{ for } H^2 = k_p \cdot t \text{ [cm}^2\text{s}^{-1}\text{]}$				
	Experimental	Simulation with $D_{Bulk}$	Simulation with $D_{eff}$	Simulation with $D_{eff}^{Exp}$	$f$
T22	$7.61 \cdot 10^{-14}$	$6.36 \cdot 10^{-14}$	$4.45 \cdot 10^{-13}$	$2.51 \cdot 10^{-13}$	4.65
T92	$1.71 \cdot 10^{-13}$	$5.36 \cdot 10^{-14}$	$3.75 \cdot 10^{-13}$	$1.85 \cdot 10^{-13}$	3.42
T122	$1.15 \cdot 10^{-13}$	$5.80 \cdot 10^{-14}$	$4.01 \cdot 10^{-13}$	$1.25 \cdot 10^{-13}$	2.01
Fe12Cr	$1.36 \cdot 10^{-13}$	$5.37 \cdot 10^{-14}$	$3.75 \cdot 10^{-13}$	$1.85 \cdot 10^{-13}$	2.58

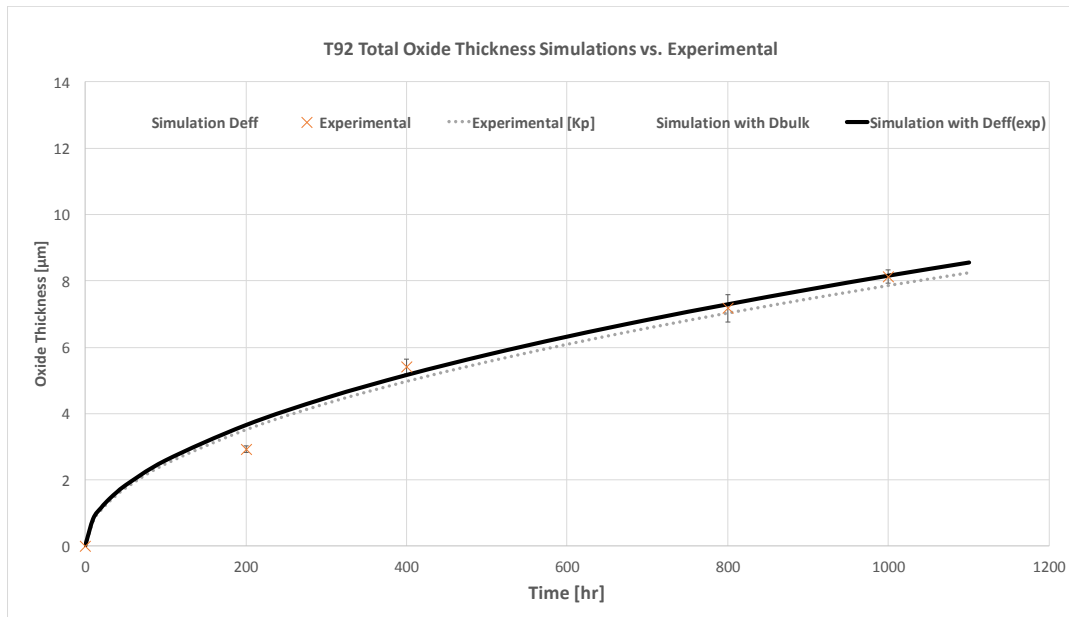


Figure 8.43: The simulation of oxide growth on T92 with respect to experimental data points.

The simulation with  $D_{eff}^{Exp}$  precisely predicts overall oxide thickness formed on T92.

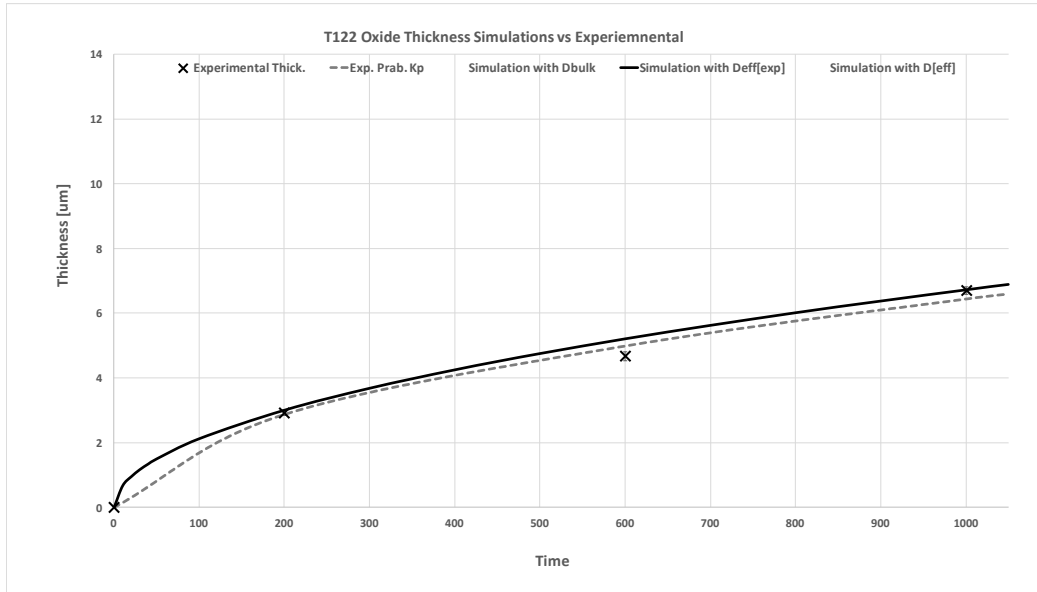


Figure 8.44: The simulation of oxide growth on T122 with respect to experimental data points.

The simulation with  $D_{eff}^{Exp}$  precisely predicts overall oxide thickness formed on T122 in comparison with the experiential observations.

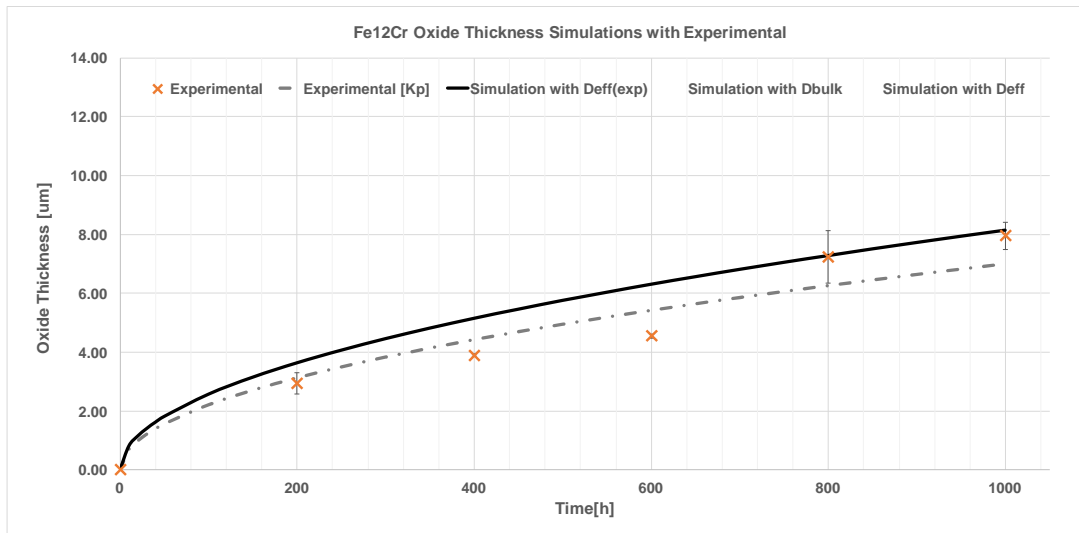


Figure 8.45: The simulation of oxide growth on Fe12Cr binary alloy with respect to experimental data points.

Regarding the simulation of Fe12Cr, simulation with  $D_{eff}^{Exp}$  seems to work. However, the inconsistencies in magnetite growth especially after 600h exposure appear to affect the estimation of  $D_{eff}^{Exp}$  leading to over estimated results. Nonetheless, over all prediction is reasonable.

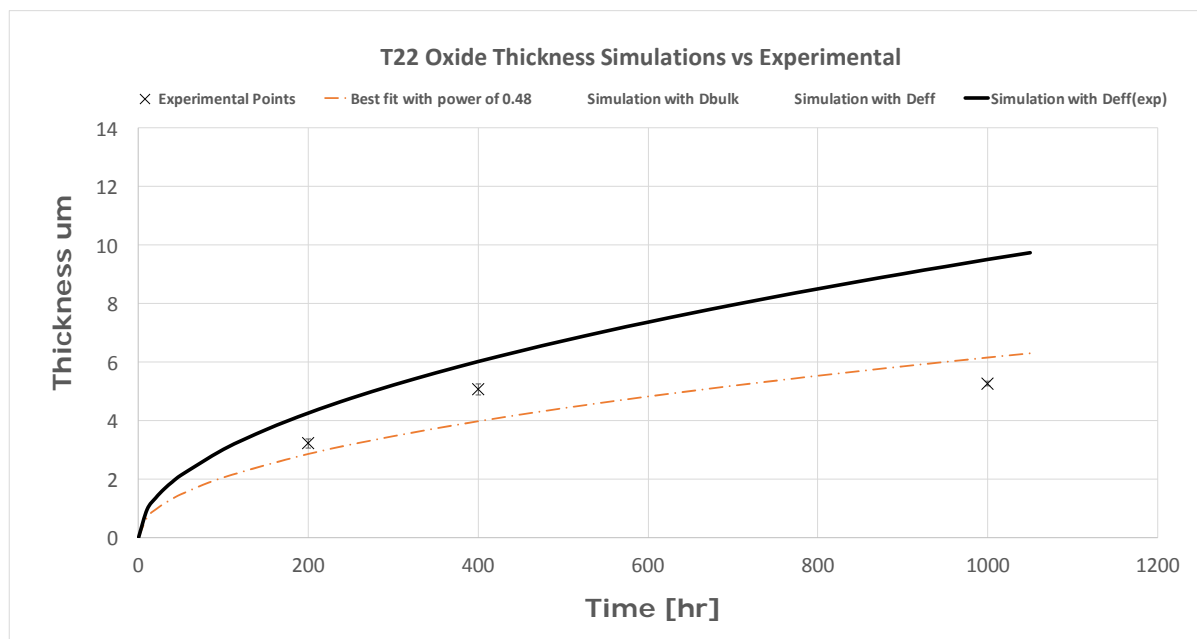


Figure 8.46: The simulation of oxide growth on T22 with respect to experimental data points.

Regarding the evaluation of the model, the simulation fails for both in the case of  $D_{eff}$  and  $D_{Bulk}$  use for all the tested alloys. However, the calculated values of  $a_{O_2}^{Sp/Mg}$  indicates that in the outer magnetite scale iron diffusion mechanism is via vacancies. Thus, the effective diffusion coefficients were deduced by comparing the magnetite growth rates from experimental results and from simulation with  $D_{Bulk}$ . The use of  $D_{eff}^{Exp}$  seems to enable the model to predict the global oxide thickness for all the alloys tested but not so well for the T22. The reason behind the failure of model for T22 is the failure of global mass balance as explained in the previous section.

### 8.3.5. Summary of the Chapter

In this chapter, the work was performed for the modeling and simulation of duplex oxide layer formation on ferritic steels. First, the basic approach for the extrapolation of diffusion coefficients in spinel and magnetite were introduced and the results of interest were presented. A model based on global mass balance was introduced. Validity of the model was tested for each alloy with three different approaches and results were presented indicating that the prediction of the model based on available space works well for T92, T122 and model Fe-12%Cr steels, but is not be suitable for T22 steel. The modeling results were then presented with the use of lattice diffusion coefficients and as expected the results were found to be underestimations with respect to actual kinetics. The concept of effective diffusion coefficients was subsequently discussed and some effective diffusion coefficient values from previous studies were applied and found to lead to an overestimation of kinetics. Thus, the concept of  $D_{eff}^{Exp}$  approximation was introduced. The simulations presented were found to be almost perfect with the use of  $D_{eff}^{Exp}$  for T92, T122 and Fe-12%Cr steels.

## 8.4. Carburization of Ferritic-Martensitic Steels in S-CO<sub>2</sub>

**8.4.1. Introduction:** Unlike many high temperature oxidative environments where an oxide layer develops on the surface and leads to consumption of structural materials' thickness, carburization of the underlying steel is also a distinct concern in high temperature CO<sub>2</sub> environments. Generally, carburization is a secondary result of oxidation through available space in which internal voids and nano-channels created during oxidation provide a pathway for the environment to reach the base steel. With this access the CO<sub>2</sub> gas can enter these cavities and further reduction of CO<sub>2</sub> to CO can occur through reactions with the surrounding metallic atoms leading in turn to an increase in local partial

pressure of CO. The result of this increased CO partial pressure is the increased carbon activity upon further reduction of CO thus creating these localized carburizing environments. This free carbon can then diffuse into the base steel and in the presence of carbide forming elements such as Cr in the steel, lead to the formation of carbide phases in the base steel. In practical applications, carburization should be a source of concern because it is likely to have an embrittling effect on materials and depending on its extent can lead to catastrophic brittle failure. In this study, carburization effects in T22, Fe12Cr, T92 and T122 steels were evaluated using optical microscopy, SEM-EDS analysis, hardness tests. EPMA-WDS and GDOES techniques were also applied for T92 steel, while GDMS technique was used for T22 and T122 steel. These experimental results are coupled with diffusion analysis using Fick's law.

#### 8.4.2 Carburization Results of Pure Fe in S-CO<sub>2</sub>

The carburization phenomenon of pure Fe becomes possible with the formation of Fe<sub>3</sub>C if only the local carbon activity becomes greater than 1 at temperature below 763 °C. The local carbon activity increase can occur due to the formation of inner voids which can provide access of local oxidizing gas environment. However, the oxidation of pure Fe to Fe<sub>3</sub>O<sub>4</sub> by S-CO<sub>2</sub> is somewhat different. Its formation is not by inner gas permeation or in other words it is not via available space for which CO<sub>2</sub> transport to inner layer is required. Since the transport of CO<sub>2</sub> to inner Fe<sub>3</sub>O<sub>4</sub> layer is not the case, local CO accumulation and its further reduction leading increased carbon activity is not expected. Therefore, the carburization of pure Fe via oxidation by SC-CO<sub>2</sub> is not necessarily expected. In order to verify this, 400h tested pure Fe was etched with 1% nital solution and examined by optical microscopy. Figures 8.47 and 8.48 presents this optical micrograph where no carburization is visible.

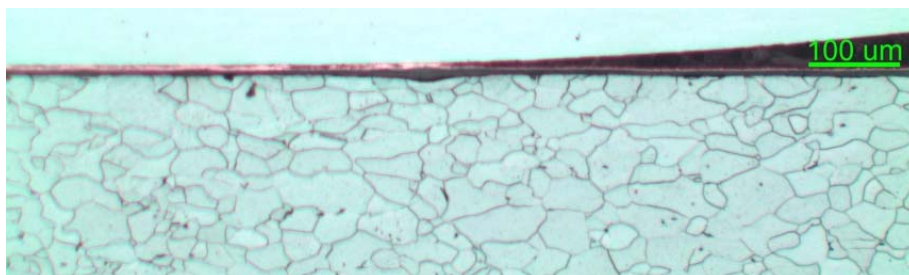


Figure 8.47: 10x magnified optical micrograph of etched (1% Nital) pure Fe sample exposed to S-CO<sub>2</sub> for 400h featuring showing only the ferrite grains and grain boundaries.

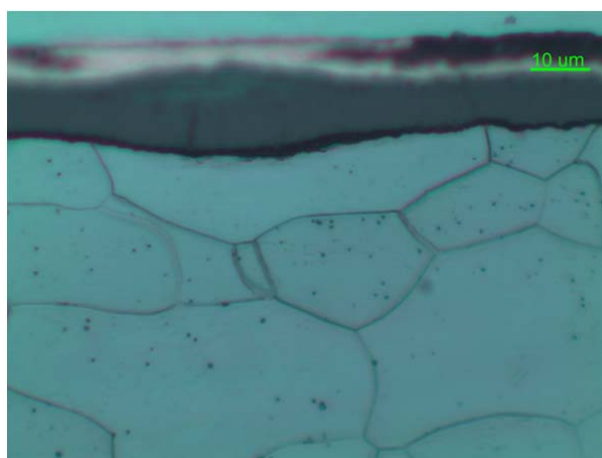


Figure 8.48: 100x magnified optical micrograph of etched (1% Nital) pure Fe sample exposed to S-CO<sub>2</sub> for 400h featuring only the ferrite grains, grain boundaries, and surface oxide layer.

As expected, no carburization was observed in pure-Fe and no further examination of the oxidized pure-Fe was performed.

### 8.4.3 Carburization Results of Fe12Cr Alloy

Carburization is expected to occur for the Fe12Cr alloy due to oxidation in SC-CO<sub>2</sub> since the oxide formation occurs via available space as presented in the earlier chapters. However, the formation was shown to be different compared to engineering steels T22, T92, and T122 to be discussed later. The surface examination of Fe12Cr binary alloy showed the surface to be generally covered with very thin protective chromia layer with some thicker duplex scale formation. The assumption of carburization in Fe12Cr was therefore dependent on the oxide scale formation such that while the inner CO<sub>2</sub> diffusion forms the duplex thick scale, the protective scale formation is due to the very surface reaction between CO<sub>2</sub> and Cr.

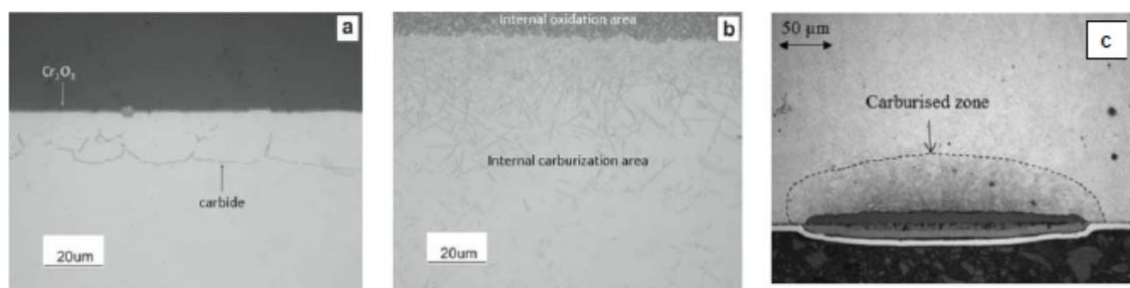


Figure 8.49: (a-b) Carburization below thin chromia layer and below thick Fe-rich oxide scale via oxidation of binary Fe-20Cr after 120h exposure to 20CO<sub>2</sub>-Ar mixture at 650 °C [85]; (c) carburization below thick-duplex oxide on 12Cr ferritic-martensitic steels after oxidation at 550 °C and 1 atm CO<sub>2</sub> [71].

Thus, carburization is expected underneath the thick-duplex scale, but not underneath the protective and thin chromia layer. These initial assumptions are also supported by the literature findings where Roulliard F. and Furukawa T. have shown that the carburization occurs only under the thick duplex oxide layer in case of nodular oxide formation of 12Cr ferritic-martensitic steel by 550 °C and 1 atm CO<sub>2</sub> while Gheno T. et. al., have shown that the carburization underneath the thin chromia layer was much smaller than the carburization underneath the thick Fe-rich oxide layer. These findings are also presented in the figure 8.49 featuring all the possible degrees of carburization through oxidation by CO<sub>2</sub>.

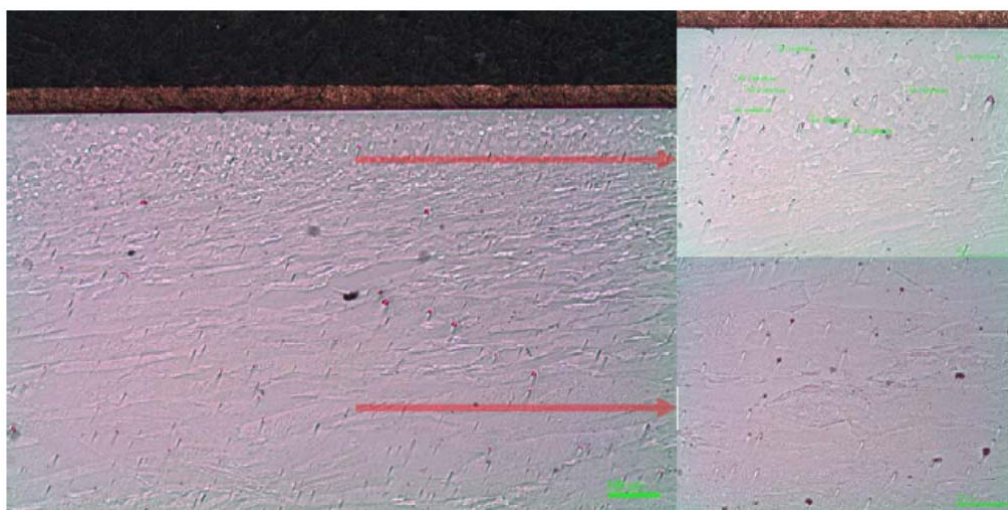


Figure 8.50: Optical micrographs of etched Fe12Cr (un-tested) featuring ferrite grains with no uniformity in size at the edges and large oriented grains in the middle.

Based on these previous studies, carburization of Fe12Cr via oxidation by S-CO<sub>2</sub> was tested by means of Vickers microhardness tests and etching of the cross-sectioned samples with 5% nital solution. Cross-sectional optical micrographs of the etched samples are shown in figure 8.50

featuring relatively small but uneven grain size distribution at the edges and relatively large oriented grains in the middle.

Micro hardness tests were conducted on 600, 800 and 1000 hour exposed samples with a Wilson Tukon 1202 microhardness tester. A sample measurement (performed on T122-1000h exposed sample) is provided in the figure 8.51 featuring the approach employed to determine the carburization depth. Vickers hardness tests were conducted using 50g load for 20 seconds. Indents were spaced laterally and vertically 20 microns apart one another. Test were performed at least from three distinct locations and averaged. As a base-line, similar tests were also performed on the as-received untested samples of Fe12Cr steel. The tests results are presented in the figure 8.52 where some degree of hardness increase can be observed. However, due to uneven grain size distribution near the oxide scale and non-uniform oxide formation (thick-duplex vs thin chromia), the results were not considered conclusive in regards to making an assessment of the depth of carburization.

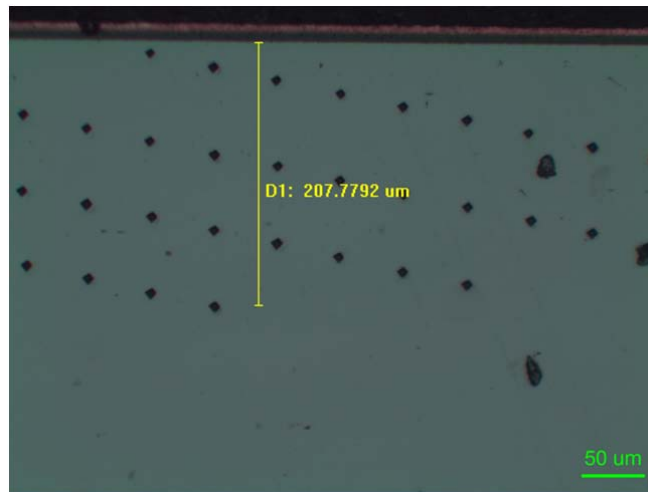


Figure 8.51: Optical micrograph of hardness tested sample (T122-1000h) featuring a sample measurement approach where indents were spaced laterally and vertically 20 microns apart one another.

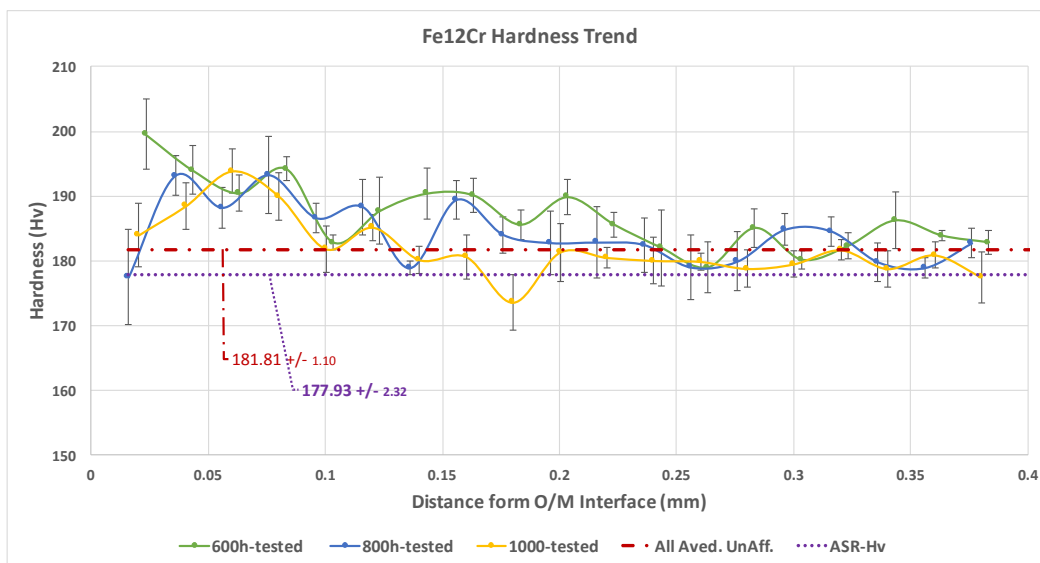


Figure 8.52: Microhardness test results of 600, 800, and 1000h exposed Fe12Cr alloy. The hardness values for the untested Fe12Cr sample given with respect to averaged hardness of un-affected region and hardness of as received Fe12Cr.



Regarding the nodular oxide formation on the Fe12Cr samples surfaces, the expected carburization, as previously alluded, is much more under the nodular regions where the oxide layers are thickest. This is shown in EDS elemental maps in figure 8.53, where regions of thicker nodular oxide formation showed carbon enrichment compared to thinner regions which constituted the protective scale.

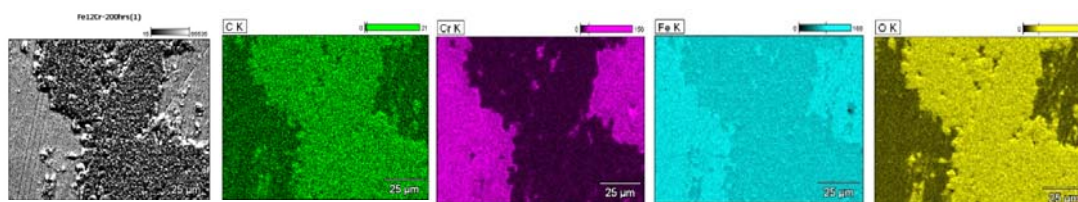


Figure 8.53: SEM-EDS elemental mappings performed on the plan views surface of Fe12Cr after 200h oxidation in S-CO<sub>2</sub> showing carbon enrichment in the region of thick nodular Fe-rich oxide. Carbon detection by EDS is deemed qualitative.

#### 8.4.4. Carburization of T22, T92, and T122 ferritic steels

As of an essential tool for evaluating carburization, etching was used for the initial assessment of carburization. Various samples of T22, T92 and T122 were etched using primarily 1-10 % nital solution. After etching sample surfaces were examined by SEM-EDS. For the T22 steel exposed for 400 hours (etched with 1% nital solution), carburization was not uniform similar to non-uniformity in the oxide scales. Figure 8.54 presents the optical micrographs featuring all different etched surfaces of T22 400h tested sample. These optical observations revealed that the degree of carbon diffusion depth varies as for the oxide thicknesses indicating the interlink between the two phenomenon.

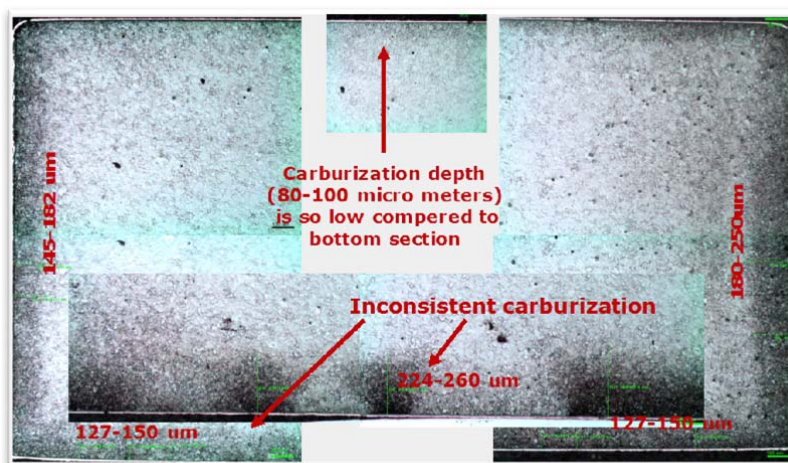


Figure 8.54: Optical micrograph taken with the etched sample of 400h exposed T22 featuring carburization (relatively darker areas) which varies throughout the sample surface.

In the third chapter, the differences of oxide thicknesses on opposite surfaces of samples were explained due to the fact that distribution of fresh CO<sub>2</sub> in the autoclave differs. In addition, local the oxide thicknesses were also shown to be significantly different around the sample possibly due to local CO partial pressure increase. With respect to previously referred carbon activity and CO partial pressure relations, the carburization expected to be significantly higher with oxide scale formation in some local regions.

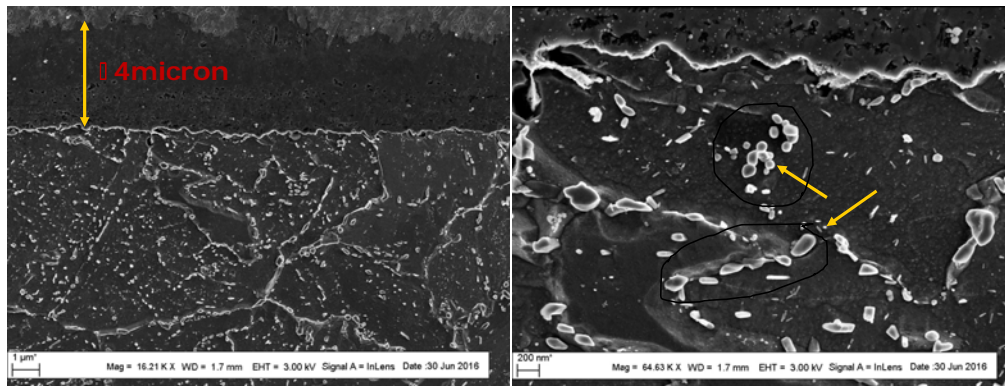


Figure 8.55: SEM micrograph taken with the etched sample of 400h exposed T22 featuring  $\approx 4 \mu\text{m}$  duplex oxide formation and individual carbide particles which are  $\approx 200 \text{ nm}$ .

Further SEM observations, presented in the figure 8.55 revealed individual carbides which are approximately 200 nm. However, as-received T22 contains 0.1 wt.% carbon which is much more than the solubility limit of C in ferrite. Therefore, no assessment regarding whether these were formed as a result of carburization or they were presented in the base beforehand was possible. Only possible explanation is that the increased C content inside the base material increases the carbide distribution density. Therefore, as for the time of exposure to S-CO<sub>2</sub> increases, the darker regions were expected to increase. This effect was successfully demonstrated for T92 and T122 but not that effectively for T22. The result of etching observation after 200 hours exposure is presented in the figure 8.56 where the level of carburization (determined as  $\approx 120 \mu\text{m}$ ) is not perfectly clear.



Figure 8.56: SEM micrograph taken with the etched sample of 200h exposed T22 featuring carburization depth of  $120 \mu\text{m}$ .

Etching of T22 steel samples exposed for 1000h did not reveal any sharp contrast between a potentially carburized region and the base steel. This could be due to lack of etching or the other possibility is that the sample is carburized through its entire thickness. Therefore, GDMS analysis was performed on this sample and the results are presented in the figure 8.57. The GDMS results did not reveal any distinct carbon depth profile, but it does not again rule out the possibility of though thickness carburization.

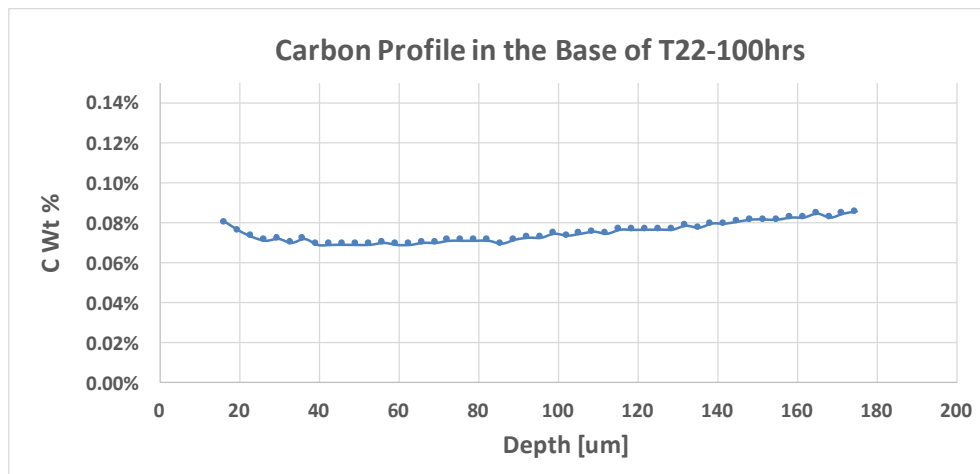


Figure 8.57: GDMS carbon profile showing carbon depth for the 1000h exposed T22 steel.

The carbon profile of T122 steel also performed by GDMS is shown in figure 8.58 along with the GDMS analysis for T22 steel. The carbon profile for T122 steel (to be discussed in detail) clearly indicates carburization. When viewed in conjunction with the profile for T122, the T22 steel does show evidence of carbon enrichment suggesting through-thickness carburization however the carburization results for T22 were still inconclusive. All GDMS analysis was performed by Evans Analytical Group.

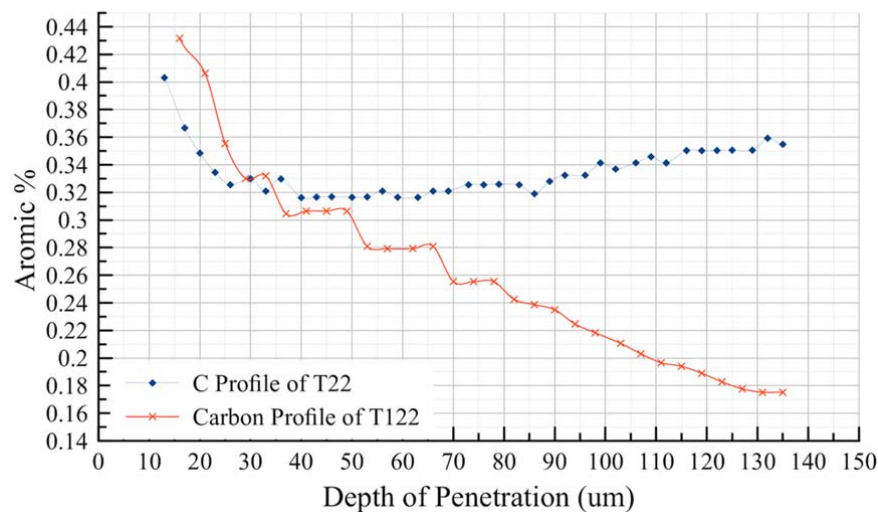


Figure 8.58: GDMS carbon profile showing carbon concentration as a function of depth for T122 steel after exposure for 1000h (the profile for T22 steel is also seen as blue line).

Fig. (8.59) shows a low magnification image of T122 steel exposed for 1000 hours (etched with nital solution), where carburization was observed uniformly around the sample.



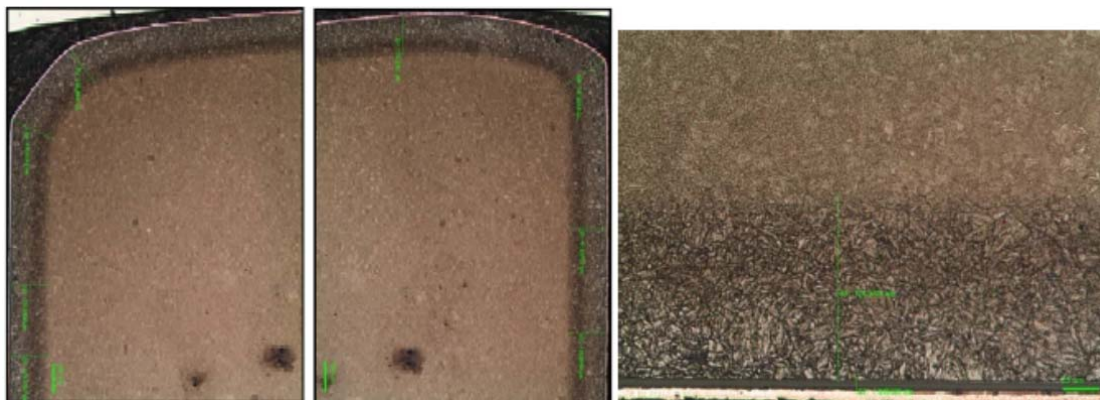


Figure 8.59: Low magnification images of T122 steel exposed for 1000 hours showing an approximately 120  $\mu\text{m}$  carburization depth around the sample.

Further SEM observations, presented in the figure (8.60) revealed individual carbides and their relative distribution in the grains and the grain boundaries, with grain boundaries being preferred sites for carbide phase formation. In addition, SEM-EDS elemental maps and line scans further performed revealed Cr-carbide enriched grain boundaries (Figure 8.61). Of particular importance is that carbon diffusion may have led to carbide phase formation of  $\text{M}_{23}\text{C}_6$  to  $\text{M}_7\text{C}_3$  type carbides, most likely those of Cr.

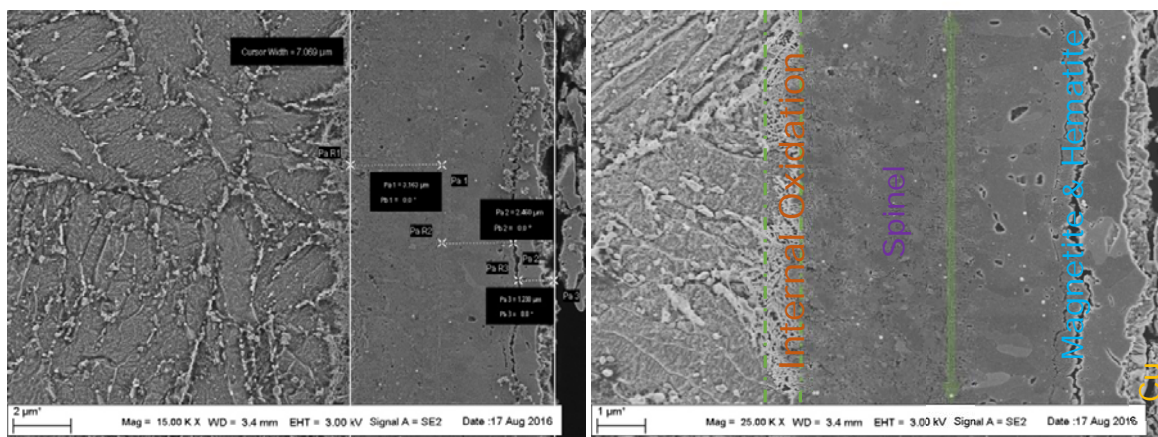


Figure 8.60: SEM micrograph taken with the etched sample of 1000h exposed T122 steel featuring  $\approx 7 \mu\text{m}$  duplex oxide formation and approximately 200 nm carbide particles located mainly at the grain boundaries in the region underneath the oxide layer (i.e. the carburized layer).

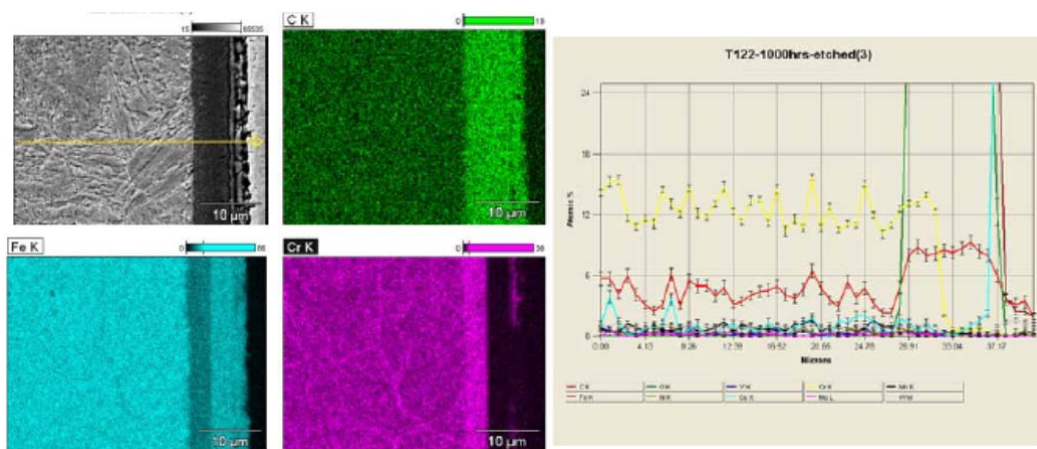


Figure 8.61: SEM-EDS analyses performed on the etched sample of 1000h exposed T122 steel where Cr and C enrichment along the grain boundaries are visible.

Microhardness measurements were performed on the cross-sectioned T122 steel samples exposed for 1000 hours and the results are shown in Fig. 8.62 along with the GDMS profiles shown earlier.

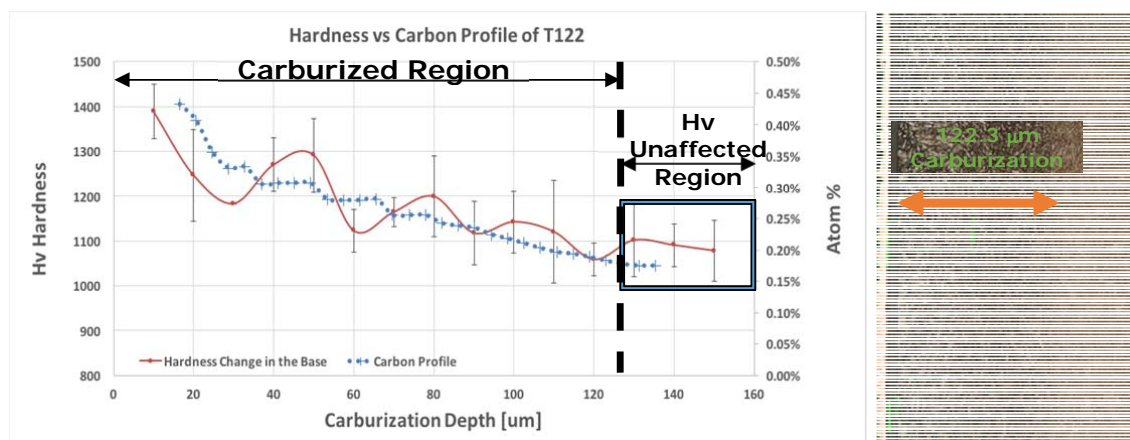


Figure 8.61: GDMS carbon and Vickers hardness profile featuring diffusion profile of C detected on T122 sample after 1000h exposure to S-CO<sub>2</sub> given with respect to optical micrograph of etched sample.

The results from GDMS analysis, microhardness test, and optical observations for T122 steel (exposed for 1000 hours) are consistent and clearly indicate the formation of an approximately 120  $\mu\text{m}$  carburization depth after 1000h exposure to CO<sub>2</sub> at 450 °C and 20 Mpa. The GDMS and hardness results appear to follow a diffusion-like profile.

#### 8.4.5. Carburization results of T92 ferritic steel

T92 steel samples after S-CO<sub>2</sub> exposures of up to 1000 hours (with 5 time intervals) were examined using optical microscopy to reveal the case depth of carburization. Additionally, microhardness measurements were performed along the depth of the carburized layer. As for T22 and T122 steels, SEM-EDS observations were also performed. EPMA-WDS, EPMA-WDS, and GDOES analyses were performed for the 1000 hour sample for a quantitative assessment of carbon intake. The obtained carbon profile inside the base steel of 1000h exposed T92 steel were compared with the profile observed with the Vickers hardness data. Polished samples in cross-section of T92 steels exposed to various intervals up to 1000 hours were etched and examined using optical microscopy and depth of carburization was measured and the results are shown figure 8.62. For 200h exposed sample, the overall carburization seems to occur up to approximately 90  $\mu\text{m}$ , while this depth increases to 180 and 200  $\mu\text{m}$  for exposure times of 600h and 1000h, respectively, indicating a parabolic growth behavior. A comparison of oxide scale growth and depth of carburization are

presented in figure 8.63 which indicates that carburization depth and oxide layer growth are interlinked.

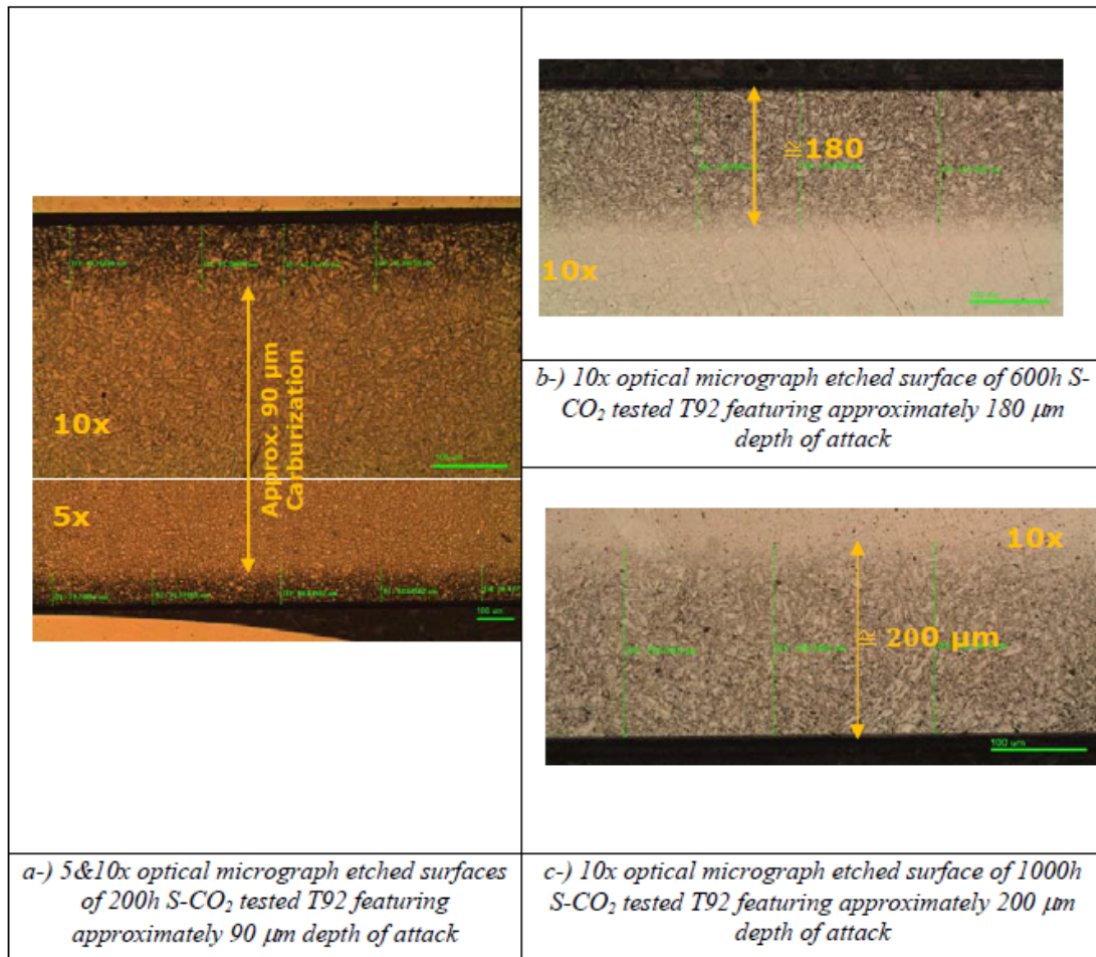


Figure 8.62: Optical observations of carburization depth on the etched surfaces of T92 steel exposed to  $\text{CO}_2$  at  $450^\circ\text{C}$  and 20 MPa for (a) 200h, (b) 600h, and (c) 1000h.

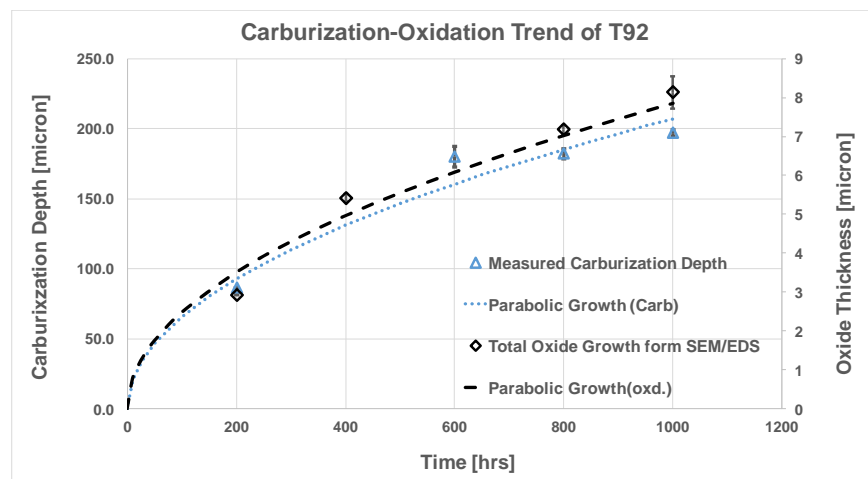


Figure 8.63: Comparison of carburization layer depth and oxide layer growth for T92 steel exposed to  $\text{CO}_2$  at  $450^\circ\text{C}$  and 20 MPa.



Figure (8.64a) shows SEM images of over-etched (with nital) samples of the carburized region (~90  $\mu\text{m}$  depth) that reveal individual carbide phase particles of approximately 200 nm in the microstructure. While the etching process no doubt removes some of the carbides, increased density of carbide distribution at the grain boundaries is observed. Figure (8.64b) presents the results of SEM-EDS elemental maps and point analyses with acquired wt.% data featuring carbide in dense and lighter areas in terms of carbide forming element enrichments. Points number 2, 4, 5 features over etched sites where base iron is removed revealing carbides. Therefore, both elemental mappings and point analyses indicate carbon and carbide forming element in quantity with respect to base metal content. On the other hand, points 1, 3, 6, represent local sites where carbides may have been removed upon etching.

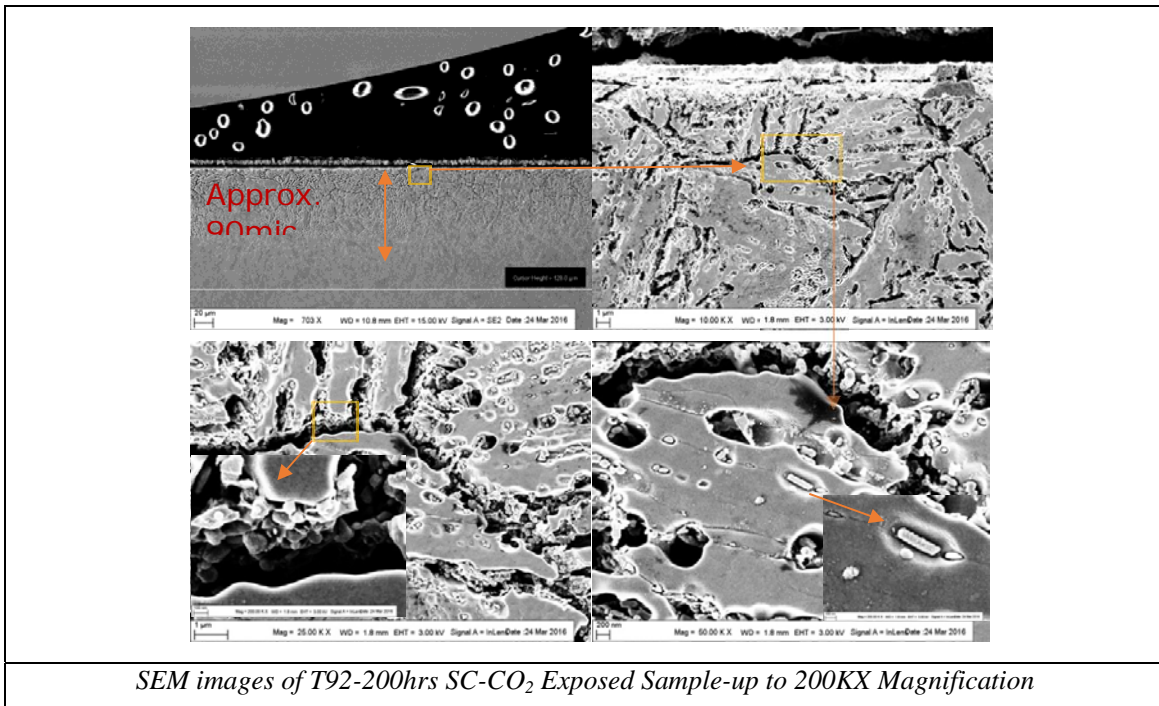


Figure 8.64a: SEM micrographs of carburized of T92 steel after 200h exposure to S-CO<sub>2</sub> featuring approximately 90  $\mu\text{m}$  depth of attack with 200 nm individual carbide particles. Samples were intentionally over-etched to reveal carbide phases.

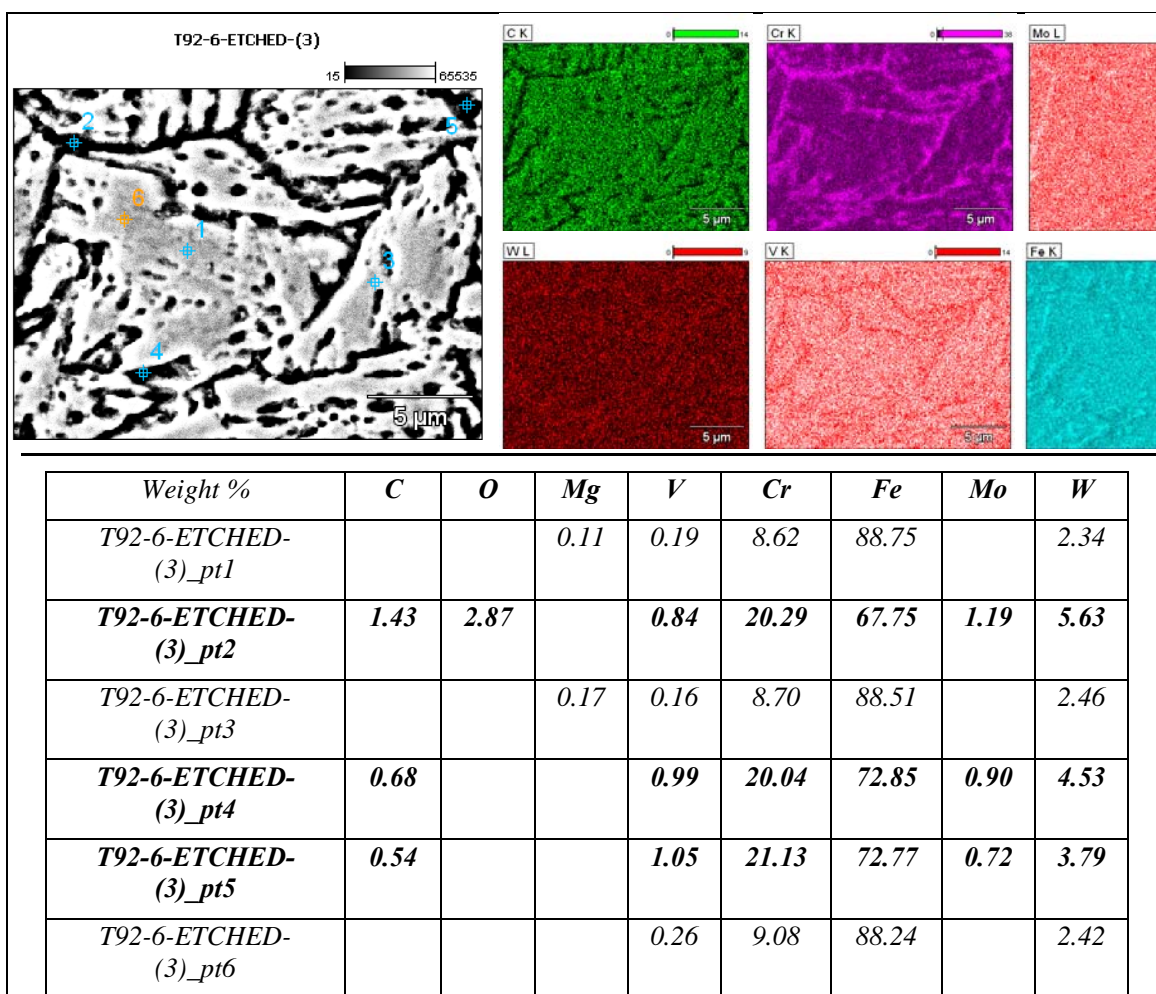
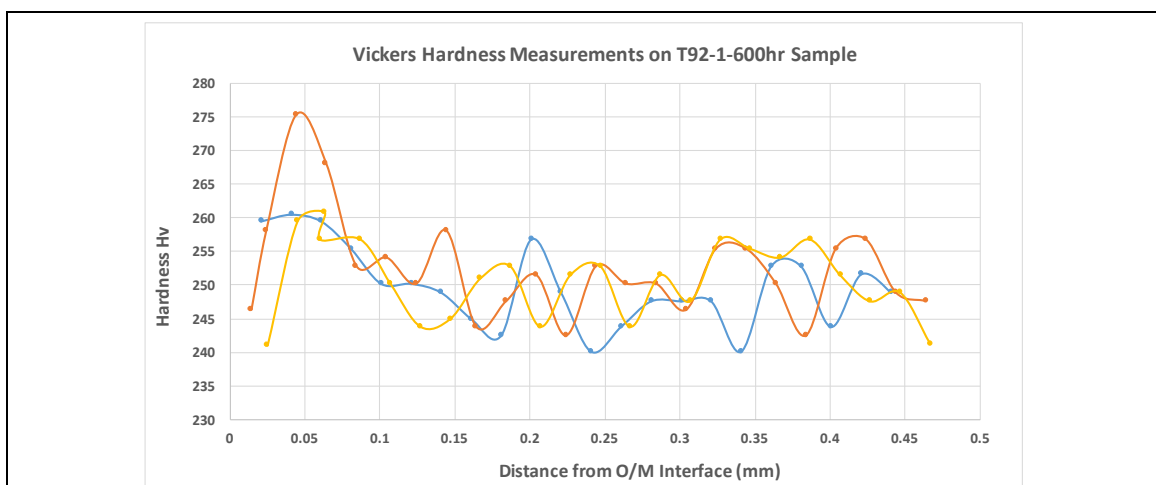
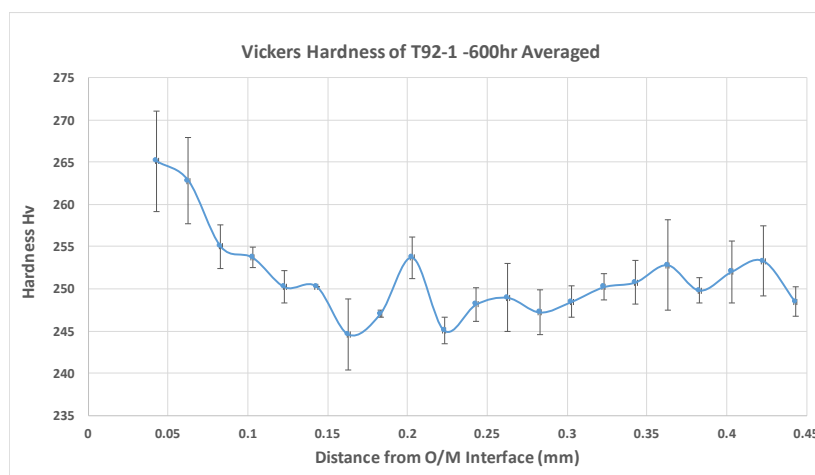


Figure 8.64b: SEM-EDS point analyses of T92-200hrs SC-CO<sub>2</sub> exposed sample with resulted data given in wt.%. The samples were intentionally over etched to reveal the carbide phases (some removal of carbide particles from their sites is therefore observed, as expected).

In addition to optical and SEM imaging of carburized layers, microhardness tests were performed as a function of depth below surface for T92 steel samples from 200h and 1000h tests. Examples of results of these measurements are shown in figure (8.65).



a-) Vickers hardness measurements performed on T92 after 600h exposure to S-CO<sub>2</sub>



b-) Averaged Vickers hardness trend in the base of T92-600h sample

Figure 8.65: Microhardness measurements (a) with hardness measurements at three locations and (b) averaged hardness value for T92 after 600h exposure.

In the figure (8.65a) three measurements performed on three distinct locations on T92 after 600h exposed to S-CO<sub>2</sub> are shown. As it can be seen, in the first 10-20  $\mu\text{m}$ , Hv values depart from the general trend. One explanation is that this is caused by plastic deformation which is not adequately supported by the oxide-metal scale under the applied force/pressure. Figure 8.66 shows the hardness profiles of T92 for 200, 600, and 1000h exposures.

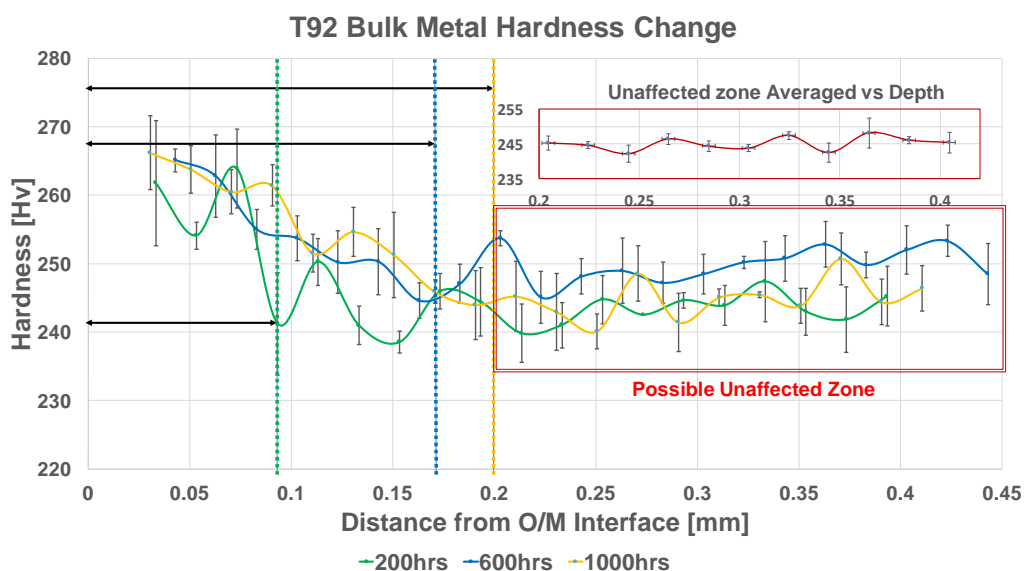


Figure 8.66: Hardness profiles of T92 after S-CO<sub>2</sub> exposures of 200, 600, and 1000h.

The hardness profiles presented in the figure 8.66 indicate approximate carburization depths of 90, 175 and 200  $\mu\text{m}$  for exposure times of 200, 600, and 1000h. These observations are consistent with optical observations of carburized regions. Based on the diffusion-based hardness and carburization profiles presented, the hardness data was further used in order to present diffusion modeling of carburization. This approach is based on the diffusion theory and has been also explored in literature [125]. Due to thermodynamic considerations, it is assumed that carbon forms carbides with alloying elements whenever carbon presence increases in the sample. Also, considering the solubility of carbon in alpha ferrite, this assumption is supported since all the excess carbon are already present as carbides throughout the sample.

In an attempt to correlate hardness changes with carbon profile, we have considered the data from work of Rouillard, F., and T. Furukawa for 250 bar 350h and 250 bar 1000h where maximum carbon concentration is fixed inside the base metal (Figure 8.67).

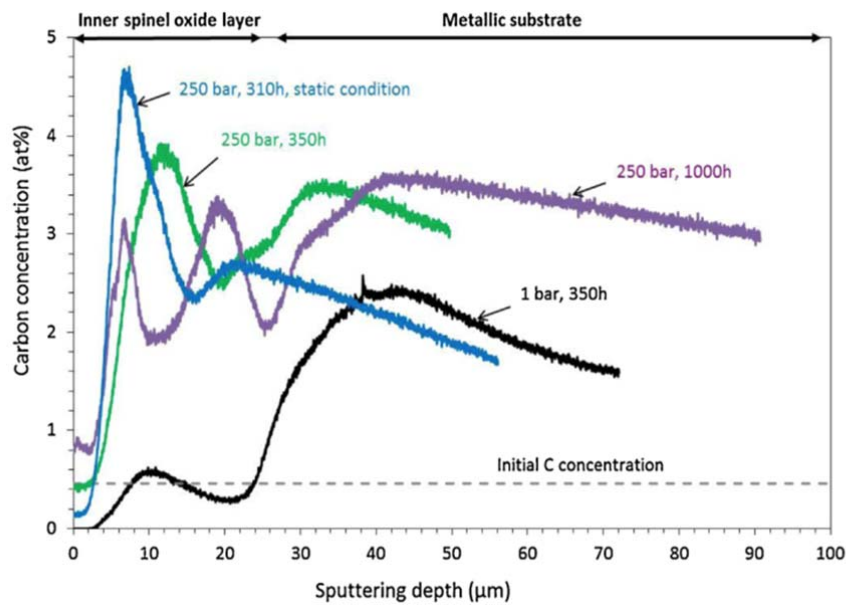


Figure 8.67: GDOES profiles of T91 after  $\text{CO}_2$  exposure at  $550^\circ\text{C}$  for various times and pressures where green line (250 bar-350h) and purple line (250 bar-1000h) present the same maximum carbon concentration underneath the oxide scale (data from Rouillard, F., and T. Furukawa).

Fick's second law of diffusion with an assumption that the diffusion is independent of carbon concentration for the carbon profile is as follows:

$$C(x, t) = C_s - (C_s - C_o) \left( \text{erf} \left[ \frac{x}{2\sqrt{Dt}} \right] \right) \quad (8.56)$$

where  $C_s$  and  $C_o$  denote the carbon concentration of surface (in this case fixed point inside the base metal after carburization) and original alloy carbon content, respectively, while  $C(x, t)$  represents the carbon concentration as a function of location of time elapsed ( $t$ ) inside the base metal at distance  $x$ .  $D$  is the diffusion coefficient of carbon in the base metal.

Thus, at the unaffected zone where no case hardening exists,

$$C(x, t) = C_o \quad (8.57)$$

Under the condition,

$$\left( \text{erf} \left[ \frac{x}{2\sqrt{Dt}} \right] \right) = 1 \quad (8.58)$$

the equation (8.58) must be satisfied for a constant value,  $K$ , even though the actual solution can be arrived at infinity.

$$\frac{x}{2\sqrt{Dt}} = K \quad (8.59)$$

Thus, the equation (8.59) can be used to extrapolate the depth of attack if both  $x$  and  $D$  are known.

However, the preliminary hardness results indicate that the diffusion coefficient of carbon in alpha-ferrite ( $D=4.58\text{e-}13 \text{ m}^2\text{s}^{-1}$  at  $450^\circ\text{C}$ ) does not match with the experimental hardness profile and optical observations of carburization depth. Therefore, using the diffusion coefficient in alpha ferrite is not a good approach with the above provided approximation with the equation (8.59). In addition, the constant  $K$  depends upon the experimental observations and would be different for each experimental case. An alternative approach could be to consider carbon concentration mid-way through the carburization depth presented as shown below:

$$C(x, t) \rightarrow \left(\frac{Cs+Co}{2}\right) = Cs - (Cs - Co) \left(\text{erf} \left[\frac{x}{2\sqrt{Dt}}\right]\right) \quad (8.60)$$

The above equation is only satisfied with the following equality:

$$\text{erf} \left[\frac{x}{2\sqrt{Dt}}\right] = \frac{1}{2} \quad (8.61)$$

where  $\left[\frac{x}{2\sqrt{Dt}}\right] \cong 0.477$ .

Therefore,

$$x \cong 2 \times 0.477 \sqrt{Dt} \quad (8.62)$$

where above relation, if  $x$  is known, gives the experimental diffusion coefficient of carbon in the base metal.

An analogous diffusion based fit for hardness profile was performed as follows:

$$H_v(x, t) = H_v^{\text{Surface(max)}} - \left(H_v^{\text{Surface(max)}} - H_v^{\text{Unaffected zone}}\right) \left(\text{erf} \left[\frac{x}{2\sqrt{Dt}}\right]\right) \quad (8.63)$$

The hardness profile as a function of depth is correlated with carbon profile in Figure 8.68.

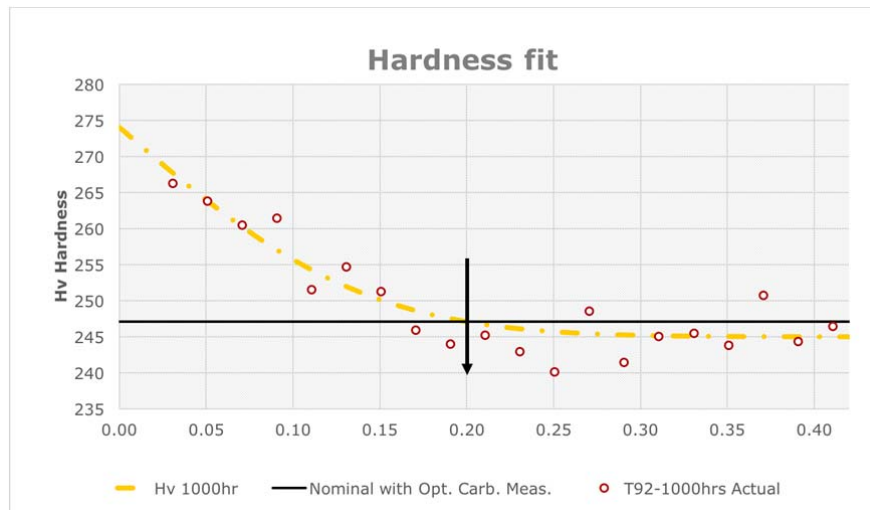


Figure 8.68: Hardness fit where red circles present the actual Vickers hardness values of T92-1000h exposed sample, yellow dashed line present the fit with R-square of 0.86, and intersect of black-line and arrow represent the optical observation of carburization depth.

As presented in the figure 8.69, the extrapolation of the fit to lower values still works with perfect-match to carburization measurements by optical observations. Since the above presented fit perfectly matches with the optical observations revealing the carburization depth. This leads to an average value of  $1.07\text{e-}14 \text{ m}^2\text{s}^{-1}$  as of carbon diffusion coefficient in T92 steel. Figure 8.70 presents carbon diffusion for extrapolated exposure times.

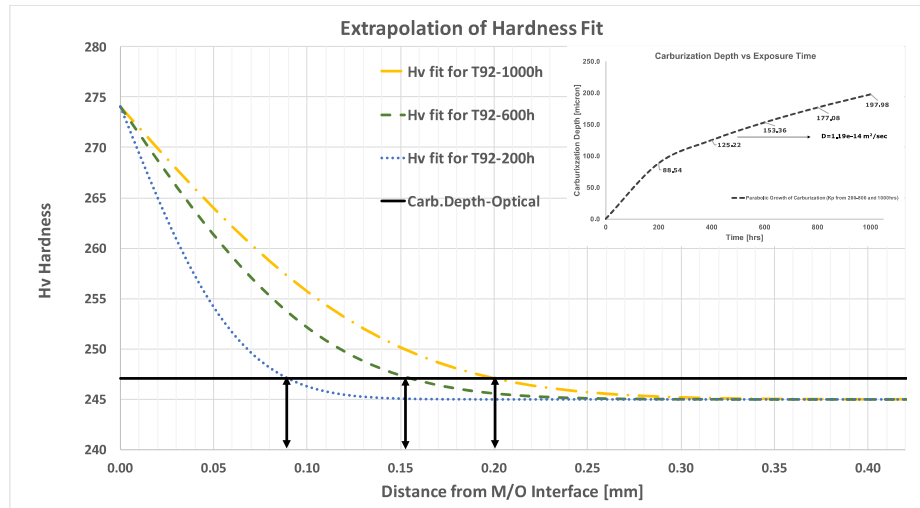


Figure 8.69: Extrapolation of hardness fit to lower exposure times given with the same intersects of black-line which still perfectly satisfies the optical observations.

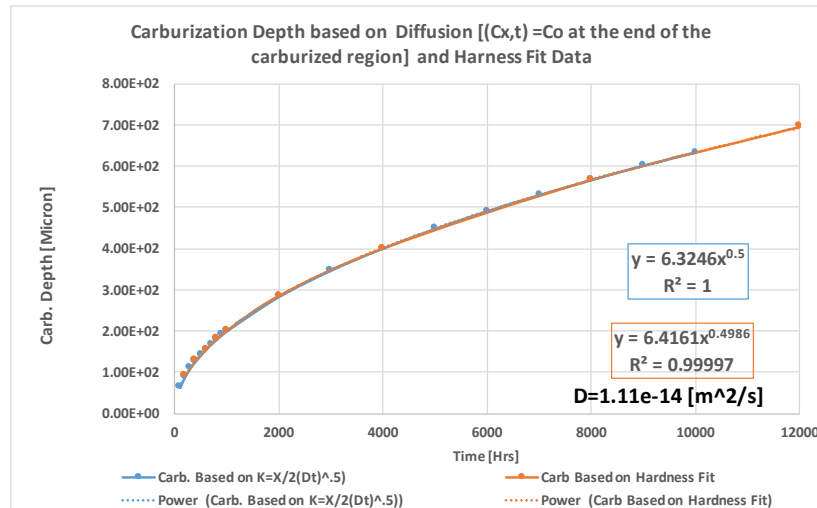


Figure 8.70: Extrapolation carburization depth for longer exposure times using experimental and models from this study.

Carbon enrichment through the carburization depth was measured with EPMA-WDS analysis technique. Test performed on the cross-sectioned T92 sample after 400h exposure to S-CO<sub>2</sub>. Prior to measurement, a mirror polished sample plasma cleaned for 40 minutes in order to eliminate all the surface hydrocarbons capable of altering the results. In order to prevent the carbon build-up point analysis approach was employed instead of continuous line-scans. The analysis points were laterally and vertically organized so that the relative spacing from oxide/gas environments was 1  $\mu\text{m}$  for first 7 data points and 5 and 10  $\mu\text{m}$  microns for the rest. Figure 8.71 depicts the carbon profile for first 30  $\mu\text{m}$  where a declining (diffusion-like) profile can be observed.



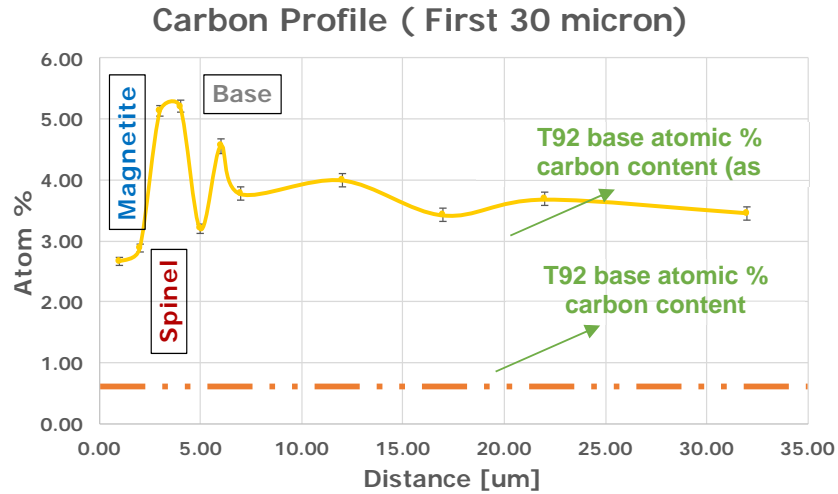


Figure 8.71: First 30  $\mu\text{m}$  carbon profile of T92 steel exposed for 400h by EPMA-WDS analysis.

To get a prediction of carbide phases present in the carburized layer (e.g.,  $\text{M}_{23}\text{C}_6$ ,  $\text{M}_7\text{C}_3$  and  $\text{M}_3\text{C}_2$ ), a part of Cr-C section of Fe-Cr-C ternary diagram at 450 °C is presented in the figure 8.72 featuring required carbon weight concentrations for the formation of various carbide phases.

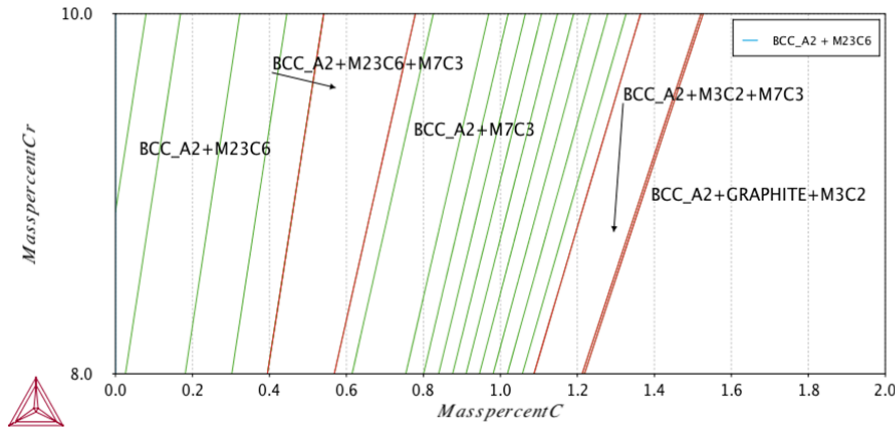


Figure 8.72: Section of Fe-Cr-C ternary diagram at 450 °C featuring required C wt. % for formation of  $\text{M}_{23}\text{C}_6$ ,  $\text{M}_7\text{C}_3$ , and  $\text{M}_3\text{C}_2$  types Cr-carbide formations.

With the previous assumptions and calculated Fe-Cr-C ternary diagram, Figure 8.73 is presented featuring carbon concentration decline with corresponding carbide formation for T92 steel after 400h exposure to SC- $\text{CO}_2$ .

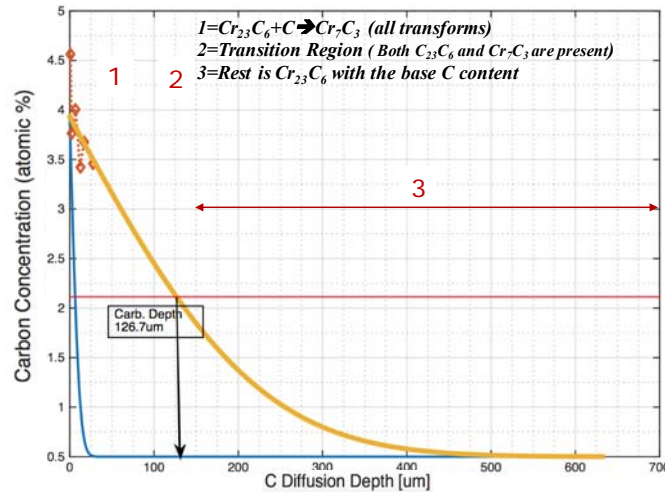


Figure 8.73: Carbide transition underneath the duplex oxide scale of T92 steel after 400h exposure showing depth regimes of carbide formation. The dashed line with rectangle points are from EPMA-WDS measurements and yellow line is obtained best fit representing diffusion profile of C in T92-400h sample.

As per the above illustration, only  $\text{Cr}_7\text{C}_3$  type carbide formation is expected to occur for up to 100  $\mu\text{m}$  and between 100-140  $\mu\text{m}$  both  $\text{Cr}_7\text{C}_3$  and  $\text{Cr}_{23}\text{C}_6$  are expected form in T92 steel for 400h exposure. To examine carburization further, GDOES analysis technique was performed for T92 steel sample after 100hr exposure. Analyses was performed outside by HORIBA Scientific. In order to determine the carbon profile both inside the duplex oxide and beneath it, samples were sputtered up to a depth of 160  $\mu\text{m}$ . The obtained carbon and oxygen profiles is shown in the figure 8.74.

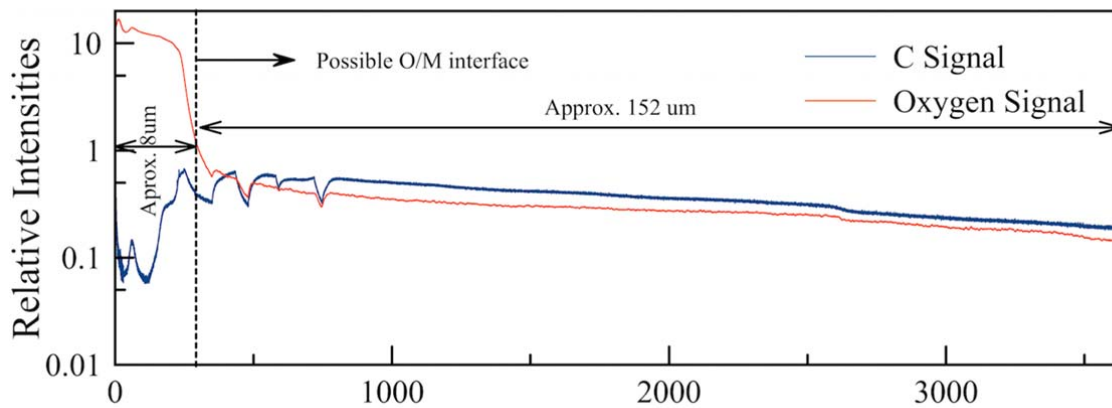


Figure 8.74: Carbon and oxygen profile of T92steels as determined by GDOES technique for T92 steel after exposure to  $\text{CO}_2$  at 450 °C and 20 MPa for 1000h.

The concentration profiles shown in figure 8.74 features three distinct regions. In the first region closest to the surface, the relatively high oxygen signal is observed signifying the presence of the outer Fe-rich oxide layer. In the first 1 or 2  $\mu\text{m}$  from surface, a spike in both O and C signals exist most likely indicating outer hematite and magnetite regions. Approximately half-way through the duplex oxide layer up to magnetite-spinel interface, the carbon profile is at its lowest value. This is expected because the presence of carbon in the outer magnetite layer is not likely because carbon from surface reactions is not expected to diffuse through. The increase in carbon signal inside the

spinel layer (last 4  $\mu\text{m}$  of the specified 8 $\mu\text{m}$ , figure (5.32)) until the metal/oxide interface is due to local voids created inside the spinel layer where CO build-up can lead to carbon formation. Assuming limited diffusion of carbon from spinel layer to base steel, the carbon flux is limited leading a concave carbon profile. The spikes of C-O signals inside the base of T92 are simply ignored since no internal changes such as internal oxidation, irregular distribution of alloying elements or impurities are expected.

Regarding the relative maximum and minimum carbon intensities shown in GDOES result, max occurs at a value of approximately 0.32 inside the sample while the minimum value obtained is around 0.18 at 160  $\mu\text{m}$  deep inside the base steel (occurs at  $(\text{Cs}+\text{Co})/2$ ) is a reasonable assumption. In general, the trend in carbon diffusion into the base steel is clearly observed consistent with the results obtained from other techniques.

#### 8.4.6: Kinetics of Carburization for T22, T92, and T92 Steels

Figure 8.75 provides the depth of carburization for the three steels and in general the carburization thicknesses appears to increase as the concentration of carbide forming elements (e.g., Cr) decreases in the base steel.

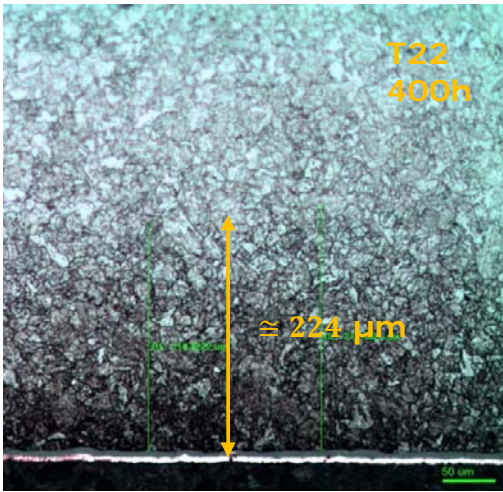
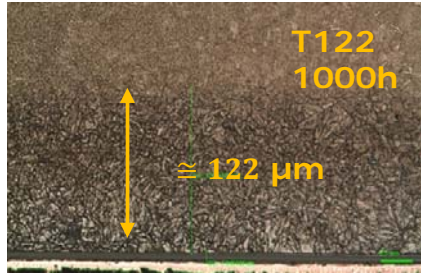
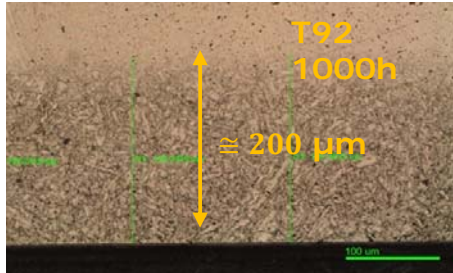
	 <p>b-) Optical micrograph etched surface of 1000h S-CO<sub>2</sub> tested T122 featuring approximately 122 <math>\mu\text{m}</math> depth of attack</p>
<p>a-) Optical micrograph etched surfaces of 400h S-CO<sub>2</sub> tested T22 featuring approximately 224 <math>\mu\text{m}</math> depth of attack</p>	 <p>c-) Optical micrograph etched surface of 1000h S-CO<sub>2</sub> tested T92 featuring approximately 200 <math>\mu\text{m}</math> depth of attack</p>

Figure 8.75: Depth of carburized layer for (a) T22 (2Cr), (b) T122 (12Cr), and (c) T92(9Cr) ferritic martensitic steels.

For steady state carburization the parabolic trend is given as:

$$x_c^2 = k_p^{carb} \cdot t \quad (8.64)$$

The constant  $k_p^{carb}$  values of T92 are presented in the table (5.1) with a reference case of C diffusion in alpha-ferrite.

Table 8.8: Experimentally determined carburization constants along with values for reference of carbon diffusion in  $\alpha$ -iron.

<i>Alloys</i>	<i>Carburization Rates [<math>m^2s^{-1}</math>] via Experimental Observations</i>
<b><math>\alpha</math>-Ferrite (by provided by Arrhenius-like relation [8])</b>	<i>4.59e-13</i>
<b>T22 (2Cr)</b>	<i>3.48e-14</i>
<b>T92 (9Cr)</b>	<i>1.07e-14</i>
<b>T122 (12Cr)</b>	<i>4.13e-15</i>

As presented in the Table 8.8 the observed carburization rates tend to decrease as the Cr concentration of the base steel increases. With respect to carbon diffusion in alpha-iron, these decreases vary by one or two orders of magnitude. This is because the carbon diffusing into the steel gets tied up as carbides (preventing further diffusion) and consequently greater the carbide forming alloying elements in the base steel, lower the carburized layer thickness. The excess carbon then diffuses over this zone until the case carburization depth  $x_C$  at which elements with present  $a_C$  can react to form new carbides. Therefore, as the carbide forming element content increases (T22<<T92<T122), the case diffusion depth of carburization decreases as has been experimentally observed in this study.

To understand why the carbon diffusion is less in alloy steels than in alpha-iron, equation (5.1.4.2) is presented (for which permeability of carbon with respect to chrome is significantly higher  $N_C^{(s)} D_C \gg N_{Cr}^{(o)} D_{Cr}$ ) [21]:

$$k_p^{int.} = \frac{\varepsilon N_C^{(s)} D_C}{v N_{Cr}^{(o)}} \quad (8.65)$$

Above  $N_{Cr}^{(o)}$  is the original chrome concentration of alloy forming  $N_{C_v}$  type carbide for which  $v$  is the stoichiometric coefficient;  $\varepsilon$  is the diffusional blocking factor can be assumed as one [21];  $D_C$  and  $D_{Cr}$  are the diffusion coefficient of carbon and chrome in the alloy respectively;  $N_C^{(s)}$  is the mole fraction of solute carbon.

#### 8.4.7. Summary of the Chapter

In this chapter, the carburization effects in ferritic-martensitic steels exposed to S-CO<sub>2</sub> environment at 450 °C and 20 MPa, are presented. The results clearly indicate that carburization and oxidation are interlinked phenomena. One of the key mechanisms for carburization is the permeation of CO<sub>2</sub> through voids and nano-channels created by the diffusion, where CO<sub>2</sub> decomposes to CO which then forms carbon by reaction with free metal. This mechanism is predicated by the available space model. The free carbon then initiates carburization in the inner scale. In support of this theory, the results indicate that pure Fe exhibits no carburization because there is no available space. For the T22, T122, and T92 steels the observations of carburization was well supported by microhardness measurements. In fact, the carbon diffusion profiles matched very well with the microhardness profiles. GDMS measurements indicated that for low Cr T22 steel through-thickness carburization was observed, while for the 12%Cr T122 steel a relatively shallow diffusion profile of carbon was observed. The kinetics of carburization, was rigorously studied for T92 steel using optical microscopy, SEM-EDS, and microhardness measurements at various test intervals. More quantitative approach regarding carburization was also conducted using EPMA-WDS technique. The first 30  $\mu m$  of profile by EPMA-WDS compared well with the literature findings using GDOES technique. These experimental studies allowed for calculation of diffusion coefficient of carbon in T92 steel which

allowed for longer term predictions of carburization depth. Finally, the kinetics of carburization for alpha ferrite was investigated and compared to the engineering alloys. The data clearly indicates that the depth of carburization correlates inversely with the concentration of Cr in the steel.

## **8.5. Conclusions and Summary**

### **8.5.1. Conclusions**

Three ferritic-martensitic steels, T22 (~2%Cr), T92 (~9%Cr), and T122 (~12%Cr) were tested in research grade supercritical CO<sub>2</sub> (99.999%) at 450 °C and 20 MPa, with the broader goal of evaluating the use of this class of steels in supercritical CO<sub>2</sub> Brayton cycle. Additionally, pure Fe and Fe-12%Cr binary alloys were also tested for achieving a more fundamental baseline understanding. Tests were performed for exposure durations up to 1000h with samples being removed at 200 hours intervals for analysis. Post-test characterization was performed using a range of techniques including weight change measurements, optical microscopy, microhardness tests, scanning electron microscopy-energy dispersive spectroscopy (SEM-EDS), x-ray diffraction (XRD), glow discharge mass spectroscopy (GDMS), glow discharge optical emission spectroscopy (GDOES), and electron probe micro analyzing-wave length dispersive spectroscopy (EPMA-WDS). The research broadly encompasses four areas, namely, experimental evaluation of oxidation, application of the “available space model” to the experimental oxidation results, experimental evaluation of carburization, and theoretical treatment of carburization based on experimental data.

### **8.5.2 Oxidation in Supercritical CO<sub>2</sub> Environment**

Pure Fe formed Fe<sub>3</sub>O<sub>4</sub> (magnetite) layer on the surface which exhibited notable spallation and severe internal oxidation was observed in the base Fe. The oxide surface was of whisker-like morphology which dramatically increased the surface area and could have led to high oxidation rates. The Fe12Cr binary alloy exhibited nodular oxide composed of an outer magnetite and an inner spinel layers. Adjacent to the nodules, surface was covered with very thin protective chromia layer. Additionally, the formation frequency of these nodules was observed to increase as time to S-CO<sub>2</sub> exposure increase. This is also supported with the observations on standard deviation of weight gain featuring a decrease trend. The T22 steel showed oxide spallation, and the surface also revealed a blister-like morphology and cracking. Cross-sectional examination showed a duplex oxide formation consisting of an outer magnetite layer and an inner Cr-rich spinel oxide layer of Cr<sub>x</sub>Fe<sub>(3-x)</sub>O<sub>4</sub> stoichiometry. T92 and T122 steels however formed a uniform duplex oxide throughout the 1000h exposure. Neither spallation nor break-away were detected by plan view or cross-sectional SEM imaging of the samples. As in the case of T22 steel, both T92 and T122 steels also exhibited a predominantly duplex oxide layer consisting of an outer magnetite layer and an inner Cr-rich spinel oxide layer of Cr<sub>x</sub>Fe<sub>(3-x)</sub>O<sub>4</sub> stoichiometry. However, grazing incident XRD and EPMA analyses also showed the formation of outermost Fe<sub>2</sub>O<sub>3</sub> (hematite) on these steel.

The basis of duplex oxide layer formation in the three steels is explained by the “available space model” where outward diffusion of Fe cations leaves behind vacancies which coalesce to form voids and nano-channels which provides pathways for CO<sub>2</sub> to enter the system and react with Cr to form a spinel oxide. No Cr diffusion to outer layer was detected by SEM-EDS and EPMD-WDS analysis, as would be dictated by this model. Regarding the analytical basis of oxide simulation model, the stoichiometric Cr content in the spinel layer were approximated from the EPMA-WDS results. The value of x in Cr<sub>x</sub>Fe<sub>(3-x)</sub>O<sub>4</sub> spinel stoichiometry was determined to be 0.19, 0.59, 0.73, for T22, T92, and T122 steel, respectively.

### **8.5.3. Oxide Layer Thicknesses and Weight Gain**

Oxide layer thicknesses were measured using SEM-EDS line scans, and categorized as internal oxide, spinel layer, and magnetite layer. Of the three ferritic-martensitic steels, T122 steel exhibited the thinnest oxide layer on account of its high Cr content, while T22 developed the thickest oxide layer. For the basis of simulation by available space model, the global mass balance between outer and inner layers and tested against experimentally measured thickness.

The weight gain measurements showed the lowest gain for Fe12Cr due to the formation of a thin

protective chromia layer. Consistent with oxide thickness measurements, the weight gain for the three martensitic steels was inversely related to the Cr content of the alloys. The least performing alloy determined was T22. Regarding the engineering alloys T22, T92 and T122, the performance was revealed to improve with increased Cr content of steel. The available space model interlinks the growth of the magnetite and spinel oxide layers such that the layers grow while maintaining a constant ratio. This was demonstrated experimentally for the three ferritic martensitic steels, and furthermore the ratio of spinel to magnetite oxide layer thicknesses increased with increasing Cr content in the steel.

#### 8.5.4. Modeling and Simulation

Oxide growth modeling based on available space model (also referred to as void-induced duplex oxide growth) was performed by using some assumptions simplifying the conditions at the multilayered oxide scale boundaries. These include:

- The oxygen activity at the oxide/gas interface are the oxygen activities required the formation of  $\text{Fe}_2\text{O}_3$  through reduction of  $\text{Fe}_3\text{O}_4$
- The oxygen activity in between spinel layer and metallic base steel is approximated as the oxygen activity required for the oxidation of Fe to  $\text{Fe}_3\text{O}_4$
- Formation of  $\text{Fe}_2\text{O}_3$  as an outermost layer ignored
- Oxygen activities are independent of time
- No mass accumulation at the boundaries or loss at the oxide scale due to spallation
- The Fe flux in the spinel is equal to the Fe flux in magnetite at all the times

In regards to the last assumption stated above, the Fe diffusion coefficient in spinel in previous literature was only approximate. Therefore, diffusion coefficient of iron in spinel was deduced as a function of iron diffusion coefficient in magnetite for all the tested alloys forming inner spinel layer with different stoichiometries. A model based on these assumptions and global mass balance between the layers was then developed. The robustness of the model was initially tested for the alloys by essentially taking into account Cr stoichiometry in the spinel layer of various steels to validate whether a mass balance between the layer exists or not. T22 steel did not hold up to this test in regards to global mass balance in between of layers, and therefore model did not perfectly predict the observed kinetics.

First, modeling was performed using lattice-bulk diffusion approach. This approach was underestimated the actual kinetics observed. Grain boundary diffusion and thus the effective diffusion coefficients were subsequently introduced to account for the higher rates of oxidation. This combined with some literature data were then successfully used for modeling oxide layer growth, with model predictions being in excellent agreement with experimentally determined data, for T92 and T122 steels.

#### 8.5.5. Carburization

Significant carburization was observed in all steels studied (not in pure Fe). The results clearly indicate that carburization and oxidation are interlinked phenomena. One of the key mechanisms for carburization is the permeation of  $\text{CO}_2$  through voids and nano-channels created by the diffusion, where  $\text{CO}_2$  decomposes to CO which then forms carbon by reaction with free metal. This mechanism is predicated on the available space model. The free carbon then initiates carburization in the inner scale. In support of this theory, the results indicate that pure Fe exhibited no carburization because there is no available space. For the carburization of Fe12Cr, notable carburization was observed under the duplex oxide nodular regions but not where only the thin protective chromia film existed. This observation supports the hypothesis that available space model is operational during carburization.

In general, optical microscopy, SEM-EDS, microhardness tests, GDMS, GDOES, and EPMA-WDS techniques were applied to evaluate carburization in T122 and T92 steels. The results of all these characterization techniques were self-consistent and indicative of parabolic diffusion of carbon



into the base steel. The carbon diffusion coefficient in T92 was calculated experimentally. The T122 steel also showed a similar parabolic trend in carbon diffusion. A rate equation available in literature was used for understanding carbide precipitation as a function of depth. The carbon diffusion profiles and depths, suggest the formation of  $M_{23}C_6$  and  $M_7C_3$  carbide phase particles. For T22, T92, T122 ferritic-martensitic steels, the depth of carburization increases as the carbide forming alloying elements (i.e., Cr) in the steel decreases.

Carburization occurs concurrently with oxidation in S-CO<sub>2</sub> environment and it has been shown in this study that the depth of carburization is substantially greater than the oxide layer thickness. Typically, carburization while hardening the material also leads to embrittlement. This loss of ductility can cause catastrophic failure. Therefore, the ductility of the samples must be evaluated with tensile tests before application into Brayton cycle components. Additionally, future work should focus on predicting carbon enrichment in the steels during the life time of the cycle and on establishing that even with the associated loss in ductility mechanical integrity of components can be preserved in the pressurized environment of the S-CO<sub>2</sub> Brayton cycle.

### Bibliography Consulted

- [1] V. Dostal, "A Super Critical Carbon Dioxide Cycle for Next Generation Nuclear Reactors", Phd thesis, Massachusetts Institute of Technology, 2004.
- [2] P. HEJZLAR et al., "Assessment of Gas Cooled Fast Reactor with Indirect Supercritical CO<sub>2</sub> Cycle", Proc. 2005 International Congress Advances in Nuclear Power Plants (ICAPP '05), Seoul, Korea, May 15–19, 2005, American Nuclear Society, 2005.
- [3] A. Moiseyev, J. S. James, "Investigation of Alternative Layouts for the Supercritical Carbon Dioxide Brayton Cycle for a Sodium-Cooled Fast Reactor", Nuclear Engineering and Design, 239 (2009), 1362–1371.
- [4] A. Yoonhan, L. I. Jeong, "Study of Various Brayton Cycle Designs for Small Modular Sodium-Cooled Fast Reactor", Nuclear Engineering and Design, 276 (2014), 128–141.
- [5] A. Yoonhan et al., "Review of Super Critical CO<sub>2</sub> Power Cycle Technology and Current Status of Research of Development", Nuclear Engineering and Technology, 47 (2015), 647-661.
- [6] T. S. Craig, M. Zhiwen, D. John, "Super Critical Power Cycle Configurations for Use in Concentrating Solar Power Systems", Proceedings of ASME Turbo Expo, Copenhagen, Denmark, 2012.
- [7] M. Zhiwen, T. S. Craig, "Advanced Supercritical Carbon Dioxide Power Cycle Configurations for Use in Concentrating Solar Power Systems", Supercritical CO<sub>2</sub> Power Cycle Symposium Boulder, Colorado, 2011.
- [8] C. Wagner, Beitrag zur Theorie des Anlaufvorgangs, Zeitschrift für Physikalische Chemie (1933) B41:25-41
- [9] Tammann, G. and Koster, W. (1922). Z. Anorg. Chem., 123.
- [10] Pilling, N.B. and Bedworth, R.E. (1923). The Oxidation of Metals at High Temperature, Journal of the Institute of Metals, Vol. 29, pp. 529-582.
- [11] Dunn, J.S. (1926). The High Temperature Oxidation of Metals, Proc. R. Soc. Lond. A. 111, pp. 203-209.
- [12] Hauffe, Karl. "The Mechanism of Oxidation of Metals and Alloys at High Temperatures." Progress in Metal Physics 4, no. C (1953): 71-104.
- [13] Fromhold Jr., A. "Parabolic Oxidation of Metals." Physics Letters A 29, no. 3 (1969): 157-58.
- [14] A. S. Khanna, "Introduction to High Temperature Oxidation and Corrosion", Materials Park, OH: ASM International, 2002, ISBN:0-87170-762-4.
- [15] E. G. Feher, "The Supercritical Thermodynamic Power Cycle", in Adv. Energy Conversion Eng., The American Soc. Of Mechanical Engineers, New York, pp.37-44 (1967).

- [16] Martinelli, L., et al. "Oxidation mechanism of a Fe-9Cr-1Mo steel by liquid Pb-Bi eutectic alloy (Part I)." *Corrosion Science* 50.9 (2008): 2523-2536.
- [17] Martinelli, L., et al. "Oxidation mechanism of an Fe-9Cr-1Mo steel by liquid Pb-Bi eutectic alloy at 470 C (Part II)." *Corrosion Science* 50.9 (2008): 2537-2548.
- [18] Martinelli, L., et al. "Oxidation mechanism of a Fe-9Cr-1Mo steel by liquid Pb-Bi eutectic alloy (Part III)." *Corrosion Science* 50.9 (2008): 2549-2559.
- [19] A. S. Khanna, "Introduction to High Temperature Oxidation and Corrosion", Materials Park, OH: ASM International, 2002, ISBN:0-87170-762-4.
- [20] N. Briks et, al., "Introduction to the High-Temperature Oxidation of Metals", 2nd Edition, Cambridge University Press, ISBN: 978-0-511-16089
- [21] D. J. Young, "High Temperature Oxidation and Corrosion of Metals", Amsterdam, Elsevier, 2008.
- [22] H. Mehrer, 'Diffusion in Solids: Fundamentals, Methods, Materials, Diffusion-controlled Processes' Berlin: Springer, 2007.
- [23] B. Gleeson, (2000) High-Temperature Corrosion of Metallic Alloys and Coatings, in *Materials Science and Technology: A Comprehensive Treatment: Corrosion and Environmental Degradation*, Volumes I+II (eds R. W. Cahn, P. Haasen and E. J. Kramer), Wiley-VCH Verlag GmbH, Weinheim, Germany. doi: 10.1002/9783527619306.ch14
- [24] P. Kofstad, *High Temperature Corrosion*, Elsevier Applied Science Publisher Ltd, London, UK, (1988)
- [25] G. Y. Lai, *High-Temperature Corrosion and Materials Applications*, ASM International, Materials Park, OH, USA, (2007)
- [26] K. G. Nickel, and Y. G. Gogotsi, (2000) *Corrosion of Hard Materials*, in *Handbook of Ceramic Hard Materials* (ed R. Riedel), Wiley-VCH Verlag GmbH, Weinheim, Germany. doi: 10.1002/9783527618217.ch5
- [27] H. E. Schoeller, "Thermodynamics and kinetics of oxidation and temperature dependent mechanical characterization of pure indium solder," M.S. thesis, Dept. Mater. Eng., Binghamton Univ., Binghamton, NY, USA, 2007.
- [28] N. Perez, "Electrochemistry and Corrosion Science" Springer International Publishing, 2016, ISBN 978-3-319-24847-9. DOI 10.1007/978-3-319-24847-9
- [29] Craig, Bruce D. *Fundamental aspects of corrosion films in corrosion science*. Springer Science & Business Media, 2013.
- [30] Yvon, P. (2016). *Structural Materials for Generation IV Nuclear Reactors*. Kent: Elsevier Science.
- [31] Gibbs, G. B. "A model for mild steel oxidation in CO<sub>2</sub>." *Oxidation of Metals* 7.3 (1973): 173-184.
- [32] Gibbs, G. B., et al. "Scale stresses during protective and breakaway corrosion of iron and rimming steel in CO<sub>2</sub>." *Oxidation of Metals* 7.3 (1973): 185-200.
- [33] Pritchard, A. M., et al. "The mechanisms of breakaway oxidation of three mild steels in high-pressure CO<sub>2</sub> at 500° C." *Oxidation of Metals* 9.2 (1975): 181-214.
- [34] Surman, P. L., and A. M. Brown. "The role of carbon in the breakaway oxidation of mild steel in high pressure carbon dioxide." *Corrosion of steels in CO<sub>2</sub>*. Proceedings of the British Nuclear Energy Society international conference at Reading University, 23-24 September 1974. 1974.
- [35] Surman, P. L. "The oxidation of iron at controlled oxygen partial pressures—II. Carbon monoxide-carbon dioxide." *Corrosion Science* 13.11 (1973): 825-832.
- [36] Antill, J. E., K. A. Peakall, and J. B. Warburton. "Oxidation of mild and low-alloy steels in CO<sub>2</sub> based atmospheres." *Corrosion Science* 8.9 (1968): 689-701.
- [37] Richardson, Tony J.A. (2009). *Shreir's Corrosion*. Elsevier Science.

- [38] Driscoll, T. J. "The initial oxidation of iron at 200° and 300° C and the effect of surface sulfur." *Oxidation of Metals* 16.1-2 (1981): 107-131.
- [39] Hussey, R. J., and M. Cohen. "The oxidation of Fe in the temperature range 450–550° C—I. The pressure range  $10^{-6}$  -  $10^{-4}$  torr." *Corrosion Science* 11.10 (1971): 699-711.
- [40] Hussey, R. J., and M. Cohen. "The oxidation of Fe in the temperature range 450–550° C—II. The pressure range  $10^{-3}$  - 760 torr." *Corrosion Science* 11.10 (1971): 713-721.
- [41] Goursat, A. G., and W. W. Smeltzer. "Kinetics and morphological development of the oxide scale on iron at 800° C in oxygen at  $2.5 \times 10^{-3}$  to  $3.0 \times 10^{-1}$  torr pressure." *Journal of The Electrochemical Society* 120.3 (1973): 390-395.
- [42] Hussey, R. J., et al. "The growth and structure of oxide films formed on Fe in O<sub>2</sub> and CO<sub>2</sub> at 550 C." *Oxidation of Metals* 11.2 (1977): 65-79.
- [43] Bertrand, Nathalie, et al. "Iron oxidation at low temperature (260–500 C) in air and the effect of water vapor." *Oxidation of metals* 73.1-2 (2010): 139-162.
- [44] Pettit, F., R. Yinger, and J. B. Wagner. "The mechanism of oxidation of iron in carbon monoxide-carbon dioxide mixtures." *Acta Metallurgica* 8.9 (1960): 617-623.
- [45] K. HAUFFE and P. PFEIFFER, Z. Elektrochem. 56,390 (1952); X. Metallk. 44, 27 (1953).
- [46] Pettit, F. S., and J. B. Wagner. "Transition from the linear to the parabolic rate law during the oxidation of iron to wüstite in CO-CO<sub>2</sub> mixtures." *Acta Metallurgica* 12.1 (1964): 35-40.
- [47] Bredeesen, Rune, and Per Kofstad. "On the oxidation of iron in CO<sub>2</sub>+ CO gas mixtures: I. Scale morphology and reaction kinetics." *Oxidation of Metals* 34.5-6 (1990): 361-379.
- [48] Bredeesen, Rune, and Per Kofstad. "On the oxidation of iron in CO<sub>2</sub>+ CO mixtures: II. Reaction mechanisms during initial oxidation." *Oxidation of Metals* 35.1-2 (1991): 107-137.
- [49] Bredeesen, Rune, and Per Kofstad. "On the oxidation of iron in CO<sub>2</sub>+ CO mixtures. III: Coupled linear parabolic kinetics." *Oxidation of Metals* 36.1-2 (1991): 25-56.
- [50] Graham, M. J. "Transition from linear to parabolic kinetics during the oxidation of iron in CO<sub>2</sub> at 400–500° C." *Corrosion Science* 12.8 (1972): 683.
- [51] Castle, P. J., and R. E. Smallman. "The protective oxidation of a 9.75% Cr-Fe alloy in CO<sub>2</sub>." *Corrosion science* 24.2 (1984): 99-109.
- [52] Gibbs, Jonathan Paul. *Corrosion of various engineering alloys in supercritical carbon dioxide*. Diss. Massachusetts Institute of Technology, 2010.
- [53] Furukawa, T., Inagaki, Y., Aritomi, M., 2010. *Journal of Power and Energy Systems* Vol. 4 (No. 1), 252-261.
- [54] Furukawa, T., Y. Inagaki, and M. Aritomi. "Compatibility of FBR structural materials with supercritical carbon dioxide." *Progress in Nuclear Energy* 53.7 (2011): 1050-1055.
- [55] Gibbs, G. B., and R. Hales. "The influence of metal lattice vacancies on the oxidation of high temperature materials." *Corrosion Science* 17.6 (1977): 487499-497507.
- [56] Rouillard, F., F. Charton, and G. Moine. "Corrosion behavior of different metallic materials in supercritical carbon dioxide at 550 C and 250 bars." *Corrosion, The Journal of Science and Engineering* 67.9 (2011): 095001-095001.
- [57] Rouillard, F., et al. "Corrosion of 9Cr steel in CO<sub>2</sub> at intermediate temperature I: Mechanism of void-induced duplex oxide formation." *Oxidation of metals* 77.1-2 (2012): 27-55.
- [58] Rouillard, F., et al. "Corrosion of 9Cr steel in CO<sub>2</sub> at intermediate temperature II: Mechanism of carburization." *Oxidation of Metals* 77.1-2 (2012): 57-70.
- [59] Rouillard, F., and L. Martinelli. "Corrosion of 9Cr steel in CO<sub>2</sub> at intermediate temperature III: Modelling and simulation of void-induced duplex oxide growth." *Oxidation of metals* 77.1-2 (2012): 71-83.
- [60] Tan, Lizhen, et al. "Corrosion of austenitic and ferritic-martensitic steels exposed to supercritical carbon dioxide." *Corrosion Science* 53.10 (2011): 3273-3280.

- [61] Cao, G., et al. "Corrosion of austenitic alloys in high temperature supercritical carbon dioxide." *Corrosion Science* 60 (2012): 246-255.
- [62] Firouzdar, V., et al. "Corrosion of a stainless steel and nickel-based alloys in high temperature supercritical carbon dioxide environment." *Corrosion Science* 69 (2013): 281-291.
- [63] He, Ling-Feng, et al. "Corrosion behavior of an alumina forming austenitic steel exposed to supercritical carbon dioxide." *Corrosion Science* 82 (2014): 67-76.
- [64] Pint, Bruce A., and J. A. Keiser. "The Effect of Temperature on the sCO<sub>2</sub> Compatibility of Conventional Structural Alloys." 4th International Symposium-Supercritical CO<sub>2</sub> Power Cycles, Pittsburgh, PA. 2014.
- [65] Lee, Ho Jung, H. Kim, and C. Jang. "Compatibility of candidate structural materials in high-temperature S-CO<sub>2</sub> environment." 4th International Symposium-Supercritical CO<sub>2</sub> Power Cycles, Pittsburgh, PA. 2014.
- [66] Lee, Ho Jung, et al. "Corrosion and carburization behavior of chromia-forming heat resistant alloys in a high-temperature supercritical-carbon dioxide environment." *Corrosion Science* 99 (2015): 227-239.
- [67] Pint, B. A., et al. "The effect of Temperature and Pressure on Super Critical CO<sub>2</sub> Compatibility of Conventional Structural Alloys." 5th International Symposium-Supercritical CO<sub>2</sub> Power Cycles, San Antonio, TX. 2016.
- [68] Pint, B. A., R. G. Brese, and J. R. Keiser. "Effect of pressure on supercritical CO<sub>2</sub> compatibility of structural alloys at 750° C." *Materials and Corrosion* (2016).
- [69] Pint, Bruce A., and James R. Keiser. "Initial assessment of Ni-base alloy performance in 0.1 MPa and supercritical CO<sub>2</sub>." *JOM* 67.11 (2015): 2615-2620.
- [70] Furukawa, Tomohiro, and Fabien Rouillard. "Oxidation and carburizing of FBR structural materials in carbon dioxide." *Progress in Nuclear Energy* 82 (2015): 136-141.
- [71] Rouillard, F., and T. Furukawa. "Corrosion of 9-12Cr ferritic–martensitic steels in high-temperature CO<sub>2</sub>." *Corrosion Science* 105 (2016): 120-132.
- [72] Holcomb, Gordon R., Casey Carney, and Ömer N. Doğan. "Oxidation of alloys for energy applications in supercritical CO<sub>2</sub> and H<sub>2</sub>O." *Corrosion Science* (2016).
- [73] Brückman, A., and J. Romanski. "On the mechanism of sulphide scale formation on iron." *Corrosion Science* 5.3 (1965): 185IN5191-190IN8.
- [74] Werber, T. "Verwendung der radioaktiven isotope desoxydators in den untersuchungen des mechanismus der hochtemperaturoxydation von metallen und legierungen." *Corrosion Science* 5.10 (1965): 717-727.
- [75] Mrowec, S. "On the mechanism of high temperature oxidation of metals and alloys." *Corrosion Science* 7.9 (1967): 563-578.
- [76] Castle, James E., and P. L. Surman. "Self-diffusion of oxygen in magnetite. Techniques for sampling and isotopic analysis of micro quantities of water." *The Journal of Physical Chemistry* 71.13 (1967): 4255-4259.
- [77] Surman, P. L., and J. E. Castle. "Gas phase transport in the oxidation of Fe and steel." *Corrosion Science* 9.10 (1969): 771IN1773-772IN2777.
- [78] Brückman, A., R. Emmerich, and S. Mrowec. "Investigation of the high-temperature oxidation of Fe-Cr alloys by means of the isotope<sup>18</sup>O." *Oxidation of Metals* 5.2 (1972): 137-147.
- [79] Atkinson, A. "Transport processes during the growth of oxide films at elevated temperature." *Reviews of Modern Physics* 57.2 (1985): 437.
- [80] Zhang, J., and Ning Li. "Oxidation mechanism of steels in liquid–lead alloys." *Oxidation of Metals* 63.5-6 (2005): 353-381.
- [81] Martinelli, L., and F. Balbaud-Célériér. "Modelling of the oxide scale formation on Fe-Cr steel during exposure in liquid lead-bismuth eutectic in the 450–600° C temperature range." *Materials and Corrosion* 62.6 (2011): 531-542.

- [82] Martinelli, L., et al. "Comparative oxidation behavior of Fe-9Cr steel in CO<sub>2</sub> and H<sub>2</sub>O at 550° C: Detailed analysis of the inner oxide layer." *Corrosion Science* 100 (2015): 253-266.
- [83] Grabke, H. J., and I. Wolf. "Carburization and oxidation." *Materials Science and Engineering* 87 (1987): 23-33.
- [84] Fujii, C. T., and R. A. Meussner. "Carburization of Fe-Cr Alloys During Oxidation in Dry Carbon Dioxide." *Journal of the Electrochemical Society* 114.5 (1967): 435-442.
- [85] Gheno, Thomas, et al. "Carburization of ferritic Fe-Cr alloys by low carbon activity gases." *Corrosion Science* 53.9 (2011): 2767-2777.
- [86] Young, D., et al. "Non-steady state carburization of martensitic 9–12% Cr steels in CO<sub>2</sub> rich gases at 550° C." *Corrosion science* 88 (2014): 161-169.
- [87] Shatynski, Stephen R. "The thermochemistry of transition metal carbides." *Oxidation of Metals* 13.2 (1979): 105-118.
- [88] Klueh, R. L. "Elevated temperature ferritic and martensitic steels and their application to future nuclear reactors." *International Materials Reviews* 50.5 (2005): 287-310.
- [89] Klueh, R. L., and A. T. Nelson. "Ferritic/martensitic steels for next-generation reactors." *Journal of Nuclear Materials* 371.1 (2007): 37-52.
- [90] Klueh, Ronald L., and Donald R. Harries. *High-chromium ferritic and martensitic steels for nuclear applications*. Vol. 3. ASTM International, 2001.
- [91] Olszewski, Tomasz. *Oxidation Mechanisms of Materials for Heat Exchanging Components in CO<sub>2</sub>/H<sub>2</sub>O-containing Gases Relevant to Oxy-fuel Environments*. Vol. 159. Forschungszentrum Jülich, 2012.
- [92] Nguyen, Thuan Dinh, Jianqiang Zhang, and David J. Young. "Effects of silicon on high temperature corrosion of Fe-Cr and Fe-Cr-Ni alloys in carbon dioxide." *Oxidation of metals* 81.5-6 (2014): 549-574.
- [93] Huntz, A. M., et al. "Effect of silicon on the oxidation resistance of 9% Cr steels." *Applied Surface Science* 207.1 (2003): 255-275.
- [94] Taylor, J. W., and P. V. Trotsenberg. "9Cr-Mo steels breakaway effects in CO<sub>2</sub> coolant media." *Corrosion of steels in CO<sub>2</sub>*. Proceedings of the British Nuclear Energy Society international conference at Reading University, 23-24 September 1974. 1974.
- [95] Zhang, Zhuyao, G. B. Holloway, and A. W. Marshall. "Properties of T/P92 steel weld metals for ultra-super critical (USC) power plant." *Weld. World* 52 (2008): 455.
- [96] Richardson, Tony JA. *Shreir's Corrosion*. Elsevier, 2009.
- [97] ASTM E3-11 Standard Guide for Preparation of Metallographic Specimens, ASTM International, West Conshohocken, PA, 2011, <https://doi.org/10.1520/E0003-11>
- [98] ASTM E407-07(2015)e1 Standard Practice for Microetching Metals and Alloys, ASTM International, West Conshohocken, PA, 2015, <https://doi.org/10.1520/E0407-07R15E01>
- [99] Kanematsu, Hideyuki, and Dana M. Barry, eds. *Corrosion Control and Surface Finishing: Environmentally Friendly Approaches*. Springer, 2016.
- [100] Birkholz, Mario. *Thin film analysis by X-ray scattering*. John Wiley & Sons, 2006.
- [101] Timár-Balázsy, Ágnes, and Dinah Eastop. *Chemical principles of textile conservation*. Routledge, 1998.
- [102] Huebschen, Gerhard, et al., eds. *Materials Characterization Using Nondestructive Evaluation (NDE) Methods*. Woodhead Publishing, 2016.
- [103] "CCWJ Teaching." CCWJ Teaching. N.p., n.d. Web. 05 Dec. 2016.
- [104] Bell, David C., and Natasha Erdman, eds. *Low voltage electron microscopy: principles and applications*. John Wiley & Sons, 2012.
- [105] "What Is EMPA?" or is it EMPA? N.p., n.d. Web. 06 Dec. 2016.
- [106] "Electron Probe Micro-analyzer (EPMA)." *Techniques*. N.p., n.d. Web. 06 Dec. 2016.

- [107] Ul-Hamid, Anwar, et al. "Quantitative WDS analysis using electron probe microanalyzer." *Materials characterization* 56.3 (2006): 192-199.
- [108] "Wavelength-dispersive Spectroscopy (WDS)." *Geochemical Instrumentation and Analysis*. N.p., n.d. Web. 06 Dec. 2016.
- [109] Jowitt, R., M. Pichilingi, and J. Davey. "Evaluation of glow discharge mass spectrometry(GDMS) for direct analysis in the steel industry." EUR(Luxembourg) (1999).
- [110] Lindon, John C. *Encyclopedia of spectroscopy and spectrometry*. Academic Press, 2010.
- [111] ASTM E1077-14 Standard Test Methods for Estimating the Depth of Decarburization of Steel Specimens, ASTM International, West Conshohocken, PA, 2014, <https://doi.org/10.1520/E1077>
- [112] ASTM E384-16 Standard Test Method for Microindentation Hardness of Materials, ASTM International, West Conshohocken, PA, 2016, <https://doi.org/10.1520/E0384-16>
- [113] Callister, William D., and David G. Rethwisch. *Fundamentals of materials science and engineering: an integrated approach*. John Wiley & Sons, 2012.
- [114] Nayar, Alok. *Testing of Metals*. Tata McGraw-Hill Education, 2005.
- [115] Martinelli, L., et al. "Comparative oxidation behavior of Fe-9Cr steel in CO<sub>2</sub> and H<sub>2</sub>O at 550° C: Detailed analysis of the inner oxide layer." *Corrosion Science* 100 (2015): 253-266.
- [116] M. Backhaus-Ricoult, R. Dieckmann, Ber Bunsenges. Phys. Chem, 1986, 90, 690.
- [117] Töpfer, J., S. Aggarwal, and R. Dieckmann. "Point defects and cation tracer diffusion in (Cr x Fe 1- x) 3- δ O 4 spinels." *Solid State Ionics* 81.3 (1995): 251-266.
- [118] Perry, Dale L. *Handbook of inorganic compounds*. CRC press, 2016.
- [119] Barthelmy, Dave. "Magnetite Mineral Data." *Magnetite Mineral Data*. N.p., n.d. Web. 28 Nov. 2016.
- [120] Blaney, Lee. "Magnetite (Fe<sub>3</sub>O<sub>4</sub>): Properties, synthesis, and applications." (2007).
- [121] Tinkler, S., and R. Dieckmann. "Limited role of cation bulk diffusion in the oxidation of pure iron to magnetite." *Journal of materials science* 27.14 (1992): 3799-3802.
- [122] Mehrer, Helmut. *Diffusion in solids: fundamentals, methods, materials, diffusion-controlled processes*. Vol. 155. Springer Science & Business Media, 2007.
- [123] E. W. Hart, *Acta Metallurgica* 5, 597 (1957)
- [124] Ueda, Mitsutoshi, and Toshio Maruyama. "Estimation of the Effect of Grain Boundary Diffusion on Microstructure Development in Magnetite Bi-crystal under Oxygen Chemical Potential Gradient at 823 K." *Journal of the Korean Ceramic Society* 49.1 (2012): 37-42.
- [125] Gegner, Jürgen. "Diffusion modeling of decarburization microhardness-distance profiles." *The fourth international conference on mathematical modeling and computer simulation of materials technologies*. 2006.
- [126] Budke, E., Ch Herzig, and H. Wever. "Volume and grain boundary diffusion of 14C in α-Fe." *Physica status solidi (a)* 127.1 (1991): 87-101.
- [127] Zang, Ling. "Diffusion: Fick's second law." N.p., n.d. Web. 22 Dec. 2016.